



**HAL**  
open science

# Architecturation de tôles métalliques par traitement laser localisé

Zhige Wang

► **To cite this version:**

Zhige Wang. Architecturation de tôles métalliques par traitement laser localisé. Mécanique des matériaux [physics.class-ph]. HESAM Université, 2022. Français. NNT : 2022HESAE065 . tel-04041478

**HAL Id: tel-04041478**

**<https://pastel.hal.science/tel-04041478>**

Submitted on 22 Mar 2023

**HAL** is a multi-disciplinary open access archive for the deposit and dissemination of scientific research documents, whether they are published or not. The documents may come from teaching and research institutions in France or abroad, or from public or private research centers.

L'archive ouverte pluridisciplinaire **HAL**, est destinée au dépôt et à la diffusion de documents scientifiques de niveau recherche, publiés ou non, émanant des établissements d'enseignement et de recherche français ou étrangers, des laboratoires publics ou privés.

**ÉCOLE DOCTORALE SCIENCES DES MÉTIERS DE L'INGÉNIEUR**  
[Laboratoire PIMM – Campus de Paris]

# THÈSE

présentée par : **Zhige WANG**

soutenue le : 15 décembre 2022

pour obtenir le grade de : **Docteur d'HESAM Université**

préparée à : **École Nationale Supérieure d'Arts et Métiers**

Spécialité : **Mécanique - Matériaux**

## Architecturation de tôles métalliques par traitement laser localisé

THÈSE dirigée par :

[**M. DIRRENBERGER Justin**]

### Jury

**M. Hatem ZUROB**, Professeur, McMaster University

**Mme. Mathilde LAURENT-BROCQ**, Chargée de recherche CNRS, ICMPE

**M. Olivier BOUAZIZ**, Professeur des universités, Université de Lorraine

**Mme Dominique POQUILLON**, Professeur des universités, INP Toulouse

**Mme Aude SIMAR**, Professeur, Université Catholique de Louvain

**M. Samuel FOREST**, Directeur de recherches CNRS, Ecole des Mines de Paris

**M. Sébastien ALLAIN**, Professeur des universités, Ecole des Mines de Nancy

**M. Justin DIRRENBERGER**, Maître de conférences, Cnam

Rapporteur

Rapportrice

Examineur

Examinatrice

Examinatrice

Examineur

Examineur

Encadrant

T  
H  
È  
S  
E



回首向来萧瑟处

归去

也无风雨也无晴

—苏轼《定风波》 公元 1082 年

# Remerciements

Je voudrais tout d'abord remercier mon directeur de thèse, M. Justin Dirrenberger, pour m'avoir choisi il y a trois ans. Justin, merci beaucoup pour proposer ce sujet de thèse très créatif avec plein d'imagination et d'idées, merci pour ta confiance et ton encouragement durant ces trois années. Je suis énormément reconnaissante d'avoir la chance de travailler avec toi.

Je voudrais exprimer mes sincères remerciements aux membres de jury : M. Zurob, Mme. Laurent-Brocq, M. Bouaziz, Mme. Poquillon, Mme. Simar, M. Forest et M. Allain, pour avoir accepté d'évaluer mon travail et apporté des précieuses opinions. Surtout, je remercie M. Zurob et M. Bouaziz, vos recherches précédentes ont bien inspiré cette thèse.

Je remercie également Pierre Lapouge pour m'apprendre à utiliser tous ces équipements durant cette thèse, merci de m'avoir répondu chaque fois quand je te sollicitais, sans toi, le travail ne pourrait pas être réalisé.

Je remercie tout le laboratoire PIMM pour m'accueillir durant ces trois années, merci à Sébastien pour les mesures SDL, merci à Zehoua et Hamza pour vos aides au MEB, merci à Jean-Baptiste pour la mesure des champs, Vincent pour les mesures Rayon-X. Je voudrais remercier Yannick et Jean-Baptiste de l'atelier de ENSAM pour la découpe des échantillons et M. Mercadié de l'IUT Cachan pour la découpe jet d'eau. Aussi merci à tous d'autres personnes du labo que j'ai croisées pour les discussions intéressantes.

Enfin, merci pour tous les doctorants du PIMM, je vous souhaite bon courage et bonne continuation.

## Résumé

Dans cette étude, le procédé laser est appliqué pour fabriquer des matériaux architecturés à base de d'acier avec des renforcements localisés de différentes géométries. Deux types de tôles d'acier ont été choisis pour réaliser cette étude, un acier inoxydable ferritique AISI 430 et un acier avec 0,2% de carbone recuit qui a une microstructure de ferrite-perlite.

Lors de la première étape, des tôles en acier inoxydable ferritique AISI 430 contenant 18 % de Cr ont été durcies par des faisceaux laser à onde continue dans différentes conditions. Une plate-forme de traitement laser a été développée avec deux lasers placés symétriquement. Ils peuvent fonctionner simultanément afin d'obtenir une microstructure homogène dans l'épaisseur de l'échantillon et d'éviter la surchauffe associée aux traitements laser simples sur une surface. L'influence de la densité d'énergie linéaire et du gaz de protection sur la microstructure et la dureté est étudiée pour les traitements laser simples et doubles. Le comportement en traction et l'effet d'oxydation pendant le traitement sont également étudiés. Avec un pic de température autour de  $T_m$ , la micro-dureté locale du matériau traité est supérieure de 90% au matériau de base, tandis que les échantillons entièrement traités par le laser multipiste présentent une augmentation de 60% de la limite d'élasticité et de 45,8% de la résistance à la rupture. Ce durcissement est introduit par la formation de martensite et de carbures de chrome lors d'un refroidissement rapide malgré une faible teneur en carbone et un grossissement des grains spectaculaire. Ces résultats pourraient être utiles afin de modifier localement le comportement de l'acier inoxydable ferritique pour répondre aux exigences industrielles. Le paramètre du laser qui conduit à la résistance la plus élevée a été choisi pour fabriquer des matériaux architecturés avec des renforcements droits et sinusoïdaux et leurs comportements mécaniques ont été caractérisés par essais de traction avec le système de corrélation d'images et comparés aux résultats de simulation par la méthode des éléments finis. Aucun effet d'amélioration des courbes sinusoïdales sur la ductilité n'a été trouvé en raison du dépliage incomplet et du contraste insuffisant de résistance entre la matrice et le renforcement.

Dans la deuxième étape, la carburation directe par faisceau laser est mise en œuvre pour la première fois sur des tôles d'AISI 430 avec revêtement en graphite dans différentes conditions. La morphologie, la constitution de phase, la teneur en carbone, la micro-dureté et le comportement en traction sont étudiés pour évaluer l'effet de carburation par laser. La zone carburée présente des morphologies différentes selon la densité d'énergie linéique. La teneur en carbone la plus faible est d'environ 0,4% et l'austénite devient la phase principale. La ferrite delta se trouve dans la zone carburée, qui ressemble à acier duplex. La dureté de la zone carburée a été augmentée d'au moins 130 %, la limite d'élasticité et la résistance à la rupture des échantillons entièrement carburés peuvent augmenter respectivement de 90 % et 85 %. Cet effet de durcissement est dû à la précipitation des carbures formés lors de la solidification, qui fixent les dislocations et les joints de grains. Ces améliorations pourraient être utiles pour modifier localement l'acier inoxydable ferritique pour répondre aux besoins industriels tels que les surfaces résistantes à l'usure. Le paramètre laser produisant le plus d'effet de durcissement a été pris pour introduire des renforcements droits et sinusoïdaux dans la matrice et leur

comportement mécanique a été caractérisé. Un effet d'amélioration très limité sur la ductilité induite par renforcement sinusoïdal a été observé.

Dans la dernière partie, la trempe laser est appliquée à l'acier ferritique ductile afin d'introduire des renforts martensitiques droits et sinusoïdaux. Le comportement en traction d'échantillons architecturés est étudié à l'aide de la simulation et d'essais mécaniques pour illustrer l'effet des renforcements sinusoïdaux sur la ductilité. Les résultats montrent qu'avec la même fraction volumique renforcée de 24 %, une augmentation de la hauteur/période de la sinusoïde conduit à un gain de ductilité avec une perte de limite d'élasticité et de résistance à la rupture. Cet effet bénéfique sur la ductilité est dû au processus de dépliage des courbes sinusoïdales qui introduisent un écrouissage géométrique lors de la traction. Des simulations étendues sont effectuées sur différentes hauteurs/périodes des sinusoïdales et les tendances d'évolution de la résistance à la rupture et de la ductilité changent avec différents volumes renforcés. Cette étude propose une perspective sur les matériaux architecturés renforcés par des courbes sinusoïdales. Les paramètres géométriques peuvent être choisis en fonction du comportements mécaniques désirés.

**Mots clés :** matériaux architecturés, procédé laser, durcissement, carburation, écrouissage, aciers, propriétés mécaniques, mesures de champs par corrélation d'image

## Abstract

In this study, laser process is applied to fabricate architected materials based on steel sheets with localized reinforcements of different geometrical patterns. Two kinds of steel sheets were chosen to realize this study, a ferritic stainless steel AISI 430 and an annealed ferrite-pearlite 0.2%-carbon steel.

At the first stage, thin AISI 430 ferritic stainless steel sheets containing 18% Cr were hardened by continuous-wave laser beams under different conditions. A symmetric double laser treatment platform was developed to operate two lasers simultaneously in order to achieve a homogenous microstructure through the specimen and avoid the overheating associated with single laser treatments on one surface. The influence of linear energy density and shielding gas on microstructure and hardness is investigated for both single and double laser treatments. Tensile behavior and oxidation effect during treatment are also studied. With a peak temperature around  $T_m$ , the single-track laser yields local microhardness that is 90% higher than the base material, while samples completely treated by the multi-track laser present a 60% increase in yield stress and 45.8% in ultimate tensile stress. These improvements in mechanical behaviors are driven by the formation of martensite and chromium carbides upon rapid cooling despite poor carbon content and dramatic grain coarsening. These results could be useful in order to locally modify the behavior of medium chrome ferritic stainless steel to meet industrial requirements. The laser parameter which leads to the most strengthening effect was chosen to fabricate straight and corrugation reinforced architected materials and their mechanical behaviors were followed by tensile test with Digital Image Correlation system and compared with Finite Element Method simulation results. No enhancing effect of corrugations on necking strain was found due to the uncompleted unbending and insufficient contrast in strength between matrix and reinforcement.

At the second stage, direct laser beam carburization is implemented for the first time on thin AISI 430 sheets with graphite coating under different conditions. Microstructural morphology, phase constitution, carbon content, microhardness, and tensile behavior are investigated to evaluate the laser carburization effect. The carburized zone presents different morphologies according to the linear energy density of the laser beam. The least carbon content is around 0.4 wt% in the carburized zone where austenite becomes the leading phase. Delta ferrite is found in a cellular carburized area, which resembles a duplex microstructure. The hardness of carburized zone has been at least increased by 130%, the yield strength and ultimate tensile strength of a fully carburized sample can be increased by respectively 90% and 85%. This hardening effect is driven by the precipitation of carbides formed during solidification offering pinning points for dislocations and grain boundaries. These improvements could be useful to modify locally ferritic stainless steel to meet industrial needs such as wear-resistant surfaces. The laser parameter resulting the most strengthening effect was taken to introduce straight and corrugated reinforcements into the matrix and their mechanical response was followed. Very limited enhancing effect on necking strain induced by corrugated reinforcement was observed.

In the last part, laser hardening is applied to ductile ferritic steel in order to introduce straight and corrugated martensitic reinforcements, effectively generating architecture steel sheets. Tensile behavior of laser-architected samples is studied both using FEM simulation and mechanical testing to reveal the effect of laser-induced corrugations on strength and necking strain. Results show that with the same reinforced volume fraction of 24%, an increase in corrugation height/period leads to a gain in necking strain with a loss in yield strength and ultimate tensile stress. This beneficial effect on necking strain is due to the corrugation unbending process which introduces a so-called geometric work hardening during tension. Extended simulations are carried out on various corrugation height/period and the evolution trends of ultimate tensile strength and necking change with different reinforced volumes. This study proposes a perspective on corrugation reinforced architected materials. Corrugation parameters can be chosen to tailor the mechanical behavior of laser-architected materials.

**Keywords:** architected materials, laser processing, hardening, carburization, work hardening, steels, mechanical properties, Digital Image Correlation (DIC)

## Notations

Ac1	Critical temperature at which pearlite begins to transform into austenite during heating
Ac3	Critical temperature at which free ferrite is completely transformed into austenite during heating
E	Young's modulus
$c_p$	Thermal conductivity
$\lambda$	Specific heat capacity
$\theta_a$	Actual temperature
Tm	Melting temperature
Ms	Martensite start temperature
$\Delta G^\circ$	Gibbs free energy
$\epsilon_u$	Uniform plastic deformation
$C_p$	Carbon potential of atmosphere
$C_s$	Carbon potential of surface

## Abbreviations

YS	Yield stress
HSS	High strength steel
AHSS	Advanced high strength steel
LED	Linear energy density
FZ	Fusion zone
HAZ	Heat affected zone
LTHAZ	Low temperature heat affected zone
HTHAZ	High temperature heat affected zone
BM	Base material
DP	Dual-phase steel
CP	Complex phase steel
QP	Quenching and partitioning steel
TRIP	Transformation induced plasticity steel
FSS	Ferritic stainless steel
ASS	Austenitic stainless steel

MSS	Martensitic stainless steel
SMGT	Surface mechanical grinding treatment
SMAT	Surface mechanical attrition treatment
LAM	Laser additive manufacturing
LTSC	Low temperature surface carburization
LC	Laser carburization
SQ	Self-quenching
UTS	Ultimate tensile strength
SEM	Scanning electron microscopy
BSE	Backscattered Electron
EDS	Energy-dispersive spectroscopy
EBS	Electron Backscatter Diffraction
GD-OES	Glow Discharge Optical Emission Spectrometry
FEM	Finite element method
DIC	Digital image correlation

# Contents

Introduction .....	1
Chapter 1 Literature review .....	5
1.1 Architected materials .....	7
1.1.1 Introduction of architected materials .....	7
1.1.2 Examples of architected materials .....	10
1.1.3 Metallic architected materials .....	13
1.1.4 Corrugation geometry .....	16
1.2 Laser treatment on metallic materials .....	19
1.2.1 Introduction of phase transformation in Fe-C system .....	20
1.2.2 Laser hardening .....	22
1.2.3 Laser carburization .....	29
1.2.4 Laser softening .....	34
1.2.5 Laser treatment on other metallic materials .....	40
1.3 Laser treatment applications on architected materials .....	43
1.4 Conclusions and the present work positioning .....	45
Chapter 2 Materials and experimental procedure .....	47
2.1 Materials .....	49
2.1.1 Introduction and properties .....	49
2.1.2 Microstructural characterization and mechanical properties .....	50
2.2 Experimental procedure .....	52
2.2.1 Laser treatment platform and temperature measurement .....	52
2.2.2 Tensile test and DIC equipment .....	57
2.2.3 Finite Element Method simulation of uniaxial tensile test .....	59
2.2.4 Micro-hardness test .....	60
2.2.5 Microstructural observation and phase identification .....	61
2.2.6 X-ray diffraction analysis .....	61
2.2.7 Glow Discharge Optical Emission Spectrometry analysis .....	62
Chapter 3 Laser hardening of 430 ferritic stainless steel for enhanced mechanical properties and corrugation reinforced architected materials .....	65
3.1 Introduction .....	67

3.2	Laser beam characterization.....	67
3.3	Temperature evolution .....	68
3.4	Characterization of laser hardened AISI 430 sheet.....	71
3.4.1	Microstructure .....	71
3.4.2	Microhardness .....	75
3.4.3	Surface state .....	75
3.4.4	Tensile test.....	77
3.4.5	Discussion of laser hardening effect on microstructural and mechanical properties 79	
3.5	Corrugation reinforced architected materials by localized laser hardening.....	82
3.5.1	Identification of matrix and reinforcement mechanical properties .....	82
3.5.2	Prediction of isolated straight and corrugated reinforcement .....	83
3.5.3	Tensile test results of architected materials and discussion.....	85
3.5.4	Future improvements.....	91
3.6	Conclusions .....	91
Chapter 4	Laser carburization strengthening effect of AISI 430 ferritic stainless steel and corrugation reinforced architected materials .....	93
4.1	Introduction .....	95
4.2	Temperature evolution .....	95
4.3	Characterization of laser assisted carburized AISI 430 FSS.....	97
4.3.1	Microstructural analysis and phase identification.....	97
4.3.2	Carburization efficiency .....	103
4.3.3	Microhardness .....	104
4.3.4	Tensile test.....	105
4.3.5	Fractography.....	107
4.3.6	Discussion .....	109
4.4	Corrugation reinforced materials by localized laser carburization .....	111
4.4.1	Identification of matrix and reinforcement mechanical properties .....	111
4.4.2	Prediction of isolated straight and corrugated reinforcement .....	112
4.4.3	Tensile test results of architected materials and discussion.....	114
4.4.4	Future improvements.....	119

4.5	Conclusions .....	119
Chapter 5	Corrugation reinforced architected materials by direct laser hardening on annealed carbon steel .....	121
5.1	Introduction .....	123
5.2	Results .....	124
5.2.1	Mechanical and microstructural characterization of the matrix and reinforcement 124	
5.2.2	Identification of matrix and reinforcement mechanical properties for FEM simulation .....	126
5.2.3	Prediction of isolated straight and corrugated reinforcement mechanical properties .....	127
5.2.4	FEM simulation results of straight and corrugation reinforced specimens.....	128
5.2.5	Tensile test of architected samples .....	129
5.2.6	Fractography.....	133
5.3	Discussion .....	134
5.3.1	Effect of corrugated reinforcement on work hardening .....	134
5.3.2	Perspective of the corrugation effect on necking strain .....	136
5.4	Conclusions .....	139
	Conclusions and Perspectives .....	140
	References .....	144

# Introduction

## Background and motivations

Architected materials have existed in the nature for a long time before the raise of its exact concept in recent years. It refers to heterogeneous materials whose topology of different constituents is well designed and arranged to yield structural or functional synergistic effect. Some trade-offs can be obtained in contradictory properties, such as strength and ductility for structural materials. It is an emerging trend in both academic research and industrial application. Traditionally, mechanical researchers aim to optimize macroscopic part structures to ameliorate the properties and metallurgists focus on chemical composition and forging process to achieve improvements. Architected materials propose the combination of these two aspects, which means to constitute pieces with parts of different natures in an optimized geometrical arrangement.

Laser processing has been developing very fast in the past several decades. It makes use of the thermal effect between laser beam and material surface to accomplish different processing. It can be employed as a thermal source to implement a local heat treatment on materials to modify their properties. Compared to traditional heat treatment in furnace, laser heat treatment has a much greater flexibility. The treatment peak temperature can be trimmed by adjusting laser parameters and the impact is limited within the treated zone without changing the whole piece. Numerous studies have been carried out on the utilization of laser as a heat source to change mechanical or microstructural properties on heat-treatable alloying systems, such as Fe-C or Al alloys.

One of the challenges during the fabrication of architected materials is how to assemble different constituents together. For structural materials, it is important to create a cohesive and strong enough interface between phases so that cracks will not initiate from the interface and lead to an early fracture of the whole piece when it is deformed. Existing fabrication methods confirm that interface strength is a key point of the synergistic effect of architected materials and few efficient solutions has been figured out. Laser additive manufacturing (LAM) has been already well applied for three dimension architected materials. Localized laser treatment can be an option to introduce other constituent phases into a base material without a sharp interface because of the gradient temperature field from treated to untreated part. By changing thermal cycles and operation environment, varying aims can be achieved, such as laser hardening, laser softening and laser alloying. Combination of appropriate base material, laser processing and the geometry of laser trajectory, multi-phase architected materials can be fabricated and may generate synergistic architectural effect. The choice of base material and laser processing is crucial because they act as constituents and its thickness is also limited by the penetration depth of laser processing. In spite of these limitations, laser process can be a potential method to manufacture architected materials and worth further study.

In this context, this study is dedicated to develop a method to fabricate architected materials by localized laser treatment on metallic sheets. Fe-C system is chosen due to plentiful phase possibilities by heat treatment and also it is the most studied and widely used alloying system. Sinusoidal corrugation in the direction of tensile direction is taken as architectural pattern. Precedent studies have shown that isolated corrugations produce a boost in work hardening evolution during tensile test due to the unbending process. Harder corrugated reinforcements embedded in soft matrix inherit this boost and have an enhanced necking strain compared to a straight reinforcement without significant loss in strength. A trade-off in strength and ductility can be realized with this corrugated architectural pattern. Reinforcement geometry and matrix/reinforcement mechanical properties generate this synergistic effect. First experimental tests on post-assembled corrugation-reinforced specimens presented early cracks at the interface which resulted in the lack of architectural effect. If this tentative research succeeds, it can be extended on other alloying systems and architectural patterns.

The first trial is carried out on a ferritic stainless steel, AISI 430. This choice of material is decided for several reasons: firstly, a ductile ferritic steel is required as the matrix material; secondly, there are not enough published research works concerning laser treatment on ferritic stainless steel and this study can fill this blank. The main objectives and methodology as well as the manuscript structure are presented in the following paragraphs.

## **Objectives**

Based on the background introduction of this study, the objectives of this research work can be outlined as follows.

- Investigation of the influence of parameters and operation environment on laser hardening effect on AISI 430 stainless steel.
- Study of the effect of laser parameters on direct laser carburization on AISI 430 stainless steel.
- Exploration of the possibility to fabricate localized laser-hardened or laser-carburized specimen.
- Fabrication of straight and corrugation reinforced architected materials and investigation of the effect of geometric parameters of reinforcement on their macroscopic and local mechanical properties.
- Identification of the necessary conditions for corrugated reinforcement geometry and possible combinations of matrix/reinforcement which allow to yield an enhancing effect on necking strain compared to straight reinforcement.
- Finding suitable matrix and induce reinforcements by laser treatment in appropriate geometry to verify this enhancing effect.

## **Methodology**

To achieve the above-mentioned objectives, following methodology is applied in this study.

- Applying different laser treatment parameters on as-received material directly and covered with graphite spray.
- Optical microscopy and scanning electron microscopy (SEM) observation of laser-hardened and laser-carburized specimens.
- Energy-dispersive spectroscopy (EDS) characterization to reveal element segregation and Electron Backscatter Diffraction (EBSD) and X-ray characterization to identify phase constitution after laser treatment.
- Glow Discharge Optical Emission Spectrometry (GD-OES) analysis to measure surface oxide formation and carburization efficiency.
- Microhardness tests and uniaxial tensile tests to characterize local and macroscopic mechanical properties of laser-hardened and laser-carburized specimens and evaluation of laser parameter effect.
- Finite Element Method (FEM) simulation to predict stress-strain behavior of straight and corrugation reinforced architected materials.
- Tensile test equipped with Digital Image Correlation (DIC) system to analyze local strain evolution and macroscopic stress-strain response of architected materials.
- Optimization reinforcement geometry and the choice of matrix and reinforcement by FEM simulation.

## **Manuscript structure**

This thesis consists of five chapters whose contents are briefly summarized as follows.

Chapter 1 is dedicated to the literature review. This chapter begins with an introduction of the concept of architected materials and different kinds of examples are provided from the natural world to industrial applications for a better understanding of this concept. Metallic architected materials and the effect of corrugation geometry are especially reviewed as they are more concerned to this study. Afterwards, different laser heat treatments on Fe-C system are introduced with their applications, whose thermal cycles vary according to the objective of treatment. Laser heat treatment on other metallic materials is also briefly presented in this part. Finally, the applications of laser heat treatment on architected materials are reviewed, which is not very abundant. That is reason why this present study has chosen laser as a tool to fabricate architected materials.

Chapter 2 presents the chosen materials and experimental procedure in this study. The microstructural and mechanical properties of AISI 430 stainless steel and an annealed steel are investigated. All characterization setups, including temperature evolution measurement, uniaxial tensile test with digital image correlation, metallography preparation and characterization and the details of Finite Element Method simulation procedure to predict the stress-strain behavior of architected materials.

In Chapter 3, the results of laser hardening effect on AISI 430 stainless steel are introduced. Several laser parameters are studied, including input laser power, single or laser irradiation sides and protection shielding gas. The parameters which lead to the most hardening effect are

adopted to fabricate straight and corrugation reinforced architected materials with different corrugation heights and reinforcement volume. The localized laser-hardened architected specimens are then submitted for tensile test and analyzed.

Chapter 4 presents the results of laser carburization effect on AISI 430 stainless steel. It focuses on the influence of laser parameters on morphology, phase constitution and mechanical properties of treated specimens. Similar to Chapter 3, the parameters which leads to the highest strengthening effect are taken to fabricate straight and corrugation reinforced architected specimens with different corrugation heights. Tensile behaviors of localized laser-hardened architected specimens are studied.

In Chapter 5, the fabrication of architected materials is realized by laser hardening on an annealed carbon steel. Varied geometric parameters, corrugation height and period, are applied on corrugated patterns and their effect on macroscopic mechanical properties is discussed. An expanded parametrical study is carried out to look forward to the future aim of laser-induced architected materials.

Finally, conclusions of this research are summarized and perspectives for the future work are described at the end of this manuscript.

# **Chapter 1 Literature review**

## Résumé

Ce chapitre résume une revue de la littérature pour le sujet de recherche : l'architecture de tôles métalliques par optimisation topologique et traitement laser local. Il comprend trois parties. La première partie est une présentation du concept et du développement des matériaux architecturaux, qui sont issus du concept de matériaux composites ou hybrides. Il s'agit des matériaux hétérogènes dans lesquels la topologie des différentes phases est conçue afin de produire des effets synergétiques structurels ou fonctionnels. Des exemples de matériaux architecturés, surtout les matériaux architecturés métalliques sont introduits pour une meilleure compréhension du concept. Dans cette étude, il est suivi par une exploitation de la structure en forme d'ondulation, qui est choisie comme architecture principale pour ses propriétés mécaniques spéciales liées au dépliage. Il peut introduire un écrouissage géométrique lors d'une charge de traction. La deuxième partie se concentre sur le procédé laser. Il s'agit d'utiliser l'effet thermique entre le faisceau laser et la surface du matériau pour différents traitements comme la découpe laser, le perçage laser, le soudage laser, le traitement de surface. Cette partie présente le diagramme de phases Fe-C, puis introduit les méthodes récentes de traitement laser des matériaux métalliques et leurs applications industrielles, y compris le durcissement par trempe laser, la carburation par laser et l'adoucissement par recuit laser. Des études du traitement laser menés sur d'autres matériaux métalliques, par exemple, les alliages d'aluminium et de titane, sont aussi présentées pour compléter cette revue. La dernière partie présente l'application du traitement laser sur les matériaux architecturés. Cette idée a été exploitée par des chercheurs avant l'apparition du concept des matériaux architecturés. Par exemple, de nombreuses méthodes pour durcir la surface des métaux sont nées dans le cadre de stratégie d'adaptation des propriétés locales des pièces pour répondre à un certain besoin. Le procédé laser participe de plus en plus à la fabrication de matériaux architecturés en tant qu'outil pour modifier les propriétés locales et former une structure hiérarchique hétérogène. Néanmoins, il y a un manque d'étude systématique sur les matériaux architecturés induits par laser et sur l'optimisation topologique des géométries des renforcements. Le présent travail vise à étudier la possibilité d'un traitement laser local sur la fabrication de matériaux architecturés. Une forme d'ondulation sinusoïdale est renforcée par laser sur des éprouvettes en acier. Le dépliage de la sinusoïde peut faire rebondir le taux d'écrouissage, au contraire d'une descente continue pour les matériaux homogènes. Ce rebond peut ralentir la descente et retarder la striction et ainsi favoriser la ductilité. Cette méthode pourrait potentiellement mener à une solution évitant l'opposition entre la résistance et la ductilité des matériaux et remplir les zones blanches des cartes de propriétés.

The literature review for this research subject is divided into several sections. The first part is a presentation to the development and designing of architected materials, followed by an exploration of existing work about the corrugation reinforcement, which is the principal archituration chosen for this study. The second part reviews recent laser treatment methods on metallic materials, including laser annealing, laser hardening and laser carburization. The last part introduces the application of laser treatment on architected materials.

### 1.1 Architected materials

#### 1.1.1 Introduction of architected materials

Architected materials, which inherits from the concept of composite and hybrid materials, refers to heterogenous materials in which the topology of different phases is engineered in order to yield structural or functional effects [1,2]. It is an emerging concept in recent years. The motivation comes from material development in order to meet more and more exigent requirements for industrial applications. Taking Figure 1-1 (a) for example, it shows a property map between Young’s modulus and density of different material families [1]. While most space in the middle of the map is occupied, some blank areas appear on the chart. One hole is the upper zone on the left, which presents the combination of a low density and a high Young’s modulus. This can be very interesting to reduce the weight but keep the high strength of some structures at the same time, such as lightening automotive structures to reduce CO<sub>2</sub> emission. However, this combination of properties is hard to access by classical homogeneous materials, architected materials are born to meet the need of pushing the limit of existing property maps [3].

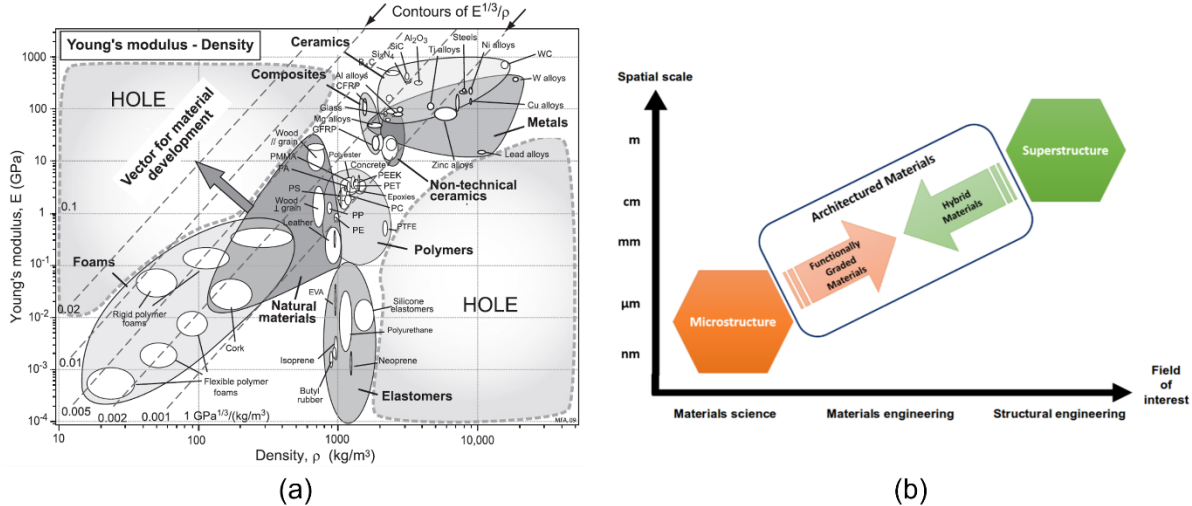


Figure 1-1 (a) Property map of Young’s modulus versus density [1], (b) Architected materials with intermediate length scale between superstructure and microstructure [3].

Figure 1-1 (b) shows architected materials development guideline. Traditionally, mechanics looks for optimizing the topological superstructure and designing the geometry and metallurgists look for controlling the microstructure and adapting the properties. Architected

materials take these two approaches into consideration [3]. It considers of the microstructure and properties of each component, their volume fractions, configurations and position arrangements, and the connection methods between them. The challenge is to combine both the material aspect, such as microstructural and mechanical properties, and the geometrical aspect together. By designing shape and scale of the architecture, architected materials may exhibit optimized properties surpassing the arithmetic average of their constituents. Synergistic effect can be obtained from the interaction and coupling from heterogeneous zones.

It needs to be clear that the heterogeneity of architected materials refers to the inter-zone heterogeneity instead of inside one component [4]. Many conventional materials have heterogeneities in different scales. For example, Dual-phase steel is composed of ferrite matrix and embedded martensite islands, among which ferrite grains provide good ductility and martensite islands increases the strength. High-strength Al alloys are hardened by intermetallic precipitations. These heterogeneities have an efficient strengthening effect but there is not much significant interaction between phases, nor evident synergistic effect. In contrast, architected materials focuses interaction and coupling between different phases to yield superior synergistic effect on taking care of size, geometry and distribution [4].

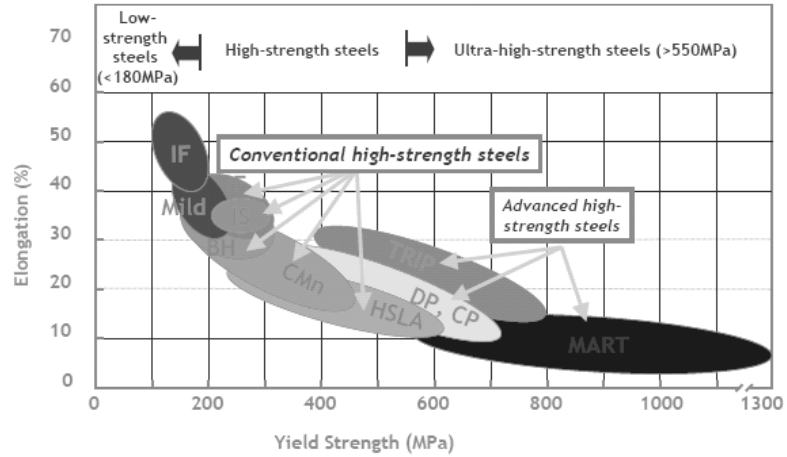


Figure 1-2 Average elongation and yield strength relationship of HSS and AHSS [3].

Like traditional composites, the advantage of architected materials is that they allow access to blank area of property chart, like the hole on the upper left in Figure 1-1 (a) is to be filled with lighter and stiffer materials. But architected materials focus more on configurations and scales of materials. For example, recent years several generations of high strength steels (HSS) and advanced high strength steels (AHSS) have been developed and their elongation-yield strength relationship is shown in Figure 1-2. A trade-off between ductility and strength always exists among these steels, moreover, other metallic materials too. To fill the upper right zone is a persistent aim for researchers, but it is hard to realize with only chemical composition and microstructure control, nor simply superposed composites of different steels. But with a well-designed archituration of steels or other alloys with different properties, the contradictory requirement may be met, and a trade-off of ductility and strength may be established. Fraser et al. [5] proposed an archituration pattern with corrugated reinforcement of steel in copper

matrix and both properties can be enhanced, which will be introduced in detail in the following paragraphs.

Architected materials can be described as ‘A + B + configuration + scale’ [6]. A and B refer to each constituent. Scale means that multiple length scales should be assembled from microscopic level to mesoscopic level, and then a spatial superstructure level [7]. Configuration consists of several aspects to ensure the synergistic benefit effect. One of them is the interface lying between different component, whose strength is a key point of the mechanical performance. A more coherent interface can transfer stress more efficiently and avoid early-stage fracture due to decohesion of interface. Both sharp and graded interfaces exist for designing architected materials. Graded interface can avoid potential problems like stress concentration while sharp interface can arrest cracks and increase the toughness of the whole structure. Thus, it is important to design an interface according to the need. Connectivity is also to take into consideration while designing architectures. For lattice structure, the number of node and struts connectivities decides the structure deformation to be bending dominated or stretching dominated when it is loaded. A lack of struts connectivities leads to a bending dominated structure and an early collapse of struts. On the contrary, sufficient struts connectivities can form a stretching dominated structure and the high structural efficiency can increase the global strength [6,8].



Figure 1-3 Typical trade-off of contradictory properties [9].

In addition to interfacial constitution, new processing technologies or changes in existing methods are needed to fabricate well-designed heterogeneous materials [7]. Recent studies provide ideas on the new routes to produce architected materials based on modifications made on classical processing. Materials with hierarchical architectures are often produced by phase transformation or mechanical deformation or the combination of them taking place during processing [7]. For example, localized carburization or decarburization in furnace with masks

and controlled gas and following quenching can create a heterogeneous repartition of martensite and ferrite on steel pieces and thus a non-uniform hardness map [10,11]. Mechanical grinding treatment can bring surface deformation on steels and introduces a gradient in twin density from the surface layer to the core, which leads to a gradient hardness in thickness and a superior strength–ductility synergy of the whole structure [12].

To conclude, architected materials are heterogeneous materials with well-designed spatial topology constituted by different components. The combination of these components and their configuration results in a synergistic effect from the interaction and coupling of heterogeneous zones to achieve a trade-off of contradictory properties, which are hard to access by classical homogeneous materials. Both structural and functional properties trade-off can be attained, like what are listed in Figure 1-3. There are many factors to consider for architected materials designing to ensure benefit synergistic effect, such as the properties of each component, their volume fraction, configuration, interface, connectivity, etc. New processing technologies or important changes on existing methods are needed to realize the fabrication of architected materials.

### 1.1.2 Examples of architected materials

In order to better understand the concept of architected materials which appears rather abstract, some concrete examples are introduced in this part as a demonstration of the interest to develop this innovative concept.

#### i. Truss structure

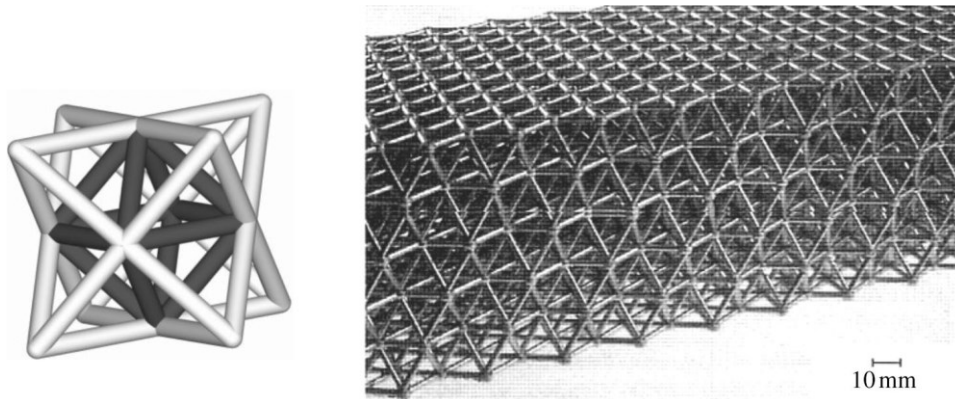


Figure 1-4 A stretch dominated micro truss unit cell and repetitive structure [8].

Truss structure can be considered as a type of architected material. It is an open and repeated lattice structure, where the members are connected at nodes to form essentially triangles and other forms. Figure 1-4 is an example of truss structure with its unit cell. Truss structure has high specific mechanical properties, such as strength, stiffness and energy dissipation with low density [13], and it has been applied in engineering and architecture at different scales for a long time. The Eiffel Tower is one of the most famous examples, steel trusses are placed in several hierarchies of triangles to reduce the weight and to maintain its stability. Nowadays truss structures of smaller size and much complicated form are usually fabricated by additive

manufacturing. They can also be combined with other materials to reinforce their performance, like increasing the strength, corrosion or aerodynamic pressure resistance [13]. As explained in the previous part, the number of nodes and struts decides the degree of freedom and the deformation type of truss structure and thus its strength. The structure in Figure 1-4 has no degree of freedom and is stretch dominated when it is loaded. According to the truss structure material nature, metallic coating can be deposited on polymer trusses [14] and polymer can also be filled into the void area between metallic truss members [13].

### ii. Auxetic materials

Auxetic materials can be recognized as a special kind of truss structure, which corresponds to a kind of structure exhibiting negative Poisson's ratio. This special response is due to a specific arrangement of periodic beam lattice phases, which can improve mechanical properties at the same time. Figure 1-5 (a) and (b) show the two principal mechanism leading to the negative Poisson's ratio, re-entrant and roll-up [15]. Figure 1-5 (c) is an example of 6-connected auxetic chiral materials, which follow the roll-up mechanism at circle inclusion when loaded. This hexachiral structure presents a Poisson's ratio near to -1 [16]. Chiral auxetic structure also exhibit a high dissipation of shear energy due to its rotational deformation [17].

Auxetic materials may exhibit reinforced mechanical properties, such as shear modulus, fracture toughness and indentation resistance, but also acoustic damping and crash resistance. Thus, they may have interesting applications [18]. These planar chiral honeycombs yield a synclastic curvature under an out-of-plane bending. This feature is useful for double-curved dome shape panel applications because they can avoid core buckling.

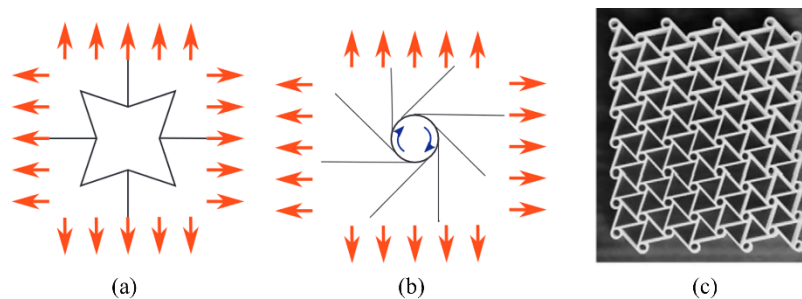


Figure 1-5 (a) Re-entrant mechanism of auxetic material (b) roll-up mechanism of auxetic material [15] (c) 6-connected auxetic chiral structure [16].

### iii. Interlocking materials

Interlocking material is another example of architected material. It consists of intermediate scale blocks which allows the cracks to localize and not propagate to the whole part. Interlocking materials refer to structures built up by jigsaw-like concave and convex blocks which are held together by their own shape. The concave and convex surface increased the contact surface and the friction between adjacent blocks and permit them to interlock with one another. The interlock system is more deflectable and provides a larger bending flexibility and energy absorption capacity, but a lower fracture strength, than uniform structure [19].

Figure 1-6 shows the failure modes of concrete interlocking and monolithic homogeneous plates. The cracks are restricted within two constitutive blocks in (a), however the crack propagated through the whole solid plate (b). When the first block is damaged, interfaces between blocks prevent the spread of cracks to the surrounding blocks, thus guarantee the whole structured integrated even with localized fracture [19]. This system is also proven to be able to maintain the structure with the removal of several blocks. The interlocking structure ensures a higher damage tolerance by jigsaw-like blocks of an intermediate scale and may lead to special applications, such as masonry and other construct fields.

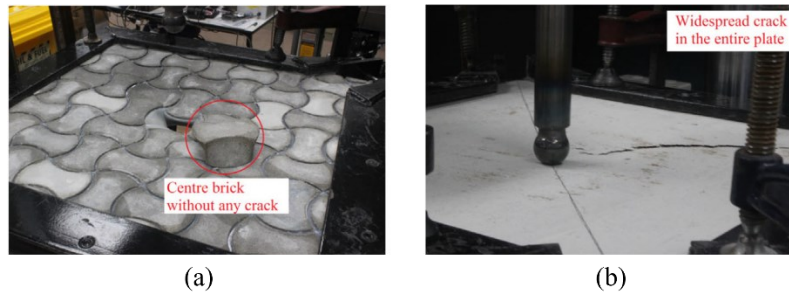


Figure 1-6 Failures in concrete plates (a) interlocking plate (b) homogeneous plate [20].

#### iv. Compositionally graded materials

Another important kind of architected materials is compositionally graded materials. Unlike auxetic or interlocking materials, whose components are often of the same nature, compositionally graded materials are a kind of materials whose chemical composition is heterogeneous within the whole volume. Properties within different parts vary because of this graded composition. The various properties and their geometries are designed to meet the needs of the role played by each part. They are considered to be architected materials for the architecturation can be designed according to functions of each part with different chemical composition. Numerous compositionally graded materials are developed in recent years, including polymers, ceramics, metallic materials, or a combination of them. Among them, metallic compositionally graded material is the most widely studied due to the abundant kinds of alloys and their diverse properties. They will be extendedly discussed in part 1.1.3.

The above is only some examples of architected materials. Other kinds of architected materials have been developed and studied, for example, layered ceramics or polymer and coil structure to increase the strength [21], core-panel structure to insulate modern buildings and improve the energy efficiency [22].

Besides these artificial architected material structures, many micro-architectures exist widely in the nature. Lamellar structure of tooth enamel and nacre can set barriers for crack propagation and increase the resistance. Bones have 6-7 structural hierarchy in different scales and thus an extraordinary combination of stiffness and toughness. Fish and snake skins consist of small and stiff scales which ensure the flexibility and resist to penetration [21]. These natural structures have existed much longer before the scientists and engineers begin to fabricate

architected materials and been optimized by nature for millions of years. It is a rich source to inspire scientific research and industrial project.

**1.1.3 Metallic architected materials**

In this section, metallic architected material is introduced individually because it is more closely related to the present work. The constitution of metallic architected materials is usually related to composition gradient or localized deformation. Metallic compositionally graded materials are the most intensely researched because the alloying element contents play a key part of their properties. The graded composition is often realized by diffusion process of interstitial atoms like C and N, as they effect mechanical properties prominently in alloys.

Different studies are carried out on the fabrication of metallic architected materials in Fe-C system because of numerous phases in the ferrous system. Chehab et al. [10] proposed a process for compositionally graded steel with carburization or decarburization technique to overcome contradiction of the elongation and the resistance of steels. This study also proposed a method to estimate the global necking strain of the architected materials using Considère’s criterion. Possible architectures are shown in Figure 1-7. In this study, for the architectures that do not cover the whole surface, i.e., Figure 1-7 (c)(d)(e)(h)(i), two kinds of masks were made to selectively carburize or decarburize austenite steel according to different architectures and different base steel.

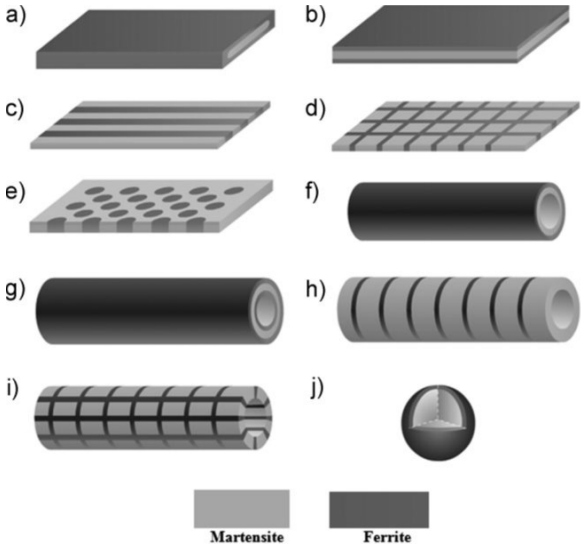


Figure 1-7 Possible architectures for compositionally graded steel [10].

In this study [10], an austenite steel is used as base material. During the decarburization, a layer of ferrite is formed in the surface and after quenching, the layer remains but the high carbon austenite core changes into martensite or bainite. As ferrite and martensite have very different properties, ferrite can be used as a ductile matrix and martensite can act as a reinforcement. It is the same principle of dual-phase steel where the martensite phase is embedded in ferrite matrix to combine ductility and strength but in this graded steel the ferrite-martensite system is applied in a higher hierarchical scale. Besides the pattern, there are many

other variables to be controlled in this process, such as diffusion degree and depth and also interfacial phase. Like this process, some treatments for hardening the surface of alloys like carburizing and nitriding can also be considered to generate compositionally graded architected materials. The presence of carbides and nitrides in the surface increases the wear resistance of alloys.

Cicoria et al. [11] also studied the diffusional heat-treatment of carbon to fabricate architected materials and tested local hardness of each part. In this study, masks were also applied to realize several steps of localized carburization and decarburization in different parts of the sample. Results showed that martensite and ferrite were formed separately according to the diffusional heat-treatment and the shapes of that masks, thus the hardness map on the surface is heterogeneous. This process makes it possible to design specific structure with a scale larger than the microstructure. It is also to note that the structure obtained did not have a sharp border between martensite and ferrite because the diffusion is gradual, which may indicate less interfacial failure when it is loaded.

Azizi et al. [23] has carried out a surface decarburization in furnace followed by quenching to form a layer of low carbon martensite on the surface of medium carbon martensitic steel core. Consecutive cold rolling has introduced a total equivalent strain over 2.0 to this compositionally graded steel, while martensitic phase is usually considered to be very fragile and difficult to impose a plastic strain. After cold rolling, local shear bands are formed within the hard core and arrested by the relatively soft surface. Their further study [24,25] shows that this surface decarburization and cold rolling process can be combined with post intercritical heat treatment to control local grain size at the shear bands and produce ultra-high strength dual phase steels with both heterogeneous carbon content and grain size.

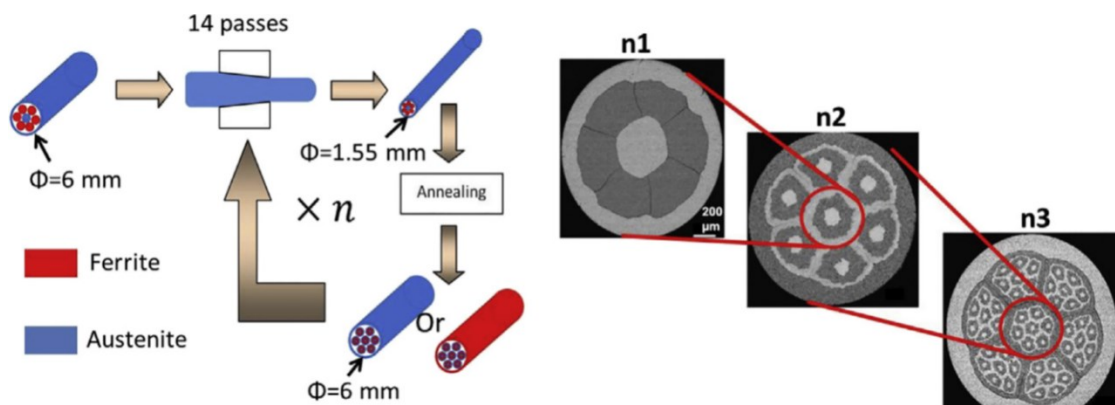


Figure 1-8 ADB process used to make architected duplex stainless steel [26].

Besides diffusion, Naser et al. [26] also proposed a process, illustrated in Figure 1-8, to obtain duplex stainless steel through Accumulative Drawing and re-Bundling (ADB) technique. Wires of 316L austenitic stainless steel and 430 LNb ferritic stainless steel were repeatedly drawn to a duplex stainless steel (DSS), whose microstructure consists almost equally of austenite and ferrite. DSS presents a good combination of ductility and strength. But their study showed that the mechanism of its properties was more complicated than a simple mixture of these two

phases and there was a complex interaction between austenite and ferrite, leading to a deviant performance in strength of DSS from the basic rule of composites. Results showed that with the increase of the number of refining drawing, the austenitic phase regressed into martensite with the diffusion of carbon at the interface due to large plastic deformation. Despite this phase transition, this architecturation method may offer a new process to fabricate duplex stainless steel with controlled phases volume fraction and distribution without meeting thermodynamic equilibrium conditions. It confirms the concept of architected materials, whose properties are superior to the simple average of each component.

In addition to architecturation composed by different phases with graded chemical composition, localized mechanical processing is also researched to develop materials with heterogeneous properties. Surface mechanical grinding treatment (SMGT) is a surface strengthening method which generates a gradient plastic strain in the treated surface with a certain depth, which refines the grains in graded level. The rolling WC/Co ball is pressed on the specimen with a given force and programmed moving velocity and rotation velocity, as shown in Figure 1-9. This technology is applied to induce nano twin boundaries at surface layer on an austenitic steel and a decreasing twin density from the surface to the core by Wang et al. [12]. This treatment brings a superior trade-off between ductility and strength in tensile tests because twinning boundaries block dislocations and serve as slip planes. Further studies have been carried out on other metallic materials and the modification on properties is promising. Similar processing on austenitic stainless steel forms a spatially gradient microstructure and enhances strength-ductility synergy [27].

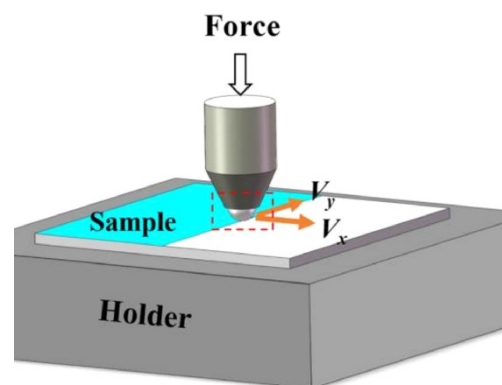


Figure 1-9 Schematic illustrations of surface mechanical grinding treatment set-up [27].

Other surface strengthening methods are also proven to be efficient to yield synergistic effect of strength-ductility. Surface mechanical attrition treatment (SMAT) is a treatment where the specimen is peened by accelerated metallic shots at high strain rate. This treatment can generate as well a sandwich microstructure in steel sheets with coarsened grains in the core and high density twinning at the surface [28]. Laser shock peening (LSP) induces high impact stress with a high strain rate on material surfaces. A recent study shows that a high entropy alloy after LSP treatment processes an excellent high strength and high plasticity [29].

In these surface strengthening studies, hierarchical microstructure is created in the direction from the surface to the core area of the metallic sheets. It can be prospected that by controlling the geometry of treated area on the sheet surface, another hierarchy level will be created within the sheet plane. Together with heterogeneous microstructures along both the thickness and the surface, particular properties may be generated.

Above are some examples of studies carried out on microstructurally graded materials in ferrous system by thermodynamical or mechanical methods. There are also researches on other alloy systems, for example, compositionally graded TiNi alloy realized by Ni electroplating and diffusion [30]. Another important emerging method is the fabrication by laser deposit, where the powder is changed during the layer-by-layer process to yield a gradient composition. This technology is very popular in recent years and attracts much attention because it is more controllable than conventional diffusion and allows more dramatic gradient in element contents and natures. It is applied in numerous alloy systems, such as stainless steel, high-entropy alloy, Ti alloy, etc.

#### **1.1.4 Corrugation geometry**

In this part, corrugation, the interested form in this study, will be discussed. Studies have been carried out on isolated corrugations and corrugated sandwich structures both in simulation works and experiments because of the special mechanical response when they are loaded. Corrugated forms are easy to fabricate, and corrugated sandwich panels have a smaller density compared to full-filled ones. Corrugated sandwich panel presented a higher tensile strength and bending stiffness along the longitude direction in comparison to simple monolithic panels of the same amount materials [31].

Extended variations are applied on corrugation-filled sandwich panels to explore enhanced performances. Adding foam infill in the sandwich voids can reduce the deflection of the panel with the cost of a slight weight increasing [32]. Sandwich cores with graded thickness can also reduce the panel deflection and absorb more plastic energy [33]. Preliminary periodic corrugated embossment on plain steel sheets can modify the Young's modulus and rigidity [34]. Results of these studies also show that geometric parameters of corrugations have an important influence on the mechanical behavior of corrugated sandwich panels. Therefore, corrugated form is very promising and worth further exploration.

For the development of metallic materials, especially for steels which are one of the most widely used structural materials, there is always a contradiction between strength and ductility. In order to bring a solution to this problem, Fraser [6] studied systematically the behavior of isolated corrugation and corrugated reinforcement composite in Figure 1-10 by changing geometrical parameters ( $P$ ,  $h$ ,  $t$  in Fig.1-5 (a)) and also material properties (Young's modulus, yield strength, work hardening coefficient and exponent).

This study carried out by Finite Element Method (FEM) simulation proves that different parameters of the corrugated core could influence the composite global tensile behavior on a system of 4130 steel reinforcement embedded in a copper matrix. Compared with straight

reinforcement of the same volume fraction, corrugated ones can postpone the necking with the cost of a loss in ultimate tensile strength (UTS), as shown in Figure 1-11 (a). For corrugations with a larger amplitude, it is even possible to attain a more important necking strain than that of the copper matrix, which allows access to the blank region of the material property map. This delay came from the boosts of work hardening rate during tensile test shown in Figure 1-11 (b).

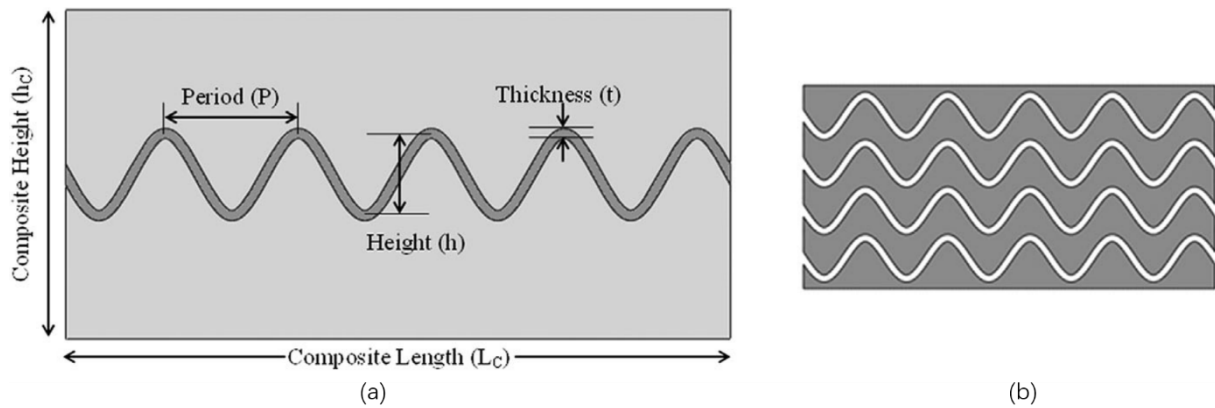


Figure 1-10 . Corrugation reinforced materials (a) single reinforcement (b) multiple reinforcements [6].

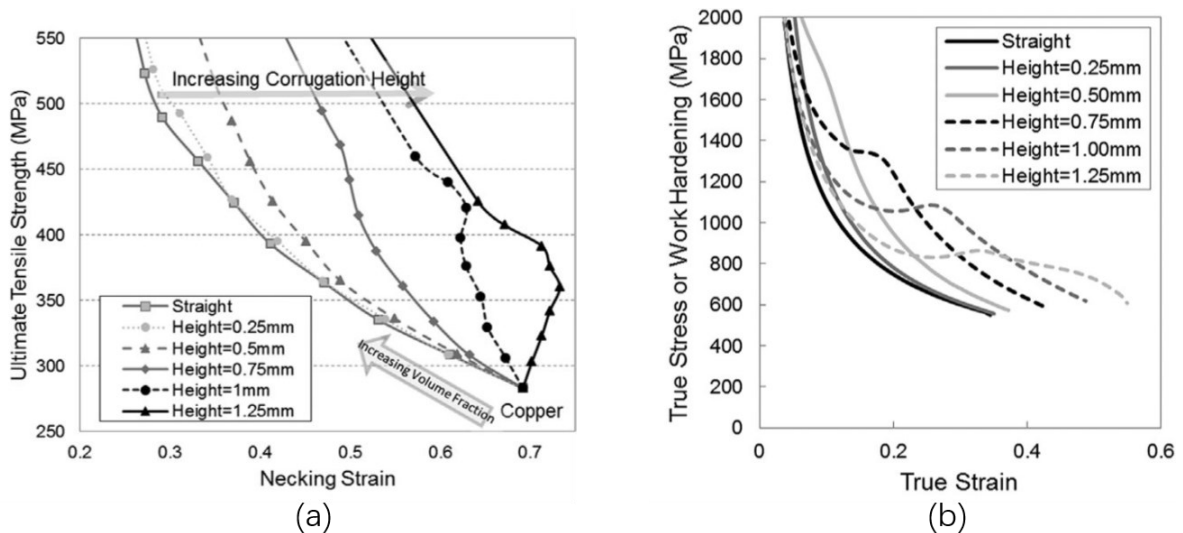


Figure 1-11 FEM simulation results of corrugation reinforced composites (a) strength necking strain (b) work hardening [6].

The boost in work hardening rate evolution comes from the corrugated form of reinforcement. Figure 1-12 (a) compares the stress-strain behavior of single corrugated form sample and straight one. For the straight sample, the nominal stress increases proportionally with nominal strain (elastic step) and then its increasing slows down (plastic step) and followed by necking and fracture. Unlike the straight sample, the nominal stresses of the corrugated ones increase slowly at the beginning (the red circle in Figure 1-12 (a)), and then the increasing accelerates and slows down similarly to a straight sample. It is the delayed acceleration in stress increasing which brings the work hardening boost. A larger curvature leads to a more later delay. This

delay is due to the unbending process which aligns the corrugations parallel to the tensile direction before being straightened.

Corrugation and straight reinforced composites are shown in Figure 1-12 (b). Compared to straight reinforced composite, corrugation reinforced one has a lower stiffness and strength because the reinforcement is less oriented to the load direction [5]. For this composite, the tensile load begins with the configuration where the reinforcement is less effective. With the increasing load, each fragment of the corrugation rotates around the junctions to unbend until the corrugations are straightened. At this step, the classical uniaxial traction begins and the work hardening rate boosts. During the unbending process, the stiffness and strength of the composite increase as the corrugations are more and more aligned to the load direction. It is this unbending step that changes the macroscopic stress-strain behavior and introduces an increasing in work hardening rate because the configuration has been changed. That is why this boost is called geometrically induced work hardening by Bouaziz [35]. With the same reinforced volume, a larger amplitude yields a more delayed work hardening boost, thus a larger necking strain, however, at the same time the loss in UTS is more important.

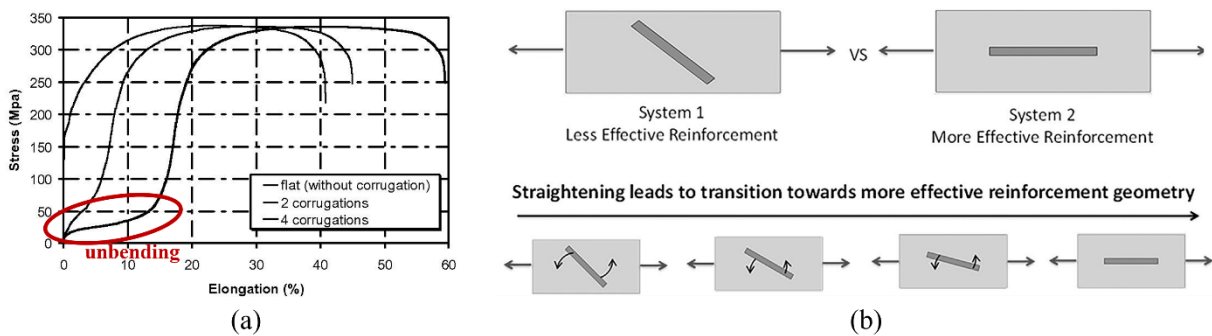


Figure 1-12 (a) Stress-strain behavior of single corrugation [35], (b) reinforcement unbending process of corrugated composite during tensile test [5].

Apart from the geometric parameters, relative mechanical properties between the matrix and the reinforcement have also been studied in [6]. Not all composite matrix and reinforcement combinations exhibit a benefit in delaying the necking strain. There will be possibly a benefit when the matrix has a relatively low yield strength and is ductile enough, and at the same time the reinforcement has a high enough yield strength. Otherwise, the constraint of the matrix transfers the stress to the corrugated reinforcements and the unbending step cannot be achieved properly. Instead of unbending, the reinforcements are stretched directly, and the fracture of fragile reinforcement leads to the composite failure.

In practice, the challenge is to create a ‘perfect’ interface which is strong enough between the matrix and the reinforcements. Uniaxial traction, uniaxial transverse compression and rolling are tested on architected lead-tin solder matrix with embedded copper reinforcements, but the poor interface cohesion result to an early failure. Another system is corrugated stainless steel fabricated by additive manufacturing process reinforcement embedded in a copper matrix, where the interfacial strength is better than solder-copper system but not stable enough.

Uniaxial transverse compression is performed to avoid the interface decohesion but it is insufficient to evaluate the necking strain with compression test [6]. Digital Image Correlation (DIC) technique was used to acquire local displacement fields, from which strain fields were computed. Results confirmed that qualitatively compression and rolling samples had a relatively good agreement with FEM simulations.

The thesis of Fraser [6] exploits the possibility to fill the material property map blank regions by architected materials with corrugated reinforcements, and inspires much the presented work. In order to realize the benefit in necking strain by corrugated reinforcement in experiment, a more coherent interface is expected to overcome the interface decohesion during tensile test and to support the theoretical simulation. As it is rather difficult to bond two different materials together, to create reinforcements and matrix from the same base material appears possible to generate a stronger interface.

In some alloying systems, different phases possess quite varying mechanical properties. In Fe-C system cited above, the difference in yield stresses between ferrite and martensite can attain 1000 MPa. Precipitation hardened 2000/6000/7000 series aluminum alloys are much stronger than annealed alloys. The yield strength of beta titanium alloys can be up to 1200 MPa compared to 800 MPa of alpha titanium alloys. Sometimes these different phases are transformable by heat treatment. The challenge is to create corrugated reinforcements by local heat treatment on a matrix with a suitable difference in their yield strengths. As a technology which is intensely developed in recent years, the use of laser processing for creating such architected materials appears as a very promising candidate to realize it.

## **1.2 Laser treatment on metallic materials**

Laser processing has been developed very fast since laser was in 1960s. It refers to the use of thermal effect between laser beam and material surface to complete the processing, such as laser cutting, laser drilling, laser welding, laser surface treatment, laser shock peening, etc. It can be applied on various, including metals, polymers, ceramics, or the combinations of them. Laser processing has many advantages. It has a great flexibility thanks to adjustable energy density, spot size and moving speed. As there is no direct physical contact between laser and material surface, no wear takes place even with materials with high hardness. Its impact is limited within the treated zone, the heat affected zone (HAZ) is small. Besides, in the past ten years, laser processing has been combined with the fast developed additive manufacturing technology to become the trending LAM.

It can be used as an external heat source to modify the properties of metallic materials for its flexibility and rapidity. Compared to traditional heat treatment in furnace which results in a homogenous microstructure of the whole part, laser heat treatment can realize a localized heat treatment without affecting too much the remaining of the specimen thanks to its precision. By changing treatment parameters, such as input power, moving velocity, focus distance, treatment duration, etc., the thermal cycle can be changed, and different results can be achieved. This part is focused on laser processing on ferrous materials. Laser hardening is one of the most

developed laser process and is a common surface strengthening method nowadays. Besides, laser treatment can bring other modifications on metallic materials, for example, laser annealing can reduce the YS and UTS but increase ductility [36], laser carburizing or nitriding can bring precipitation on the treated surface to improve its strength.

These kinds of treatments will be introduced in the following paragraphs. To better understand laser processing, it begins with a presentation of phase transformation and their features in Fe-C system, followed by different laser treatments on ferrous materials, including laser annealing, laser hardening and laser alloying. And laser processing on other metallic materials is also reviewed.

### 1.2.1 Introduction of phase transformation in Fe-C system

As steels are the most widely used metallic material, laser heat treatment on steels is also one of the most well-studied and extensively practiced subjects among laser applications. For its short interaction time and small penetration depth, most of the treatments aim to modify the surface property to adapt to its function, such as increase the wear resistance. The metallurgy of Fe-C system has much to exploit because microstructural and mechanical properties can be well controlled by the chemical component and heat treatment cycle. Each phase in the Fe-C phase diagram (Figure 1-13) has diverse features and their combination brings different effects to yield stress, work hardening rate and fracture strength of steels. Basic features of principal phases are summarized as follows.

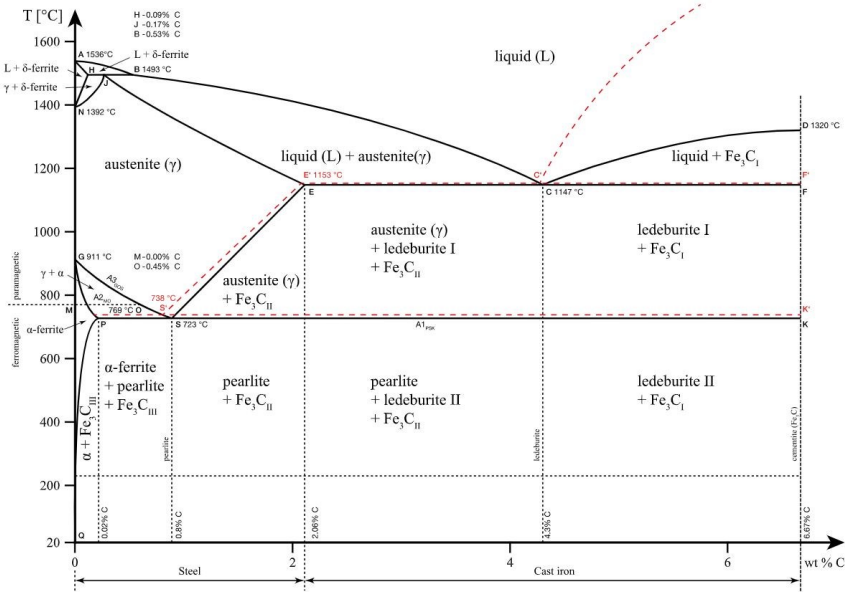


Figure 1-13 Fe-C phase diagram.

- Ferrite is ductile and stable phase at room temperature in binary system Fe-C and has a poor carbon solubility. It has a good formability and low work hardening rate. Refining the grain can increase both the yield and fracture stress. The grain size and morphologies can be controlled by temperature and duration of transition from austenite to ferrite.

- Austenite is a metastable phase at room temperature and has a higher carbon solubility than ferrite. It increases both the yield stress and the UTS because its high work hardening rate can delay necking [10]. But as austenite is a high-temperature stable phase, usually intercritical annealing is needed to control the volume fraction and sometimes additional elements as Cr, Ni, Mn, etc. Recrystallization can control the grain size of austenite.

- Martensite is the strengthening phase that presents a high hardness and wear-resistant ability but is very brittle. Tempering of martensitic phase decreases the yield stress, the work hardening and the Bauschinger effect but increases ductility.

- Cementite is a C-enriched main strengthening phase in steels. Its yield stress depends on its morphology. Lamellar cementite together with ferrite in pearlite has a higher yield stress while spheroidized one has a lower yield strength. Cementite can change from lamellar into spheroid by an annealing process [10].

Different combinations of phases can lead to various properties for steels. Dual-phase (DP) steel is the most developed and most widely used steel in automotive industry. It contains a microstructure of an island-like martensite, which increase its strength and work hardening rate, embedded in a ferrite matrix, which ensure the ductility. Transformation induced plasticity (TRIP) steel composed by retained austenite in a ferrite matrix has a good combination of strength and ductility. Retained austenite transforms into martensite and increases work hardening rate when a stress is applied. Complex phase (CP) steel contains small amounts of martensite, pearlite and retained austenite embedded in an extremely fine ferrite-bainite matrix. These phases and precipitation hardening generate a high yield strength and a good local formability.

Phase constitution can be controlled by critical heat treatment, more specifically, the cooling rate after austenitization temperature. Figure 1-14 is the continuous cooling transformation diagram of carbon steel containing 0.25wt% carbon. The microstructure at room temperature depends on the cooling rate. At less than 0.1 °C/s, only ferrite and pearlite are formed, which corresponds to furnace cooling. Between 0.1 and 1 °C/s by controlled furnace cooling or air cooling, ferrite, pearlite, bainite and sometimes martensite can be found. Between 1 and 30 °C/s by oil quenching, the final microstructure consists of ferrite, bainite and martensite. Beyond 30 °C/s, a fully martensitic microstructure can be obtained, and this cooling rate usually corresponds to a water quenching. The critical cooling rate changes with alloying element contents but in general, a larger cooling rate to the room temperature on the same steel leads to a higher hardness.

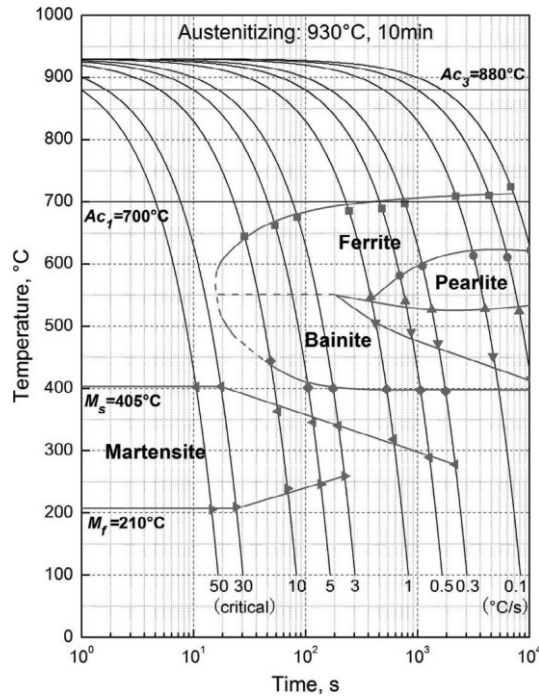


Figure 1-14 Continuous cooling transformation phase diagram of 0.25 wt% carbon steel [37].

In metallurgical industry, complicated steel phase constitution, especially for AHSS development in the last several tens of years, is controlled by the combination of alloying element content, critical annealing time and temperature and cooling rate. DP steel is cooled down from an intermediate temperature between  $A_{c3}$  and  $A_{c1}$ , where austenite is partly transformed into ferrite and the rest is quenched into martensite islands. Martensitic volume fraction is determined by initial temperature before quenching. Quenching and partitioning (QP) steel is new and promising candidate among the 3<sup>rd</sup> generation AHSS, it is quenched between martensite start temperature ( $M_s$ ) and martensite finish temperature ( $M_f$ ) followed by a partitioning at this temperature or above. This partitioning process enriches carbon in the untransformed austenite from martensite in order to stabilize retained austenite in room temperature, and its time and temperature impact the volume fractions of martensite and retained austenite and their carbon contents [38].

### 1.2.2 Laser hardening

Laser hardening is one of the most developed laser processing technologies and is often utilized as a surface strengthening method. Thanks to its flexibility with respect to input power and spot size, laser processing allows to attain a large range of density energy for treatment, so is the treatment temperature. Laser hardening is one of the most studied laser processing, which resembles to a quench as the cooling rate is high. It can increase the wear resistance of the surface as a strengthened martensitic layer is formed.

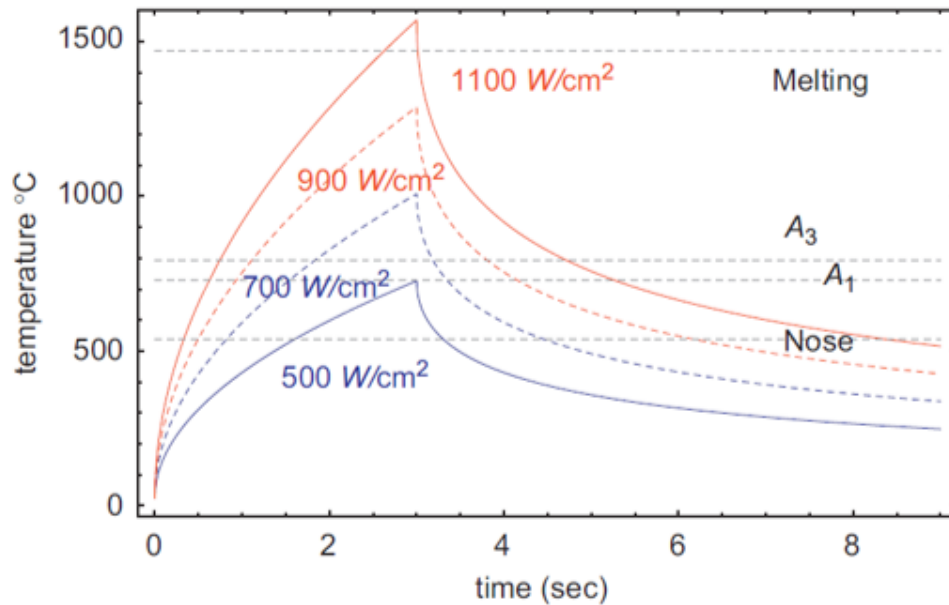


Figure 1-15 Temperature evolution at different laser energy densities on AISI 1035 steel for an interaction time of 3 s simulated by Ki et al [39].

A typical temperature evolution is shown in Figure 1-15. The first step is to heat steels above the austenite transition temperature or even to the melting point to obtain a partial or fully austenitic structure, and then to quench rapidly to obtain martensitic phase. Due to the specific features of laser treatment, the treated region usually cools down with hundreds of degrees per second even without any extra cooling system. Thus, it is possible to harden a relatively soft ferritic steel or retained austenitic steel whose carbon content is suitable into martensite with carefully chosen condition to increase the strength of the surface layer and to extend the lifetime of engineering parts. The diffusion process of carbon atoms is limited during the rapid cooling so that the phase transformation does not pass through the austenitization criteria, and this allows a fully quenched martensitic microstructure.

Several conditions should be fit in order to harden steel surface by laser treatment. Steels with carbon content below 0.1 wt% are usually considered as not hardenable because of the low carbon content and low fraction volume of martensite formed [40]. At the same time, the peak temperature and duration for temperature above  $A_{c1}$  should be adjusted. The ideal peak temperature should not be above melting point because the cooling rate may be reduced by the latent heat and resolidification may destroy the surface state by introducing residual stress. The duration above  $A_{c1}$  should be long enough to ensure the transformation from ferrite to austenite and the homogenization of austenite. Laser power, spot size, laser beam shape, scan velocity and steel chemistry and metallurgy should be taken into consideration to achieve the most satisfying result [40].

Numerous steels are proven to be laser hardenable by various processing strategies. Ashby et al. [40] studied laser hardening of a Nb microalloyed steel and a medium carbon steel and established models of hardening depth as a function of process parameters, among which the

most important were the energy density, the laser interaction time and the component and microstructure of original steels.

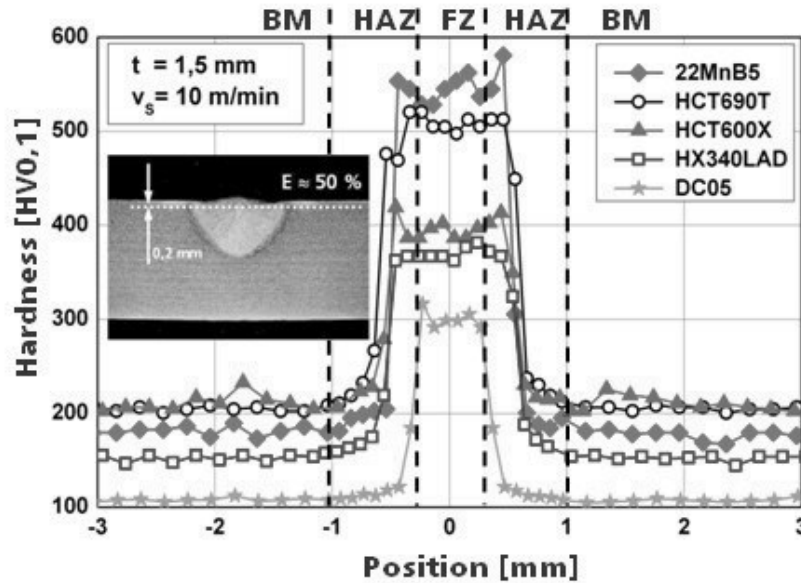


Figure 1-16 Hardness profiles of different steel grades across laser hardened zone [41].

Other grade steels which are mainly utilized in automotive industry are also studied for localized laser strengthening, including mild steel, micro-alloyed steel, DP steel, TRIP steel and press hardening steel with various carbon component from 0.031% to 0.252% [41]. All grades show a significant increase in hardness within the laser-treated zone, but the hardening level varies with the content of carbon in the base steels as shown in Figure 1-16. High carbon content steels (TRIP steel HCT690T with 0.233% carbon and press hardening steel 22MnB5 with 0.252% carbon) have a much greater difference in hardness after laser treatment. The laser treated zone has a hardness of more than 500 Hv compared to 200 Hv of the base material. The other grades with less than 0.1% carbon are also hardened but in a less important level.

SEM images show two kinds of hardening mechanism in this process. For steels with a relatively low carbon content (below 0.1%), acicular ferrite with carbon precipitation at the grain boundary is formed. The hardness increased mainly because of grain refining. But for the steels with a higher carbon content, the formation of martensite results in the hardness increasing, which agrees with the study of Ashby [40]. Richer content in carbon leads to a higher volume of martensitic structure and a higher final hardness.

The effect of laser moving velocity is especially studied. As shown in Fig.1-17, laser penetration depth decreases with increasing moving speed. But at the same time, a higher moving speed leads to a larger cooling rate, which encourages martensite formation and reduces self-annealing softening effect [41], thus the average hardness of treated zone is more important. Microstructure examination shows that a full penetration though the whole sheet can be achieved, even though with a slight loss in hardness.

Compression and bending tests prove laser treatment reinforced steel parts, especially for bending test, where an even small strengthened volume gave a very steep rise to the crash resistance. Tensile tests were carried out on the same grade of steel with different hardened depths. Results show that there is always an increase in yield strength and ultimate tensile stress for treated steels no matter how deep the penetration is. But with the penetration depth doubled (from 50% to 100%), the increase in strength is much higher thanks to a much larger reinforced zone [41]. This means that a more expanded hardened zone can compensate the slight loss in hardness for tensile behavior. Thus, a maximum hardening depth should be attained to obtain the most benefit, for steel sheet, a uniform treatment through the thickness is expected. In this study, the sheets are 1.5 mm thick, thinner sheets may be adopted if a full penetration is desired with an optimized strengthening effect.

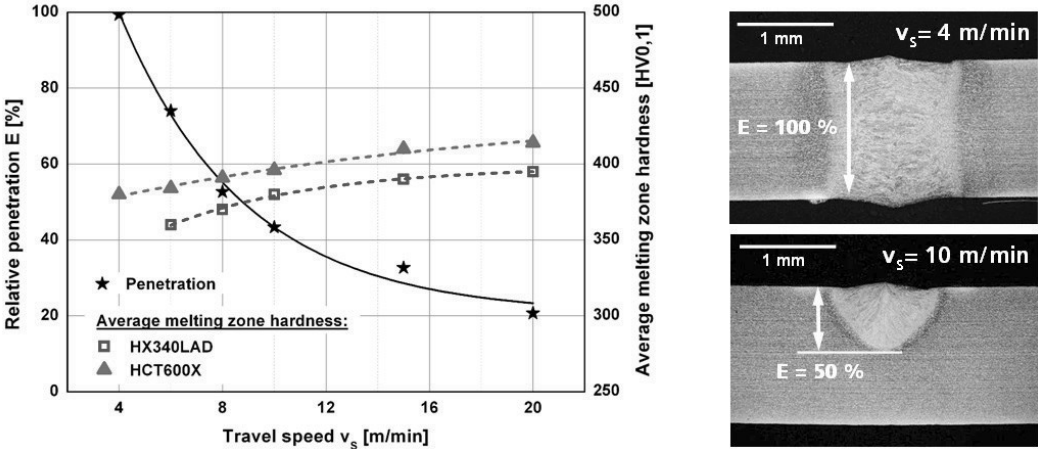


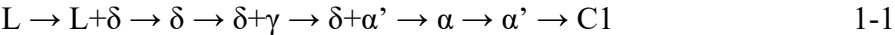
Figure 1-17 Penetration depth and average hardness of laser hardened steels at different speed; macroscopic section of steel sheets with different penetration depths [41].

This study is introduced in detail because it is very inspiring to the present research work. Instead of inducing only a strengthened layer on the steel sheet surface, this study focuses also on the penetration depth which can be attained by laser hardening. It proves that it is possible to induce a fully hardened zone though the whole thickness of steel sheets with a rather uniform microstructure (Figure 1-17). It also researches hardness evolution according to penetration depth. These results provide the possibility to utilize laser treatment as a hardening method to modify local microstructure and mechanical properties soft steel sheet as reinforcements to design a heterogeneous material. It makes it clear that this idea can be realized with optimized laser parameters and more satisfying results can be achieved with thin steel sheets. In this way, the treated zone is larger, and the cooling rate is high enough to generate a sufficient strengthening effect. At the same time, available lasers in the present research work have limited powers. It is thus necessary to adopt very thin steel sheets to yield maximum strengthening effect.

Besides carbon steels, laser hardening on stainless steel also attracts much attention. Among which, ferritic stainless steel (FSS) are often considered not adapted to be hardened by thermal treatment compared to martensitic stainless steel and austenitic stainless steel (ASS) because of

their poor carbon content [42]. But studies show that both traditional furnace and laser heat treatment can reveal a much higher micro-hardness and failure strength. According to different treatment conditions, this improvement in mechanical properties can be attributed to the grain refining, the intergranular and intragranular martensite formation or carbide precipitations that appeared during the rapid cooling process [43–45]. But often laser heat treatment yields a significant grain coarsening in the fusion zone (FZ) and the heat effect zone (HAZ), the ductility and elongation are heavily reduced due to these changes [44]. Some recent studies on stainless steel hardening are presented in the following paragraphs.

Stainless steel laser welds attract much attention because the rapid heating and cooling rates of welding process bring a self-quenching effect, which leads sometimes a much tougher weld than base material. Zhang et al. [46] studies spot welding joint of austenitic AISI 304 and ferritic AISI 430 steel. Macrostructures of welding sections and their corresponding hardness profiles are shown in Figure 1-18. The weld of AISI 304 is softer than base material. On the opposite, weld of AISI 430 and dissimilar weld present a micro-hardness around 300 Hv compared to 180 Hv of AISI 430 and 220 Hv of AISI 304 in spite of obvious grain coarsening. Also, on AISI 430 side, a special softened zone of about 250 Hv is found in the HAZ near the weld due to excessive grain coarsening. This improvement in hardness is due to the martensite formation appearing mostly at grain boundaries and also the formation of chromium carbides during rapid cooling. The phase transformation path is represented as follows.



Where L refers to liquid,  $\delta$  is delta ferrite, which is stable at high temperature,  $\gamma$  is austenite,  $\alpha'$  is martensite,  $\alpha$  is ferrite and C1 is primary carbide. Liquid phase solidifies in the first place as delta ferrite and a part of it transforms into austenite. Primary carbide is precipitated from this austenite and martensite is formed due to the high cooling rate. This martensite is usually found at the grain boundaries of ferrite transformed directly from high temperature delta ferrite [46].

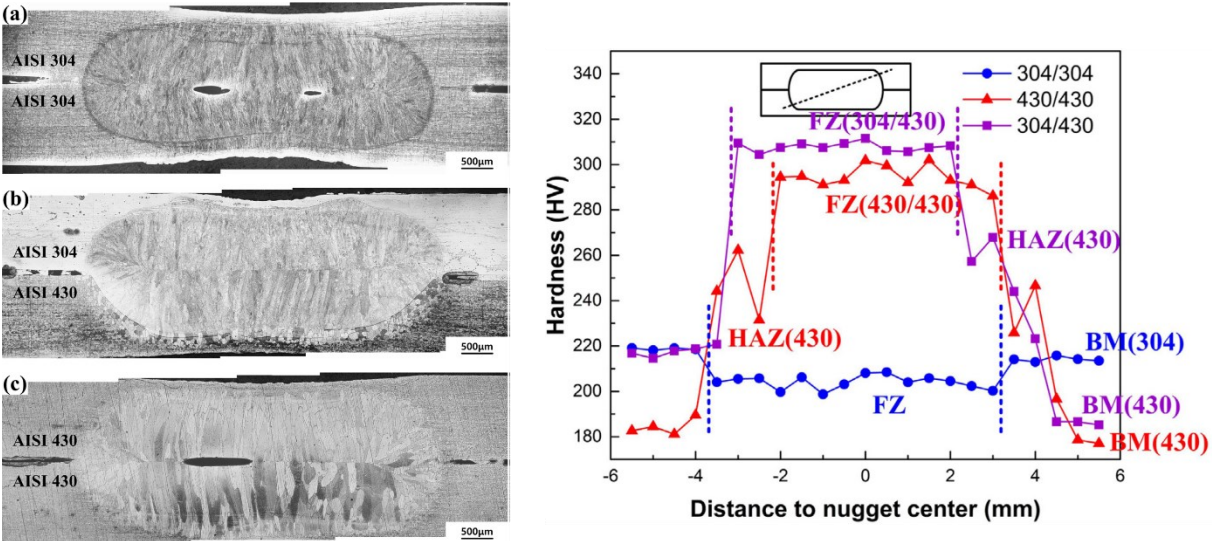


Figure 1-18 Macrostructure of dissimilar welds between AISI 304 and AISI 430 and corresponding hardness across welding section [46].

Characterization of weld joints on a ferritic stainless steel with 12% Cr and 0.02% C has been investigated by Taban et al. [47]. The weld HAZ present distinct high temperature HAZ (HTHAZ) and low temperature HAZ (LTHAZ). Microstructures of base material, LTHAZ, HTHAZ and fusion zone are shown in Figure 1-19. HTHAZ is cooled down from a temperature near liquidus and consists of coarsened ferritic grains directly from  $\delta$  ferrite with martensite islands at grain boundaries transformed from reversed  $\gamma$ . LTHAZ is heated just above  $A_{c1}$ , upon cooling an important fraction of  $\gamma$  is reversed and transformed into martensite so that the grains in LTHAZ is finer. Hardness of HAZ can be increased to 280 Hv compared to 160 Hv of base material (BM). The melting pool does not possess structural defects after remelting and solidification. No evident negative effect on mechanical behaviors have been found on neither tensile nor bending resistance due to grain coarsening but it reduces the local toughness of the welds. It is necessary to restrict the grain coarsening of fusion zone to increase its toughness.

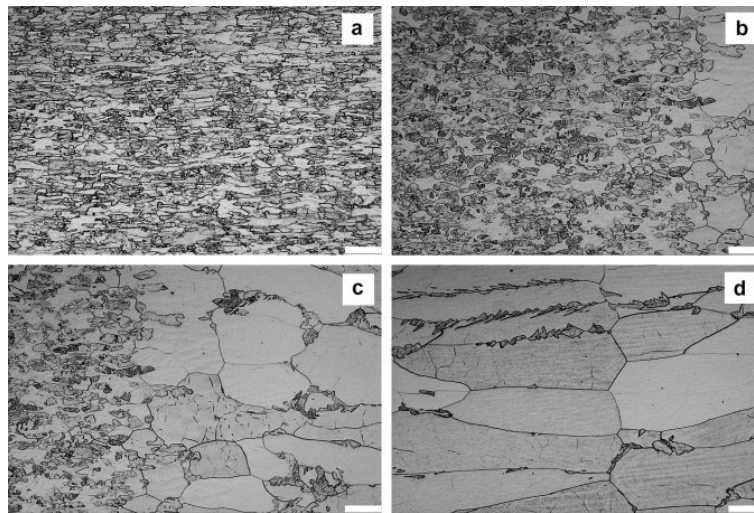


Figure 1-19 Microstructure of (a) base material, (b) LTHAZ, (c) HTHAZ, (d) fusion zone of 12% Cr ferritic stainless steel weld [47].

This improved hardness of welds is also confirmed on dissimilar welding and filler welding studies implemented between other grades of FSS, ASS and martensitic stainless steel (MSS). A complex ferrite-martensite microstructure is formed at the fusion zone and HAZ of FSS side where the temperature is around  $A_{c3}$ , which leads to a much improved hardness compared to base material [48,49]. But these welds are usually brittle and present crack formation problem, post annealing or tempering process above  $600^{\circ}\text{C}$  is needed to obtain a better combination of tensile stress and elongation.

Besides welds where the peak temperatures are above the liquidus, certain stainless steels are proven to be hardenable by conventional furnace heat treatment followed by rapid cooling. Vafaeian et al. [50] reported a study on FSS with cold-rolling and annealing near  $800^{\circ}\text{C}$  (below  $A_{c1}$ ) in a tradition furnace followed by water quenching. They obtained a nano-scale refined microstructure and an ultimate tensile strength around 1000MPa but a worsened ductility. Jha et al. [51] studied annealing of hot bands of FSS between  $A_{c1}$  and  $A_{c3}$  followed by water quenching they obtained about 18% volume fraction of martensite.

Stainless steel is also studied for laser surface hardening processing. Sundqvist et al. [52] studied the continuous-wave fiber laser beam treatment on EN1.4003 FSS of 12% Cr with single tracks and overlapping tracks. Their research focused on peak temperatures below 1500°C and found that the hardness in the treated area could reach 350Hv compared to 175Hv in the base material. The section of single and multi-track treated specimen is shown in Figure 1-20 with the micro-hardness profile at 0.25 mm and 0.5 mm underneath the surface. There is no obvious softening effect on overlapped zone between two tracks (A and B), which is encouraging for this present study. Because this absence of softening on overlapped zone provides the possibility to evaluate laser hardening effect on a certain grade of steel sheet by fabricating a fully treated sample covered by multi-track laser. The available lasers have small spot size (around 1 mm), and the machining of tensile test specimens of this dimension is complicated.

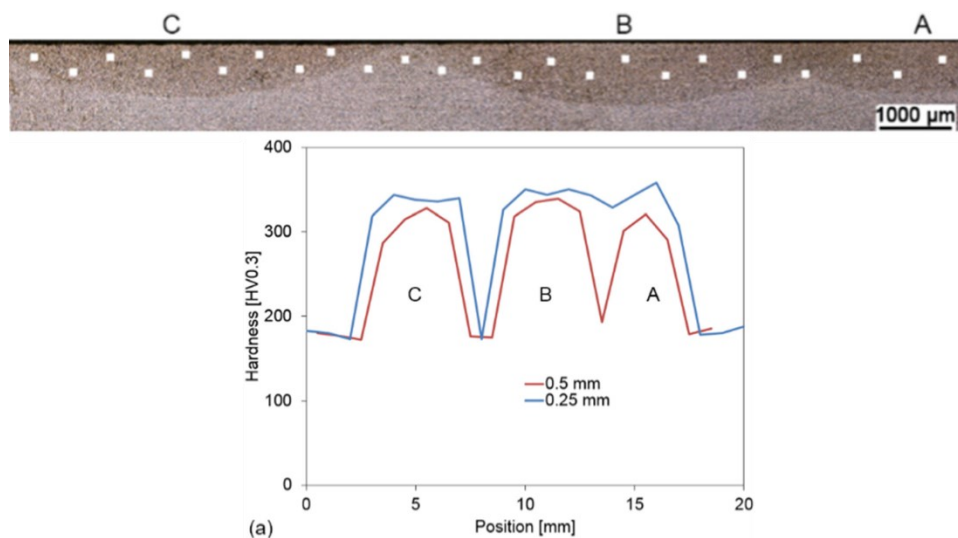


Figure 1-20 Section of 11% Cr FSS hardened by single and multi-track laser treatment and hardness profile [52].

Mahmoudi et al. [53] reported a surface treatment of an annealing AISI 420 martensitic stainless steel (MSS) with full ferritic microstructure and carbides by a pulsed Nd:YAG laser. Their study achieved an increase of 90% in surface hardness but also a tempering in overlapping zone, which causes a carbide deposit and less corrosion resistance in grain boundaries. Pantzar et al. [54] studied the diode laser hardening on low alloy steel and MSS and the effect of shielding gas during treatment. They found that the input energy required to attain Ac1 for treatment in air was significantly reduced with the presence of oxidation layer, which could depend strongly on base material and be difficult to control.

To summarize this section, laser hardening on steels has been well developed and applied on numerous grades. The principle is to heat steels above austenization temperature by laser irradiation, a self-quenching effect is generated thanks to the rapid cooling rate, usually hundreds of degrees per second, during which the diffusion of carbon atoms is limited, and hard martensite phase is formed. This section reviews the studies on carbon steels and stainless

steels. And the hardening process includes surface strengthening and whole bulk strengthening, by both laser welding and laser heat treatment below liquidus. It can be concluded that even with very low carbon content (0.02%), carbon steels and stainless steels can be remarkably hardened by direct laser heat treatment. This improvement in hardness is always accompanied with a loss in ductility and can be enhanced by post heat treatment. This strengthening effect is more important with the increasing of carbon content, and it can be extended into the whole sheet thickness with a uniform microstructure with suitable laser parameters. This extension into material bulk is worth exploring because it provides the possibility to modify thoroughly mechanical properties of a localized area on steel sheets and potentially fabricate architected materials.

### **1.2.3 Laser carburization**

As introduced above, laser hardening is usually used as a surface strengthening method to increase surface layer hardness by forming martensite. This process can be further developed by inducing other alloying elements to reinforce hardening effect. This laser alloying process is usually about small interstitial atoms like carbon or nitrogen. It enables the introduction of carbon or nitrogen atoms into the metallic matrix in order to form solid solution or carbides/nitrides to increase the surface hardness and wear resistance [55]. It is extensively studied on ferrous materials and other alloy systems. This section will present principles and recent studies of laser carburization on steels.

Traditionally surface carburization is obtained by liquid salt bath, solid carbonaceous material, gas treatment in furnace or plasma technique, especially by gas or plasma which are well-researched and widely used in industry. At high temperature, carbon atoms are decomposed from alkanes or CO<sub>2</sub> gas atmospheres and transferred into the matrix. The carbon-rich layer is hardened by quenching. Figure 1-21 is an example of 0.19% carbon AISI 8620 steel carburized in air/propane atmosphere with constant CO<sub>2</sub> for more than 10h at 925 °C [56]. A fully martensitic layer of nearly 1 mm is formed and the hardness is improved to 750 Hv compared to 500 Hv in the core. Conventional gas carburization can increase the carbon content to around 0.8%, and super-carburized layer containing 2-4% carbon can be realized by repeated carburizing treatment. At this stage, not only martensite is generated but also numerous carbides are precipitated and spheroidized, which improves the wear resistance still further [57].

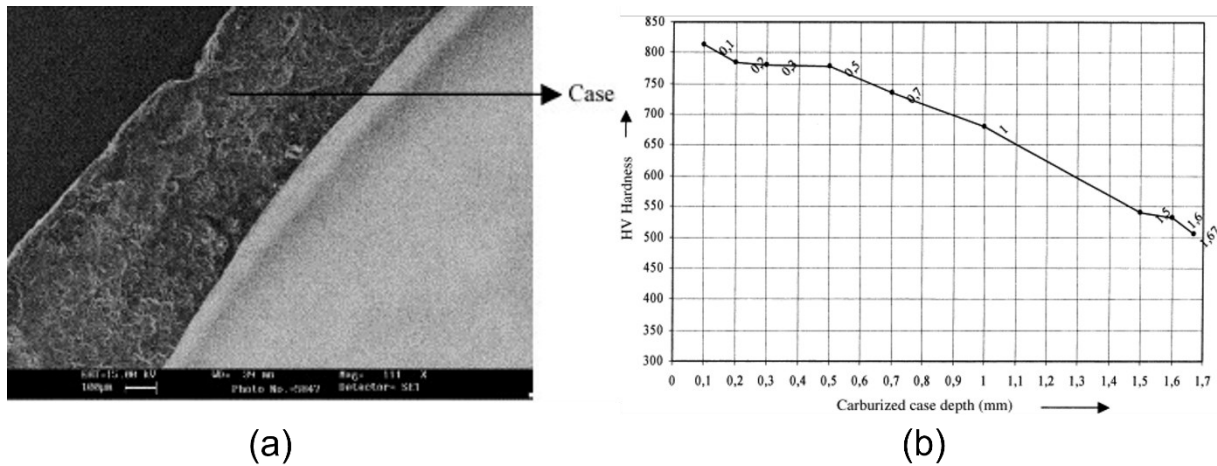


Figure 1-21 Gas carburized AISI 8620 steel initially containing 0.19% carbon and hardness profile from surface to core [56].

Carbon steels are usually carburized above austenization temperature, but a process called low-temperature surface carburization (LTSC) is firstly introduced in 1980s receives more and more attention [58]. It focuses mostly austenitic grades, such as 316 or 304 stainless steel, in a gas or plasma environment below 500 °C. This temperature is chosen to avoid undesired Cr carbide precipitation and loss in corrosion resistance [59]. This LTSC process results in an expanded austenite, which is a solid solution austenite supersaturated in carbon under metastable equilibrium condition. This expanded austenite is improved in hardness, fatigue performance and wear resistance but the corrosion resistance is not effected [58].

Michal et al. [60] reported LTSC process on 316L austenitic stainless steel and the results are shown in Figure 1-22. X-ray diffraction patterns confirm that only austenitic phase exists after carburization but the peak shift towards a smaller  $2\theta$  means a lattice expansion. And the peak broadening signifies the increasing of local plastic deformation from the untouched core to the carbon saturated surface. A large quantity of interstitial carbon atoms generates very high compressive residual stress near the surface. The carbon content near the surface is more than 10%, which is  $10^4$  times more than carbon equilibrium solubility at 465°C and the hardness is more than 1000 Hv, four times of the untreated base material. This hardness is even higher than fully martensitic steel and some carbides.

LTSC process is extensively explored on ASS, less studies are carried out on MSS, which are widely used in hydraulic component because of their high strength and corrosion resistance. Scheuer et al. [61] studied gas carburization on tempered AISI 410 in  $\text{CH}_4$  and confirmed the formation of  $\text{Fe}_3\text{C}$ . Similar to LTSC on ASS, lattice expansion and residual stress increasing are also observed. Surface hardness is doubled compared to as-tempered material and this result is very promising for tribological applications. Ravoni et al. [62] compared effect of carburizing gas and nitriding gas under the same operating conditions on MSS. Their results show that even though nitriding leads to a higher hardness on the surface, but the incoherent hardness profile of nitrided samples leads to a less satisfying tribological performance.

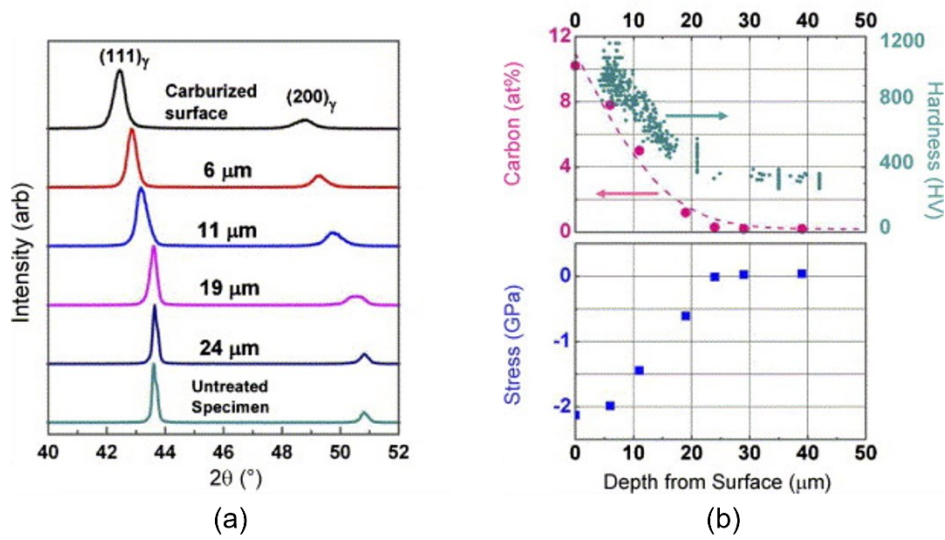


Figure 1-22 (a) X-ray diffraction of LTSC AISI 316L austenitic stainless steel at different depth from the surface, (b) hardness, carbon content and residual stress versus depth [60].

This process is efficient to increase the surface layer carbon content and thus hardness and wear resistance but it takes usually several to hundreds of hours [63]. Even though certain stainless steel grades present higher kinetics during the treatment, the strengthened layers are often limited in thickness from a few  $\mu\text{m}$  to tens of  $\mu\text{m}$  after hours of treatment [61], which is rather inefficient for surface strengthening. New process assisted by laser treatment has been developed to accelerate carburization and allow deeper penetration.

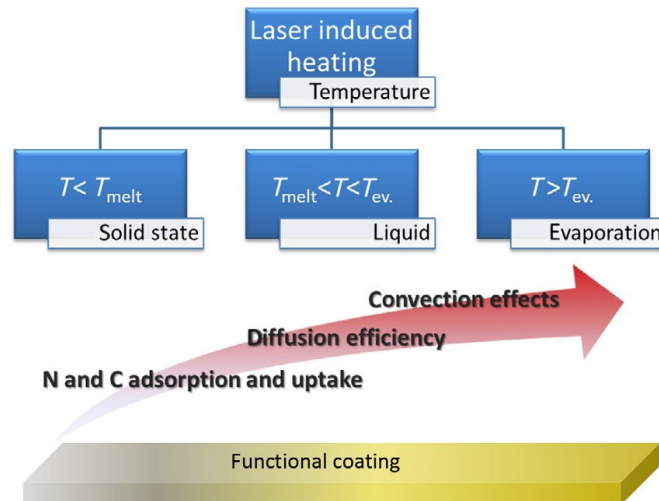


Figure 1-23 Laser carburization and nitriding mechanisms involved at different temperatures [64].

Laser hardening through self-quenching involves relatively simple reaction mechanisms, but laser carburization and nitriding process is much more complex and more interaction mechanisms are concerned according to different temperatures as the schematic in Figure 1-23. The absorption and uptake of carbon and nitrogen atoms depend on the surface temperature of metallic sheets. Different reaction efficiencies are determined by the surface state, solid or

liquid and also by the convection effect within the bulk itself. Laser carburization and nitriding consists of a part or all of following processes: laser absorption and heating, material melting and evaporation, plasma expansion and dissociation, metal/carbon and nitrogen atoms reaction, nucleation and solidification [64].

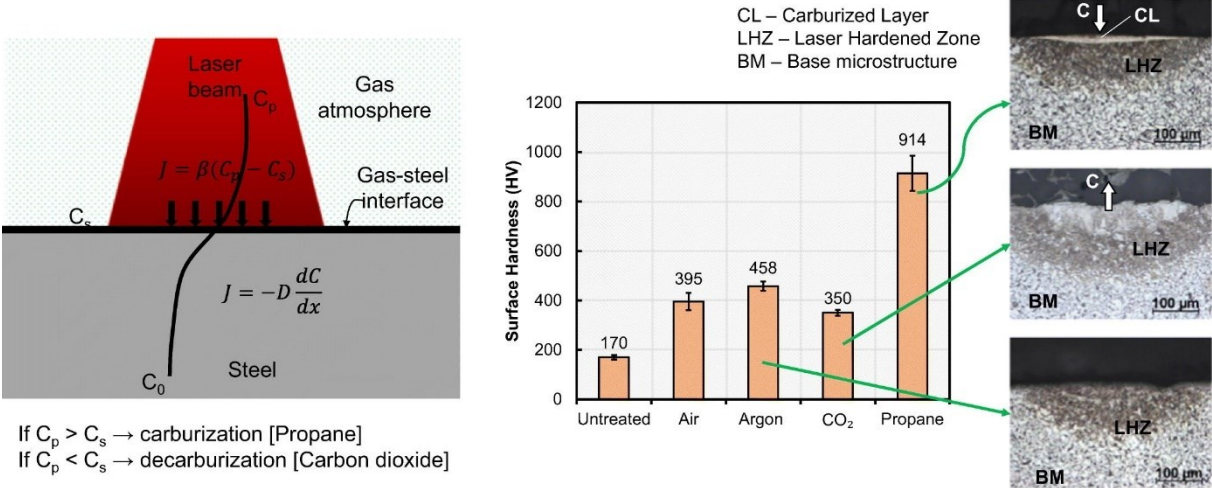


Figure 1-24 Schematic process of laser assisted carburization (left), effect of shielding gas on hardness and corresponding microstructure (right) [65].

Figure 1-24 presents a schematic illustration of laser assisted carburization by Maharjan et al. [65] and their work compared laser strengthening effect on low carbon steel in different shielding gas. The transfer of carbon atoms from shielding gas to treated surface depends on the carbon potential of the atmosphere ( $C_p$ ) and the carbon at the surface ( $C_s$ ). If  $C_p$  is superior to  $C_s$ , the process yields a carburization effect, which is the case of propane atmosphere. On the contrary, decarburization of the steel surface occurs and the surface hardness is inferior than that executed in inert shielding gas, which is the case of CO<sub>2</sub> atmosphere. Schaaf et al. [55] proposed a new technique to perform pulsed laser treatment on AISI 316 ASS in a mixed methane and nitrogen reactive gas. Laser irradiation produces a plasma which interacts with the molten pool, numerous carbides and nitrides are formed. Hirata et al. [63] studied laser induced carburization on a low-alloy steel of 0.16% carbon in propane gas below the liquidus to avoid deterioration of surface state and mechanical properties. Carburization depth of 0.1 mm is realized with a surface carbon content of more than 1% by a single laser track heating up to around 1500 K, which may take hours to attain the same effect without laser irradiation. Direct laser beam heat treatment allows a deeper and faster penetration thanks to its high energy density, which leads to a thicker strengthened surface. Therefore, laser assisted carburization is very attracted in industry to save both time and energy.

Another carburization method consists in direct heating the material surfaces coated by graphite above critical temperatures, or even melting temperature, by laser to diffuse carbon atoms [64]. Direct laser carburization has also been studied on different ferrous materials. Carbon coat increases the laser beam absorption, which leads to a more elevated temperature in the irradiated area, thus crystal nucleation and growth are more favored and numerous

carbides are formed [66,67]. This direct laser carburization can be achieved by two mechanisms: diffusion of carbon into a liquid melting surface or solid diffusion of carbon atoms [68]. Most existing research are focused on the former mechanism because it allows a much deeper and faster reaction thanks to the convection effect in the liquid melting pool. Due to the abrupt temperature gradient between the molten pool and substrate, various microstructures can be achieved in different zones depending on the induced carbon content and laser parameters [69]. But this melting and solidification process may increase the risk of crack initiation and existence of porosity [68].

Chen et al. [66] reported a localized laser carburizing process on gray cast iron coated by amorphous carbon powder. The base material gray cast iron, containing about 3% carbon, consists of graphite and ferrite embedded in pearlite matrix and the initial hardness is 260 Hv. Their study compares the laser hardening effect without carbon powder and carburizing effect with carbon powder coat on microstructure, hardness and fatigue behavior. Laser carburized specimens present a large quantity of ledeburite network and a more improved performance in both surface hardness and wear resistance. This process removes crack initiation sources and bridging between cracks. Further study carried out on similar material adopted a two-step laser carburizing process [67]. A laser ablation at higher energy density and frequency was proposed to fill carbon powder into a semi-closed pool before laser carburization. It can extend carburization depth and service life by increasing the utilization rate of carbon powder and stabilizing obtained microstructure.

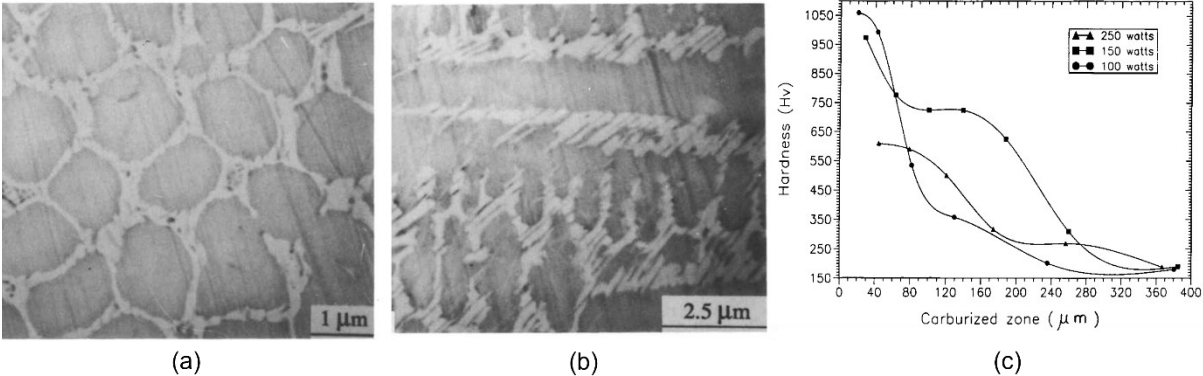


Figure 1-25 (a) Cellular grains after laser carburization, (b) dendritic grains after laser carburization, (c) hardness profiles from surface on carburized specimen sections at different input powers [69].

Low carbon steels are also investigated for laser carburization, which may have more industrial significance than gray cast iron due to its initial low carbon content. Tayal et al. [69] are among the firsts to execute direct laser carburization on low carbon steels coated by graphite. As shown in Figure 1-25 (a) and (b), cellular and dendritic austenite grains are developed during the solidification of with an inter-cellular or inter-dendritic eutectic microstructure, while the initial AISI 1018 steel has a ferritic microstructure with a small amount of pearlite. The volume fraction of eutectic structure increases with a thicker graphite

layer. A ledeburite solidification, which is similar to carburization result of above introduced gray cast iron, occurs when carbon content approaches to eutectic point 4.3%. The influence of laser power density is shown in Figure 1-25(c), a smaller power density leads to more strengthened carburized zone because it is less extended and the carbon is less diluted.

Different carbon sources can be used for laser carburization. Katsamas et al. [68] reported laser carburization on 15CrNi6 low-alloy steel by both solid-state carbon diffusion and surface remelting which incorporates carbon atoms using commercial graphite spray and a slurry graphite powder. Both carbon sources are efficient to introduce carbon atoms into the base material. According to different process parameters, the carburized layer exhibited a microhardness from 2.5 to 4 times higher compared to the substrate, but most of them are carburized through the remelting mechanism. Carbon nanotube slurry coat was studied by Yao et al. [70] on medium carbon steel and mild steel to be compared with the effect of graphite coat after laser carburization. Both coats yielded a carburized hardening layer with comparable peak values, but carbon nanotube presented a higher dissolution into the substrate.

Other elements can also be applied for surface alloying along with carburization. Bataev et al. [71] reported a study on electron beam cladding of Ti, Mo and graphite powders on a middle carbon steel. The depth of clad layer was more than 2 mm and the hardness was at least 4 times of that of the base material, mainly due to the presence of 30% TiC particles. The addition of Ti and Mo powders increased the wear resistance by more than 75% compared to quenched and tempered base material and carburized low carbon steel. This addition of other element powders besides graphite may be also applied on laser alloying to induce other reinforcing precipitations to increase surface or bulk strength.

To conclude, this section presents recent development and effect of different steel carburization methods, including conventional gas carburization in furnace, LTSC process, laser assisted carburization in carbonaceous atmosphere and direct laser irradiation on steels coated by carbon powder. Compared to furnace or LTSC process which are realized by pure diffusion driven by thermodynamics, laser process yields a faster and deeper treatment by forming numerous carbides precipitations and other strengthening carbon rich phases, such as martensite and ledeburite. It also allows selective area carburization on parts with complex geometries. In this present study, direct laser carburization on graphite coated steel sheets will be studied. The strengthening effect will be compared with laser hardening without graphite coat. The aim is to not only realize a surface hardening, but also expand carburization effect into the bulk to create a localized fully carburized zone. And it will be used to introduce reinforcements in soft base material matrix to achieve architected materials.

#### **1.2.4 Laser softening**

Laser hardening, laser carburization and laser nitriding increase local hardness by forming martensite, carbides, nitrides, and other strengthening phases from a softer base material upon rapid cooling of laser treatment. On the contrary of this hardening process, another idea is to soften the more fragile and strengthening phases, which is less studied compared with the

former. It usually refers to heating hard and brittle steels to critical temperatures in order to gain ductility at a relatively lower peak temperature than that of laser hardening. This section will present recent studies on laser softening effect on ferrous materials.

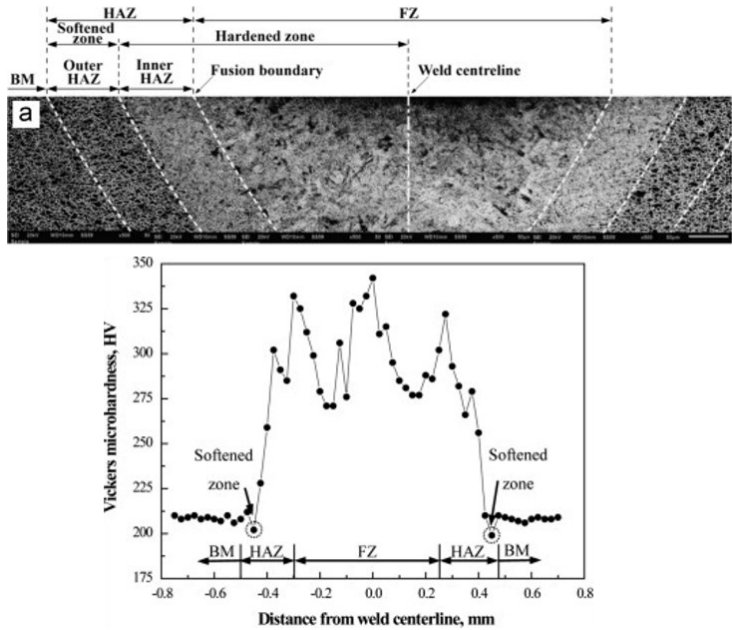


Figure 1-26 Laser welded DP 600 steel and hardness profile across the weld [72].

The idea of laser softening comes from the performance of as-quenched martensite followed by heat treatment. Weld joints of steels initially containing martensite present sometimes a HAZ whose hardness is even smaller than the base material as illustrated in Figure 1-26 [72]. This HAZ is usually near the base material and there are not any evident microstructure changes. This softened HAZ leads to a structural weak area of the welds [36]. And also, a reduce in hardness is often observed at the overlapped area between two tracks during laser surface hardening process [73]. This softening effect is attributed to a tempering of martensite. Normally this softening effect is considered as a disadvantage for steel welding process, but it also provides another way to modify steel properties by laser treatment.

Krauss [74] reviewed the tempering effect on lath martensite after quenching. Figure 1-27 shows the stress-strain behavior of a 0.22% carbon steel quenched and tempered at different temperatures in conventional furnace for 1 h. Tempered specimens show reduced strength but improved ductility. This change in mechanical properties can be attributed to the dislocation density decreasing and transition carbide precipitation at the beginning of tempering. And then cementite nucleates at martensite grain boundaries and replace carbides. Retained austenite between martensite laths transform also into coarse cementite. With higher temperature and longer tempering duration, equiaxed ferrite grains and coarse spheroidized cementite can be produced. The hardness drops dramatically when equiaxed coarse ferrite and cementite are formed.

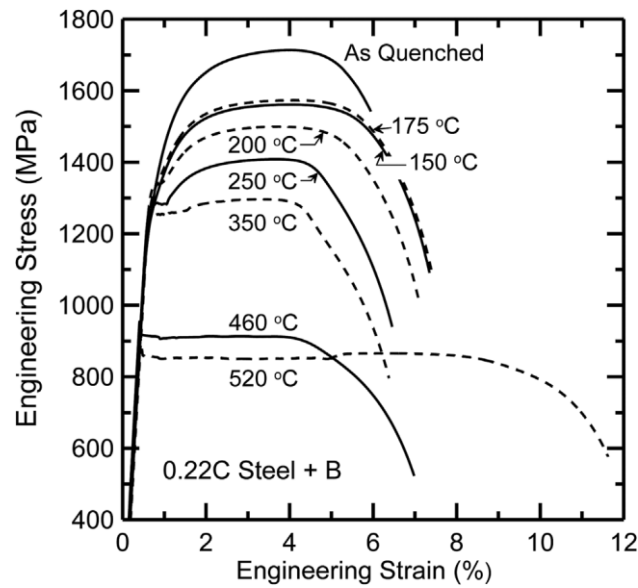


Figure 1-27 Stress–strain behavior for 22MnB5 steel quenched and tempered at different temperatures for 1 h [74].

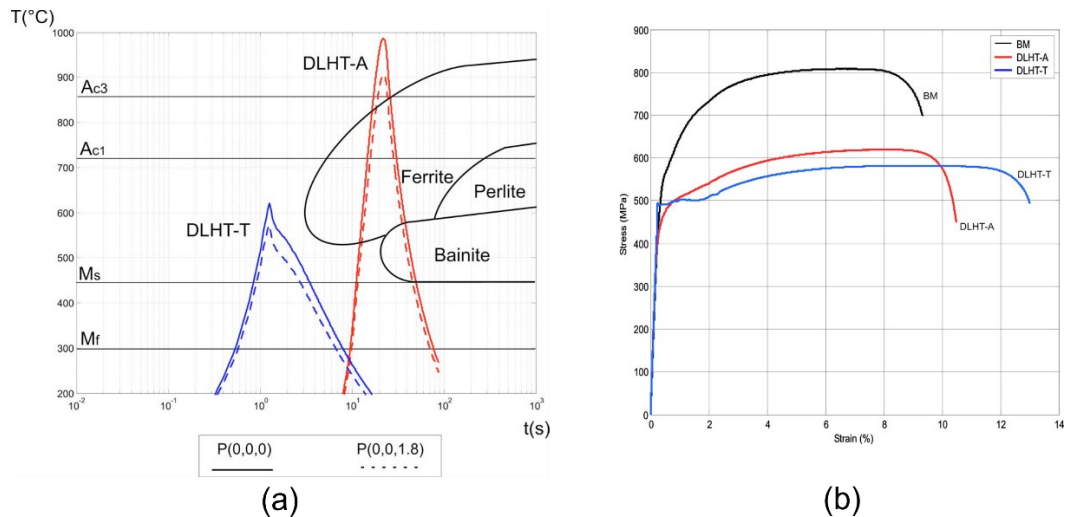


Figure 1-28 (a) Temperature evolution of diode laser heat treatment tempering and annealing process measured by thermocouple, (b) stress-strain behavior of base material, annealed and tempered DP800 steel [75].

The aim of laser softening is to reproduce this martensite tempering process by laser heat treatment instead of furnace. Capello et al. [75] propose two temperature ranges to soften DP800 steel by diode laser heat treatment as shown in Figure 1-28 (a). Annealing process (DLHT-A) reaches a peak temperature above  $A_{c3}$  and its long cooling time favors the formation of ferrite and bainite, whose hardness is smaller than the initial martensite. Tempering (DLHT-T) attains a peak temperature below  $A_{c1}$  and the volume fraction of ferrite and martensite do not change much from the initial base material. The softening effect comes from martensite morphology change during the tempering. Figure 1-28 (b) shows that tempering strategy allows a better softening result to increase the formability. This study is among the very first studies

on laser softening effect and inspires the following studies, especially on martensite tempered at relatively low temperature.

Neugebauer et al. [76] implement laser softening on steels containing martensite, including DP steel, TRIP steel and martensitic steel. They focus on temperatures below 800°C. Except TRIP steel, other grades show a significant reduction in strength and increase in elongation. Laser heat treatment has the most effective modification on martensitic steel, and the stress-strain behavior before and after laser softening is illustrated in Figure 1-29 (a). Deep drawing tests on specimens in Figure 1-29 (b), which are pre-softened on locations to be most deformed, show that the slide force is reduced by more than 20% compared to untreated sheet. This study inspires that laser heat treatment can increase the formability of steel containing martensite. Also, the idea of localized softening process is in accord with the concept of architected materials, which aims to adapt material local properties to corresponding needs.

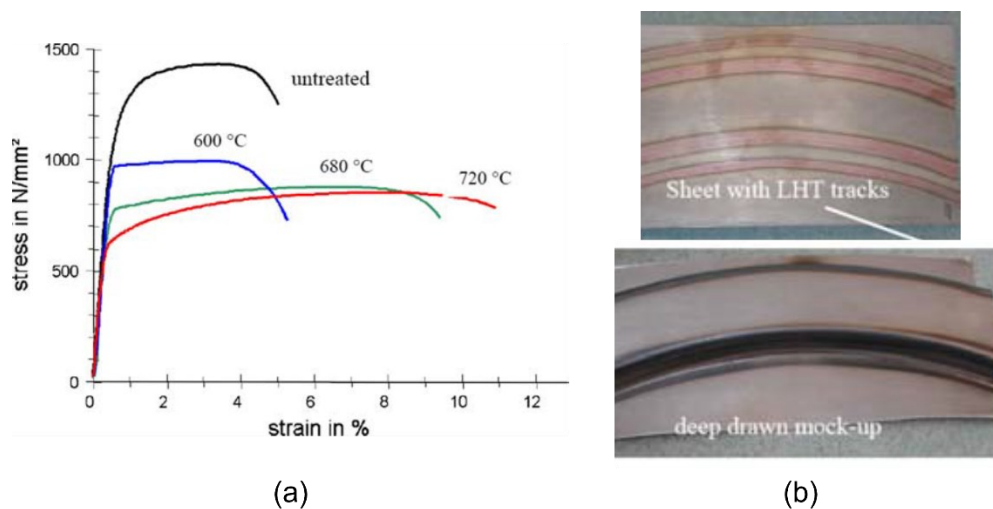


Figure 1-29 (a) Stress-strain response of untreated and laser heated martensitic steel, (b) deep drawing of martensitic steel sheet with localized laser treatment [76].

Lapouge et al. [36] studied continuous laser heat treatment of high martensitic content steels, a fully martensitic steel and 80% martensitic DP steel, which are among the most strengthened AHSS and used widely in automotive industry. Tensile tests are carried out on fully treated steel sheets of 1 mm thickness. Large spot size and small thickness ensure that the temperature difference between the front and the back face is not too important, and the annealing treatment is almost uniform through the whole thickness. A large range of laser powers is used to attain various peak temperatures from below the martensite transformation point ( $M_s$ ) to above the austenization temperature ( $A_{c1}$  and  $A_{c3}$ ), but liquidus is avoided. Figure 1-30 summarizes YS, UTS and elongation of annealed martensitic steel and DP steel according to annealing temperatures. Intercritical heat laser treatment close to  $A_{c3}$  can multiply the elongation by 3 and decrease the yield stress by a factor of 2. As the two grades consist of large quantities of martensite, they present very similar evolution trends.

This gain in ductility and loss in strength can be explained by microstructural changes during heat treatment. SEM images in Figure 1-31 show laser heated martensitic steel sections after different peak temperatures. With the temperature increasing close to Ac1 (Figure 1-31 (a)), numerous spheroidal carbides appear in martensitic matrix because of carbon diffusion. And both its quantity and size increase with high temperature. At a temperature between Ac1 and Ac3, the microstructure changes from a tempering of martensite to a dual-phase microstructure and the quantity of carbides is reduced (Figure 1-31 (b)) [36]. And the increasing of peak temperature towards Ac3 results in significant increase of ferrite volume fraction [76]. Above Ac3, both martensitic steel and DP steel are almost reversed to their initial microstructure (Figure 1-31 (c) (d)).

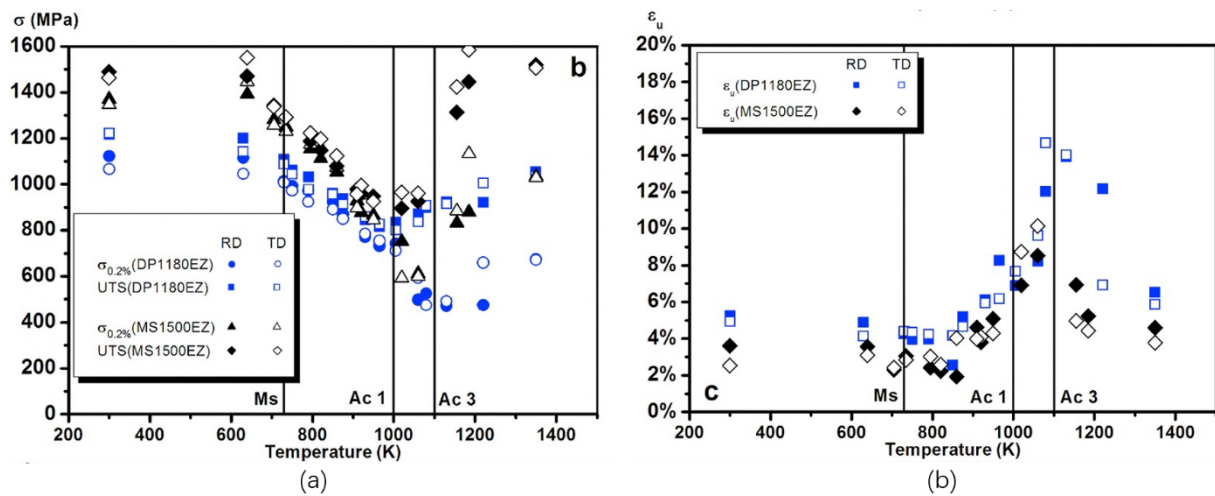


Figure 1-30 Yield strength and ultimate tensile stress (b) elongation of laser tempered MS1500 and DP1180 steel [36].

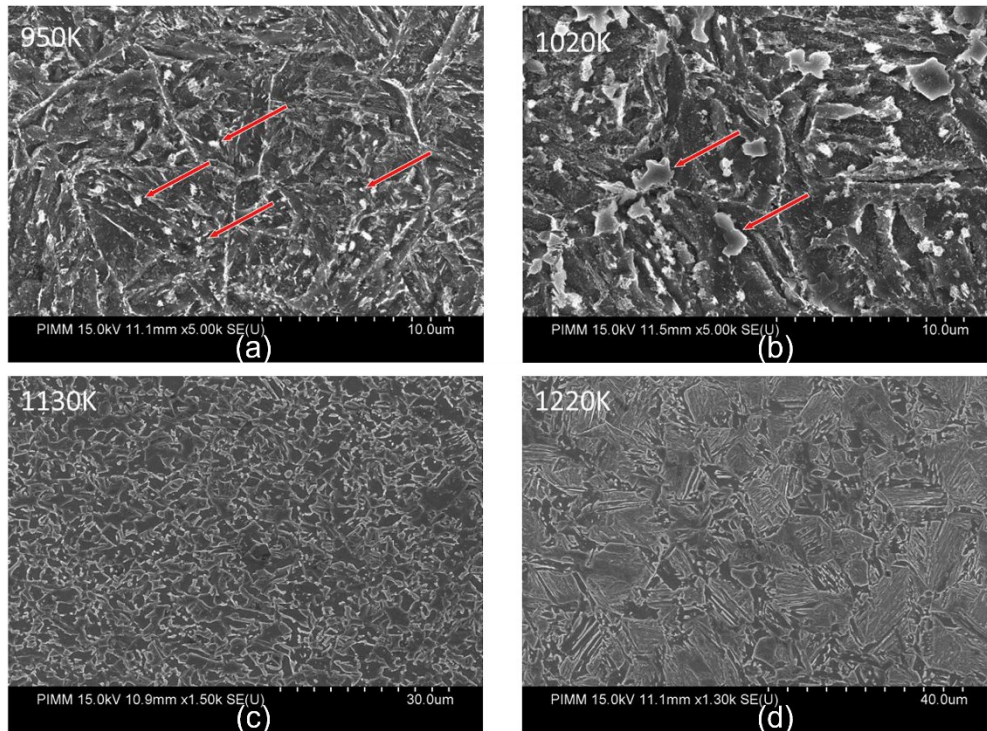


Figure 1-31 SEM images of laser treated (a) (b) martensitic steel (c) (d) DP steel at different peak temperatures [36].

Another study by Saastamoinen et al. [77] also confirmed the apparition of the carbides in direct-quenched low-alloy steel after tempering in conventional furnace. Carbides started by precipitating along the grain boundary of martensite and spheroidized when the temperature increased both at the subsurface and quarter-thickness position. For tempering temperatures above 400°C, dislocation density decreased with the increasing temperature, which led to a better ductility. But they observed that above 600°C there was no further improvement in bendability, even though the strength continued to decrease. This tempering process may be applied on high martensitic content steels to be compared with the effect of laser heat treatment.

Thus, a laser treatment below  $A_{c3}$  may soften high martensite content steels and increase the ductility. Appearing spheroidized cementite in tempered martensite has a lower yield stress, for another, new ferrite grains are formed from austenitic islands at high temperature.

Raghavan et al. [73] also studies the laser tempering effect of a hyper eutectoid AISI 52100 steel (0.980-1.10% C) on phase constitution and hardness change. Unlike the low and medium carbon steels, with this relatively high carbon content, about one-third weight percentage of austenite and two-thirds ferrite/martensite are found in the initial material. After the treatment the subsurface is a tempered martensitic region. At the beginning of tempering, martensite starts to decompose into ferrite and carbides, with the temperature increasing, carbides transform into ferrite and cementite. A larger overlapping area and a lower scanning speed generates a thicker tempered martensitic region on the surface, and thus a more expanded hardness-reduced layer.

After the tempering, hardly any retained austenite could be found in the microstructure of the subsurface region. The hardness is reduced to 25 HRC on the surface compared to 50 HRC in the core.

From the above introduction, it can be concluded that laser heat treatment is a hopeful method to soften martensite containing steels to increase their formability. For example, B pillar of DP600 which is locally pre-softened by laser and followed by deep drawing can take a higher blank holder force without any cracks compared to untreated sheets [76]. Compared to laser hardening, which is completed within a very short instant, more factors need to be well controlled for softening, such as peak temperature range, longer holding time, smaller cooling rate, etc. It can also be another method to induce a heterogeneous microstructure and fabricate architected materials.

### **1.2.5 Laser treatment on other metallic materials**

Besides steels, laser heat laser treatment has also been applied in a large range of different metals and alloys to alter their properties, such as copper, aluminum, titanium and their alloys. Some representative studies are introduced in this part.

Laser heat treatment was studied as a healing for fatigue damage on thin copper film by Ren et al. [78]. Single pulse laser was applied on films with a fatigue damage of 50%, which means 50% of the original fatigue life, and then these samples submitted to fatigue test to a full damage. The second part fatigue life was compared with 50% of the original fatigue life to identify the healing effect. Results showed that at the optimal condition, the fatigue life of treated copper film was 5 times that of the untreated film by process hardening of the specimen. The plastic strain after cyclic fatigue was reduced and the strain energy increased. Partial surface melting and resolidification happened and resulted in a grain refinement. This laser treatment improved the surface state of fatigued film and repaired the existing damage.

Shmorgun et al. [79] researched the formation of intermetallic coating of copper on a titanium surface by laser heat treatment to improve its wear resistance, as copper is an ideal hardener for titanium. A thin layer of copper (200-800 $\mu\text{m}$ ) was rolled together with titanium and a laser spot was applied on the copper surface. The relative component of copper and titanium in the formed intermetallic phases depended on the thickness of the deposited copper layer and the laser velocity. Results showed that a thinner layer (200  $\mu\text{m}$ ) improved more the wear resistance, by 1.9 times higher at most.

Aluminum alloys are widely used in automotive and aeronautic industry for its low density, high resistance to corrosion and good thermal conductivity. Due to its relatively low hardness and poor wear resistance, surface hardening process is often required. Laser alloying treatment is well-studied on aluminum and its alloys because compared to other methods, laser can create a rather solid interface between hardening layer and substrate. Chi et al. [80] reviewed different process parameters and material systems for existing laser surface alloying process on aluminum. Laser can change the surface microstructure through non-equilibrium solidification of rapid melting and cooling effectively. Transition metal powders like Cu, Fe, Ni are often

used by laser surface alloying to create intermetallic compounds at the surface of aluminum alloys. The interface between hardening layer and substrate shows a coherence and the hardness can be improved by 2-3 times. Combinations of ceramic and metallic phases generated by laser alloying process, such as TiC, TiAl<sub>3</sub> and Al<sub>3</sub>Ni, allow a highly strengthened surface with few defects. And laser alloying process is also a potential choice to develop compositionally graded surface, high entropy and amorphous surface coatings [80].

Due to the aging effect of some grades of Al alloys, post heat treatment should be considered after laser alloying process. Dubourg et al. [81] characterized the alloy obtained by laser heating of a mixture of aluminum and copper powder deposited on aluminum surface. Microstructure studies showed that with the increase in copper content in the powder, the microstructure of the alloying layer changed from Al + eutectic to Al<sub>2</sub>Cu + eutectic. Micro-hardness increased by 4.5-12.5 times of that of untreated material and it appeared a homogenous within the alloying layer, as shown in Figure 32 (a). An annealing was carried out and only hardening layer rich in copper remained and even increased its hardness. But hardness of coatings with lower copper contents are remarkably reduced due to the reorganization and coarsening of precipitations as shown in Figure 32 (b). Thus, initial alloying powder composition and post treatment should be taken into consideration to stabilize laser alloyed surface on certain Al alloys.

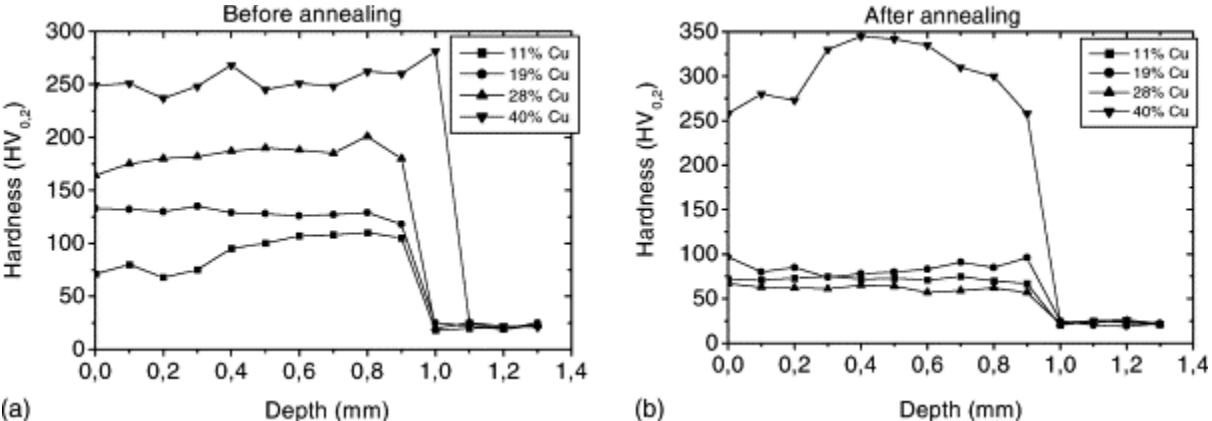


Figure 1-32 Annealing effect on hardness of laser alloyed Al surfaces with different copper content [81].

Apart from metallic materials, many others have also been applied as a hardening layer on aluminum by laser. Ceramics like carbides are also widely used in laser hardening of aluminum alloys. One part of ceramic particles can decompose during laser treatment and form new phases with aluminum substrate and some others remain. Both mechanisms help to improve wear and corrosion resistance [80]. Composites are also used, especially metal-ceramic composites, which have the advantages of both sides and the metal part in the composites act as the binding phase [80].

Titanium and its alloys become widely used in the recent years, especially in aerospace, automotive, marine, biomedicine fields. They present satisfying corrosion resistance, low elastic modulus, excellent strength/weight ratio and excellent biocompatibility. But low hardness and wear resistance limit their applications. Surface strengthening is needed for Ti

alloys submitted in friction and wear condition. Laser heat treatment, carburizing, nitriding, boriding and the combinations of them can provide a strengthened surface and improve tribological performance [82].

One important application of titanium is shape memory alloy due to the phase transformation between martensite and austenite, such as Ni-Ti and Ti-Nb system. Classic heat treatment is not very conventional for Ni and Ti alloys because they are sensitive to temperature and their grains coarsen at a relatively low temperature, which decrease its durability [83]. Tada et al. [83] investigated laser irradiation on microstructure and properties of Ti-Nb system shape memory alloy and compared the results with classic furnace treatment. Microstructures are shown in Figure 1-33, both furnace and laser treatment can reduce plastic strain by cold roll and obtain uniform equiaxed grains. X-ray results showed that the phase constitutions were the same after laser heat treatment and furnace heat treatment and specimens both possess superelasticity after aging. This study confirmed that laser can achieve the same effect as conventional heat treatment but is only 1/1000 time-consuming.

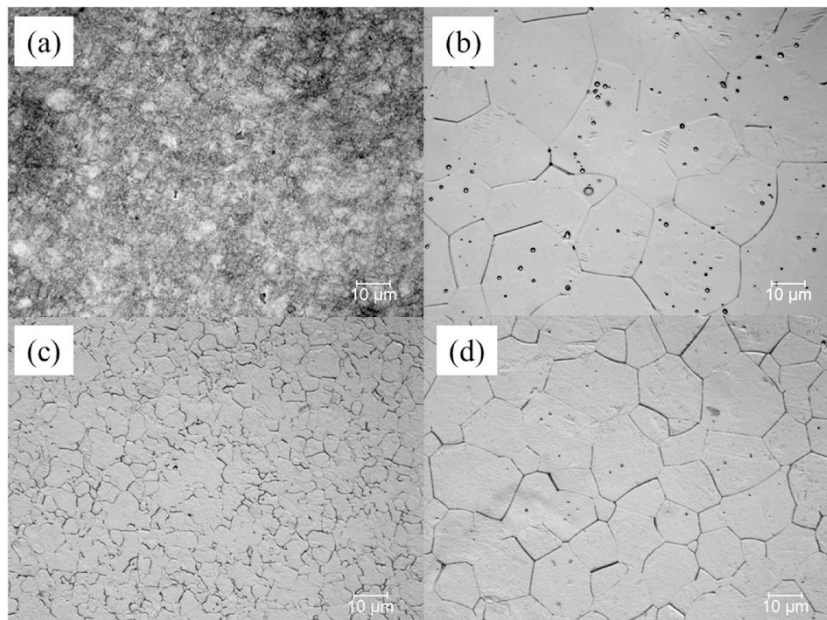


Figure 1-33 Optical microscope images of Ti Nb shape memory alloys, (a) cold rolled (b) furnace heat treated, laser heat treated at 100W for (c) 1s (d) 10s [83].

In another study carried out by Pantoni et al. [84], a NiTi shape memory alloy wire was heated to fully remelt by laser. Microstructural and mechanical studies showed that the resolidification and HAZ caused coarse-grain, large inclusions and surface defects, which decreased the fatigue resistance. But a following thermomechanical treatment including solid solution and cold work refined the microstructure, which not only recovered the original properties but also showed an increase in ductility.

Ti-6Al-4V is one of the most widely used titanium alloys and laser alloying to reinforce its surface strength attracts much attention. Saleh et al. [85] implemented a carburization process on Ti-6Al-4V alloy by laser irradiation on graphite coat and found that the use of graphite

powder increased the microhardness notably by forming carbide particles and dendrites. A carbonitriding process by Seo et al. [86] was carried out with the same alloy in a nitrogen shielding gas and the result showed that laser hardening effect were more enhanced by carbon/nitrogen-rich phases. Similar study by Makuch et al. [82] showed that wear resistance of laser-carburized titanium and its alloys increased significantly.

These laser treatments can modify locally mechanical behaviors of Cu, Al and Ti alloys and they are potential candidates of laser induced architected materials with suitable laser parameters and post treatment.

### 1.3 Laser treatment applications on architected materials

Even though the concept of architected materials is raised only in recent years, the idea has been practiced by researchers much earlier and more widely. For example, numerous surface strengthening methods introduced above are born under the strategy of adaptation local properties of parts to meet a certain need. Laser process participates more and more into architected materials fabrication as a tool to modify local property and form a heterogeneous hierarchy structure. This part will present some applications of laser treatment on architected materials.

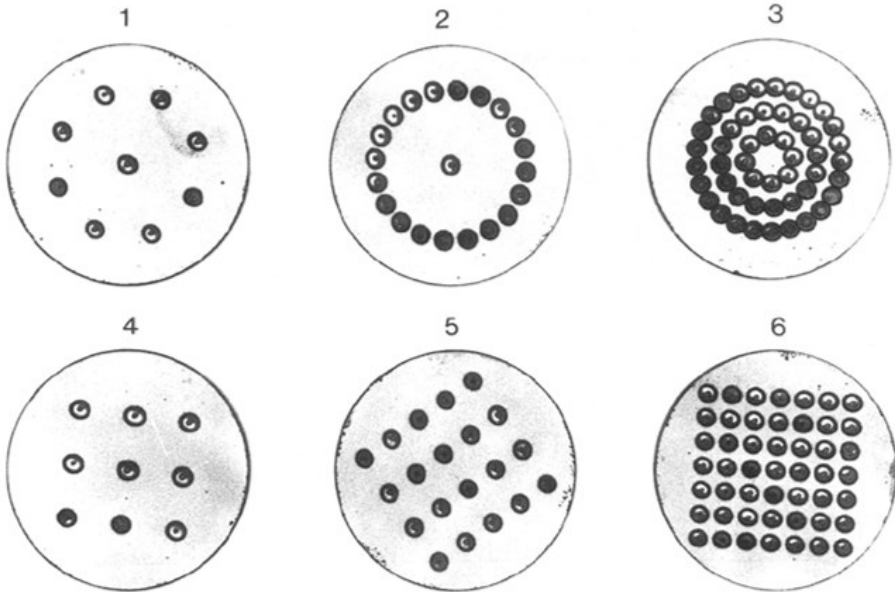


Figure 1-34 Laser spot patterns for wear test [87].

Papaphilippou et al. [87] performed discrete spot laser hardening on cast iron with different patterns shown in Figure 1-34. Following wear test did not show an obvious effect of patterns, but this method has paved the way for designing of architected surface by laser process.

A more completed study used biomimetic method to design architected surface [67]. Patterns of beetle and dragonfly structures are chosen (Figure 1-35 (a) (b) (c)) to be imitated on cast iron by selective laser hardening and their combinations have been tried out ((g) and (h)).

With the same hardened fraction, the pattern inspired by dragonfly wings in (f) has the best wear resistance.

Bouaziz [35] applied an oscillating laser treatment in a dual-phase steel above the austenization temperature. According to the chosen path of laser, straight or corrugated treated zone were created in the base DP steel, as shown in Figure 1-36 (a) and (b). The microstructure of the section is in Fig.1-36 (c). As in the center of the laser treated area, a fully martensitic zone was obtained and a graded microstructural zone was at the interface between treated zone and the base materials, which is the heat affected zone (HAZ). The microstructure in the base DP steel remained unchanged. The sample sheet is thin enough to have a rather homogenous microstructure along the thickness direction. In this way, a much harder zone was created out of as-received DP steel. This study provides a possibility to fabricate architected materials with corrugation reinforcement by laser process.

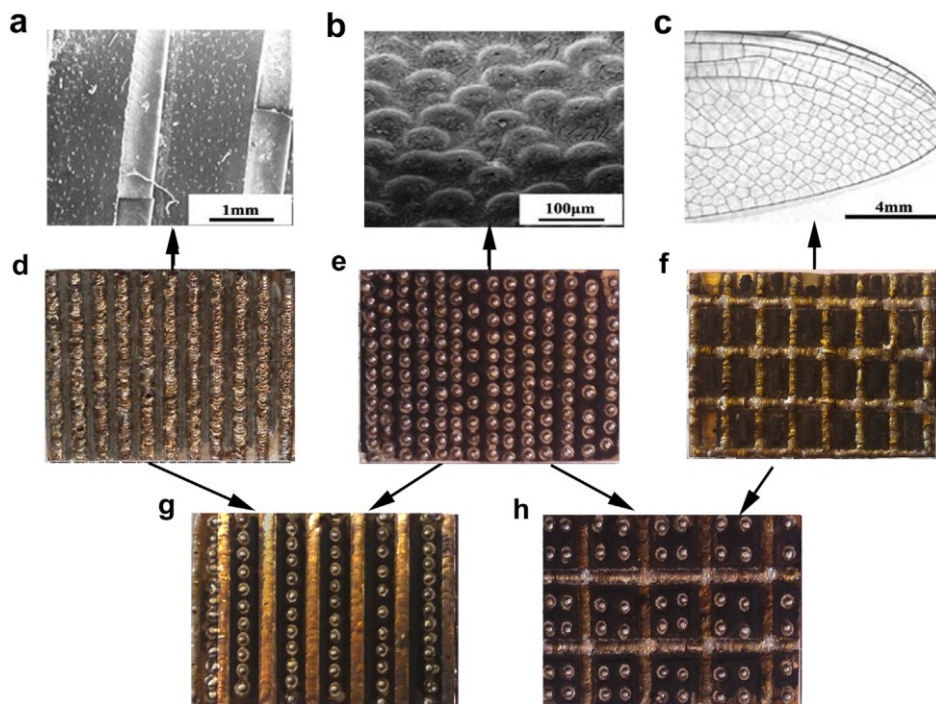


Figure 1-35 Biological structures and their biomimetic patterns on cast iron surface selectively treated by laser [67].

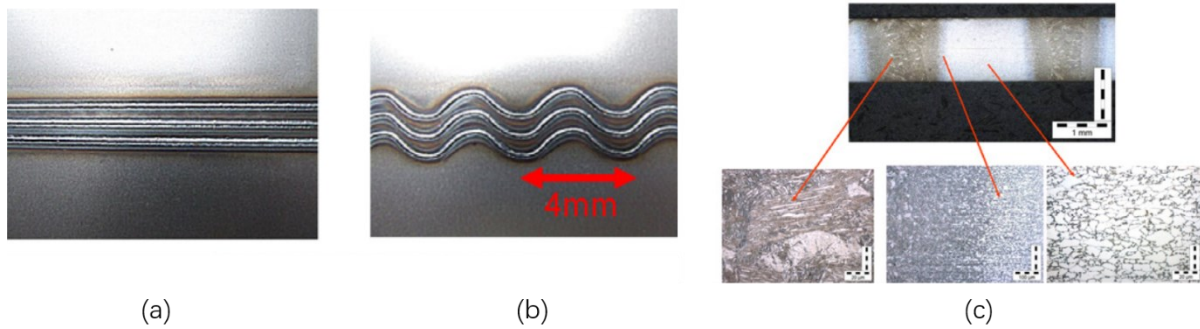


Figure 1-36 . Laser treated DP steel (a) straight laser treatment (b) corrugated laser treatment (c) microstructures of treated and untreated area [35].

Another important laser application on architected material is additive manufacturing, which is one of the most rapidly progressing technology nowadays. Selective laser melting layer by layer allows the fabrication of complex geometry which are difficult to realize by conventional metallurgical method. For example, periodic truss lattices can be fabricated rather easily by additive manufacturing [88]. Also, the laser moving trajectory can be varied locally to build a heterogeneous structure. A recent study shows that a heterogeneous stainless steel AISI 316L by rotating laser scanning angle between every layer during selective laser melting process demonstrated a better combination of strength and ductility than homogeneous one [89]. Varying the metallic powder element constitution allows the fabrication of compositionally graded material. Jiang et al. [90] successfully prepared a corrosion-wear-resistant alloy whose composition varies from carbon steel to stainless steel by direct laser deposition. Laser parameters and powder compositions can also be combined together to develop architected materials with gradient in both chemical composition and topology.

#### 1.4 Conclusions and the present work positioning

This literature review presents the concept of architected materials and its development in recent years. It refers to heterogeneous materials where the geometric topology of each component is well designed to yield certain synergistic effect between them when it is loaded [1,2]. Some examples are given for better understanding, especially concerning metallic architected materials and corrugated geometry. It is a popular trend to develop heterogeneous materials to achieve a trade-off between contradictory properties of homogeneous materials, like increasing strength and ductility at the same time [4]. Most existing metallic architected materials are fabricated by ‘post assembly’ of different components. This usually results in a poor bonding and cohesion at the interface, which is not strong enough and leads to cracks and an early-stage failure. Therefore, the quality of interface and connectivity is the key point to the mechanical performance of architected materials. Instead of ‘post assembly’, the interface decohesion problem can be resolved by making use of different existing phases out of one initial material. A well-arranged spatial architecture of different phases, such as ferrite and martensite, may have a synergistic effect.

Then some common laser heat treatments are introduced, including laser hardening, carburization, softening. Different aims can be achieved by controlling operation parameters. Compared with conventional furnace heat treatment, laser processing is much less time-consuming to obtain the same effect. The dramatic temperature evolution rate during laser treatment can achieve a phase transformation which is impossible for furnace treatment. And its highly concentrated energy density can modify local microstructure and mechanical properties with a small range of HAZ and leave a minimum level of deformation and distortion [69]. Some metallic materials present a large contrast in mechanical properties when they are in different heat-treated states. Selective laser heat treatment is a potential tool to practice local heat treatment with complex geometric trajectory to bring new phase in existing one to fabricate architected materials.

Several laser process applications on architected materials are presented. Even though some studies have been implemented on selective patterns by laser hardening on ferrous materials [35,67,87], there is a lack of systematic study on laser induced architected materials and topological optimization of patterns. The present research work aims to investigate the possibility of localized laser treatment on architected material fabrication. For this purpose, two grades of steels are chosen to be the base materials for laser treatment, AISI 430 ferritic stainless steel and a fully martensitic steel MS 1500. By changing the carbon content and atom distribution, numerous phases with quite different strengths can be formed, which provides a large range of combinations for architected material components. AISI 430 is chosen for laser hardening and laser carburization because few studies of laser heat treatment have been carried on this most widely used stainless steel. MS 1500 is austenitized and cooled down in furnace into ferrite and pearlite as ductile matrix and then laser hardened.

Concerning architecture patterns, corrugation is chosen to be reinforcement in soft and ductile matrix and the mechanical behavior in uniaxial tensile test is investigated. The unbending process of corrugated curves can reduce the decrease of work hardening rate or even introduce a boost during uniaxial tensile test [5,6,35]. This effect can delay the necking onset and enhance the ductility without much strength loss, which is a trade-off for the classical contradiction of strength and ductility. This may bring a new way for the development of AHSS. Archituration effect can be investigated though changing key geometric parameters, such as period or amplitude.

This study can be extended on other alloying system like Al and Ti alloys, and also on other architecture patterns like auxetic patterns. It can pave the way of laser process applications on architected material fabrication.

## **Chapter 2 Materials and experimental procedure**

## Résumé

Ce chapitre comprend l'introduction des matériaux et la procédure expérimentale utilisée dans cette étude. Les matériaux choisis sont l'acier inoxydable AISI 430 et l'acier initialement martensitique MS 1500. AISI 430 est sous forme de feuilles de 0,5 mm d'épaisseur et il est la nuance d'acier inoxydable la plus utilisée dans l'industrie. Il présente une microstructure ferritique. Cette nuance est choisie dans cette étude pour sa ductilité qui pourrait se servir comme une matrice des matériaux architecturés et aussi pour compléter le manque d'études existants concernant le traitement thermique sur des aciers inoxydables. MS 1500 est sous forme de feuilles de 1 mm d'épaisseur et il a été mis au four pour une austénitisation à 850 °C et refroidit à température ambiante dans le four éteint. Il présente finalement une microstructure de ferrite/perlite et devient ductile après ce recuit. Cette nuance est choisie dans cette étude pour sa teneur en carbone qui propose une excellente trempabilité et un contraste important entre la matrice et le renforcement. Trois types de traitement laser ont été réalisés : (1) le durcissement du AISI 430 par laser, (2) la carburation par laser du AISI 430 couvert du graphite, (3) le durcissement de l'acier recuit. Ensuite les matériaux architecturés ont été fabriqués par ces trois méthodes. Les principales méthodes expérimentales incluent le traitement thermique au laser et la caractérisation mécanique et microstructurale. La microstructure des matériaux de base et les échantillons traités par laser ont été étudiées par microscopie optique (MO), microscopie électronique à balayage (MEB), spectroscopie à dispersion d'énergie (EDS) et diffraction d'électrons rétrodiffusés (EBSD). L'analyse par diffraction des rayons X (RX) est utilisée pour identifier la constitution des phases des échantillons traités par laser. Les essais de traction et de micro-dureté sont réalisés pour caractériser les propriétés mécaniques des échantillons complètement traités par laser à différentes conditions. Les paramètres qui résultent les propriétés mécaniques les plus élevées ont été adoptés pour fabriquer des échantillons localement renforcés par des lignes droites et ondulées de différentes géométries. Les champs de déformation des matériaux architecturés ont été mesurés par un système de corrélation d'image (DIC) combiné avec les essais de traction. L'analyse par spectrométrie de décharge lumineuse (SDL) a été réalisée pour étudier le changement de contenu des éléments après le traitement au laser, principalement sur le signal d'oxygène pour évaluer l'oxydation des surfaces et le signal de carbone pour analyser l'efficacité de carburation. La méthode des éléments finis (FEM) a été utilisée pour simuler l'évolution de la température pendant le traitement laser par le logiciel COMSOL, et également pour prédire le comportement mécanique des matériaux architecturés par logiciel Abaqus et Z-set. Ces méthodes sont présentées en détail dans la partie suivante.

## 2.1 Materials

### 2.1.1 Introduction and properties

Two kinds of steel sheets are extensively studied in this research, stainless steel AISI 430 and a commercialized steel by ArcelorMittal as MS1500EZ. AISI 430 is a fully ferritic grade with 18% of Cr and one of the most widely used stainless steels in various fields, such as white goods and automotive industries. It exhibits a good combination of ductility, thermal conductivity, and corrosion resistance. The carbon content is very low. Sheets of AISI 430 with a thickness of 0.5 mm were received as mirror-polished on both sides. In order to increase the absorption ratio of laser beam, they were sand blasted to get a uniform and mat finish. In this study, this grade is used as a base material to study the strengthening effect of direct laser hardening and laser assisted carburization. Once the optimized parameters resulting the highest strength are found, these methods are used to create reinforcements for architected materials.

ArcelorMittal MS1500EZ is a fully martensitic grade, which presents a high strength but poor ductility. It is among the highest strength carbon steels and has a good formability. Martensitic steels are a promising candidate for anti-intrusion applications in automobile industry where their high strength guarantees the safety and contributes to reducing the structure weight. But in this study, this grade is used only due to its carbon content, which is around 0.2%. Because as introduced in the previous part, even though high content martensitic steel can be softened by laser heat treatment, the change is not suitable for this study. Martensitic sheets of 1 mm thickness are at first immersed in HCl solution to remove galvanizing zinc layer and then austenitized above Ac3 and cooled down in furnace to obtain a ferritic matrix. Annealed steels are immersed again in HCl solution to remove oxide and then sand blasted. This grade is studied in this research for direct laser hardening and then the treated zone serves as reinforcements within architected materials. The chemical compositions of these two grades are shown in Table 2-1.

Table 2-1 Chemical composition [wt %] of the studied AISI 430 and MS1500EZ.

Grade	C	Si	Mn	Cr	Ni	P	Fe
AISI 430	0.026	0.30	0.50	18.70	0.14	0.03	Bal.
MS1500EZ	0.228	0.242	1.730	0.190	0.014	0.01	Bal.

As a matter of fact, before starting the study on these two grades of steels, other steel grades or the same grade of other forms have been tried. MS1500 steel has been annealed by laser treatment for softening, but localized softened zone on steel sheets will bring in concentrated strain and thus early fracture. Dual phase (DP) 600 sheets have been directly laser hardened, but the contrast between base material and strengthened part is rather limited because DP600 has a relatively high strength, and the carbon content is not high enough to produce a much more strengthened martensitic microstructure. An extra soft steel (XSG) is also studied, but due

to its low carbon content, there is almost not any hardening effect after laser hardening, but only grain coarsening.

In this study, global mechanical properties are characterized by tensile test to evaluate laser strengthening effect of fully treated samples, it is important to realize a more consistent microstructure evolution through the whole thickness instead of only on the surface. Hence it needs a uniform temperature field during the laser heating and cooling cycle. And because the two available lasers for this study have small spot sizes (around 1 mm) and one of them has a limited maximum power of 110 W, very thin sheets, ideally less than 1 mm, are required for this study to achieve a larger ratio treated zone depth/whole thickness. 0.5 mm thick AISI 430 and 1 mm thick MS1500 after annealing are chosen because they have suitable thickness and can be hardened prominently by laser irradiation, especially there is few studies on laser hardening on ferritic stainless steel. It is certainly possible to carry out laser architected material studies on other laser hardenable metallic sheets with suitable operation conditions, such as larger laser spot size or output power.

### **2.1.2 Microstructural characterization and mechanical properties**

Microstructural observations are realized on the section of as-received materials and after laser treatment for two studied steel sheets AISI 430 and annealed martensitic steel using both optical microscope (OM) and scanning electron microscope (SEM) equipped with energy dispersive X-ray spectrometry (EDS) and electron backscatter diffraction (EBSD) detector. The rolling direction and transverse direction are not specified on the as-received AISI 430 sheets and microstructural examination do not reveal evident difference along different directions. And annealed martensitic steel is fully heat treated above  $A_{c3}$  before laser treatment, following tests show that there is not any obvious difference in neither microstructure nor mechanical properties in neither initial rolling direction and transverse direction. Therefore, in this work, rolling direction and transverse direction of the sheets will not be distinguished in characterization nor laser treatment.

Prior to the microstructural observations, the samples are prepared by grinding with silicon carbide (SiC) abrasive papers with grit sizes of 240, 400, 800, 1000, followed by cloth polishing using 9, 3, and 1  $\mu\text{m}$  diamond suspension solutions, each step for 3 minutes. AISI 430 steel samples are finished by 0.04  $\mu\text{m}$  colloidal silica suspension (OP-S suspension produced by Struers) for 5 minutes and are etched in Kalling's No.1 solution (1.5 g  $\text{CuCl}_2$ , 33 ml HCl, 33 ml ethanol, 33 ml distilled water) for a few seconds to reveal the microstructure. The etching solution outlines the grain boundaries and carbides, and colors martensite in dark brown in OM. Annealed martensitic steel samples are etched by 3% nital solution for around 10 seconds. Ferrite appears light, cementite is dark in OM, and martensite is etched.

Figure 2-1 shows the microstructure of as-received AISI 430 section (a) by OM (b) by SEM. It presents a complete equiaxed ferritic microstructure with evenly distributed very fine chromium carbide precipitation. The average grain size is 11.3  $\mu\text{m}$ .

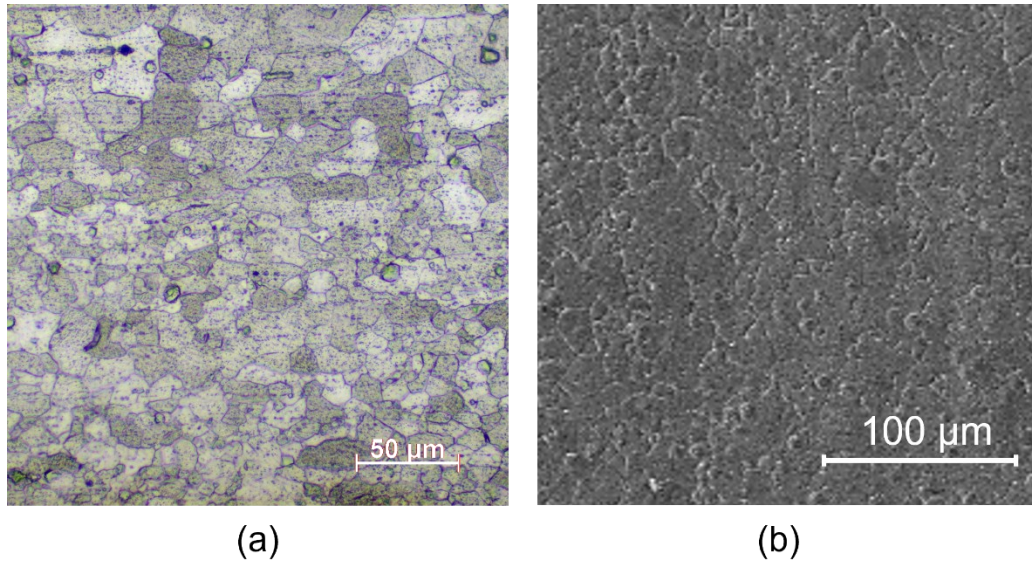


Figure 2-1 Microstructure of as-received AISI 430 sheet section (a) OM (b) SEM.

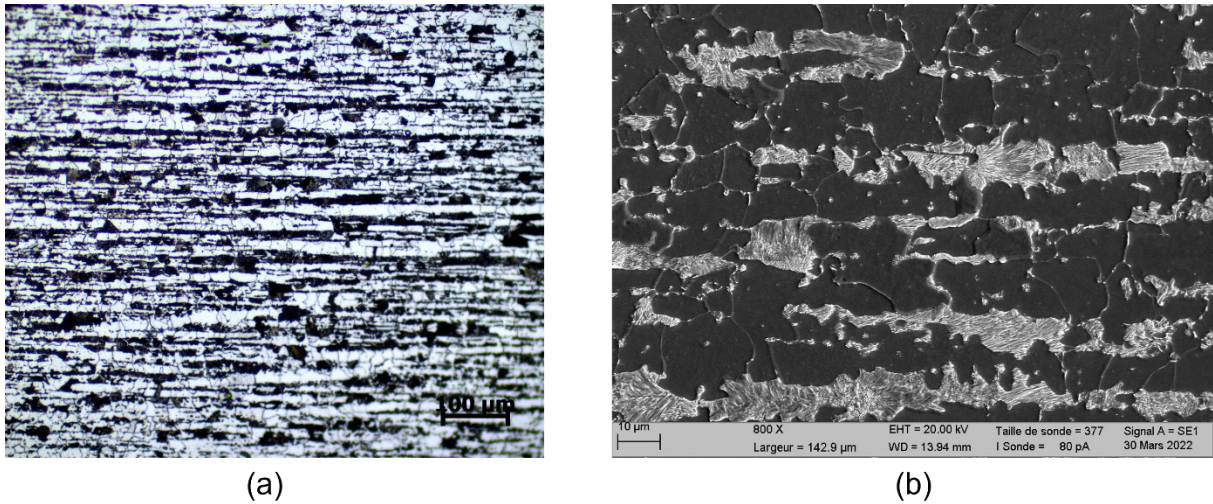


Figure 2-2 Microstructure of annealed MS1500 steel sheet section, (a) OM, (b) SEM.

MS1500EZ steel sheets are austenitized in furnace at 850 °C for one hour and cooled down to room temperature in turned off furnace, whose cooling rate is around 2 °C/min. Figure 2-2 shows the section microstructure of annealed steel, (a) by OM, (b) by SEM. It presents linear arranged pearlites islands (dark in OM but bright in SEM) embedded in ferritic matrix (bright in OM but dark in SEM). The average grain size is 15.7 μm and the interlamellar spacing of pearlite is around 250 nm.

Axial tensile tests are carried out on as-received AISI 430 stainless steel and as-annealed martensitic steel to characterize their mechanical properties. Results are show in Table 2-2, including Young's modulus (E), yield stress (YS), ultimate tensile strength (UTS), elongation (e) and micro-hardness. These two kinds of materials which are relatively ductile will serve as base materials in this study and used as matrix concerning architected materials.

Table 2-2 Mechanical properties of as-received AISI 430 and as-annealed steel.

Grade	E (GPa)	YS (MPa)	UTS (MPa)	e (%)	Hardness (Hv)
AISI 430	210	346±12	500±15	19.39±0.07%	165±5
Annealed steel	210	300±7	534±12	16.7±0.3%	167±6

## 2.2 Experimental procedure

In the present research work, principal experimental methods include laser heat treatment and mechanical and microstructural characterization. Laser heat treatment consist of direct laser quenching and laser carburization. Axial tensile tests and microhardness tests are carried out to characterize mechanical properties. Digital image correlation (DIC) is combined with tensile test to follow strain fields for architected materials. OM, SEM, EDS and EBSD are used to observe laser treated materials. X-ray diffraction analysis is used to identify phase constitution of laser treated materials. Glow Discharge Optical Emission Spectrometry (GD-OES) analyze is implemented to investigate the element content change after laser treatment. Finite Element Method (FEM) is used to simulate both temperature evolution during laser treatment and also tensile behavior of laser architected materials. These methods will be presented in detail in the following part.

### 2.2.1 Laser treatment platform and temperature measurement

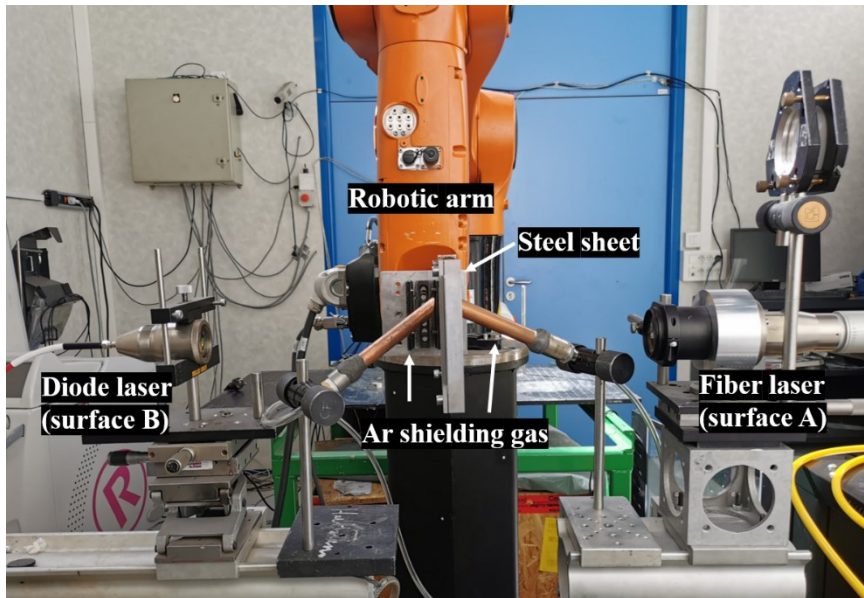


Figure 2-3 Laser treatment platform for this study

The laser treatment platform was developed as shown in Figure 2-3. Two lasers are placed on each side to be used either simultaneously or separately, in order to achieve a more uniform treatment through the thickness of the sheets and to compare different effects between laser treatment from one single side and laser treatment from double sides. The two lasers available

for this study are a single-mode 500 W fiber laser from SPI (surface A) at a wavelength of 1080 nm and a multimode 110 W laser diode from DILAS (surface B) operating at a wavelength of 980 nm. The fiber laser has a single mode Gaussian beam, and the diode laser has a multi-mode top-hat beam. For single laser treatment, only the fiber laser SPI is used. For double laser treatment, due to different modes of the two lasers, the energy density on surface A is much more intense than surface B at the beam center with the same input power. Thus, the impact on surface A penetrates deeper into the sheets than surface B, where the heated zone is more expanded but shallower, thus the spot size on surface B is larger than surface A. Thanks to the synchronization effect of irradiation from both sides, following microstructural examination results show that the treated zone is almost symmetric on two sides.

The steel sheets are clipped on an aluminum alloy frame to be flattened and to avoid deformation due to internal stress introduced by heat treatment which may cause defocalization. The frame is fixed on a robotic arm which can move freely in space with pre-programmed trajectory with a given linear velocity. The treatment can be operated under argon shielding gas with a nozzle on each side to reduce oxide formation on the sheet surfaces during high temperature, especially above melting point. The oxide can cause an early fracture for treated samples and significantly increases the absorption rate, thus sometimes overheat.

Before applying laser treatment, both laser energy distribution profiles are measured. The exact efficiencies of both laser fibers between demanded power and true emitted power are also investigated.

#### i. Laser hardening on AISI 430 steel

As explained above, three kinds of laser treatments are realized in this study and different laser parameters are applied. Table 2-3 shows laser parameters for the first subject, direct laser hardening process, on AISI 430 stainless steel sheets, whose aim is to study the effect of input linear energy density (LED) on mechanical behavior of fully treated samples. Fully treated samples with dimensions in Figure 2-4 (b) are fabricated and characterized, and the LED leading to a highest strength is adopted for corrugation reinforced architected materials.

Double laser treatment at 100 W from both sides with Ar shielding gas is applied for architected materials. In this study, AISI 430 direct laser hardening is tested from one to four reinforced architecture for different reinforced volumes. Schematic sketches of useful gauge length on samples are shown in Figure 2-5. (a) and (b) are respectively single straight and corrugation reinforced sample. Reinforced part is strengthened treated part by direct laser hardening or laser carburization, which is surrounded by soft matrix. For corrugation reinforced samples, the geometry is defined by a sinusoidal wavy curve. The key parameters are period (P), height (H) and thickness (t), among which P and H decide the corrugation form and t is adjusted to keep the reinforced volume among different corrugation forms. (c) shows multi corrugation reinforced sample, where several corrugations are placed parallelly with the same interval on one specimen.

Table 2-3 Direct laser hardening parameters for AISI 430 stainless steel sheets.

Laser	Single laser (surface A)		Double laser (surface A +surface B)		Linear velocity (mm/s)	Linear energy density (LED) P/v (kJ/m)	
	Shielding gas	Ar	Air	Ar			Air
Power/W		100	100	50+50	50+50	10	10
		150	150	75+75	75+75	10	15
		200	200	100+100	100+100	10	20
		250	250	150+100	150+100	10	25

Reinforcement geometries are shown in Table 2-4. The spot size for straight reinforcement is set at 1 mm, which corresponds to a reinforced volume of 10% in the gauge part. The spot size of corrugated reinforcement is reduced to keep the identical reinforced volume. One to four reinforcements within one specimen are applied, which equals to 10% to 40% reinforced volume.

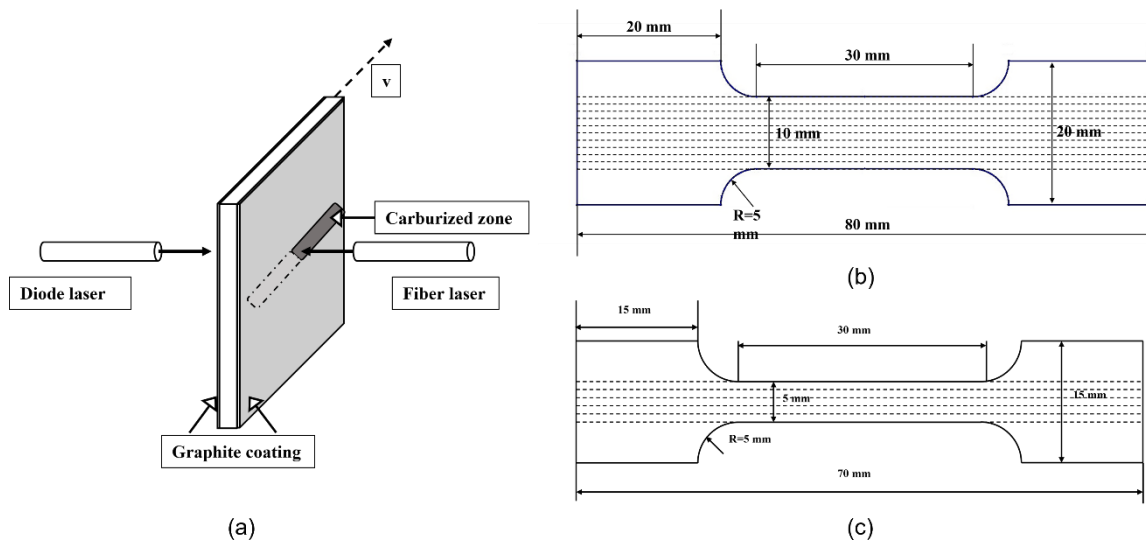


Figure 2-4 Schematic sketch of (a) laser carburization, (b) (c) fully treated samples.

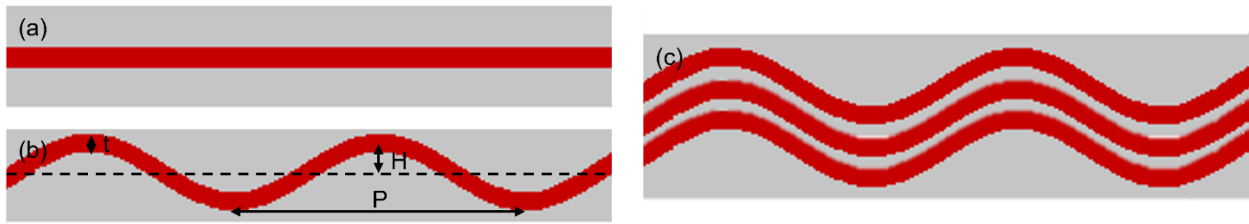


Figure 2-5 Schematic sketch of (a) single straight reinforced sample, (b) single corrugation reinforced sample, (c) multi corrugation reinforced sample.

Table 2-4 Geometric parameters of reinforcements adopted on laser hardened AISI 430.

Period P (mm)	Height H (mm)	Inclination (H/P)	Thickness t (mm)	Reinforcement number
- (straight)	0 (straight)	0	1	1-4
6	1	0.17	0.84	1-4
6	1.5	0.25	0.78	2
6	2	0.33	0.74	1-4
6	2.5	0.42	0.66	2
6	3	0.5	0.59	2

## ii. Laser carburization on AISI 430 steel

The second interested subject in this study is laser assisted carburization on AISI 430 stainless steel sheets. The process is illustrated in Figure 2-4 (a) by a schematic sketch. The robot is programmed in the same way and the lasers are in the same positions as direct laser hardening process. A commercial painting graphite spray of Orapi brand is used for laser carburization. It has been applied to both two surfaces of sand blasted sheets and then dried up in air for at least 24 hours before laser carburization. Based on the results of the first step, only two LED are chosen in this procedure by single laser treatment and double laser treatment to guarantee an obvious carburizing effect and avoid overheat. The parameters are shown in Table 2-5. Fully treated samples with dimensions in Figure 2-4 (c) are submitted for tensile test to characterize the strengthening effect, and the treatment condition which results in the highest strength is adopted for corrugation reinforced architected materials.

Table 2-5 Laser carburization parameters for AISI 430 stainless steel sheets.

Type of process on SQ and LC samples	Power (W)	Velocity (mm/s)	LED P/v (kJ/m)
1 - Single laser	150	10	15
2 - Double laser	75 + 75	10	15
3 - Single laser	200	10	20
4 - Double laser	100 + 100	10	20

Double laser treatment at 100 W from both sides is chosen for architected materials. Single reinforcement configuration is employed, and geometry parameters are shown in Table 2-6. The spot size for straight reinforcement is set at 1 mm, which corresponds to 20% of the gauge volume reinforced. The spot size is adjusted for corrugated reinforcements to keep the same reinforced fraction.

Table 2-6 Geometric parameters of reinforcements adopted on laser carburized AISI 430.

Sample	Period P (mm)	Height H (mm)	Inclination (H/P)	Thickness t (mm)
1	-(straight)	0 (straight)	0	1.00
2	15	0.5	0.033	0.99
3	15	1.0	0.067	0.96
4	15	1.5	0.1	0.92

### iii. Laser hardening on annealed steel

The last interested subject in this study is laser hardening on annealed steel and corrugation reinforced architecture. Robot programming and laser position are always the same. But only one LED is applied with 150 W on surface A and 100 W on surface B, preliminary examination proves that this input energy can generate an almost fully martensitic microstructure within treated zone.

Single reinforcement configuration is adopted in this experimental series. Straight and corrugation reinforcement geometries are shown in Table 2-7. The spot size of straight reinforcement is set at 1.2 mm, which corresponds to 24% of the whole sample reinforced. For the corrugated reinforcement, the spot size is slightly adjusted to keep the same reinforced volume in the gauge area.

Table 2-7 Geometric parameters of reinforcements adopted on annealed steel.

Sample	Period P (mm)	Height H (mm)	Inclination (H/P)	Thickness t (mm)
1	- (straight)	0 (straight)	0	1.20
2	15	0.5	0.033	1.19
3	15	1.0	0.067	1.15
4	15	1.5	0.1	1.10
5	30	1.5	0.05	1.16
6	10	1.5	0.15	1.01

The temperature evolution during laser treatment for single laser treatment in Ar shielding gas are measured every millisecond with several type K thermocouples welded on the backside surface of the laser beam (surface B). Heating and cooling thermal cycle is simulated by FEM using the software COMSOL Multiphysics and suitable absorption ratio for laser hardening and laser carburization are trimmed according to the experimental results. The temperature on the beam side not measured directly because direct laser irradiation applied on thermocouples is to be avoided and the results are affected. Instead, this process is simulated with the same absorption ratio determined by the measurement for single laser treatment.

### 2.2.2 Tensile test and DIC equipment

Fully and localized laser treatments are realized on steel sheets. According to predefined dimensions, tensile specimens are cut from steel sheets. Even though laser treatment introduces internal stress into steel sheets due to phase transformation and distort them, it is better to keep the cutting step after laser treatment. Because certain laser parameters heat steel sheets to very high temperature, even above fusion point, if this is applied on already cut specimen, the heat dissipation will be affected by specimen borders and localized overheat will take place. Laser treated zone risks to be less homogeneous according to geometries and this ununiformity will cause stress concentration and early fracture of specimens. That is the reason why tensile specimens are cut from the sheets are cut after laser treatment despite of some disadvantages like distortion or slight centering defects. Figure 2-6 shows several examples of single straight a corrugation reinforced architected samples.

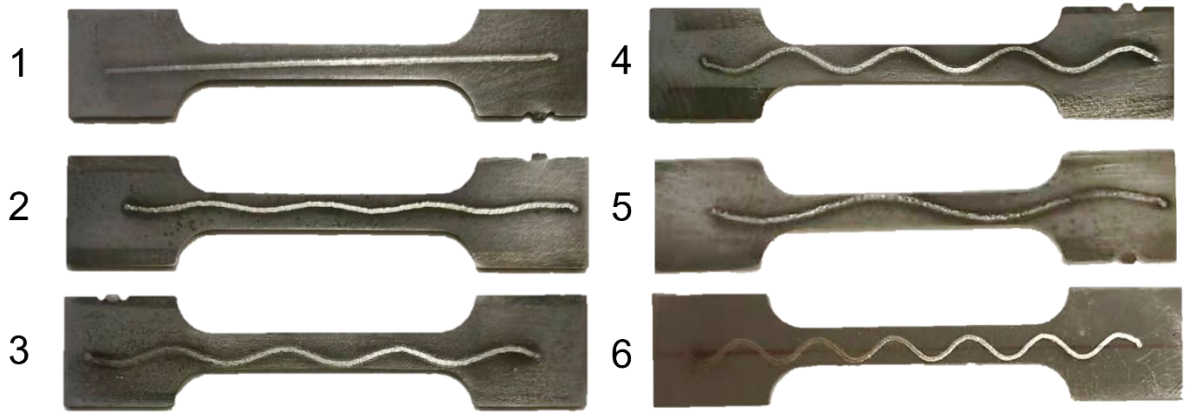


Figure 2-6 Single straight and corrugation reinforced architected samples.

Axial tensile tests are carried out on samples with a gauge length of 30 mm with an Instron 5581 tensile machine at room temperature. The tensile tests were conducted under displacement control at a constant crosshead speed of 1 mm/min. As-received and fully treated specimens of laser hardened and carburized AISI 430 are machined according to the dimensions in Figure 2-4 (b) and (c) respectively. A mechanical extensometer (Instron) is placed on the gauge to acquire the strain, and the stress is calculated from the load output by tensile machine. As-annealed steel specimens are machined according to Figure 2-4 (c) and tested in the same method.

Straight and corrugation reinforced architected tensile specimens of each category are machined in the same shape and tensile tests are carried out by the same tensile machine. Instead of a mechanical extensometer on the gauge, DIC displacement field measurement is performed on experimental tensile tests to follow the local strain evolution of matrix and reinforcement of laser architected materials with the software VIC-2D. Figure 2-7 (a) presents the set-up. A fixed focal lens of 20 cm is used with a speed camera. Extra illumination is added to increase the picture quality, but it is to note that saturation is to avoid. After adjusting the focus and obtaining a satisfying initial position, pictures are taken on the gauge part every 0.2 s during tensile test. With a synchronization system between the tensile test machine and the speed camera, the instant force is exported at every moment when a picture is taken, which reveals the instant stress with a given strain field map. Figure 2-4(b) is an example of speckles made by commercial paintings. Black painting is applied at first to fully cover the whole gauge length and dries up, white one is added to create speckles to be followed for the correlation calculation. Fine speckles are expected to increase the precision of correlation.

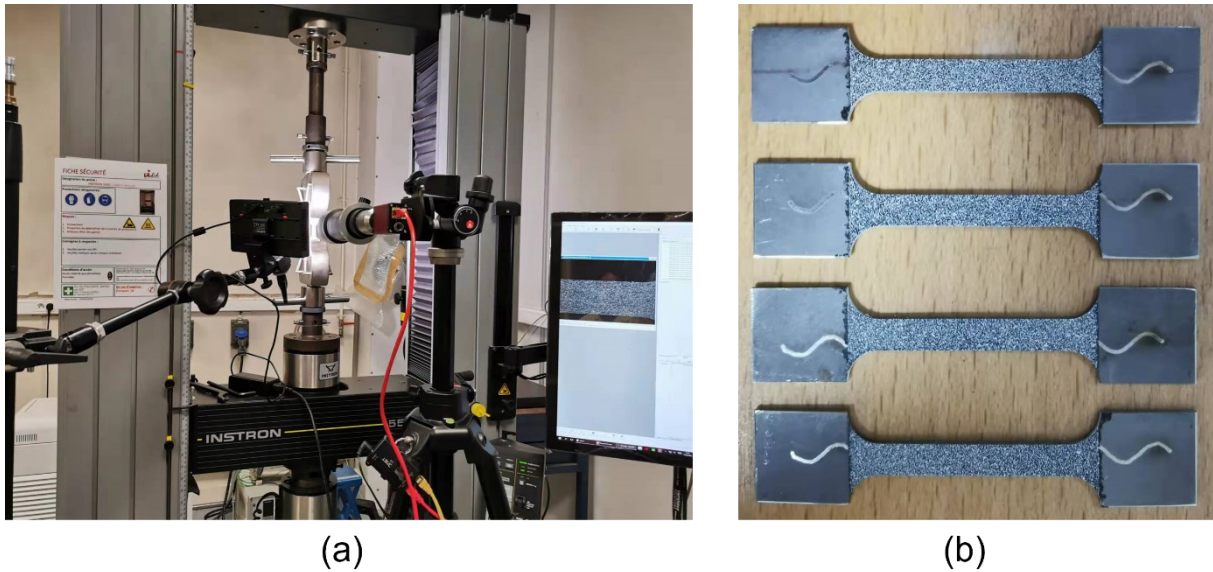


Figure 2-7 (a) DIC strain field measurement set-up, (b) corrugation architected samples with painting speckle.

After each tensile test, the series containing hundreds of photos is proceeded with post process in software Vic-2D. Instant strain fields in tensile direction (X direction), transverse direction (Y direction) are calculated and depicted with a given average strain and stress. Thanks to this method, it is possible to trace heterogeneous strain of matrix and reinforcement and evaluate the archituration effect.

### 2.2.3 Finite Element Method simulation of uniaxial tensile test

The axial tensile tests of architected samples with geometries described in part 2.2.1 are simulated by FEM with both softwares Abaqus and Z-set. Mesh examples for AISI 430 localized laser hardened are shown in Figure 2-6 with (a) single straight reinforced specimen, (b) single corrugation reinforced specimen and (a) multi corrugation reinforced specimen, the colored parts are reinforced. Mesh size of reinforcements and the matrix nearby is set at around 0.3 mm to reveal the precise strain evolution during tensile test. And other parts of the specimen are meshed with more coarsened size. Other kinds of specimens are constructed in the same method with similar mesh size. These geometries are extruded in their real thickness (0.5 mm or 1 mm) and simulations are carried out in three dimensions.

To imitate the uniaxial tensile test, left side of the model is fixed with encastre boundary condition where  $U_1 = U_2 = U_3 = UR_1 = UR_2 = UR_3 = 0$ . And a uniform displacement ( $U_1$ ) is imposed on the right side and  $U_2 = U_3 = UR_1 = UR_2 = UR_3 = 0$ . An initial step of 0.0001 is adopted and a maximum step size of 0.002 is applied. For this maximum step size, it corresponds to a total strain of 0.04%. Trials with different the step sizes confirms that the step size does not have a significant effect on global stress-strain curves extracted from simulation results but is small step size is chosen to have more data points during the simulation.

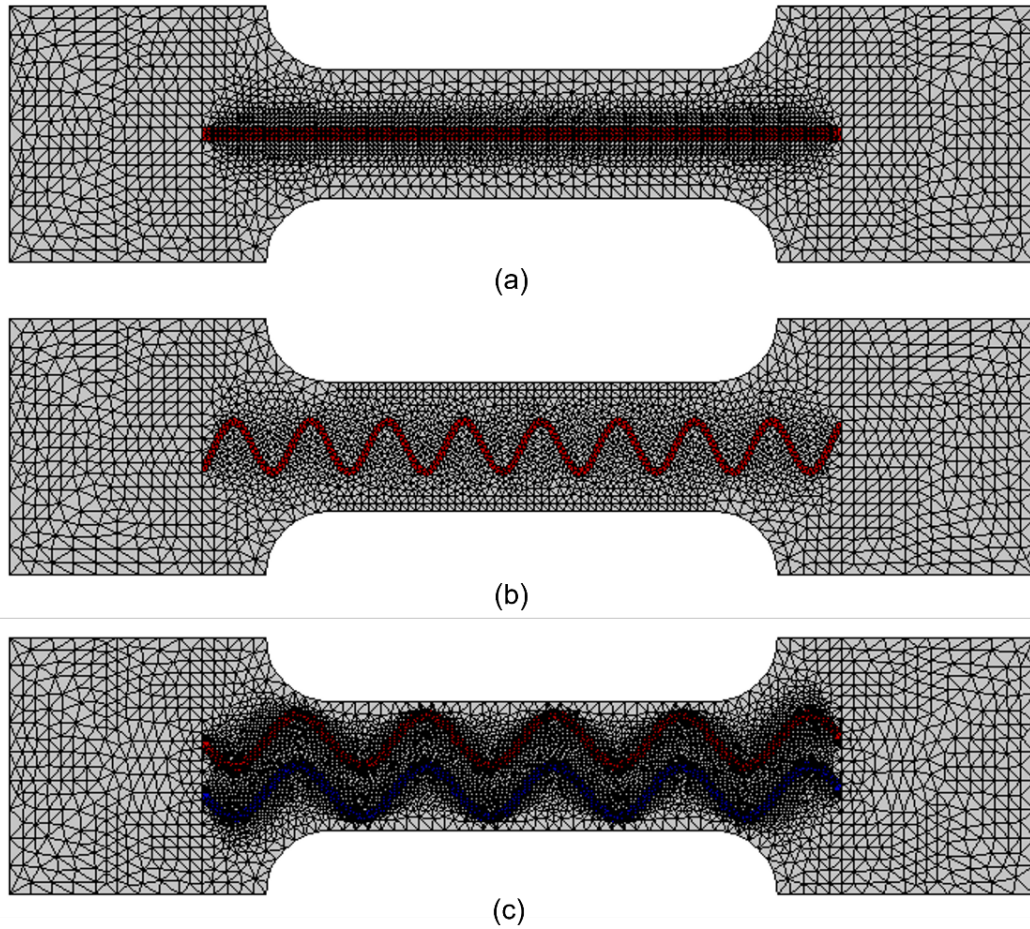


Figure 2-8 Model of corrugation reinforced sample with mesh and boundary condition.

Beyond the yield strength, a power-law hardening is adopted to predict the plastic stress-strain behavior. Specific material parameters for each component will be listed in each relevant part. The behaviors of all phases are assumed to be elastically and plastically isotropic.

Onset necking strain point of tensile test simulation is defined by Considère criterion, where the true stress equals to the tangent of true stress-true strain curve as in Equation 2-1 [91].

$$\sigma = \frac{d\sigma}{d\varepsilon} \quad 2-1$$

With the same condition and imported mesh model, results from Abaqus and Z-set do not have any obvious differences. Stress-strain curves and strain maps are extracted. Simulation strain maps are compared with DIC strain map at the same average global strain. These comparisons will be introduced in following chapters.

#### 2.2.4 Micro-hardness test

The Vickers micro-hardness of laser treated samples are taken on the section. AISI 430 is measured with a force of 100 g and a load time of 10 s. Annealed steel is measured with a force of 200 g and a load time of 10 s. The difference in force is because the laser hardened zone of

annealed steel has a higher hardness and also the annealed steel sheets are thicker, which allows larger indentations with enough distance between them.

Figure 2-9 shows the tracks of micro-hardness tests on the section of AISI 430 hardened by laser with three laser tracks. Tests are realized along the section center line (on the left) to reveal the hardness evolution from as-received material to laser treated zone and also along laser track center (on the right) to study the laser effect through the cross-section depth. Micro-hardness is taken on similar tracks on annealed steel section.

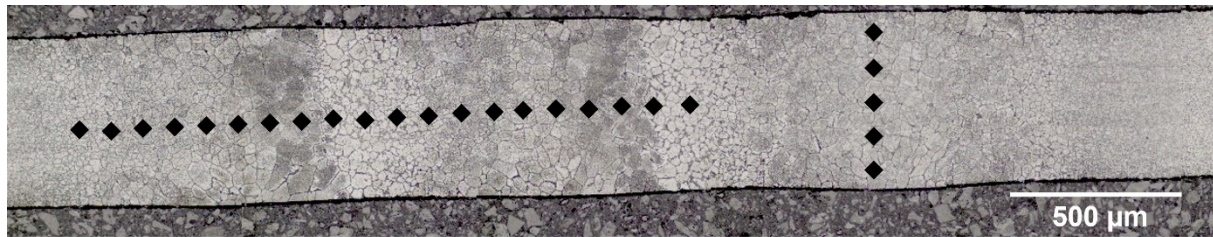


Figure 2-9 Micro-hardness tracks on laser hardened AISI 430 section.

### 2.2.5 Microstructural observation and phase identification

Two kinds of laser treatments are studied in this research and microstructures of treated sample sections are examined. AISI 430 is submitted to laser self quenching (SQ) and laser carburization (LC). SQ samples are prepared by the same method of as-received material and etched by Kalling's no.1 solution for microstructure observation. LC samples are polished by the same steps but etched by diluted aqua regia (15 ml HCl, 5 ml HNO<sub>3</sub>, 100 ml distilled water) for about twenty seconds. Annealed steel is submitted to laser self quenching and the same metallurgical preparation is done and finished by 3% nital solution for treated samples as the as-annealed material.

EDS examinations are carried out on etched samples. EBSD samples are prepared by the same polishing steps but finished with 30 minutes of OP-S polishing in order to remove tiny scratches and to improve diffraction.

### 2.2.6 X-ray diffraction analysis

In order to determine the present phases of laser treated samples, X-ray diffraction analysis was conducted on a PANalytical X'Pert diffractometer on surface layers of samples after removing the oxidation. A cobalt anode was used emitting mainly through the K $\alpha$  ray at a wavelength of 0.179 nm. The 2 $\theta$  diffraction data were collected from 40° to 140 °with a step size of 0.025° with an integrated acquisition time of 300 s. All scans were carried out in continuous mode. As-received AISI 430, laser hardened AISI 430 at 100 W from both sides, laser carburized AISI 430 at 75 W and 100 W from both sides are analyzed and the phase constitutions are calculated. Laser hardened annealed steel is not tested for its relatively simple phase transformation.

### 2.2.7 Glow Discharge Optical Emission Spectrometry analysis

In this study, the chemical composition measurement is carried out by Glow Discharge Optical Emission Spectrometry (GD-OES) analysis. GD-OES is a surface analytical technique, an atomic emission spectrometer system employing a non-thermal glow discharge source for atomic excitation [92]. In a glow discharge, cathodic sputtering is used to remove material layer by layer from the sample surface. The atoms removed migrate into the plasma where they are excited through collisions with electrons or metastable carrier gas atoms. The characteristic spectrum emitted by these excited atoms is measured by the optical spectrometer [93].

The distribution of elements is determined qualitatively by depth profiling using a Horiba JY 10000 RF spectrometer equipped with a 4 mm diameter anode. The power to the plasma is supplied by a radio-frequency generator at a frequency of 13.56 MHz. A moderate power of 40 W is used for all analyses. High-purity argon is employed as the discharge gas, at a constant pressure of 750 Pa. The following atomic emission lines (O: 130 nm, C: 156 nm, Fe: 372 nm, Cr: 425 nm, Ni: 225 nm, Mn: 403 nm, Si: 288 nm, P: 178 nm, S: 181 nm) are selected. Compared with EDS detector, which is not sensible enough for quantitative measurement of light elements like carbon or oxygen because of low dispersive energy, GD-OES analysis detects wavelength instead, so it allows precise measurement for all elements.

The sputter erosion of glow discharge creates a crater of 4 mm diameter as shown in Figure 2-10. The sputtered atoms are deposited on the border of the crater. The crater shape with the chosen parameters is relatively clean: the crater bottom is sufficiently flat and, the bottom and the surface roughness similar. This method is advantageous because with progressive erosion, evolution of chemical composition along the depth can be detected layer by layer. In this study, two kinds of GD-OES analysis are interested. For AISI 430 direct laser hardening, the oxygen signal is especially followed to study the oxidation layer formed on the surface due to the treatment with and without protective shielding argon gas, which is only a qualitative measurement. On the contrary, exact carbon contents through the whole thickness of AISI 430 sheets for laser carburizing treatment are analyzed quantitatively.

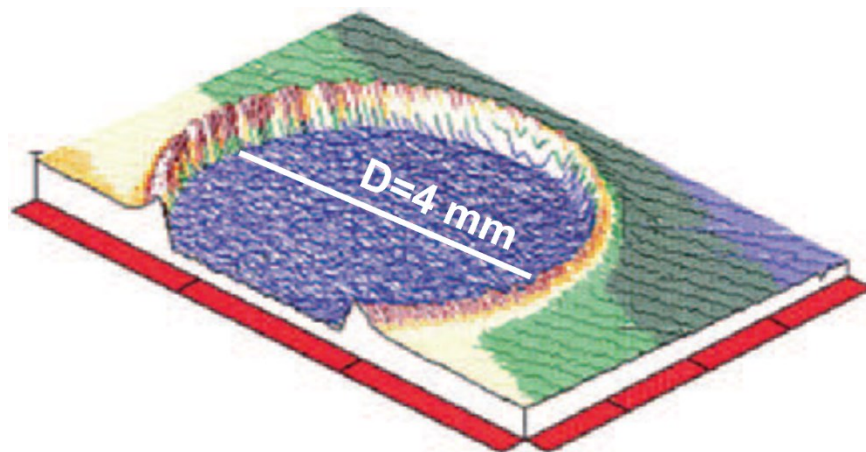


Figure 2-10 Erosion crater formed by glow discharge.

Preliminary study to determine the erosion rate is implemented on as-received AISI 430 material for 20 minutes and the crater is characterized by a profilometer, and the depth profile is shown in Figure 2-11. This rather long duration is chosen to erode a deep enough crater to reduce the systematic error related to profilometer. The average depth of the crater is 85.84  $\mu\text{m}$  and the average erosion rate on AISI 430 sheet is 4.29  $\mu\text{m}/\text{min}$ . The erosion rate with the same parameters on a given material keeps unchanging. The conversion between sputtering time and depth in the following measurements are calculated by this rate. The oxide layer thickness and carbon content at different depths can be deduced in this way.

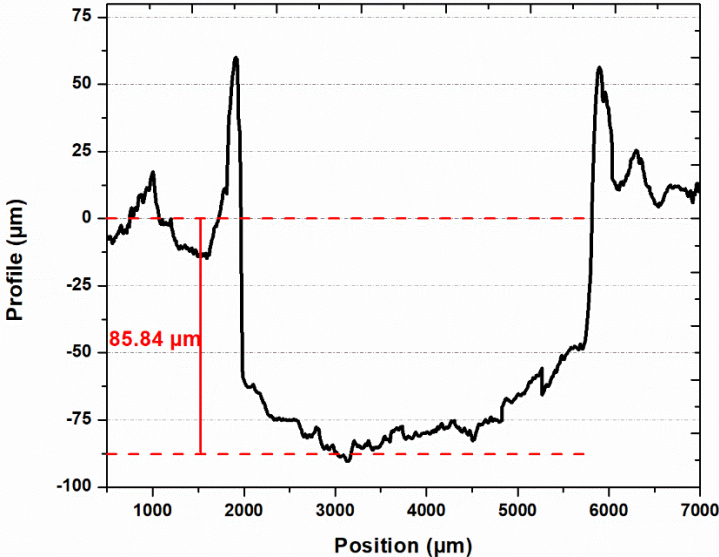


Figure 2-11 Profile of preliminary eroded crater for 20 minutes.

The general experimental method of this study is summarized in Figure 2-12. Following chapters are developed by these three categories of researches.

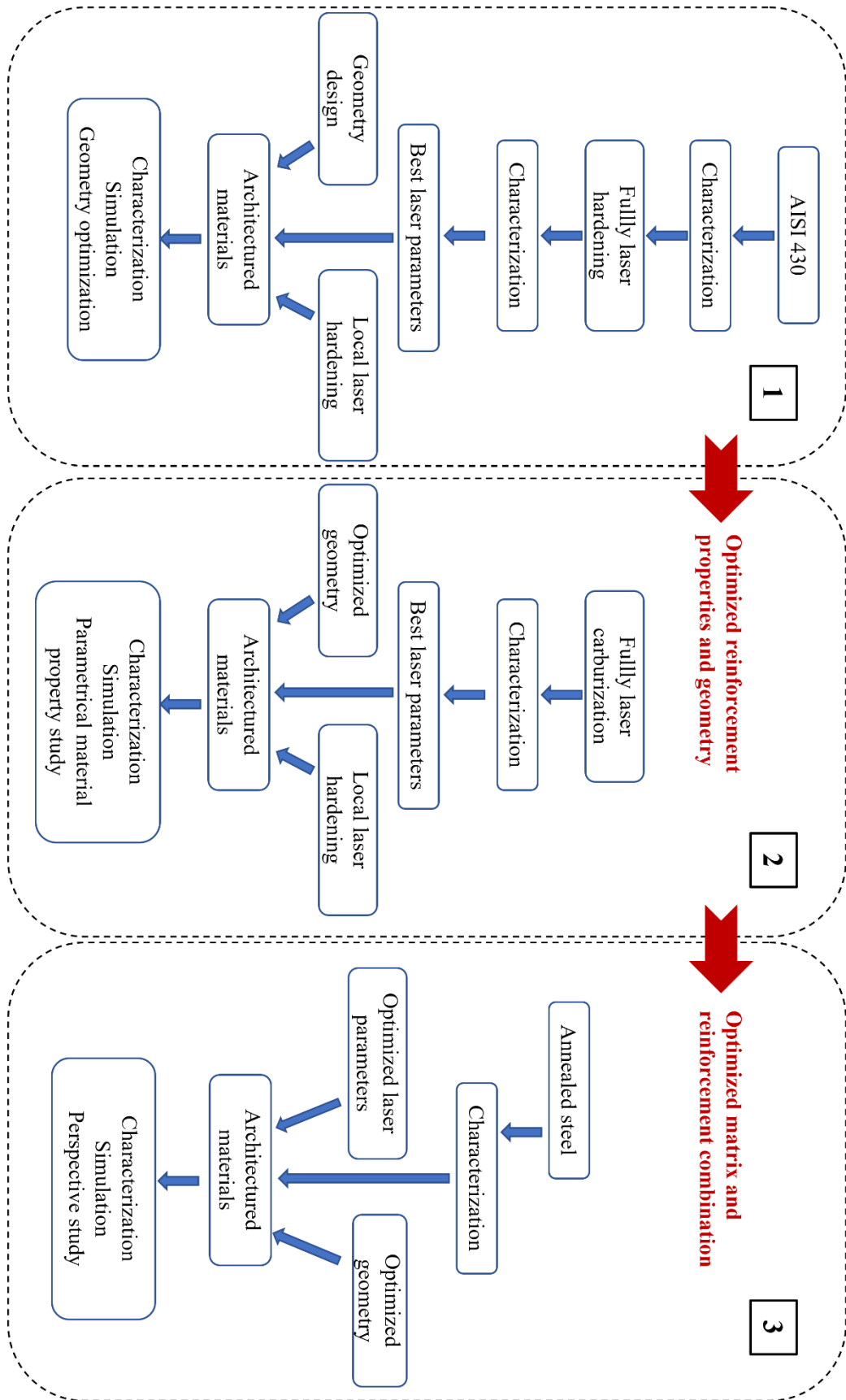


Figure 2-12 Experimental procedure for this study.

# **Chapter 3 Laser hardening of 430 ferritic stainless steel for enhanced mechanical properties and corrugation reinforced architected materials**

## Résumé

Dans ce chapitre, une méthodologie a été développée pour modifier les propriétés mécaniques des feuilles d'acier inoxydable ferritique AISI 430 par un traitement laser. Pour réaliser cette étude, la distribution d'énergie et l'efficacité du faisceau laser ont été caractérisées. L'évolution de la température a été simulée par COMSOL et mesurée par des thermocouples. Des échantillons entièrement traités ont été soumis pour caractérisation microstructurale et mécanique. L'effet du gaz de protection lors du traitement et de la densité d'énergie linéaire (LED) du laser sur la microstructure et les propriétés mécaniques a été étudié. La LED conduisant à l'effet le plus fortifiant a été adoptée pour fabriquer des matériaux architecturés renforcés par lignes droites et ondulées en différentes géométries. Leurs comportements mécaniques ont été suivis par des essais de traction équipés du système DIC. Les résultats montrent que le traitement laser améliore les comportements mécaniques de AISI 430 par la formation de martensite et de carbures de chrome lors d'un refroidissement rapide. La microdureté locale peut être augmentée de 90% au maximum et la limite d'élasticité augmente de 60% et la résistance à la rupture de 45,8%. Des couches d'oxyde épaisses formées durant ce traitement fragilisent les matériaux traités au laser. L'utilisation d'argon est efficace pour pallier ces inconvénients. Le traitement laser par double faces génère une microstructure plus homogène dans l'épaisseur, permettant ainsi un compromis optimal entre renforcement et perte de ductilité. Quant aux résultats des éprouvettes architecturées, les renforcements droits et ondulés peuvent augmenter le YS et l'UTS des éprouvettes par rapport au matériau de base. Alors que les éprouvettes renforcées par lignes droites présentent un champ de déformation homogène lors de l'essai de traction, les éprouvettes renforcées par ondulations présentent un champ de déformation hétérogène. Un rapport d'inclinaison d'ondulation plus grand H/P donne un champ de déformation plus hétérogène. Pour une géométrie de renforcement donnée, l'augmentation du volume renforcé peut augmenter l'UTS mais réduire la ductilité. Mais pour un même volume renforcé, des différentes géométries ne modifient pas le comportement global de traction. Les renforcements ondulés n'augmentent pas la ductilité par rapport aux renforts droits. Aucun effet d'architecture a été observé sur l'amélioration de la ductilité. Ce manque d'amélioration est dû à la déformation locale excessive dans la matrice et au dépliage retardé de l'ondulation. Une optimisation topologie des renforcements est attendue pour résoudre ces problèmes. En même temps, un traitement de durcissement plus efficace peut également augmenter l'écrouissage introduit par géométrie et bénéficier de l'amélioration de la ductilité.

### 3.1 Introduction

The development and applications on laser hardening on ferrous materials are introduced on the literature review. Numerous studies have reported on the mechanical properties of FSS welds and dissimilar welds between FSS and other stainless steels, where a hardening effect is reported. Nevertheless, few studies have been carried on the modification on global mechanical properties of fully thermally treated FSS by laser heat treatment and the influence of operation condition and parameters. In this present study, a methodology has been developed to use continuous-wave laser as a thermal source to modify mechanical properties of FSS thin sheets. A medium-chromium stainless steel AISI 430 is chosen to be studied, which presents a fully ferritic microstructure with chromium carbides inside the grains [94]. It is one of the most widely used FSS in engineering. Based on this strengthening effect, corrugation reinforced architected materials are fabricated.

For this propose, the energy distribution and the efficiency of laser beam and were characterized. Temperature evolution was simulated and measured by thermocouples. Fully treated samples were submitted for characterization. The effect of the utilization of shielding gas and laser linear energy density (LED) on microstructure and mechanical properties was investigated. The LED leading the most strengthening effect was adopted to fabricate architected materials with corrugated reinforcements with geometries introduced in Table 2-4 and their mechanical behaviors were followed by tensile tests equipped with DIC system. The obtained results are presented in this chapter. It should mention that part of the results, mostly concerning the laser treatment to enhance the mechanical properties of AISI 430 steel, has been published in *Materials Science and Engineering: A* [95].

### 3.2 Laser beam characterization

The real output power and demanded power of SPI fiber laser and Dilas diode laser are compared in Figure 3-1. For SPI laser, the real output power and demanded power are almost identical. There is no loss of the demanded power and the efficiency of the fiber is 100%. On the contrary, for Dilas laser, the loss of the demanded power due to the fiber transmission is not negligible. The efficiency is only 74%. To attain a real output power, the input demanded power should be calculated. Even though the maximal power of this laser is 160 W, the real maximal output power is limited to 115 W. At the same time, for security reasons this maximal value should not be used for a long time to avoid heat accumulation. In this present study, it is the real output power that is considered when laser powers are mentioned.

The energy density distributions of two lasers are shown in Figure 3-2. It can be concluded that SPI fiber laser beam has a perfect Gaussian distribution and its spot has a diameter of 32  $\mu\text{m}$  at its focal distance of 19.9 mm and that the Dilas diode laser has a nearly top-hat distribution and the spot diameter is 1.2 mm at the focal distance of 20.6 mm. In practice, the SPI laser is defocalized of 23.24 mm from the focal distance for a spot size of 1 mm. The defocalization distance is calculated by Equation 3-1,

$$w(z) = w_0 \sqrt{1 + \left(\frac{z}{z_0}\right)^2} \quad 3-1$$

where  $w(z)$  is spot radius,  $w_0$  is the spot radius at focal distance  $16 \mu\text{m}$ ,  $z_0 = \frac{\pi w_0^2}{\lambda}$  is the Rayleigh range,  $\lambda = 1080 \text{ nm}$  and  $z_0 = 0.7443 \text{ mm}$ . Dilas laser is fixed at its focal distance. Even though the measured spot size is larger than that of SPI, subsequent examinations show that this set-up can generate a rather uniform microstructure in case of double laser treatment.

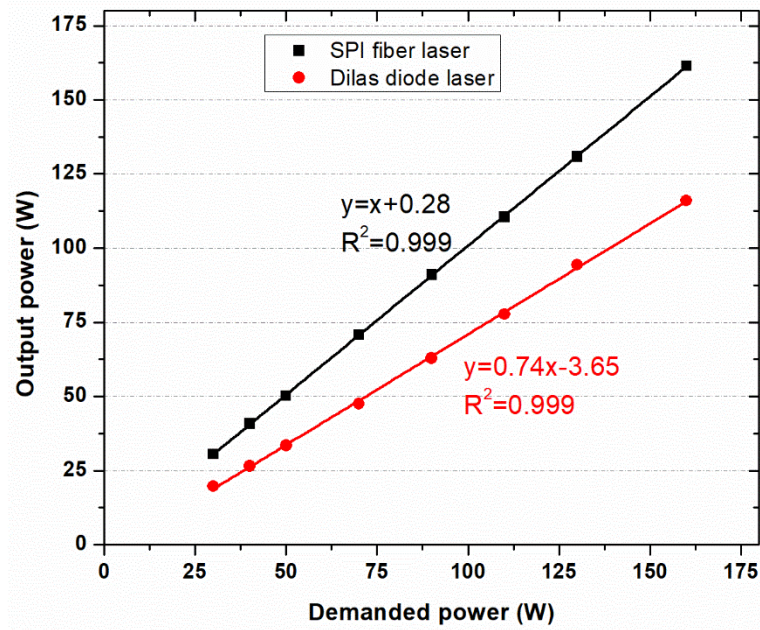


Figure 3-1 Measured output power versus demanded power of two lasers.

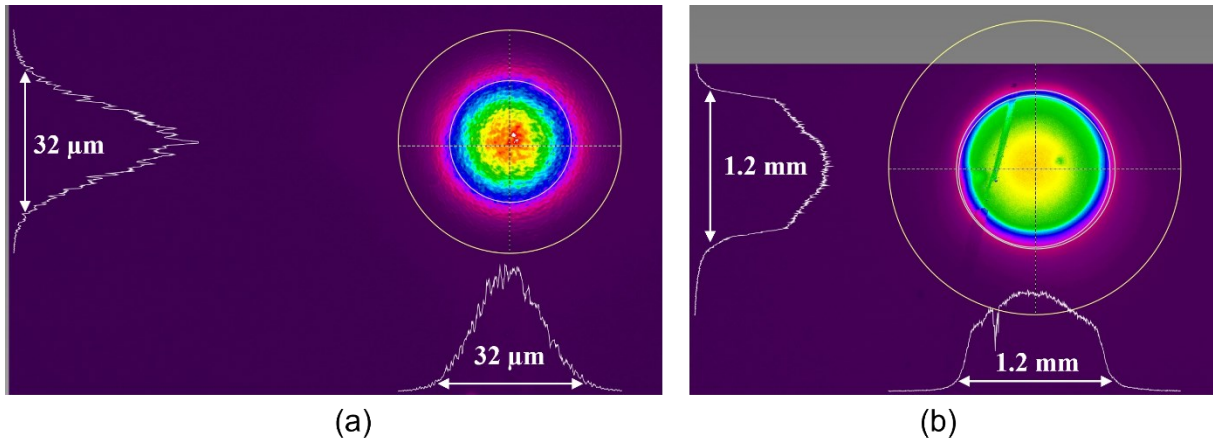


Figure 3-2 Energy density distribution of two lasers at their focal distances.

### 3.3 Temperature evolution

The temperature evolution of single laser treatment during laser treatment was measured by type K thermocouples welded on the back side of AISI 430 sheets. Figure 3-3 describes the experimental and numerical temperature evolution at the beam center on the backside during the treatment at different LED. The temperature during the laser treatment is modeled with

specific heat capacity ( $c_p$ ) and thermal conductivity ( $\lambda$ ) calculated from the following equations [96], where  $\theta_a$  is the actual temperature in °C, the melting temperature ( $T_m$ ) is set at 1698 K, and the latent heat of fusion is 285 kJ/kg. Both laser beams were modeled as a Gaussian beam.

$$c_p = 450 + 0.280 \times \theta_a - 2.91 \times 10^{-4} \theta_a^2 + 1.34 \times 10^{-7} \theta_a^3 \text{ [J. kg}^{-1} \cdot \text{K}^{-1}] \quad 3-2$$

$$\lambda = 14.6 + 1.27 \times 10^{-2} \theta_a \text{ [W. m}^{-1} \cdot \text{K}^{-1}] \quad 3-3$$

However, the coefficient of absorption depends on several factors such as the operating environment, the surface state, the wavelength of laser, the power, and so on. In this study, a value between 0.41 and 0.43 [54] is taken with Ar shielding gas after comparing the melting at the surface during treatment and  $T_m$ . While operating in air without shielding gas, the absorptivity is expected to increase by around 50% because of oxidation at the surface [97]. Because shielding gas escapes from the nozzles with nonnegligible velocity, a heat transfer coefficient of  $200 \text{ W.m}^{-2} \cdot \text{K}^{-1}$  [98] caused by forced convection is considered for the simulation.

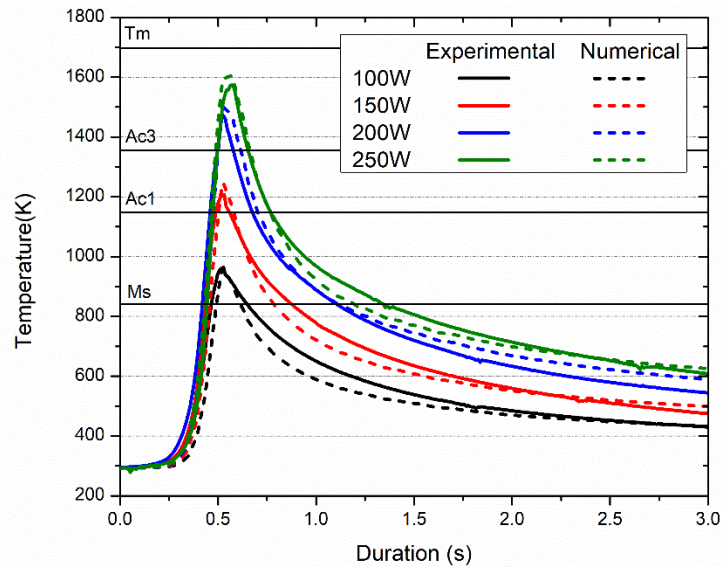


Figure 3-3 Experimental measurements and simulation results of backside temperature for single laser treatment.

The critical temperatures for the austenization phase transformation are calculated according to the model proposed by Stone et al. [99] using the element composition in Table 2-1 ( $Ac_1=1148 \text{ K}$  and  $Ac_3=1355 \text{ K}$ ) with Equation 3-4 and 3-5. The martensite start temperature is estimated using the model of Capdevila et al. [100] with Equation 3-6, which is adjusted by the addition of Cr compared to the classic formula ( $Ms=841 \text{ K}$ ).

$$Ac_1=712.54+211.1C+10.83Cr-15.77Ni+14.73Mo+19.07Si-55.06Mn-5.26Cu-281.0N \quad 3-4$$

$$Ac_3=569.9+45C+31.60Cr-64.11Ni+54.93Mo+22.15Si-49.00Mn-50.54Cu-699N \quad 3-5$$

$$Ms=764.2-302.6C-30.6Mn-16.6Ni-8.9Cr+2.4 Mo-11.3Cu+8.58Co+7.4W-14.5Si \quad 3-6$$

The same parameters are used to predict the temperature changes on the laser beam side. Figure 3-4 (a) shows the temperature evolution during the single laser treatment of the beam center on both the front and back surface for all the selected powers with Ar shielding gas. All front surface temperatures exceed  $A_{c1}$ . For all input powers, the temperature difference between the two surfaces is very pronounced, being more than 230 K. There is always a slight delay in the temperature change on the back surface during heating. Temperature changes during treatment with the double laser on both sides are shown in Figure 3-4 (b), with the fiber laser SPI on surface A and the diode laser DILAS on surface B. As the spot size of the DILAS laser is slightly larger than that of the SPI, the peak temperature is tens of K lower. For both conditions, the temperature evolution rates are very high, ranging from 1000 to 3000 K/s for heating and from 400 to 1000 K/s for cooling depending on the powers.

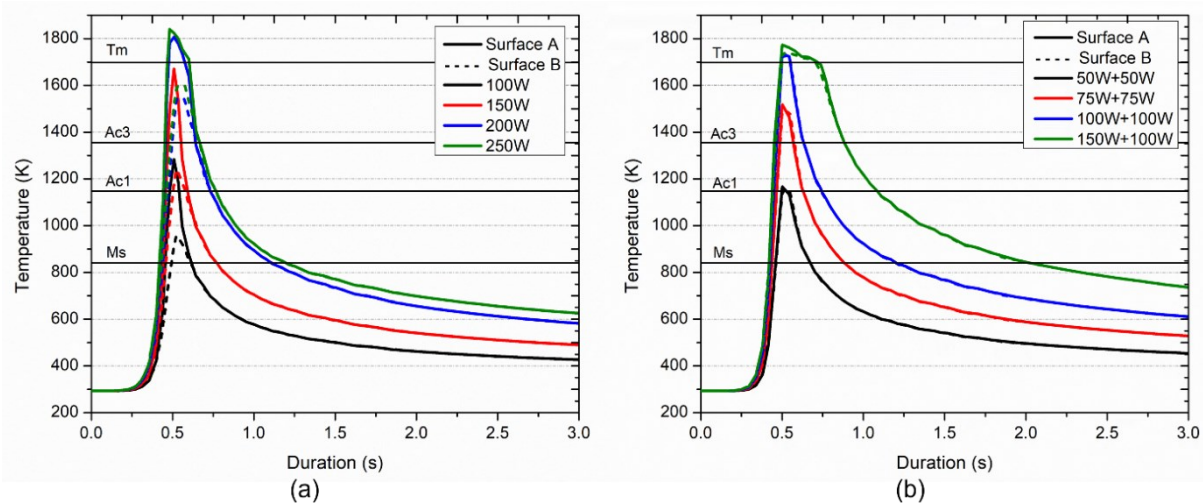


Figure 3-4 Temperature evolution during laser treatment of different powers under Ar shielding gas (a) with one single laser, and (b) with laser on both sides.

The temperatures and isothermals are illustrated in Figure 3-5 with a LED of 20 kJ/m with (a) one laser and (b) double lasers. The gap between the highest and lowest temperatures through the thickness of the laser track center is around 260 K with a single laser compared to only around 10 K with the double lasers. Thus, the laser thermal treatment is distributed more uniformly throughout the thickness when two lasers are used from both sides.

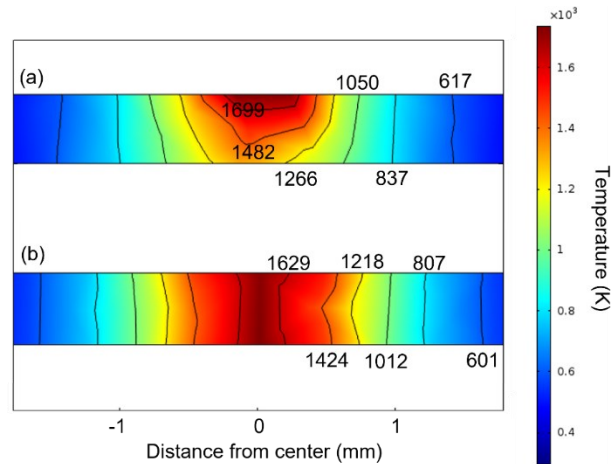


Figure 3-5 Isothermals on the section of laser track center while treatment in Ar (a) 200 W with single laser (b) 100 W + 100 W with two lasers.

### 3.4 Characterization of laser hardened AISI 430 sheet

#### 3.4.1 Microstructure

Figure 3-6 (a)-(h) is the macrograph of the single-track laser-treated area at different powers with Ar shielding gas. In (a) and (e), there is a slight growth of the grain size on the surface layer with 10 kJ/m. In (b) and (c), the grains in the middle of the treated zone are almost equiaxed and homogenous through the thickness by symmetry laser spots. In (f) and (g), grains near the front surface, where the laser is applied, are columnar in the normal direction of the arc-shaped treated zone. In (d) and (h), columnar grains are produced along the thickness in the center line and parallel to the adjacent surface. Columnar grains are formed along the solidification direction in a melt pool because the high power (25 kJ/m) results in a total fusion in the treated zone. The columnar grains in (h) are more elongated than (d) due to the higher cooling rate. Grain size decreases progressively with the distance from the center, except for (a), where the laser powers on both sides are relatively low. No evident porosity is observed even for 25 kJ/m, where total fusion is achieved through the section.

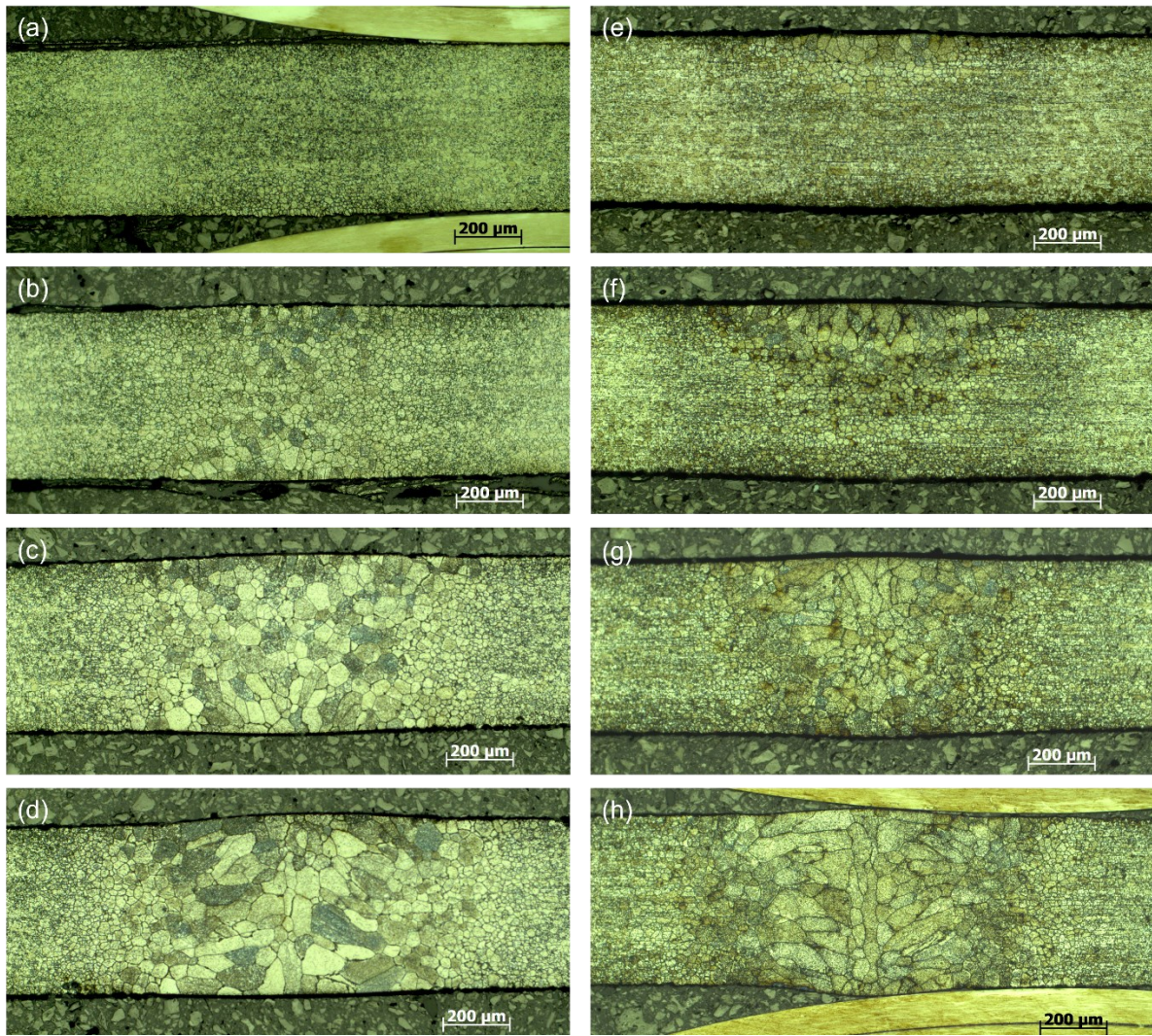


Figure 3-6 Macrostructure of single-track laser treated area in Ar (a) 50 W+50 W (b) 75 W+75 W (c) 100 W+100 W (d) 150 W+100 W (e) 100 W (f) 150 W (g) 200 W (h) 250 W.

With the same input LED, single and double laser treatments reveal rather different microstructures due to the thermal gradient and cooling rate. As described in section 3.1 above, with a symmetric double laser treatment (Figure 3-6 (a)-(d)), both surfaces are irradiated so that the temperature is more homogeneous through the thickness. However, with the single laser treatment (Figure 3-6 (e)-(h)), the temperature gradient between the irradiated and reverse sides is much higher, being a few hundreds of Ks. Thus, at the same LED, the double laser treatment yields a more uniform microstructure. As shown in Figure 3-4, the cooling rate of the single laser (a) is nearly twice as high as that of the double laser (b), which favors the growth of the columnar grains upon cooling. With the same LED, more columnar grains appear in the treated zone.

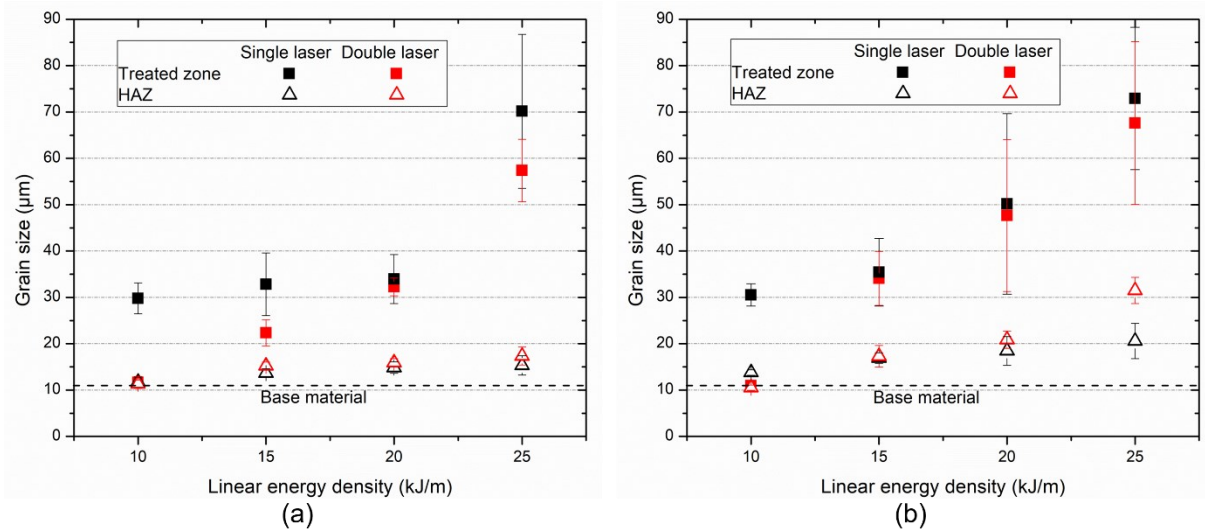


Figure 3-7 Average grain size of treated zone and HAZ of specimens treated at different LED in (a) Ar (b) air.

Average grain sizes in the treated zone and HAZ in Figure 3-6 (a)-(h) are depicted in Figure 3-7 (a), and those treated in air in Figure 3-7 (b). Average grain sizes in the treated zone and HAZ increase with the higher LED. For the double laser process, the grain coarsening is less dramatic in the treated zone, although the average grain size in HAZ is slightly larger. With the same LED, the average grain size is larger in air than in Ar due to the higher laser absorption.

The typical section microstructure can be described in three parts as shown in Figure 3-8: the treated zone with dramatic grain coarsening that corresponds to the fusion zone in this case; the heat affected zone (HAZ) with a gradient that follows the enlargement of the grain size; and the base material (BM). There is no sharp boundary between each zone, and the transition is successional.

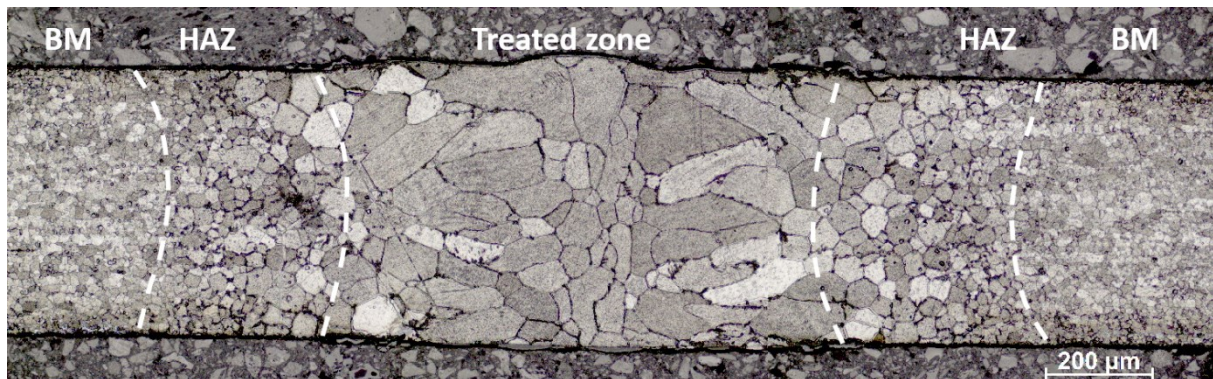


Figure 3-8 Macrograph of the section of a single-track laser treated sample at 100 W from both sides in air.

Studies on the optical microscope and SEM (Figure 3-9) reveal that martensite formation occurs in the treated zone and HAZ in most circumstances (except for at the lowest power), principally with intergranular formations but sometimes with intragranular formations. With the higher input power, more martensite is formed. In the treated zone in Figure 3-9 (a),

martensite is more needle-like, germinating along the new grain boundaries and growing toward the inside. A large quantity of carbides is found inside the grains, and the sub-grain boundaries are revealed. There is a carbide-free zone near the grain boundaries due to the local low carbon concentration. Carbon atoms in this zone are diffused in the austenite region at elevated temperatures, which transforms into martensite during rapid cooling [101].

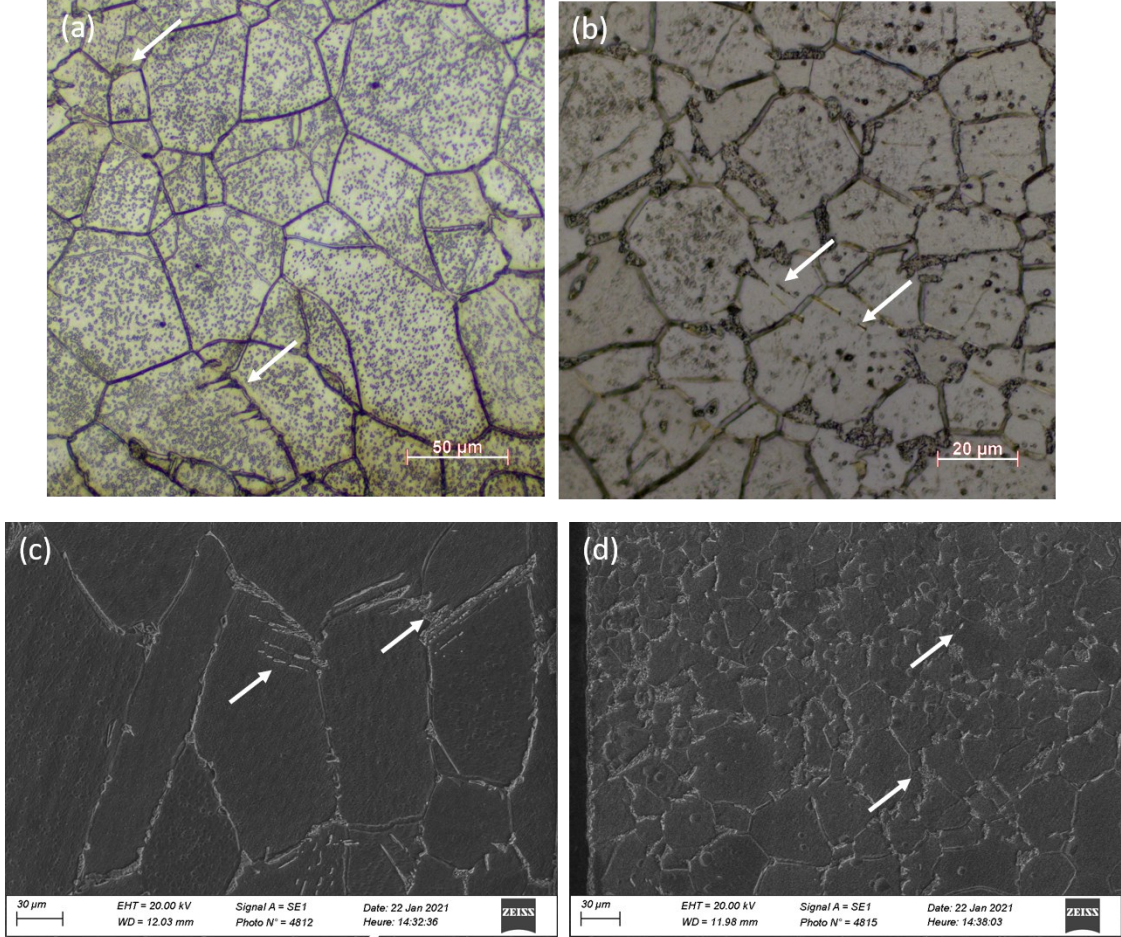


Figure 3-9 Microstructure by OM of a sample treated at 100 W from both sides in Ar (a) treated zone (b) HAZ, by SEM of a sample treated at 150 W+100 W from both sides in air (c) treated zone (d) HAZ, white arrows indicate martensite.

In HAZ in Figure 3-9 (b) and (d), a few martensite needles can be found in the HTHAZ, and some martensite islands are distributed at triple junctions in the LTHAZ. This difference of phase presence can be explained by the temperature change. As the temperature at the treated zone and HTHAZ is much higher than  $A_{c3}$ , and the cooling is extremely rapid, austenite formation is insufficient to avoid grain coarsening [101]. In the LTHAZ, the peak temperature is above  $A_{c1}$ , and the cooling rate is lower, meaning that a small amount of austenite has enough time to form along the ferrite grain boundaries, which are pinned by this nucleation. The entire HAZ shows a clear recrystallisation [102].

Microstructures of the samples treated in air and Ar shielding gas present similar properties. Nevertheless, due to the much higher absorption rate with oxidation, the HAZ in air is more

expanded, which results in an overlapping HAZ between two laser tracks during the multi-track treatment.

### 3.4.2 Microhardness

The microhardness test shows that the base material presents a Vickers hardness of around 160 Hv. Figure 3-10 reveals the hardness along the middle line of the section with a single-track (a) and multi-track (b) laser treatment at 100 W from the two sides in both air and Ar. Track centers are marked by dashed lines. With a single-track laser, a maximum hardness of around 310 Hv is produced in the treated zone, which is 90% higher than the base material. The hardened zone in Ar is narrower than in air, and the maximum value obtained is also lower. The hardened zone in Ar presents a wave-like profile with the peak values almost unchanged in the middle of each track, although the hardened zone in air presents a hardness that repeatedly dropped to around 220 Hv, even for the laser track center.

For other conditions, except at 50 W from each side where the highest temperature in the adjacent layer of the sheets is below Ac1, microhardness also increases at the different levels. This softening with the multi-track laser treatment exists for samples with a high input power in both air and Ar, although in Ar the required power is higher (25 kJ/m).

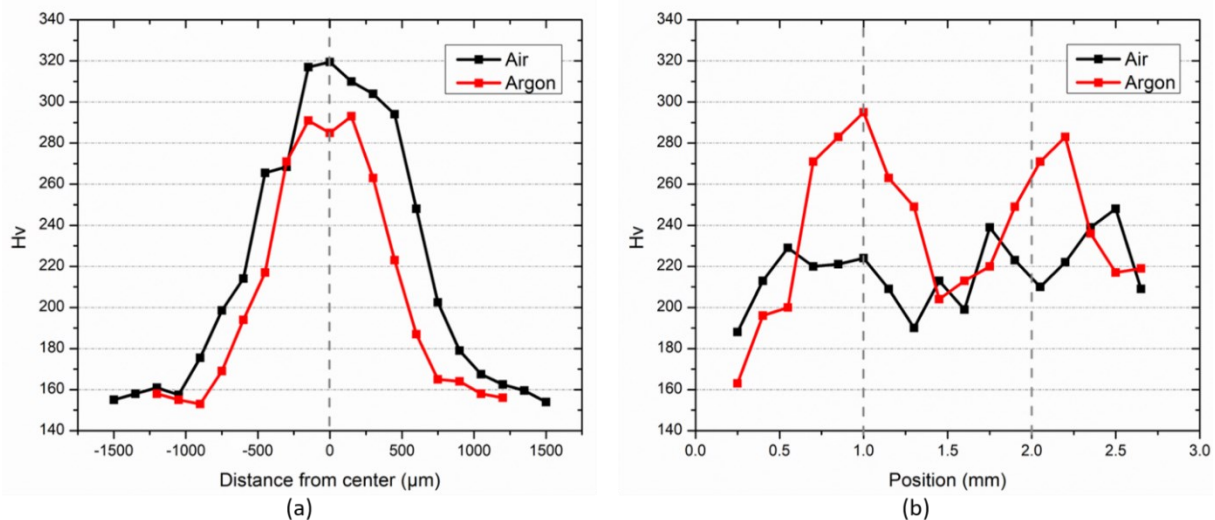


Figure 3-10 Micro-hardness at the specimen core after a laser treatment at 100 W from both sides (a) single-track (b) multi-track laser treatment.

### 3.4.3 Surface state

As the surface temperature during the treatment is relatively high (above Ac1 for the lowest power and above the melting point for the highest power), oxidation is not negligible. Fully treated samples are characterized by GD-OES to determine the thickness of the oxide layer on both surfaces after the laser treatment. The preliminary experiment indicates that the sputtering rate of GD-OES on this material with the selected argon pressure and RF power parameters is 0.068 μm/s, which is consistent with the sputtering rate reported in [103]. Figure 3-11 (a) allows us to observe the GD-OES depth profiles of major elements from the front surface to the

adjacent layer of a sample at 200 W in air. The signal of oxygen is found to be stable around 19.4  $\mu\text{m}$  after being amplified. Besides the signal of O, the signals of Cr and Mn are also stronger at the surface (around 3.4  $\mu\text{m}$ ) compared to the adjacent layer. However, the signal of Fe is weaker at the surface and increases with the erosion depth. As the main oxides formed are  $\text{Cr}_2\text{O}_3$  and  $\text{Fe}_2\text{O}_3$  [104], this evolution means that the formation of  $\text{Cr}_2\text{O}_3$  is greater than that of  $\text{Fe}_2\text{O}_3$  on the surface during high-temperature oxidation. This may be explained by the fact that the Gibbs free energy ( $\Delta G^\circ$ ) to oxidate Cr is much more negative than for Fe, which makes it thermodynamically favorable to generate  $\text{Cr}_2\text{O}_3$  [104]. This affinity for Cr oxidation may decrease the Cr concentration of the substrate metal. The same trend has been observed on all samples treated in air. The GD-OES depth profiles at the same power with Ar in Figure 12(b) do not show the same evolution. The signals of all elements become stable in less than 2  $\mu\text{m}$ , and there is no decrease for either Cr or Mn.

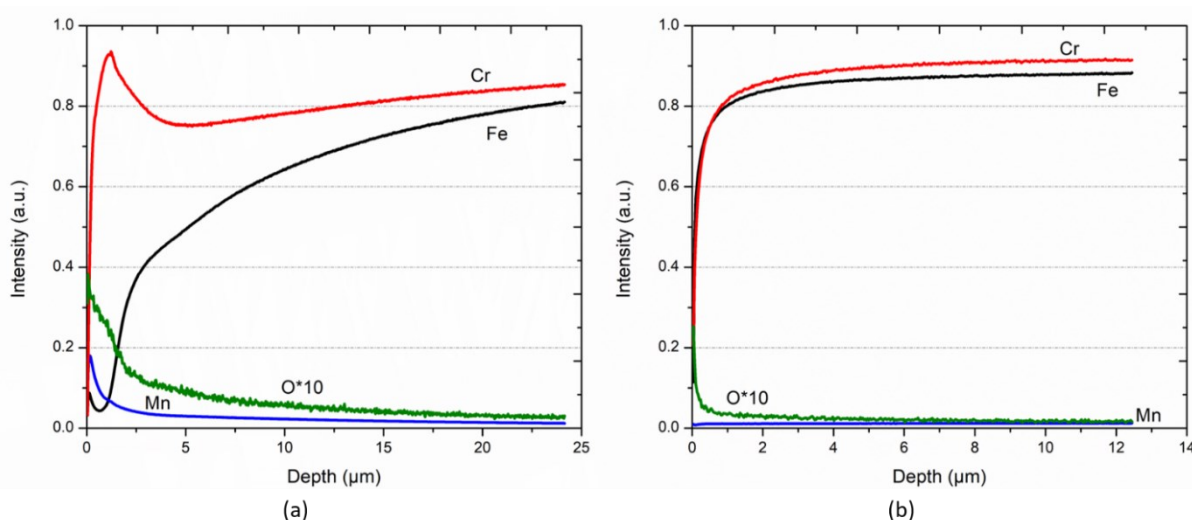


Figure 3-11 GDOES signal of the front surface of a sample at 200 W (a) without, and (b) with Ar shielding gas.

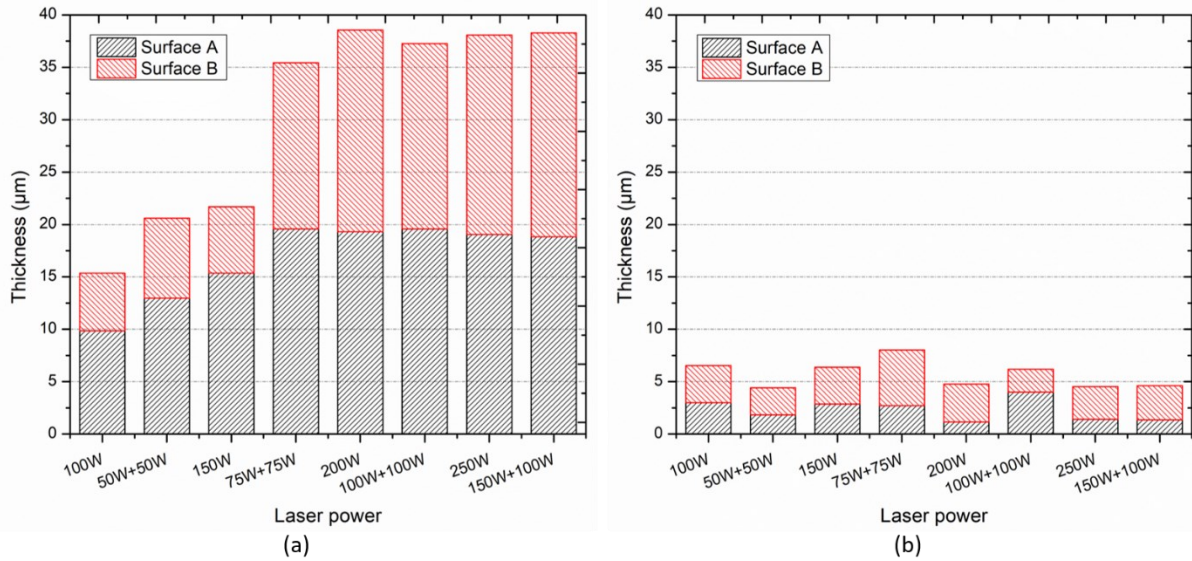


Figure 3-12 Thickness of oxide layers on both surfaces after laser treatment (a) without shielding gas (b) with Ar shielding gas.

The thickness of the oxide layers on both surfaces of the samples in each condition is reported in Figure 3-12. In Figure 3-12 (a), the thickness increases with the laser power before the temperatures of both sides reach the melting point (200 W and 250 W). The difference in thickness between the two surfaces is greater with the single laser at relatively low powers (9.0 µm more on the front surface for 150 W and 3.7 µm for 75 W from both sides), where temperatures differ more. The total thickness of both sides with double lasers is greater than that with a single laser at lower powers (35.4 µm for 75 W from both sides and 21.7 µm for 150 W), which can be explained by the lower temperatures on surface B. For the specimens heated above  $T_m$ , the thickness of the oxide layer almost stops increasing when the total thickness is around 38 µm. As the steel sheets are thin (0.5 mm), the oxidation is considerable (7.6%). In Figure 3-12 (b), the oxide layer formed in Ar shielding gas is not greatly affected by the operation parameters, and the average thickness is only around 5.0 µm (1%), with a maximum value of 8.0 µm. This flaky and brittle oxide layer has an effect on mechanical behavior, which is discussed in the following section.

### 3.4.4 Tensile test

Figure 3-13 shows the uniaxial tensile test results of the treated samples in air (a) and with Ar shielding gas (b). The base material presents ductile behavior with yield stress (YS) of around 350 MPa, ultimate tensile strength (UTS) of around 500 MPa, and uniform plastic deformation  $\epsilon_u$  of 19.5%. With the temperature increase during laser treatment, the samples become more strengthened but less ductile.

As oxide increases the laser absorption rate [97], the peak temperatures are much higher with the same power in air than in Ar when the temperature is below  $T_m$ . At lower powers (100 W and 150 W), the strengthening effect in mechanical properties is more obvious. However, at higher powers in air as shown in Figure 3-13 (a),  $\sigma$ - $\epsilon$  curves begin to overlap at 150 W and

become less ductile. In Figure 3-13 (b), the changes in properties at different powers are more dispersed. The strength continues to increase with higher powers until 250 W.

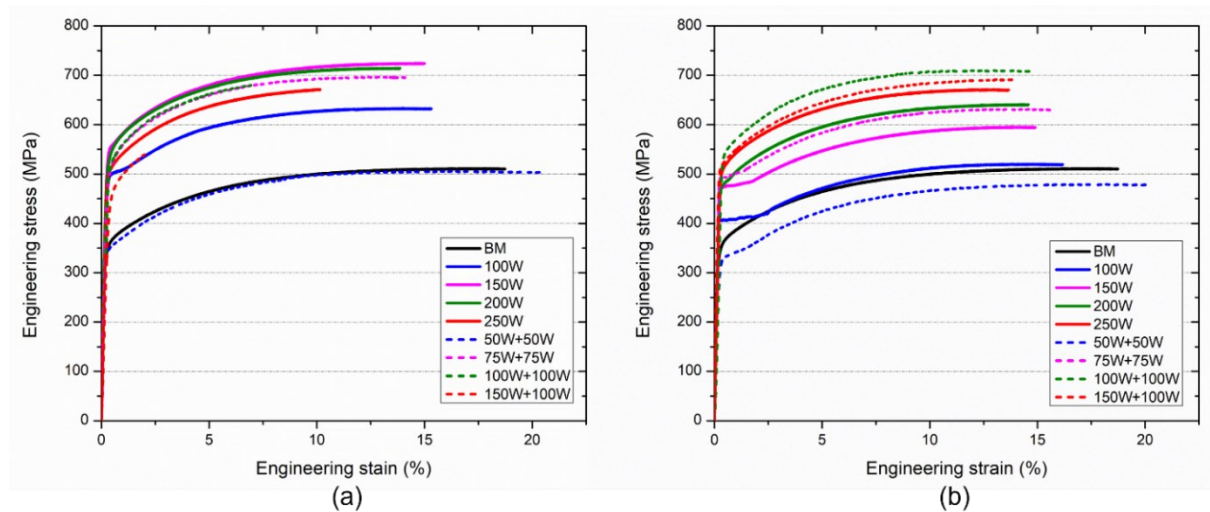


Figure 3-13 Tensile test results of laser treated samples (a) without shielding gas (b) with Ar shielding gas.

Figure 3-14 shows (a) YS, (b) UTS, (c)  $\epsilon_u$ , and (d) absorbed energy density for samples treated in each condition, where each point is the average value of four samples. In Figure 3-14 (a), all treated samples have a more elevated yield stress than the base material except for 50 W with two lasers. Obviously, YS increases with a single laser at all chosen powers in air, with a maximum of 560 MPa (60% more than the base material) at 150 W and a minimum of 506 MPa at 100 W. However, for both treatments in air,  $\sigma_{0.2\%}$  decreases after 150 W or 75 W on both sides. With shielding gas,  $\sigma_{0.2\%}$  does not greatly change at lower powers (100 W or 50 W+50 W) and begins to increase when raising the powers. With the single laser,  $\sigma_{0.2\%}$  continues to increase, but with double lasers, it decreases at 150 W+100 W.

Similar trends can be found for the UTS in Figure 3-14 (b). All treated samples have a higher UTS than the base material except for the lowest power in Ar. Without shielding gas, UTS increases when raising the laser power for both single and double laser beams. For a single laser beam, UTS reaches 729 MPa at 150 W and 200 W (45.8% more than the base material) and subsequently decreases. For double laser beams, the maximal value is 686 MPa at 75 W from both sides. With shielding gas, the gain in UTS with the double-face treated samples is more pronounced than with the single-face samples. UTS continuously improves with the single beam power and reaches 666 MPa at 250 W, although with 100 W from both sides, UTS is 702 MPa.

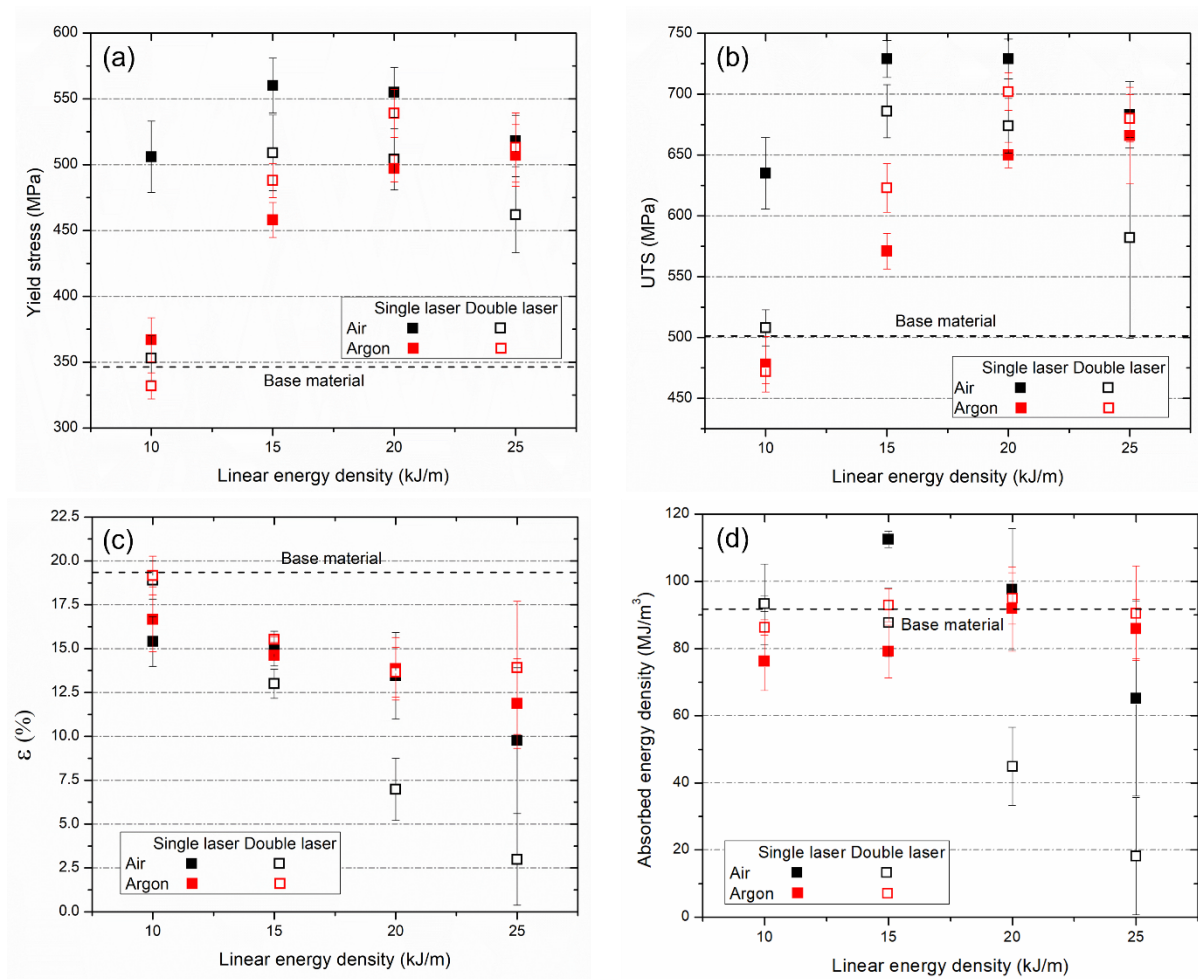


Figure 3-14 Average (a) yield stress (b) ultimate tensile strength (c) uniform plastic deformation (d) absorbed energy density of treated samples in each condition.

In Figure 3-14 (c),  $\epsilon_u$  is worsened by laser treatment and decreases with the power growth in each condition by different levels. Laser treatment in air fragilizes the sample much more than in Ar shielding gas.  $\epsilon_u$  is only 2.99% at 150 W+100 W compared to 12-14% at the highest power in Ar.

Fracture energy density is shown in Figure 3-14 (d). Compared to the base material (91.3 MJ/m<sup>3</sup>), laser treatment in Ar has a smaller effect on the fracture energy density (lowest 76.18 MJ/m<sup>3</sup> and highest 94.99 MJ/m<sup>3</sup>), especially with two lasers. Treatment in air has a much more variable effect with 112.50 MJ/m<sup>3</sup> at 150 W and only 18.14 MJ/m<sup>3</sup> at 150 W+100 W. Double lasers rapidly deteriorate the energy density at higher powers.

### 3.4.5 Discussion of laser hardening effect on microstructural and mechanical properties

Even though FSS are often considered to be non-hardenable [42], high power laser treatment can effectively increase the local microhardness of AISI 430. Despite dramatic grain coarsening in the treated zone, the maximum microhardness is caused by the substantial chromium carbide precipitates [105] and the martensite needles at the grain boundaries. Hardness decreases when moving away from the laser beam center due to less martensite formation and carbide

precipitation. In Figure 3-10 (b), the different profiles of microhardness in the samples treated in air and Ar can be explained by the effect of the adjacent tracks. Figure 3-15 shows the macrostructures of the sections of specimens at 100W on both sides, with the positions of the beam centers marked by white dashed lines. The energy absorption in Ar is less, and as a result, the HAZ is much less expanded. A smaller zone along the former tracks is reheated by the adjacent ones above critical temperatures. On the one hand, the martensite formed during rapid cooling is softened by this reheating phase, which serves as tempering or annealing depending on the different distances [36,106]. On the other hand, the carbide precipitates are also partly dissolved into the matrix by the adjacent track [105].

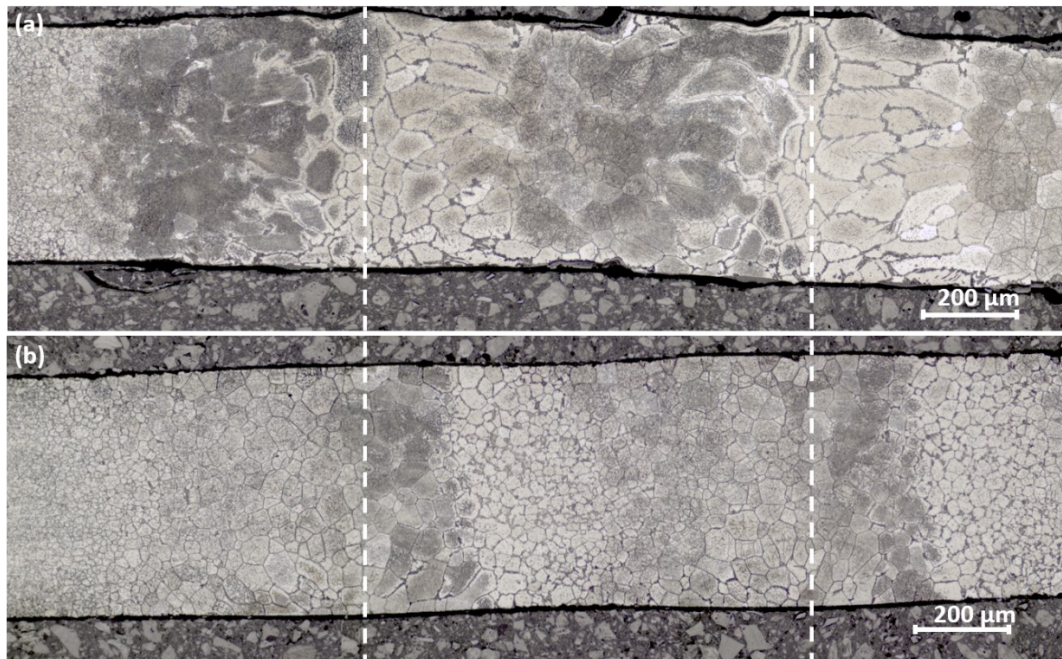


Figure 3-15 Macrostructure of multi-track section of specimens treated at 100 W at both sides (a) in air (b) in Ar.

The mechanical properties are summarized in Table 3-1 for the base material and specimens treated by double laser in Ar. With a higher LED, the average microhardness, YS, UTS, and absorbed energy density increase to peak values at 20 kJ/m and then decrease at 25 kJ/m. Results for other treatment conditions present similar trends with different optimal LED.  $\epsilon_u$  continues to worsen with higher LED. When the surface temperature reaches  $A_{c1}$ , the superficial grains begin to coarsen but the underlying material is not heated enough to result in microstructure changes, meaning that the tensile behaviors are similar to the base material. With a higher input power, a larger underlying zone has reached  $A_{c1}$ , even  $A_{c3}$ . Coarsening equiaxed grains appear in the treated zone. YS and UTS are well enhanced (maximum 60% and 45.8% increase, respectively) by martensite and carbides rich in Cr that are formed upon cooling, although  $\epsilon_u$  is slightly reduced. When the temperature reaches  $T_m$ , dramatic anisotropic columnar grains are formed along the solidification direction. Such structures are susceptible to tearing and favor crack initiation and propagation along the grain boundaries and reduce the tensile properties [107,108]. At 25 kJ/m, a complete fusion is achieved through the depth, which

widens the standard deviation. Solidification ripples on the surface also add instability to the mechanical properties. HAZ is broader at higher powers, martensite is tempered, and carbides are partly dissolved by adjacent laser tracks, which reduces YS and UTS.

Table 3-1 Mechanical properties of base material and samples treated by double laser at different LED.

	Base material	10 kJ/m	15 kJ/m	20 kJ/m	25kJ/m
Micro hardness (Hv)	160.0	158.0	211.5	241.8	233.6
YS (MPa)	346.0	332.0	488.7	539.7	513.0
UTS (MPa)	502.9	472.0	623.5	702.5	680.6
$\epsilon_u$ (%)	19.39	19.17	15.52	13.65	13.91
Dissipated energy density (MJ/m <sup>3</sup> )	91.30	86.31	92.92	94.99	90.53

During the tensile test of samples treated in air, the flaky oxide layers on the weld-side surfaces crack and peel off before the final rupture, because they are less ductile than the substrate metal. This oxide layer may cause microcracks in the substrate-treated metal by several mechanisms. Due to the differential thermal expansion, internal stresses along the interfaces increase, and cracks can initiate in the brittle oxide layer and then penetrate into the substrate perpendicularly for several microns during cooling [109]. When the brittle film and the ductile substrate share a solid interface, cracks appear in the film when it is loaded mechanically, thus creating a premature failure in the substrate [110]. Nevertheless, the fracture and peeling of the oxide in the early stages reduce the specimen section, which causes local stress concentration. The strain is not uniformly distributed over the gage section, and the specimens crack earlier. Thus, without shielding gas, the brittle oxidation layer worsens the ductility at a faster rate with the same input power by introducing microcracks beneath the metal surface. These microcracks reduce the mechanical properties during the tensile test. The surface roughness is also worsened with the simultaneous increase in oxide thickness, especially at high powers above  $T_m$ , as shown in Figure 3-15 (a).

As mentioned above, the oxide layer increases the laser absorption coefficient by at least 50% and makes it cumbersome to properly manage the peak temperature during treatment. This also enlarges HAZ on account of the higher absorption rate, so that the reheat effect is even more obvious. In this case, the oxide layer impedes the mechanical behavior of the samples and adds uncertainties to the procedure, thus making it important to control it.

The changes in the mechanical properties result from the combination of microstructure and surface state after the laser treatment. A proper equiaxed microstructure and a surface without thick oxidation led to a more enhanced resistance with lower ductility.

### 3.5 Corrugation reinforced architected materials by localized laser hardening

After microstructural and mechanical property characterization of specimens fully treated at different LED, the treatment at 100 W from both sides under Ar shielding gas is chosen to fabricate localized laser hardened architected materials with corrugated reinforcements. This parameter is adopted because it yields a uniform microstructure of equiaxed grains through the whole thickness with limited grain coarsening and a small HAZ. It results in the highest YS and UTS among fully treated specimens with a less-reduced ductility. Also, the smooth surface under shielding gas protection excludes early fracture caused by micro cracks on the laser treated surface. The parametric study of Fraser [6] indicates that for a given matrix, a threshold YS value of reinforcements should be attained to obtain a benefit in necking strain with corrugation compared to straight ones. Therefore, untreated AISI 430 and laser hardened parts at 100 W from both sides are taken as matrix and reinforcement in this part of study. Architected materials with geometric parameters in Table 2-4 are fabricated. The corrugation period is fixed at 6 mm and the height varies from 0 (straight reinforcement) to 3 mm. Each reinforcement represents 10% of the volume in the gauge area.

#### 3.5.1 Identification of matrix and reinforcement mechanical properties

Table 3-2 Mechanical properties of matrix and reinforcement in FEM simulation.

	Matrix (untreated)	Reinforcement (treated)
Young’s modulus (GPa)		210
Poisson ratio		0.3
Yield stress (MPa)	280	460
Hardening coefficient K (MPa)	711	880
Hardening exponent n	0.453	0.434

Based on results of Section 3.4.4, mechanical properties of matrix and reinforcement are shown in Table 3-2. Beyond yield strength, a power-law hardening behavior is taken for both materials. Relative parameters are input for FEM simulation. Numerical engineering stress-strain responses are compared to experimental ones in Figure 3-16. It can be concluded that numerical results correspond well are experimental ones. In the following part, the numerical tensile behavior is predicted by these two performances.

Beyond the yield strength, all materials are assumed to follow Ludwik's strain hardening model in Equation 3-7, where  $\sigma_0$  is the onset of plasticity, K and n are respectively hardening coefficient and hardening exponent.

$$\sigma = \sigma_0 + K\varepsilon^n \tag{3-7}$$

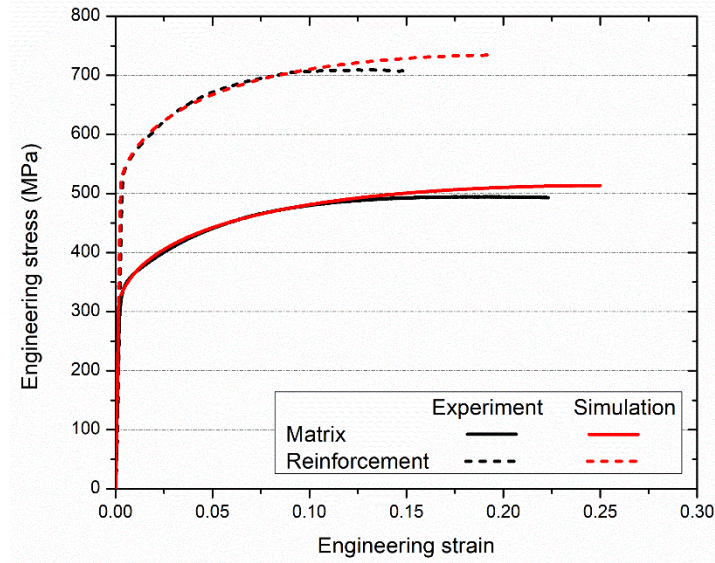


Figure 3-16 Engineering stress-strain behavior of matrix and reinforcement.

### 3.5.2 Prediction of isolated straight and corrugated reinforcement

Isolated reinforcements are hard to be machined due to their small but complex geometries by available equipment, thus their mechanical properties are difficult to measure by tensile test in this study. Instead, they are predicted by FEM simulation. Engineering stress-strain curves of straight and corrugated reinforcements are depicted in Figure 3-17. The straight reinforcement has a classical stress-strain behavior with elastic strain at the beginning and plastic work hardening and the work hardening rate decrease continuously with the increase of total strain.

Corrugated reinforcements experience an unbending process at the first step of tensile test, which is characterized by a slow increasing in stress at the beginning in Figure 3-17 (a) before the rapid increasing. Figure 3-18 describes the progression of (a) stress and (b) strain map in the tensile direction at different total strain from 0 to 1 of a 2-mm-high corrugation. When the total strain is below 0.7, the corrugation unbends with the increasing of average strain, and the average stress increases slowly. The local strain in the tensile direction  $\varepsilon_{11}$  increases also slowly in this period, the maximal value is found in the inner side of corrugation peaks. Once it is straightened, the specimen is stretched as a straight band and the average stress increases rapidly. At this stage, the inner side of corrugation peaks has the largest tensile strain and the outer side has the largest compressive strain.

This unbending process results in a boost in work hardening rate before it decreases again and intersects with true stress (as shown in Figure 3-17 (b)), where the onset of necking strain is defined by Considère Criterion in Equation 3-8. It signifies that when the work hardening rate  $w$  decreases below the value of true stress  $\sigma$ , this intersection is considered as the criterion of plastic instability and the beginning of localized plastic flow [111].

$$w = \frac{d\sigma}{d\varepsilon} = \sigma \quad 3-8$$

The uniaxial strain of a corrugation with a height of  $h$  and a period of  $p$  after complete unbending process can be approximated by Equation 3-9 [35]. With a given period, a larger height of the corrugation leads to a larger uniaxial strain before unbending, which can be explained by the fact that a larger corrugation height needs to unbend more before straighten out [6]. This larger unbending region results in a more important boost in work hardening rate, which occurs at a larger total strain. This increase in boost size and onset strain enhances the necking strain of corrugated reinforcement compared to the straight one. The larger corrugation height is, the more enhancement in necking strain happens. But it is to note that the change of corrugation heights has little effect on the UTS.

$$\epsilon_c = 2 \sqrt{\left(\frac{2h}{p}\right)^2 + \frac{1}{4}} - 1 \tag{3-9}$$

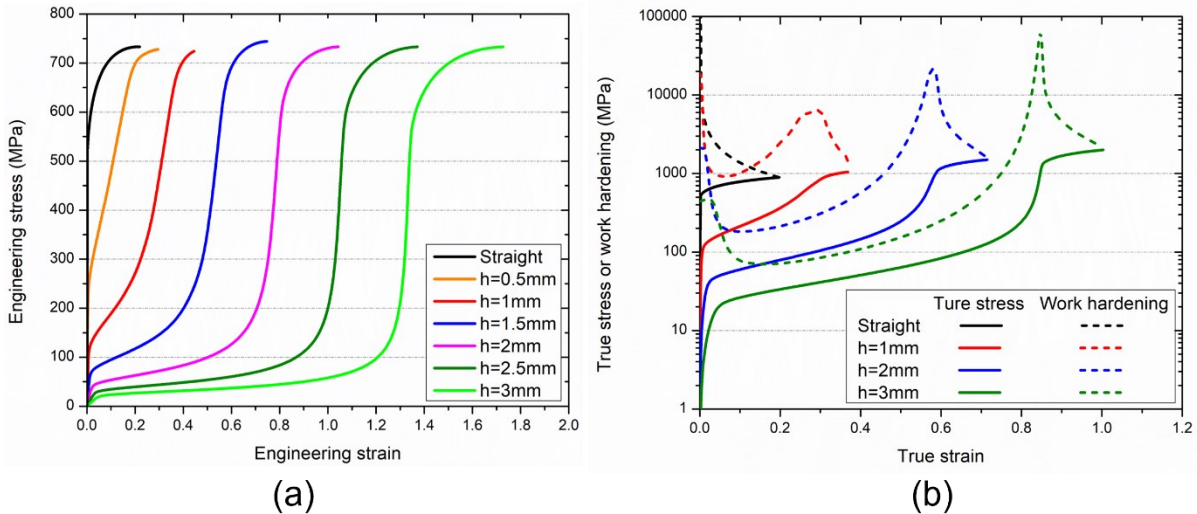


Figure 3-17 (a) Engineering stress-strain behavior of isolated straight and corrugated reinforcement, (b) work hardening rate and true stress-strain of isolated reinforcement.

The study of Fraser [6] confirms that isolated corrugations with various heights of several other materials have the same trend. It can be easily supposed that the work hardening rate of a specimen with a straight reinforcement should decrease continuously during tensile test and the fragile reinforcement should fracture at the first place. But the work hardening of a combination of a matrix with a corrugation is unknown. The aim of this study is to investigate the possibility to utilize this boost to increase the necking strain of architected materials where the corrugations are embedded in matrix.

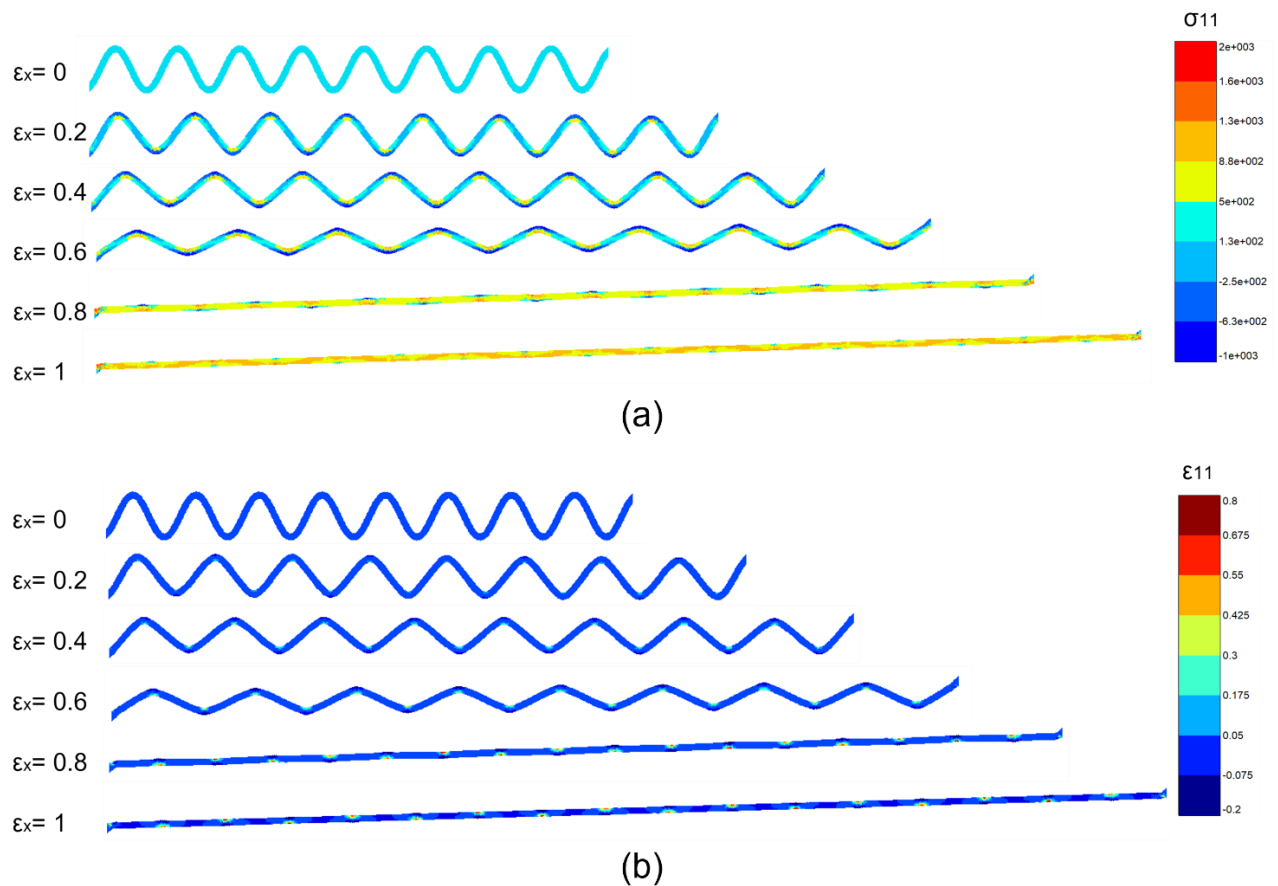


Figure 3-18 (a) Stress and (b) strain map of a 2-mm-high isolated corrugation in the tensile direction at different total strain by FEM simulation.

### 3.5.3 Tensile test results of architected materials and discussion

Figure 3-19 present experimental and numerical stress-strain behavior of specimens with one to four reinforcements introduced by localized laser hardening, (a) with straight reinforcements and (b) with corrugated reinforcements of  $h=1$  mm. Both straight and corrugated reinforcements are efficient to increase the UTS compared to base material and the enhancement is more important with the increasing reinforced volume. But the loss in necking strain is larger with the increasing number of reinforcements. Unfortunately, there is no evident differences between straight and corrugation reinforced specimens with the same number of reinforcements, neither in experiments nor in FEM simulations. Unlike what is pointed out in the study of Fraser [6], corrugated reinforcements do not enhance the necking strain compared to straight ones. Specimens reinforced with one to four corrugations of  $h=2$  mm present similar trend, UTS is improved but the necking strain decreases with the increasing reinforced volume. But comparing straight reinforcements and corrugations, the necking strain is not improved, it is even worsened by corrugated reinforcements with  $h=2$  mm.

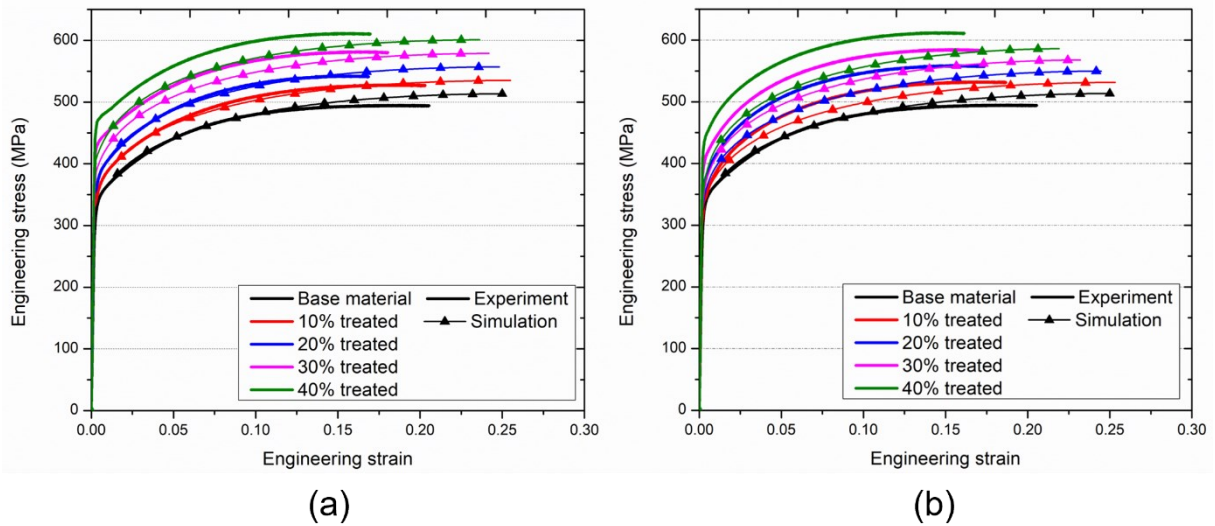


Figure 3-19 Experimental and numerical stress-strain behavior of architected materials with different localized laser hardened volume from 10% to 40% (a) straight reinforcement (b) corrugated reinforcement of  $h=1$  mm.

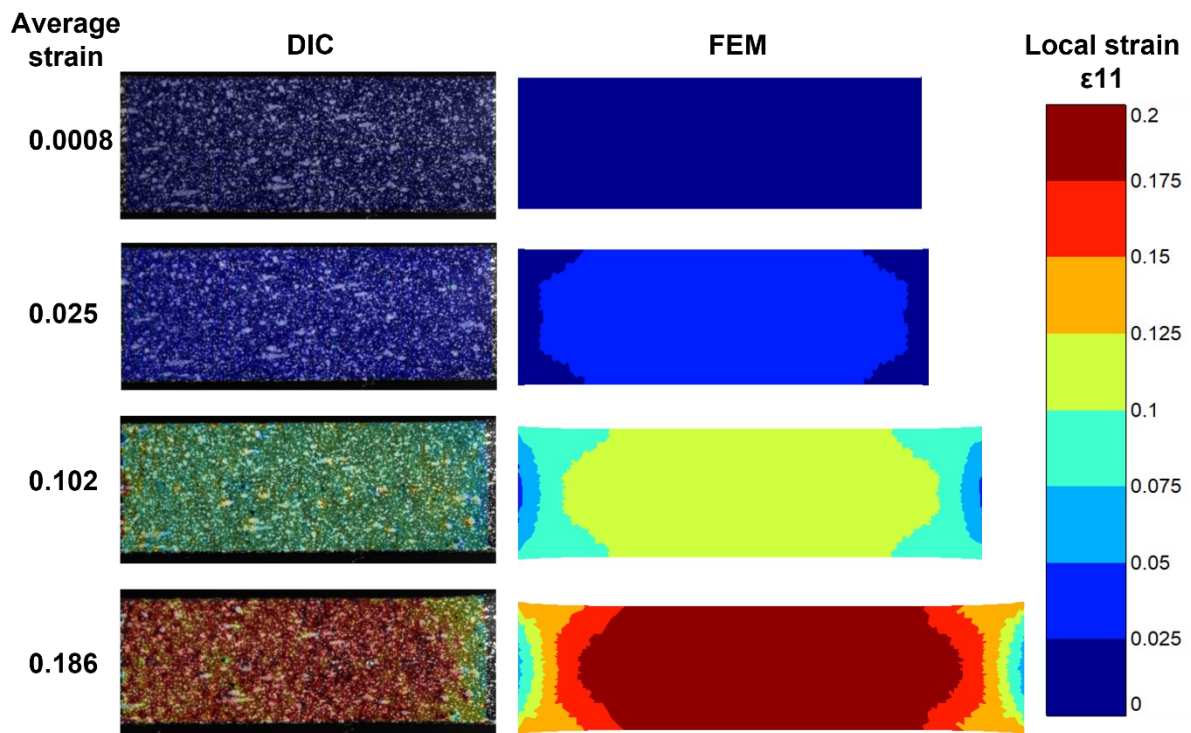


Figure 3-20 DIC results and FEM simulation of local strain evolution during tensile test of specimen with one straight reinforcement.

DIC analysis was also carried out during tensile tests, some representative results are presented and compared with FEM simulation results. Figure 3-20 presents the local strain evolution of a specimen with one single straight reinforcement. The local strain field map is always homogeneous on the whole gauge length before necking and it corresponds to the average global strain. Figure 3-21 presents the local strain evolution of a specimen reinforced

by one single corrugation with a height of 1 mm. The strain field is homogeneous at the beginning before plasticity onset and then becomes heterogeneous. The largest local strain is found in the matrix under the corrugation arc and the smallest is situated in the middle of each inclined fragment connecting the corrugation. When the average strain is 0.186 just before final fracture, the largest strain is near 0.3, while the smallest is less than 0.09.

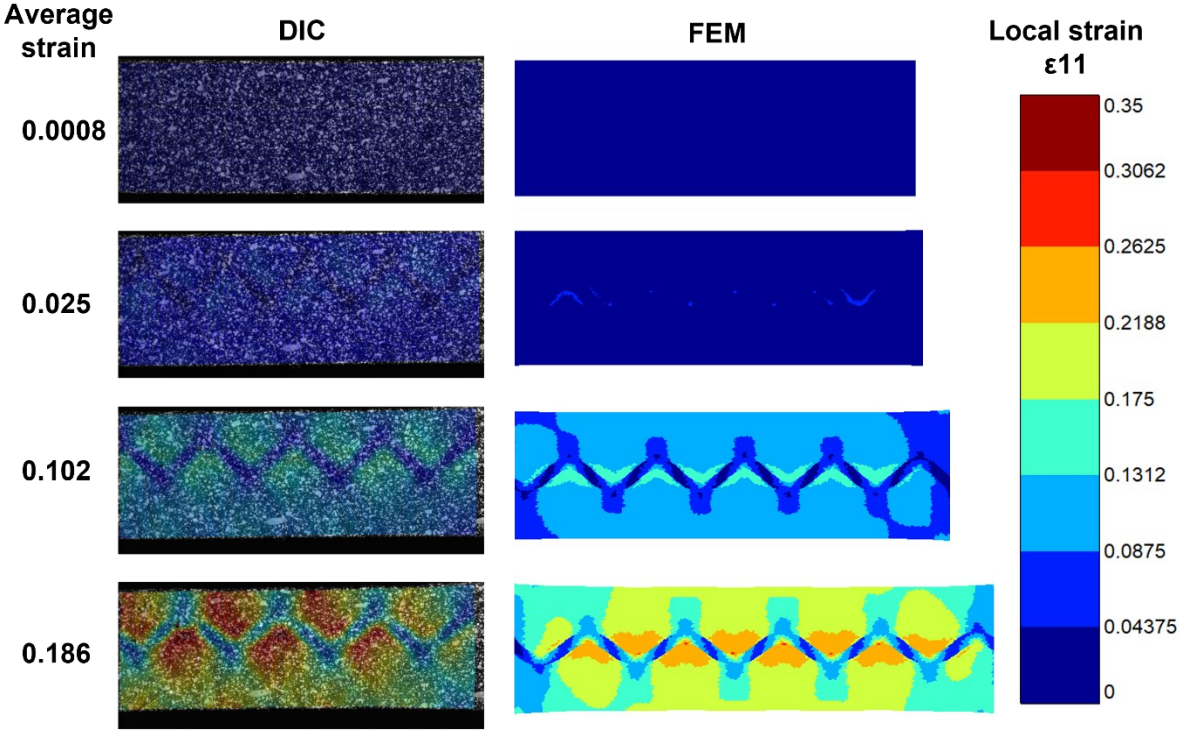


Figure 3-21 DIC results and FEM simulation of local strain evolution during tensile test of specimen with one reinforcement of corrugation height  $h=1$  mm.

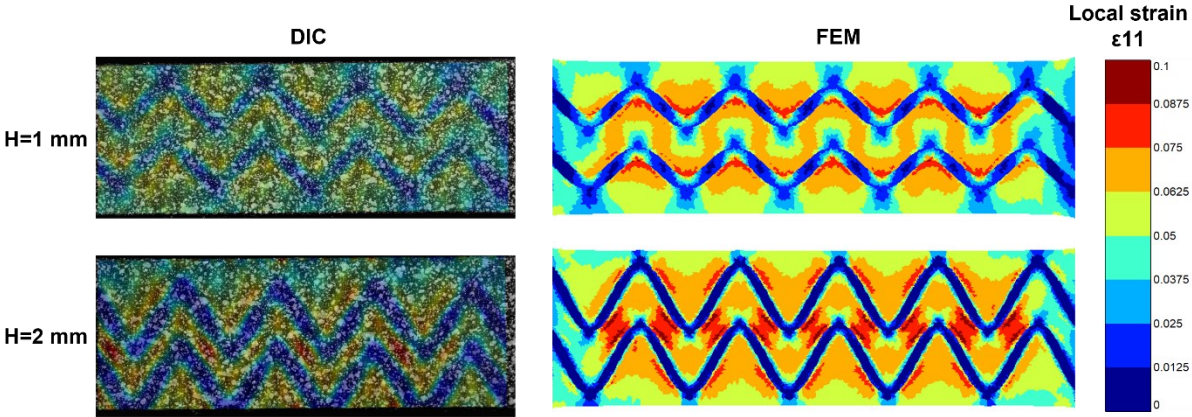


Figure 3-22 Experimental and numerical strain fields of specimens with two corrugated reinforcements at an average strain of 5%, corrugation height  $h$  of 1 mm and 2 mm.

For multi-reinforced specimens, straight reinforcements result always a homogeneous strain field because they are aligned to the tensile direction. Heterogeneous strain fields are obtained from specimens with several corrugated reinforcements and the strain distribution depends on

the corrugation height. Figure 3-22 shows the strain fields from DIC and FEM simulation of specimens with two reinforcements whose corrugation heights are 1 mm and 2 mm respectively at an average strain of 0.05. For both geometries, similar to specimens with single corrugated reinforcement, the matrix under corrugated arc is one of the parts which are the most deformed, and the reinforcement segments between two curvatures have the smallest strain. Furthermore, between two reinforcements, the matrix which is located in the middle of two least deformed segments, is another most deformed part, especially for corrugation height of 2 mm. From both experimental and numerical results, the specimen with corrugation height of 2 mm is more deformed within matrix but less deformed within reinforcement. It can be concluded that the local strain distribution is even more heterogeneous with a larger corrugation height.

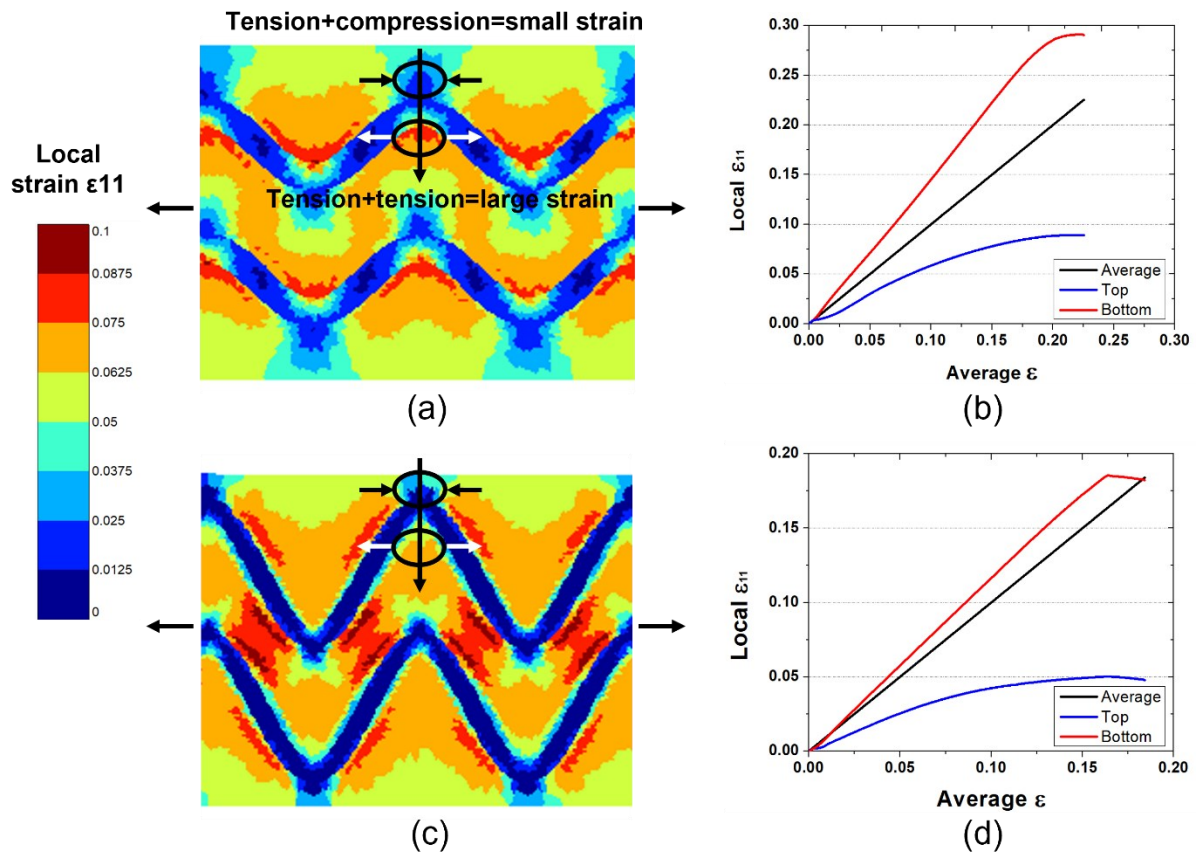


Figure 3-23 (a) (c) Illustration of tensile stress and unbending superposition effect on local strain of matrix on the top and bottom of corrugated peak for corrugation height of 1 mm and 2 mm specimen, (b) (d) evolution of matrix local strain on the top and bottom of corrugated peak for geometry (a) and (c) versus average strain extracted from experimental DIC results.

This strain field heterogeneity can be explained by a superposition effect of external tensile stress and the internal stress introduced by the unbending process of reinforcements [6]. As shown in Figure 2-23 (a) and (c), when the corrugation reinforced specimen is stretched in the horizontal direction, the corrugation is stretched to unbend. The corrugation peaks tend to be flattened, which leads to a compression to matrix under the peak and a tension to matrix above the peak in the vertical direction. This effect can be equivalent to a tension for the region under

the peak and a compression for the region above the peak in the horizontal direction. Therefore, besides the tensile strain of the whole specimen introduced by the uniaxial tensile test, the region underneath the peak presents an additional tensile strain and the total strain in this part is more than the average. On the contrary, the region on the top of corrugation peak has an additional local compressive strain due to the corrugation unbending process, which explains the total strain in this area is less than the average. Figure 3-23 (b) and (d) depict qualitatively the strain evolution of the top and bottom area of a corrugation peak compared to the average strain. For a given average strain, the stress required to unbend the corrugation is smaller when the height is larger, as shown in Figure 3-17 (a). Thus, the extra tensile strain for the region under the peak for  $h=1$  mm is larger than that of corrugation height of 2 mm. But this reason is not enough to explain the total strain on the top for  $h=1$  mm is larger than that of  $h=2$  mm at the same average strain, it may be also due to the continuity of strain between matrix and reinforcement. Because reinforcement of larger corrugation height has a smaller strain, the connective matrix should have a smaller strain at the same time.

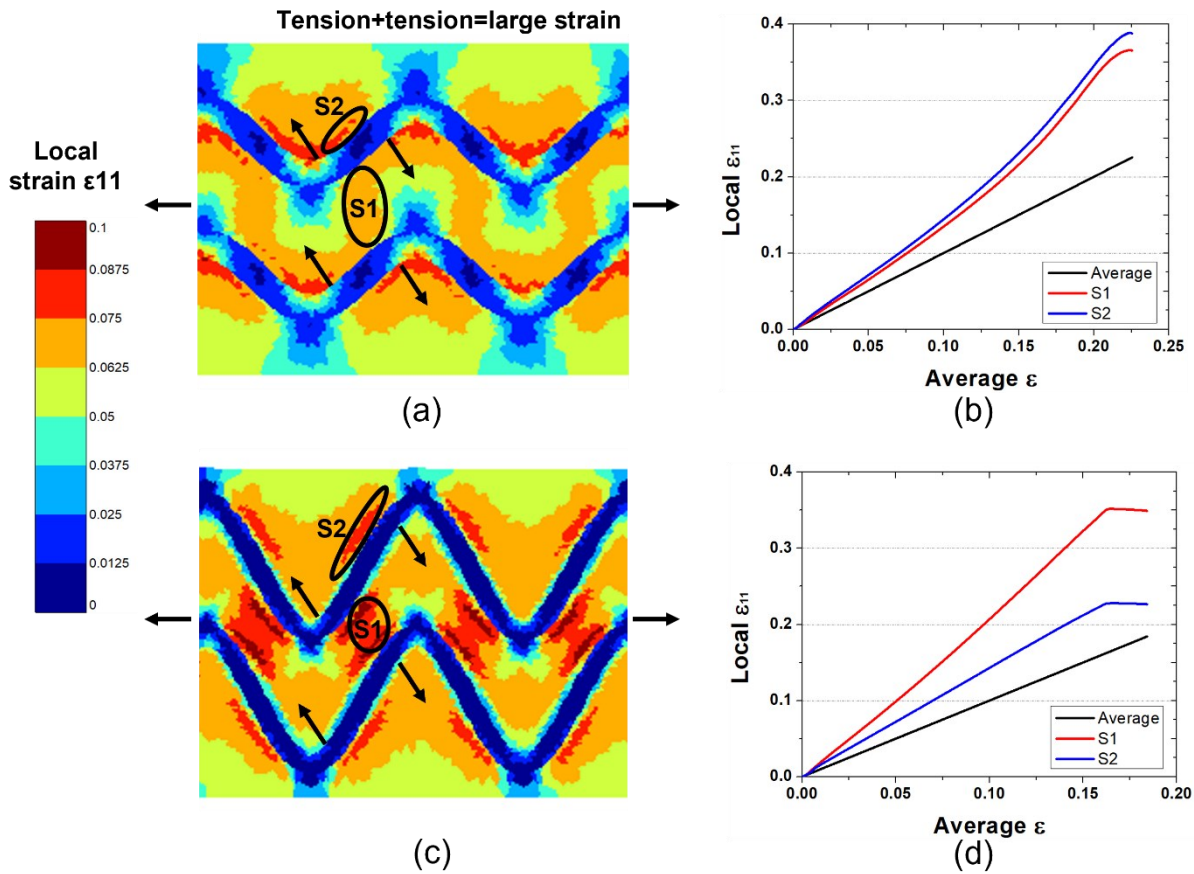


Figure 3-24 (a) (c) Illustration of tensile stress and unbending superposition effect on local strain of matrix beside reinforcement fragment for corrugation height of 1 mm and 2 mm specimen, (b) (d) evolution of matrix local strain beside reinforcement fragment for geometry (a) and (c) versus average strain extracted from experimental DIC results.

Another interesting region to analyze is the matrix beside the fragments which connect the peaks and valleys of corrugations. Figure 3-24 (a) and (c) describe the superposition effect

between the external tensile test and unbending process. The unbending of corrugation tends to align this fragment to the horizontal direction. The region S2 has a larger strain than the average due to the additional tensile strain as explained above. But the region S1, which is between two reinforcements, is also much more deformed than the average because the two adjacent fragments are unbent to the opposite direction. This leads to an additional tensile strain, which is more pronounced when the corrugation height is larger as the spacing between reinforcements is reduced. As shown in Figure 3-24 (b) and (d), qualitatively, the total strain of S1 and S2 is similar for  $h=1$  mm, but S1 is much more deformed than S2 for  $h=2$  mm.

From local strain analyze and qualitative local strain depiction, it can be concluded that the strain field is more heterogeneous with a larger corrugation height. On the opposite, a straight reinforcement ( $h=0$ ) leads to a homogeneous strain field. The untreated AISI 430 has a maximal elongation around 0.23, but some regions have a local strain more than 0.3 before the fracture of architected specimen. This means the final cracking begins in the ductile matrix, instead of in the less ductile reinforcement. The corrugations are not unbent enough to have an enhancement effect on the necking strain when the matrix is already so deformed that it fails. Figure 3-25 depicts the true stress and work hardening rate from FEM simulation versus the true strain of specimens with two straight or corrugated reinforcements, which corresponds to 20% volume of the gauge length. The intersection of true stress and work hardening rate is advanced with the increasing in corrugation height. The corrugations do not enhance the necking strain, but deteriorate it instead, which was not expected at the beginning in this study. The main reasons are excessive local strain of matrix and the delayed boost in work hardening rate of corrugated reinforcements.

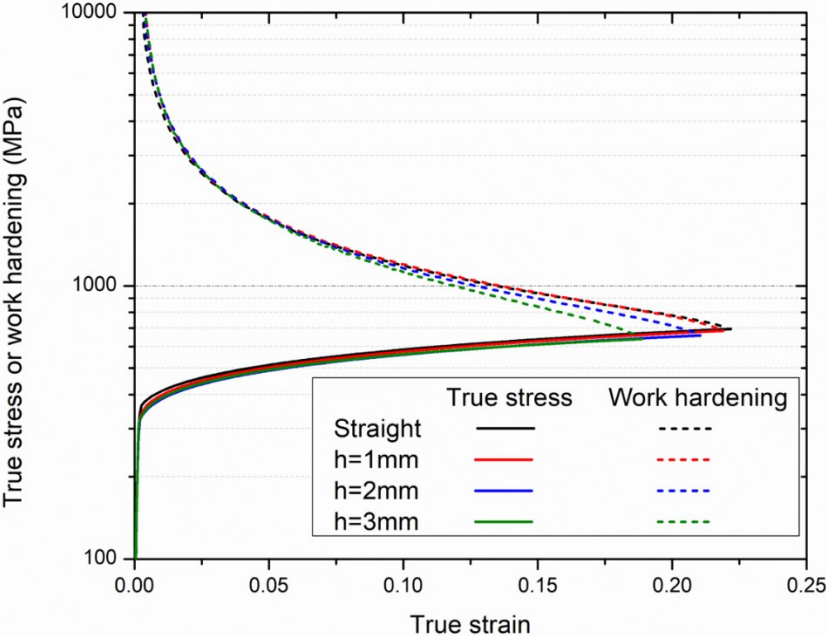


Figure 3-25 True stress and work hardening rate of specimens reinforced by two corrugations of different heights from FEM simulation.

### 3.5.4 Future improvements

The first reason of the negative effect of corrugated reinforcements is the large local strain of matrix. The strain between adjacent reinforcements is the most important, and sometimes it can be twice as much of the average strain when the corrugation height is larger. Therefore, the first trial in the following step is to utilize only one reinforcement. But as the available lasers have relatively small spot size ( $\sim 1$  mm) and the architecturation effect may be more visible with a larger volume reinforced, the gauge part width should be reduced. That is the reason why the tensile specimens are 5-mm-wide in the gauge length in the following part instead on 10 mm in this chapter.

The second reason of the architecturation effect is not satisfying is that the corrugations are not unbent enough to generate the boost in work hardening rate. The unbending process needs to be advanced. From Equation 3-9, it can be deduced that a smaller corrugation ratio  $H/P$  results in a smaller strain when the corrugation is fully unbent. In addition, another reason to reduce corrugation height  $H$  is that the robot arm which moves according to preprogrammed trajectory utilizes an approximate linear velocity. When the architecturation geometries become more complicated and it needs to change much the moving direction, for example, when  $H=3$  mm, the corrugation hardened by laser becomes less coherent. Also, as the reinforcement thickness should be adjusted to keep the same strengthened volume, the laser spot size needs to be more reduced with higher corrugations. This may lead to an untreated region in the middle of the sheet thickness and the reinforcement may not be enough strengthened. Thus, in the following step, the ratio  $H/P$  will be reduced, smaller  $H$  and larger  $P$  will be adopted.

A more strengthened reinforcement is also expected. A higher yield stress of reinforcement can avoid the corrugation to be stretched and foster the unbending when it is under traction. The boost in work hardening effect may be more evident and it will postpone the necking strain [112]. In the following step, a more effective hardening method needs to be investigated to introduce a more strengthened reinforcement in the ductile matrix in order to enhance the necking strain by corrugations.

## 3.6 Conclusions

In this chapter microstructural and mechanical property changes of thin AISI 430 sheets were studied here under different treatment conditions relating to the linear energy density, inert shielding gas, and treatment sides. Several conclusions emerge from microstructural and mechanical characterization.

(1) Despite the poor carbon content and grain coarsening, the laser heat treatment was shown to enhance the mechanical behaviors of 18% Cr FSS by the formation of martensite and chromium carbides during rapid cooling. Local microhardness can be increased by 90% at most using a single-track laser treatment. Fully treated samples by multi-track laser treatment are characterized for the first time, and the yield stress is increased by 60% and UTS by 45.8%.

(2) Thick oxide layers formed at high temperatures on the weld-side surfaces, especially above  $T_m$ , fragilize the laser-treated material and make the results less repeatable. Argon shielding gas is efficient to mitigate these disadvantages.

(3) Double-sided laser treatment enables a more homogeneous treatment through the thickness, hence allowing for an optimal trade-off between strengthening and loss of ductility.

(4) With the flexibility of the laser treatment trajectory and the small spot size, localized heat treatment can be achieved, thus enabling the architecturation of laser-based materials.

In the second part of this chapter, the laser parameter which leads to the most hardening effect was adopted to fabricate architected materials with straight and corrugated reinforcements. Different geometries and reinforcing volumes were carried out and the mechanical properties of architected materials are evaluated. Some conclusions are issued from this study.

(1) Straight and corrugated reinforcements can increase YS and UTS of specimens compared to untreated material. Larger reinforced volume leads to higher reinforcing effect.

(2) While straight reinforced specimens present a homogeneous strain field during uniaxial tensile test, corrugation reinforced specimens have a heterogeneous strain field. A larger corrugation inclination ratio  $H/P$  results in a more heterogeneous strain map.

(3) For a given reinforcement geometry, increasing the reinforced volume can increase the UTS but reduce the ductility. But for the same reinforced volume, different geometries do not change much the stress-strain behavior. Corrugated reinforcements do not enhance the necking strain compared to straight ones in this material system.

(4) The lack of enhancement is due to the excessive local strain in the matrix and delayed corrugation unbending, the following step is to optimize the geometry. A more effective hardening treatment may also benefit the enhancement in necking strain.

# **Chapter 4 Laser carburization strengthening effect of AISI 430 ferritic stainless steel and corrugation reinforced architected materials**

## Résumé

Dans ce chapitre, le procédé de carburation par laser sur les feuilles d'AISI 430 a été étudié. La carburation laser directe est envisagée sur des tôles revêtues de graphite car il est facile de préparer les éprouvettes et de contrôler le procédé. L'évolution de la température au cours du processus de carburation laser (LC) a été prédite par simulation et mesurée par thermocouples. L'effet du traitement par un seul laser et du traitement par deux lasers de chaque côté durant ce procédé à différentes LED a été comparé. La microstructure des échantillons a été examinée par MO et MEB. Les analyses EBSD et rayons X ont été effectuées pour identifier la constitution des phases. Les propriétés mécaniques ont été comparées sur des échantillons directement durcis et carburés sous les mêmes paramètres de laser. La teneur en carbone a été mesurée pour évaluer l'efficacité de la carburation par SDL. Le paramètre qui conduit aux propriétés mécaniques les plus élevées a été choisi pour fabriquer des matériaux architecturés localement renforcés par des lignes droites et des ondulations de différentes géométries. Ils ont été soumis aux essais de traction et aux mesures des champs de déformation locale par le système DIC. Les résultats montrent que l'irradiation laser sur le revêtement de graphite est efficace pour carburer l'acier inoxydable ferritique à une profondeur de plusieurs centaines de microns. La plus faible teneur en carbone dans la région carburée est d'environ 0,4 % contre 0,026 % dans le matériau de base. La morphologie de la zone carburée dépend du rapport entre le gradient de température et la vitesse de solidification provoqué par différentes LED. Un traitement par deux lasers avec une LED adaptée permet d'obtenir une zone uniformément carburée sur toute l'épaisseur des tôles. La micro-dureté augmente à 469 Hv au maximum par rapport à 160 Hv du matériau de base. YS et UTS augmentent de 90% et 85% au maximum. Cette amélioration pourrait être appliquée pour durcir la surface des pièces en acier inoxydable ferritique afin d'augmenter la résistance à la fatigue et à l'usure. Les essais de traction des matériaux architecturés montrent que 20% de renforcement peut augmenter YS et UTS d'environ 100 MPa par rapport à un matériau non traité. Mais l'effet d'amélioration introduit par les ondulations sur la ductilité est bien limité. La ductilité augmente très légèrement avec l'augmentation de la hauteur du renforcement ondulé. Les éprouvettes renforcées par lignes droites présentent un champ de déformation homogène lors de la traction, mais les éprouvettes renforcées par ondulations ont un champ de déformation hétérogène. Un rapport H/P d'ondulation plus important résulte à un champ de déformation plus hétérogène. La rupture de tous les éprouvettes s'initie de la rupture fragile des renforcements. La raison pour laquelle l'effet des ondulations est très limité pour bénéficier la ductilité est que l'augmentation du taux d'écroutissage induite par ondulations est insuffisante durant la traction. Un contraste de résistance plus important entre la matrice et le renforcement peut amener plus d'effet bénéfique.

## 4.1 Introduction

Laser hardening can strengthen AISI 430 FSS sheets, whose local hardness is increased by at most 90% through rapid quenching, as introduced in Chapter 3. Architected materials are fabricated with untreated AISI 430 as matrix and laser hardened material as reinforcement in straight and corrugated geometries in the expectation of enhancing the necking strain of reinforced specimen with corrugations compared with straight ones. Even though experimental DIC results and FEM simulations confirm an apparent contrast in longitudinal strain between matrix and reinforcement during tensile test, the macroscopic stress-strain behavior does not show any obvious differences due to the uncompleted unbending process. This is caused by early fracture of matrix which is too deformed and insufficient yield strength of reinforcement.

Reinforcements with a higher yield strength is needed to prioritize corrugation unbending instead of stretching in order to benefit the necking strain. As AISI 430 is very poor in carbon, only 0.02%, it is difficult to achieve a higher hardness than what is presented above by self-quenching (SQ). Laser alloying method is considered to create a more strengthened microstructure as reinforcement. Different laser carburization (LC) process is introduced in the literature. Most existing studies on stainless steel concern of austenitic and martensitic grades in gaseous or plasma atmosphere at a relatively low temperature. The laser treatment platform developed for this study is not adapted for laser assisted carburization in carbonous gas or plasma because a shielding gas chamber is hard to be placed when laser treatment comes from both sides of the steel sheets. Therefore, direct laser carburization is envisaged on sheets coated by graphite as it is easy to prepare the specimens and to control the process.

The temperature evolution during LC process was predicted by simulation and measured by thermocouples. The effect of single laser treatment and double laser treatment for LC process at different LED was investigated. Microstructure of LC specimens were examined and EBSD and X-ray analysis were carried out to identify phases constitution. Mechanical properties were compared on fully treated SQ and LC specimens under the same laser parameters. The carbon content was measured to evaluate carburization efficiency. The parameter which leads to the highest yield strength is chosen to fabricate architected materials locally reinforced by straight lines and corrugations of different geometries in Table 2-6. They were submitted for uniaxial tensile test and local strain field was followed by DIC system. Results are presented in this chapter. The first part of the chapter concerning the carburization process and characterization is published in the Journal of Engineering Materials and Technology [113].

## 4.2 Temperature evolution

The temperature evolution was measured by the same method in Section 3.2. Figure 4-1 depicts the experimental temperature evolution and numerical approach during single laser treatment in the beam center on the back surface for both SQ and LC processes. For the same process, the peak temperature is more elevated with a higher LED. And for a given LED, peak temperatures of LC process are superior to those of SQ process as graphite coating has a greater absorptivity and favors the heat transfer between laser beam and metallic substrate [86].

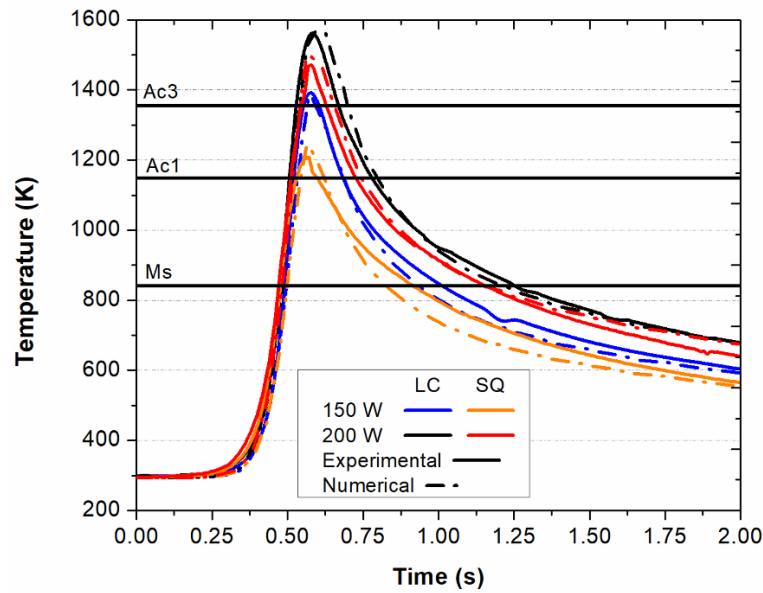


Figure 4-1 Temperature evolution measured by thermocouples and numerical results simulated by COMSOL Multiphysics.

For modelling parameters, specific heat capacity  $c_p$  and thermal conductivity  $\lambda$  of AISI 430 are calculated using Equation 3-2 and 3-3 [96]. The fusion point is set at 1698 K, and the latent fusion heat at 285 kJ/kg. A heat transfer coefficient of  $200 \text{ W}\cdot\text{m}^{-2}\cdot\text{K}^{-1}$  between the irradiated substrate and the environment is included in consideration of shielding gas flux [98]. The absorption coefficients for SQ and LC samples are trimmed to adjust to the experimental results, taken as 0.41 and 0.52 respectively. Critical temperatures are calculated according to the main alloying elements by Equations 3-4, 3-5 and 3-6 [26], [27],  $Ac1=1148 \text{ K}$ ,  $Ac3=1355 \text{ K}$  and  $Ms=841 \text{ K}$ .

The same parameters are used to estimate the temperature evolution under all conditions, as shown in Figure 4-2. All results present an asymmetric form where the heating rate is higher than the cooling one. The influence of LED and graphite coating is similar to what is shown in Figure 4-1. For all direct irradiated side, the peak temperatures exceed  $Ac3$ , and the melting point is attained except for LC samples at 15 kJ/m. At 20 kJ/m for both cases, the peak temperatures on direct irradiated sides of LC and SQ process are very close, less than 10 K, because of the latent fusion heat. For double laser treatment in (b), two irradiated sides present alike aspects and slower cooling process compared to single laser treatment. LC sample at 100 W from both sides generates a longer maintain duration above the melting point and the melting pool size is wider than other conditions because of higher LED and absorption rate. Thus, its cooling rate is obviously lower than the others, but still over 800 K/s.

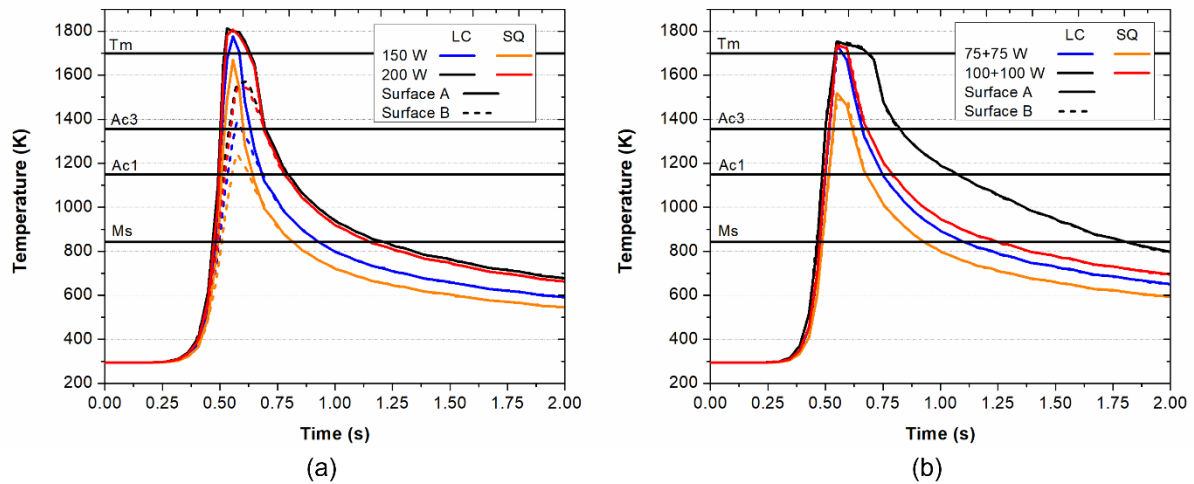


Figure 4-2 Temperature evolution prediction of LC and SQ process by (a) single laser treatment (b) double laser treatment with different LED.

Former results in Section 3.2 [95] has already proven that double laser treatment yields a more uniform temperature field at the beam center through the thickness with the same LED compared to single laser treatment.

### 4.3 Characterization of laser assisted carburized AISI 430 FSS

#### 4.3.1 Microstructural analysis and phase identification

Figure 4-3 (a) - (d) reveals the section microstructures of SQ samples and LC samples (e) – (h) with different laser parameters. Former results [95] shows that SQ samples exhibit dramatic grain coarsening with the increase of LED and martensite formation occurs due to rapid cooling both intergranularly and intragranularly. And compared to single laser treatment, double laser treatment achieves a more uniform microstructure evolution through the thickness thank to a smaller temperature gradient because both surfaces are irradiated.

With the same LED, the LC samples exhibit a wider and deeper melting pool because graphite increases the laser absorption rate and thus improve the coupling efficiency between the laser beam and metal substrate [114]. While SQ samples present a consistent microstructure evolution from laser treated zone, in some case fusion zone (FZ), to heat affected zone (HAZ), LC samples show a clear boundary between carburized zone and HAZ. The average grain sizes of the treated zones are reported in Table 4-1. The grains of LC samples are finer than SQ samples thanks to the pinning effect at grain boundaries by carbides. Similar to SQ samples, the grain sizes increase the higher LED and for the same LED, double laser treatment yields a smaller grain size than single one.

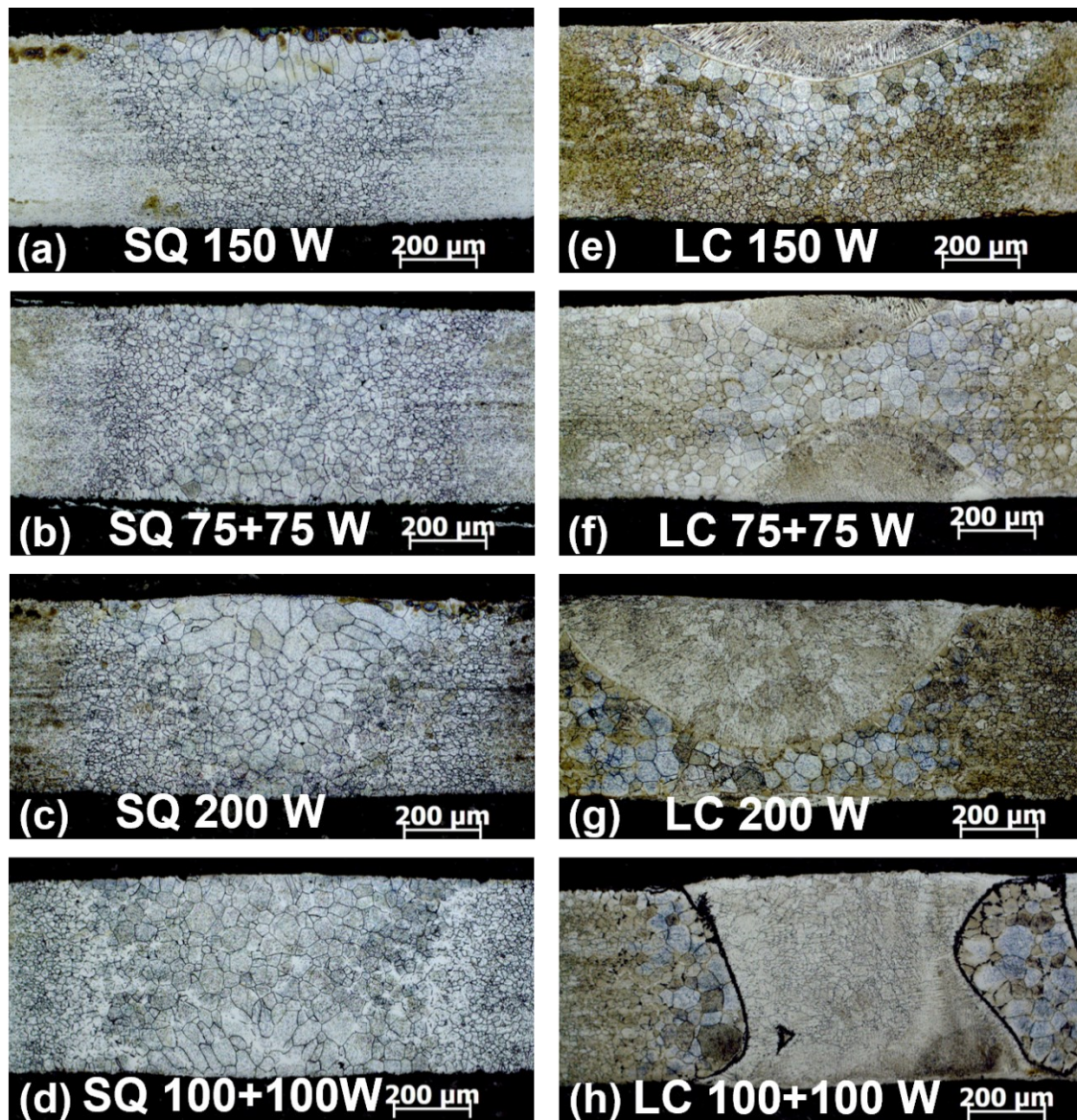


Figure 4-3 Microstructure of SQ and LC samples under different treatment conditions.

In the carburized zone, two typical microstructures are identified as shown in Figure 4-4. With a relative lower LED at 15 kJ/m for both single and double laser treatment, the carburized zone consists of dendrite grains mostly. In Figure 4-4 (a), equiaxed dendrites are formed near the surface and columnar dendrites are formed in the adjacent layer in FZ. Inside the dendritic grains, alloy elements exist in solid solution. At 20 kJ/m for both single and double laser treatment, the carburized zone is dominated by cellular grains with fine equiaxed grains in the center and columnar grains along the solidification direction of FZ (Figure 4-3 (g) and (h)). Numerous carbides of around 1  $\mu\text{m}$  in diameter are observed inside the grains and at the grain boundaries. But it is to note that the presence of these two kinds of microstructure is not contradictory as they can be found in the same FZ. In Figure 4-4 (a), even though the microstructure is mostly dendritic, several cellular grains are formed below the columnar

dendrites near the interface between FZ and HAZ. Similarly, small quantities of columnar dendrites can be found in the carburized area near the surface when a higher LED is applied.

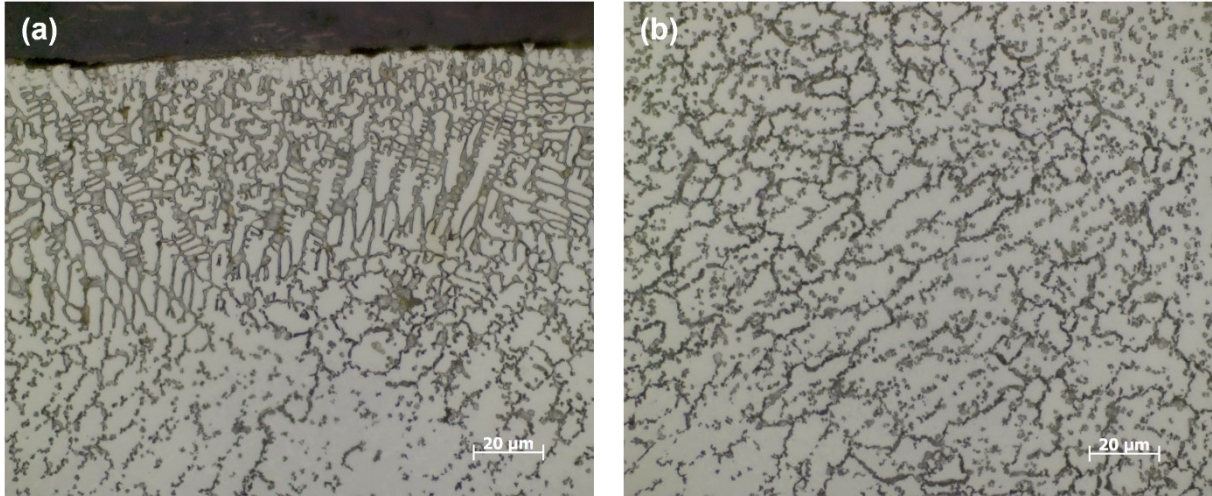


Figure 4-4 Optical micrographs of sample treated at (a) 75 W (b) 100 W both sides.

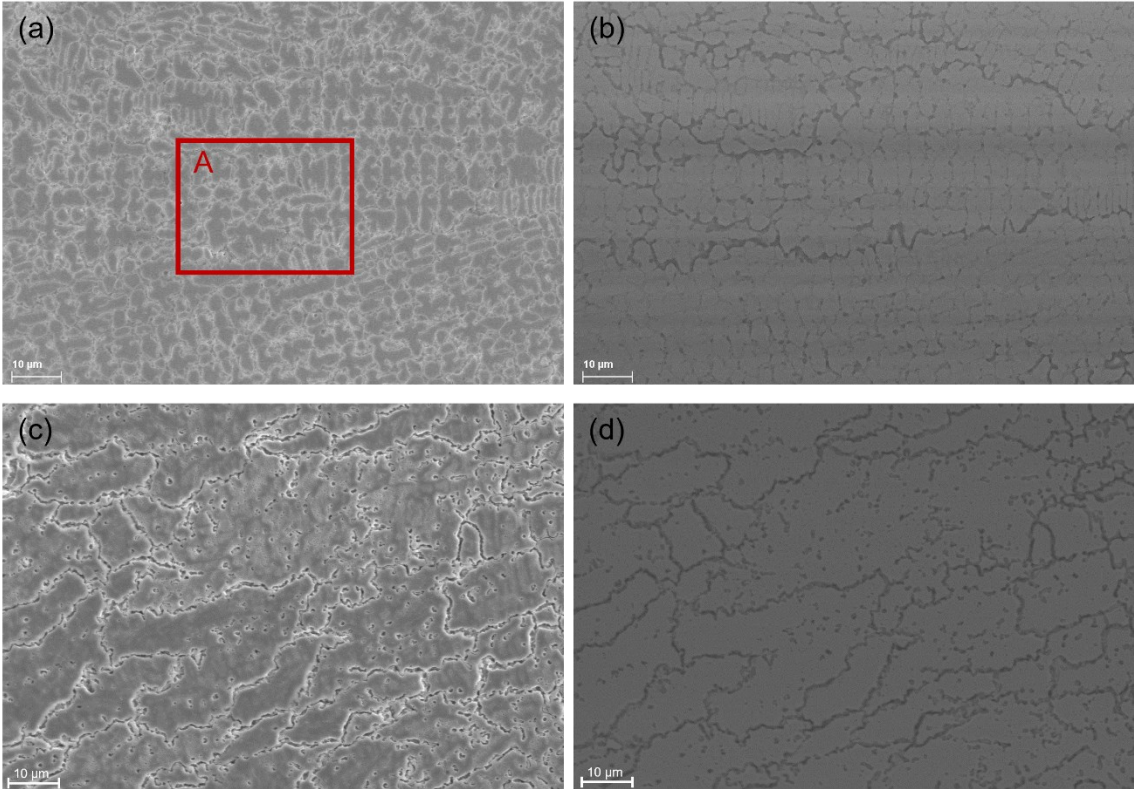


Figure 4-5 SEM images of LC samples at (a) (b) 75 W both sides, (c) (d) 100 W both sides, (a) (c) SE signal, (b) (d) BSE signal.

SEM observation is carried out using both secondary electron signal (SE) and backscattered electron signal (BSE) to investigate dendritic and cellular grains. Figure 4-5 (a) presents short dendritic grains by SE signal and (b) is the same area by BSE signal, where the interdendritic regions appear darker than dendrites. This means that these regions may be richer in C and Cr and poorer in Fe. Zone A is submitted to EDS mapping analysis in Cr, Fe and C content. Figure

4-6 confirms qualitatively that interdendritic regions contain more Cr and C than dendritic regions, but less Fe, which implies an element segregation upon solidification. Figure 4-5 (c) shows cellular grains in high magnification, where the bright lines are grain boundaries and (d) is this region by BSE signal. The darker grain boundaries and small discontinuous precipitations insides grains suggest that the C and Cr content in these parts are more elevated than the matrix.

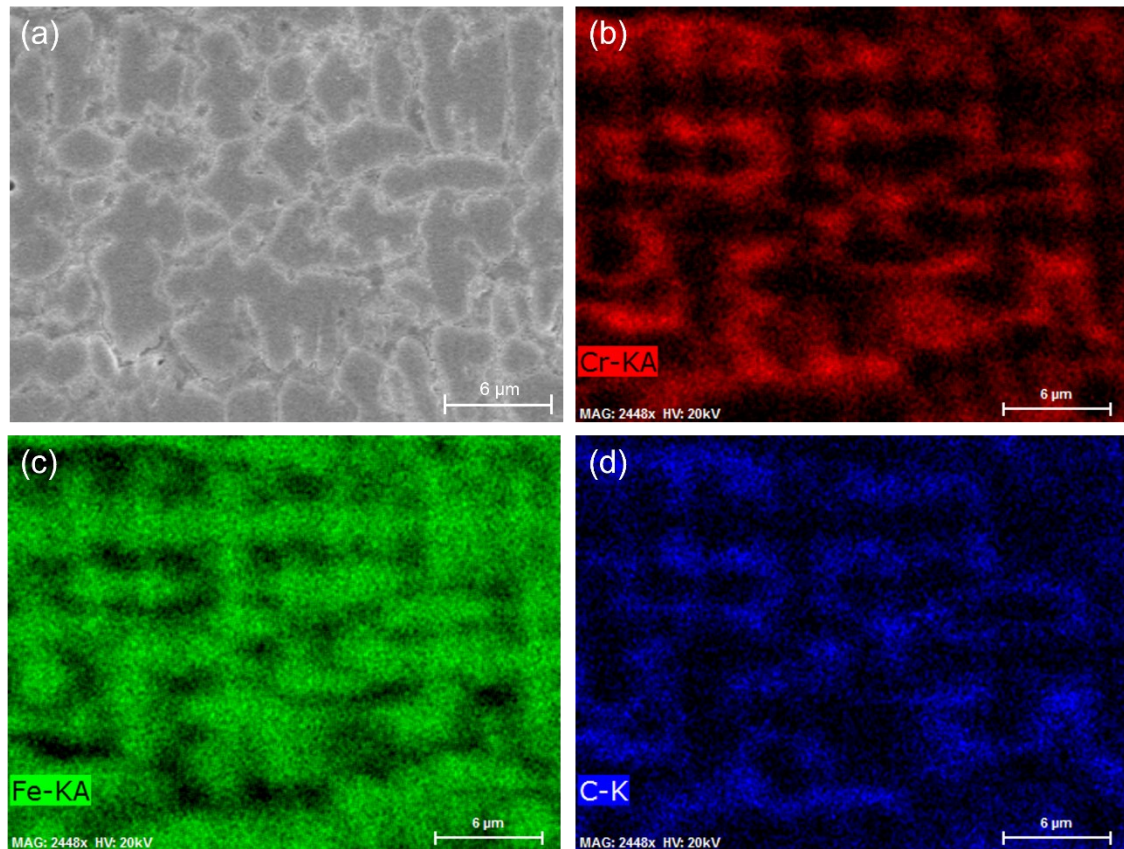


Figure 4-6 EDS mapping of dendritic microstructure of samples treated at 75 W both sides (a) SEM image by SE signal, (b) Cr, (c) Fe, (d) C.

Microstructure of interdendritic region in Figure 4-5 (a) is zoomed in Figure 4-7. The interior presents a eutectic morphology, whose average lamellar spacing is less than 100 nm. Solidification begins by forming dendritic austenitic grains, excess carbon atoms are separated out to the left liquid phase and concentrate between dendrites. As Cr has a higher solubility in liquid  $\gamma$  phase than in solid [115], Cr atoms are also segregated to liquid phase and accumulate in interdendritic regions with C atoms. The interdendritic region seems to solidify at latest to be a eutectic structure containing carbides and  $\gamma/\alpha$  phases, which resembles to the results of study in [114] of laser carburized austenitic stainless steel.

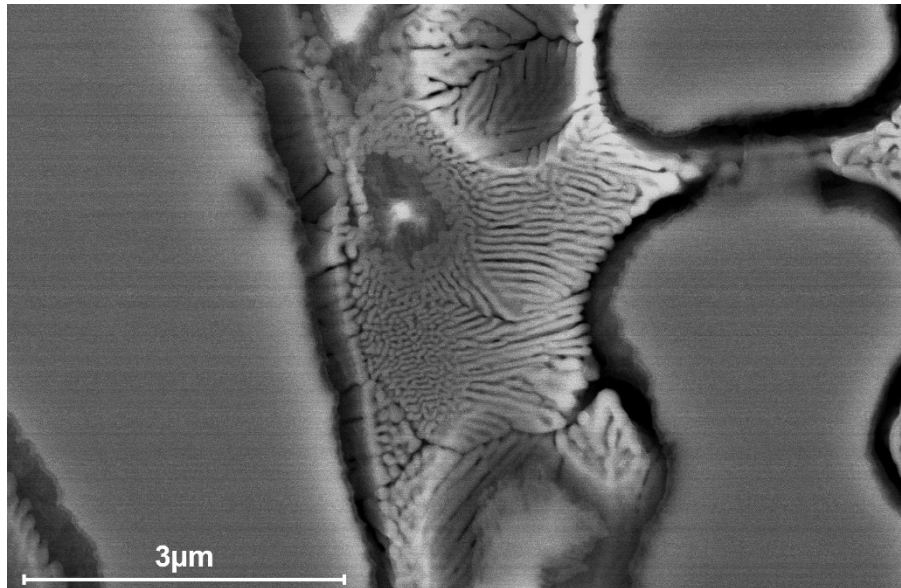


Figure 4-7 SEM image of interdendritic region.

Figure 4-8 reveals an EBSD examination of the microstructures introduced in Figure 4-4, generated with double lasers at different LED. (a) and (c) show the inverse pole figure (IPF) of the global microstructure at 15 kJ/m and 20 kJ/m, (b) and (d) are magnified carburized zone respectively. (e) (f) (g) (h) are corresponding phase distribution map. In both cases, the HAZ present similar coarsened ferritic grains with small amount of retained austenite at grain boundaries. Excess carbon atoms accumulate at the interface between carburized zone and HAZ and therefore form a complex band which is hard to identify. But due to different cooling rates and carbon concentrations, the carburized zone at different LED manifests dissimilar morphology.

In the carburized zone at 15 kJ/m, the dendritic region is austenitic solid solution and the interdendritic region is rather complicated to detect because of the extra fine lamellar structure and limit resolution of EBSD step size. A tiny amount of ferrite is identified in the interdendritic area, so the eutectic lamellar structure is likely to contain chromium carbides and  $\alpha$ -Fe. Dendrites within the same prior austenite grain solidify in the same preferred orientation. At 20 kJ/m, the carburized zone consists mostly of cellular austenitic matrix with intergranular and intragranular island-like mixture of carbides and  $\alpha$ -Fe. Similarly, the nature of chromium carbides in this mixture is also hard to index as for the former interdendritic region. It is worth noting that vermicular ferritic grains are found to be surrounded by austenite near the interface between FZ and HAZ. It concerns  $\delta$ -ferrite issued from the liquid phase directly, which remains stable in a large temperature range within high-alloy stainless steel welds [116]. Crystallographic orientation of cellular grains is more randomly distributed compared to dendritic grains.

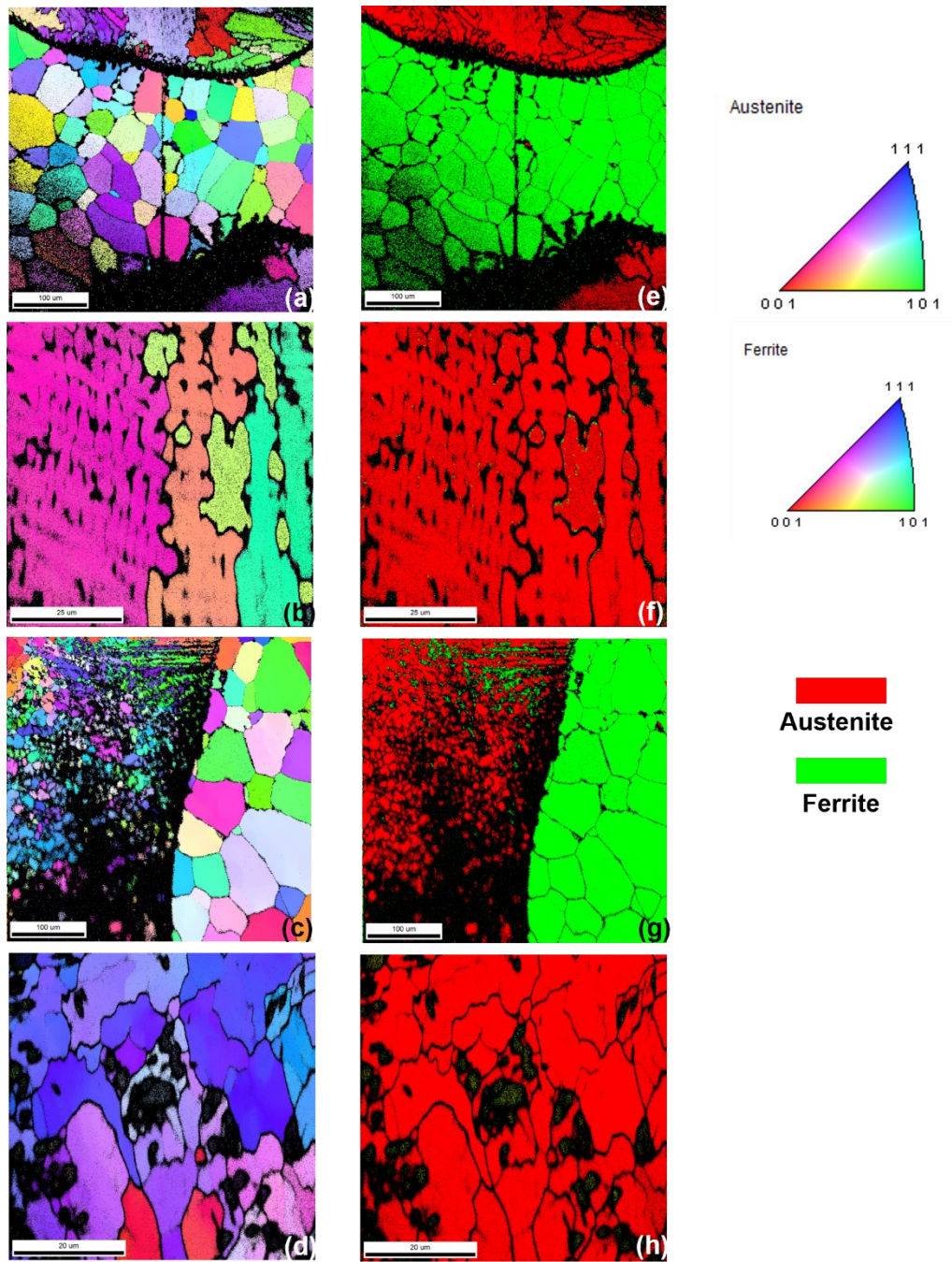


Figure 4-8 EBSD measurement of carburized zone section, (a) (b) IPF of sample at 75 W from both sides, (c) (d) IPF of sample at 100 W from both sides, (b) (d) are magnified characterization in carburized zone of (a) (c) respectively, (e) (f) (g) (h) phase distribution of (a) (b) (c) (d).

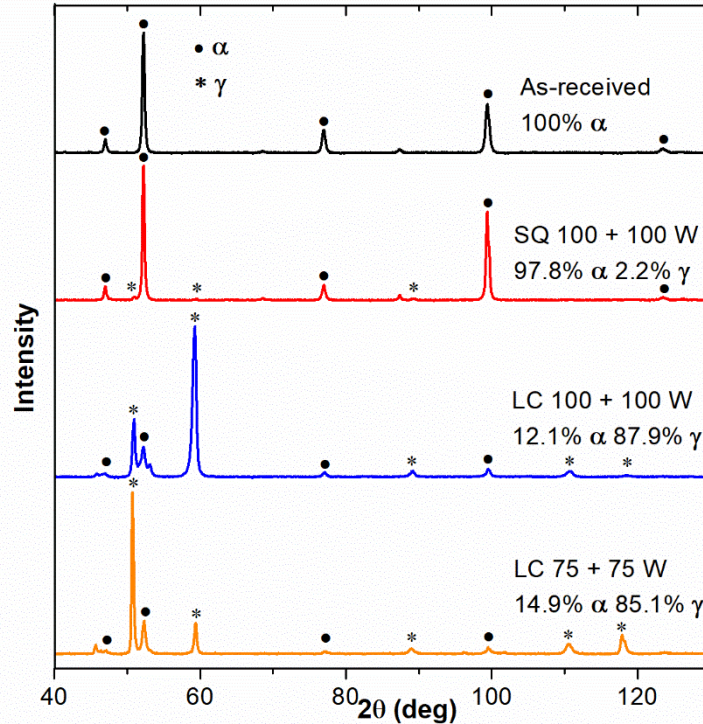


Figure 4-9 XRD patterns and phase composition of samples treated under different conditions.

Figure 4-9 compares the XRD spectra of the surface layer on the as-received material and samples treated under different conditions and their phase composition. The diffraction peaks of the as-received material correspond to a single  $\alpha$  ferrite phase. After laser treatment without graphite, similar peaks are detected on SQ sample and also a small amount of retained austenite (2.2%) appears, which is formed between coarsening ferritic grains upon rapid cooling. However,  $\alpha'$  martensite and  $\alpha$  ferrite peaks cannot be distinguished. The patterns of LC samples contain strong peaks of  $\gamma$  austenite, and the ferrite peaks are much weaker, which indicates that austenite becomes the leading phase after carburization. The relative difference in austenitic peak intensities between LC samples with different LED may be resulted from preferred orientation under different cooling rate. Carbides could not be detected on any of the samples due to the low percentage and weak intensities.

### 4.3.2 Carburization efficiency

The carbon mass content is difficult to be determined through EDS analysis because the carbon peak has a low energy, it is measured by GD-OES through the whole thickness to evaluate the carburizing efficiency. The as-received material contains about 0.026 wt% of carbon and the SQ samples show no evident changes in carbon content after laser treatment. The evolution in C wt% in LC samples is described in Figure 4-10. It is noteworthy that since the measurements are taken on a 4-mm diameter surface of fully treated samples containing multi laser tracks, Figure 4-10 does not represent the exact mass fraction of carbon in carburized region but a lower one because of the uncovering regions between tracks whose carbon content equals to

that of as-received material. The results near the irradiated surface are closer to the real mass fractions of C as the uncovering regions are thinner.

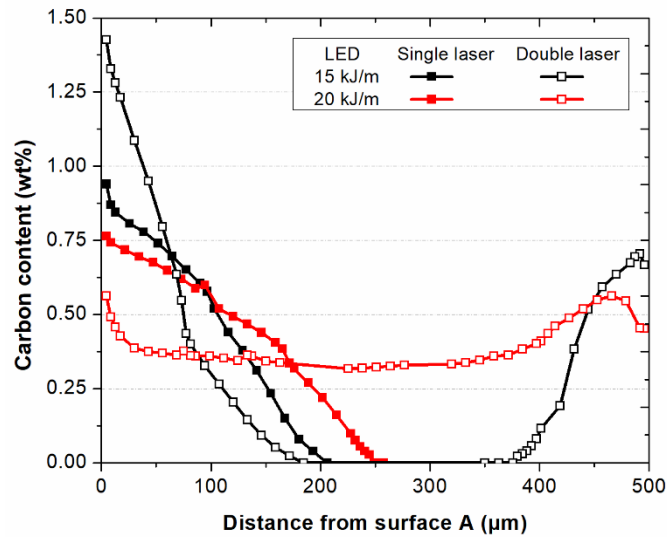


Figure 4-10 Carbon mass fraction through the thickness of single and double laser treated samples measured by GD-OES.

With all chosen parameters, laser treatment is efficient to introduce carbon into the low carbon matrix with different depths from the irradiated surface. In the HAZ where grain coarsening and martensite formation happen, C wt% remains the same with the base material. The C wt% at the surface A:  $75\text{ W} + 75\text{ W} > 150\text{ W} > 200\text{ W} > 100\text{ W} + 100\text{ W}$ , from the section microstructures in Figure 4-3, a smaller depth of carburized region leads to a more important carbon mass fraction. A complete FZ through the whole thickness by 100 W from both surfaces yields an almost stable C wt% in the bulk, around 0.4%. The asymmetry aspect of C wt% of two irradiated surfaces may be due to the different intensity distributions of laser beams. The higher C wt% ( $>0.8\%$ ) within lower LED 15 kJ/m treated samples confirms the large quantity of interdendritic eutectic microstructures in Figure 4-4 (a), and the relatively lower one ( $<0.8\%$ ) by 20 kJ/m results in a cellular-dominated microstructure in Figure 4-4 (b).

### 4.3.3 Microhardness

Vickers microhardness tests are taken along the laser track center through the thickness of the sample under different conditions, the results are shown in Figure 4-11 (a) single laser treatment, (b) double laser treatment. All treatments lead to a more important hardness compared to that of as-received material, which is around 160 Hv. For both single and double laser treatments, with the same LED, LC samples exhibit a much more elevated hardness than SQ samples in the fusion zone. Higher LED increases the peak hardness of fusion zone for SQ samples because more martensite and carbides are formed. But for LC samples, a relatively lower LED yields a shallower but much more hardened carburized region.

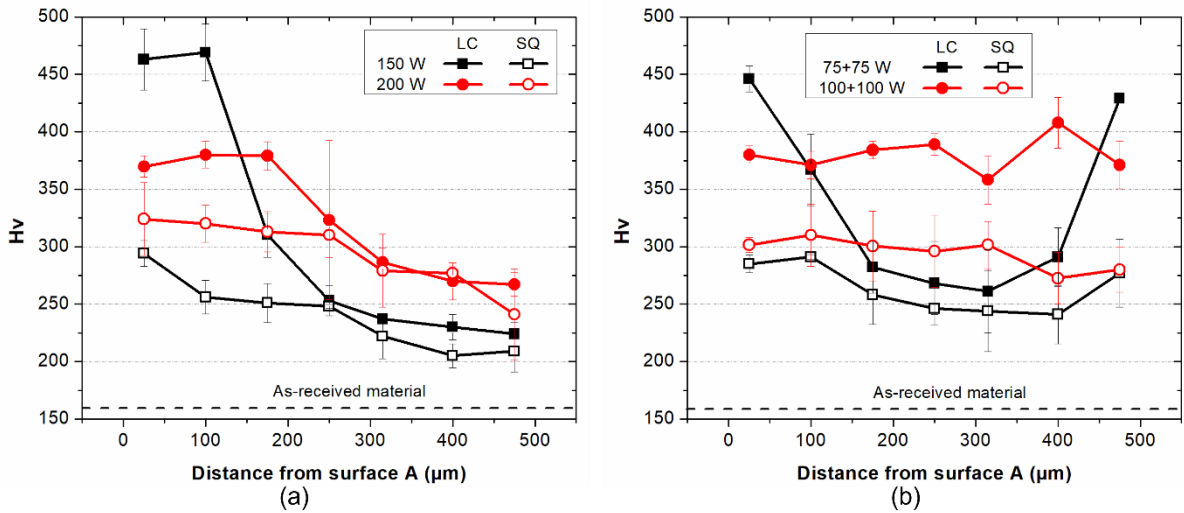


Figure 4-11 Microhardness along laser beam center in the section (a) single laser treatment (b) double laser treatment.

For single laser treatment in Figure 4-11 (a), the hardness decreased from the irradiated side for both SQ and LC samples, but the reduction for LC samples is more dramatic. The highest value is found in the fusion zone at 150 W, 469 Hv. At 200 W, a deeper zone is carburized but it exhibits a lower peak value (380 Hv). Hardness values in the HAZ under the same LED are close in this case because the peak temperatures in HAZ do not differ much from each other. For double laser treated samples in Figure 4-11 (b), a FZ through the whole thickness is achieved by 100 W from both sides, so the hardness does not evolve much, around 380 Hv and 300 Hv for LC and SQ samples respectively. On the contrary, 75 W from both sides creates a much harder surface (450 Hv) and the values in the adjacent HAZ area are close to SQ samples. Comparing dendritic and cellular grains formed at different LED, it can be concluded that the former yields a much more important microhardness than the latter.

#### 4.3.4 Tensile test

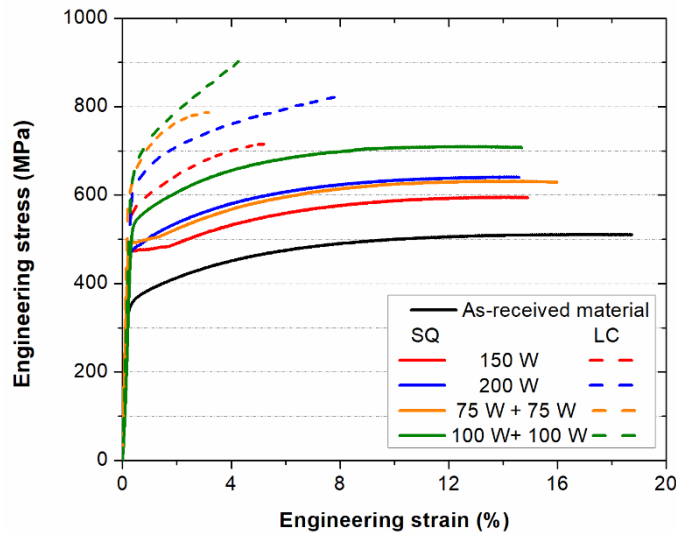


Figure 4-12 Tensile test results of SQ and LC samples.

Table 4-1 Mechanical properties and morphology of as-received material and laser treated samples.

	Power (W)	YS (MPa)	UTS (MPa)	$\epsilon_u$	Grain size ( $\mu\text{m}$ )	Morphology
As-received	-	346 $\pm$ 12	503 $\pm$ 15	19.39 $\pm$ 0.07%	11.2 $\pm$ 0.5	Equiaxed grains
	150	458 $\pm$ 53	571 $\pm$ 49	14.62 $\pm$ 0.09%	32.8 $\pm$ 6.7	
SQ sample	75+75	488 $\pm$ 24	623 $\pm$ 20	15.54 $\pm$ 0.17%	22.3 $\pm$ 2.8	Coarsening grains
	200	497 $\pm$ 10	650 $\pm$ 16	13.85 $\pm$ 1.82%	33.9 $\pm$ 5.3	
	100+100	540 $\pm$ 18	702 $\pm$ 18	13.67 $\pm$ 1.42%	32.2 $\pm$ 1.9	
LC sample	150	565 $\pm$ 19	711 $\pm$ 19	4.86 $\pm$ 0.54%	4.7 $\pm$ 0.5	Dendrite dominated
	75+75	659 $\pm$ 26	773 $\pm$ 11	2.57 $\pm$ 0.35%	3.9 $\pm$ 0.6	
	200	638 $\pm$ 20	827 $\pm$ 21	5.63 $\pm$ 0.72%	17.6 $\pm$ 1.5	
100+100	667 $\pm$ 22	923 $\pm$ 39	3.47 $\pm$ 0.53%	13.5 $\pm$ 1.9		

Figure 4-12 depicts the uniaxial stress-strain behavior of SQ and LC samples in different conditions, the mechanical properties are summarized in Table 4-1. Former results in Chapter 3 [95] reveal that for SQ samples, the increase in LED results in a higher yield stress (YS) and ultimate tensile strength (UTS) because more carbides and martensite are formed. And for the same LED, double laser treatment yields a higher YS and UTS because of more uniform temperature field through the sample thickness. The highest value for YS and UTS is 579 and 702 MPa at 100 W from both sides compared to 350 and 500 MPa for the as-received material. The uniform plastic deformation ( $\epsilon_u$ ) is reduced from 19.5% to around 14% for the SQ samples.

The LC samples present quite different characteristics. Similar to SQ samples, both increase in LED and double laser treatment lead to higher YS and UTS due to the expansion of carburized zone. Compared to SQ samples under the same condition, LC samples have a more elevated YS and UTS due to the large quantity of austenite and carbides formed in the carburized zone, at most 667 and 923 MPa for 100 W from both sides because a fully carburized region is formed through the whole thickness, which is 90% and 85% more than the as-received material. But the carburization deteriorates severely the ductility,  $\epsilon_u$  is less than 6% with all chosen parameters. It is worth noticing that higher LED present a slight better  $\epsilon_u$ , which can be explained by the cellular-dominated microstructure, which is less brittle than dendritic microstructure.

4.3.5 Fractography

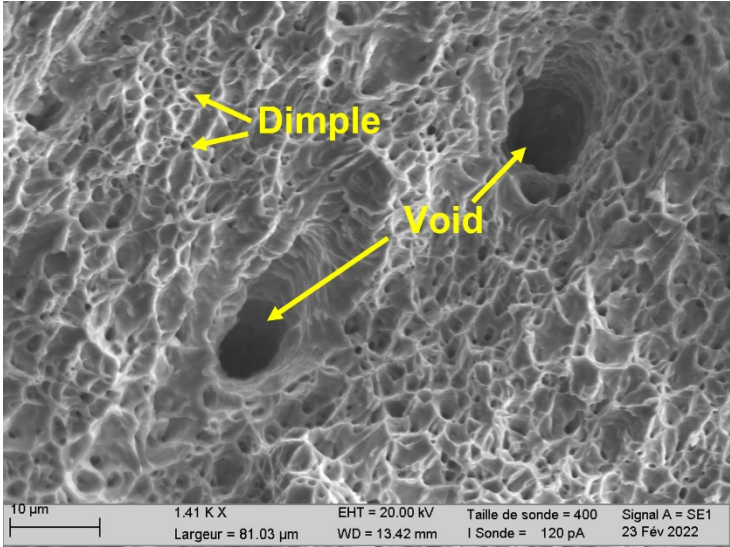


Figure 4-13 SEM micrograph obtained from the fracture surface of as-received AISI 430 specimen after tensile test.

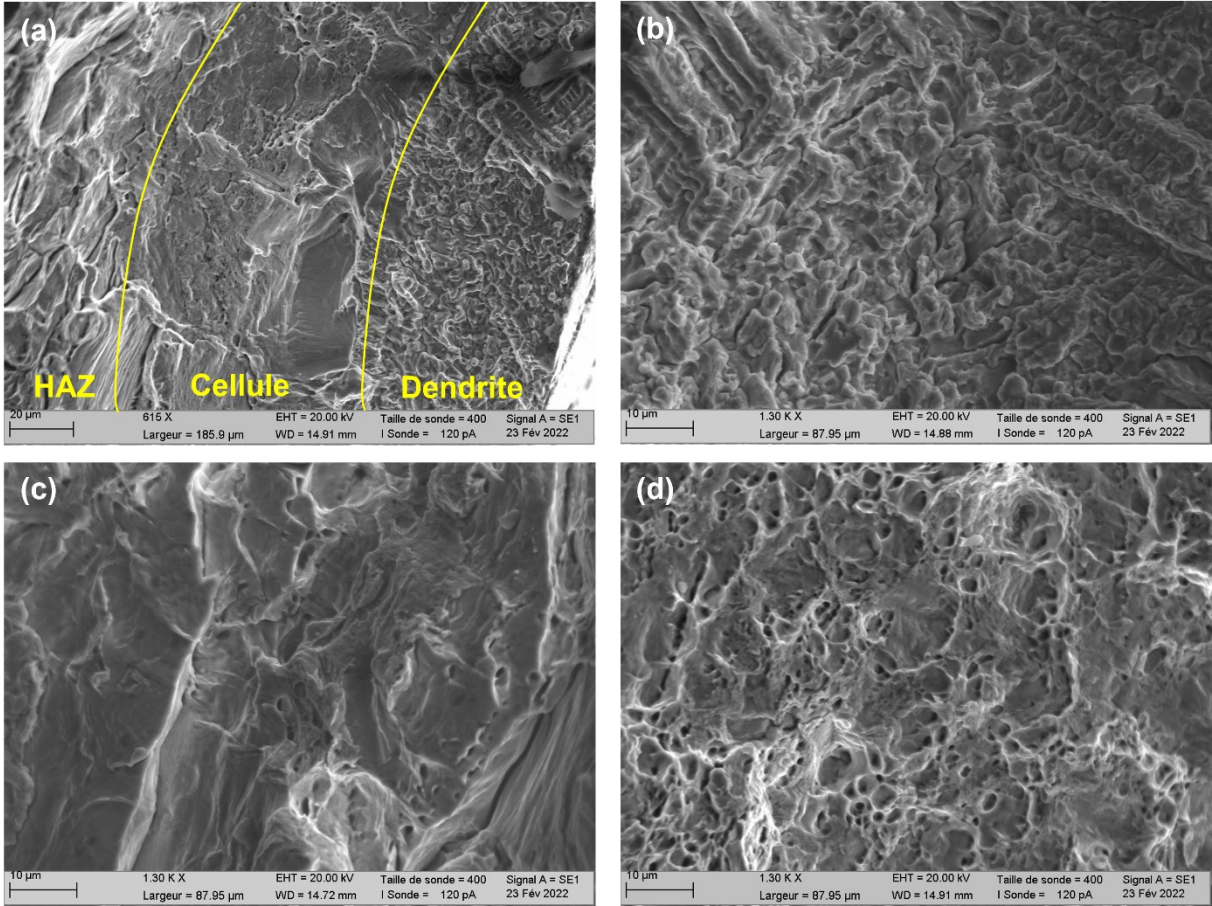


Figure 4-14 (a) SEM micrograph from the fracture surface of laser carburized specimen at 75 W from both sides after tensile test, (b) (c) (d) magnified image of carburized dendrite region, cellular region and grain coarsened HAZ zone.

Fracture surfaces were examined by SEM after uniaxial tensile test. Figure 4-13 shows the fracture surface of as-received AISI 430 specimen. It can be inferred from the surface fractography that the as-received material has undergone ductile fracture by the presence of dimples and voids.

Figure 4-14 (a) presents the fractography of laser carburized specimen at 75 W from both sides after tensile test. The fracture morphology can be separated into three different regions according to their initial microstructure. The dendrite dominated zone near the specimen surface cracks intergranularly along the dendrites and there are few voids (Figure 4-14 (b)). This region experiences brittle fracture. The cellular dominated region is farther from the surface, where the fracture presents a mixed appearance of ductile fracture and brittle fracture (Figure 4-14 (c)). A few hallows are found among the cleavage fracture. Beyond the carburized zone, the grains are dramatically coarsened but the ductility is less effected. Dimples and voids are found in the HAZ (Figure 4-14 (d)), which has a ductile fracture similar to the untreated material.

Fracture surfaces of laser carburized specimen at 100 W from both sides are shown in Figure 4-15 (a). It presents an intergranular cleavage and brittle fracture at most of the surface with a small amount of dimples in the HAZ. Details of steps and ridges can be seen in Figure 4-15 (b). According to EBSD and X-ray patterns, carburized zones consist of mostly of FCC austenite. Cleavage fracture is rare among FCC materials at room temperature [117] because they are usually considered as ductile thanks to numerous slip systems. Laser carburization process has changed the fracture mode from ductile to brittle by forming a large quantity of carbides.

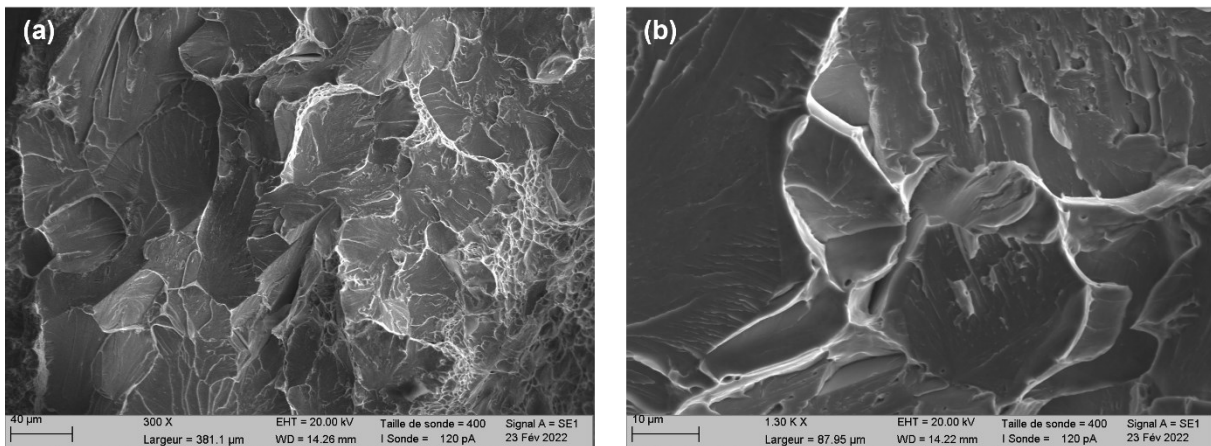


Figure 4-15 SEM micrograph obtained from fracture surface of laser carburized specimen at 100 W from both sides after tensile test, (a) cellular zone and HAZ, (b) zoomed cellular zone.

### 4.3.6 Discussion

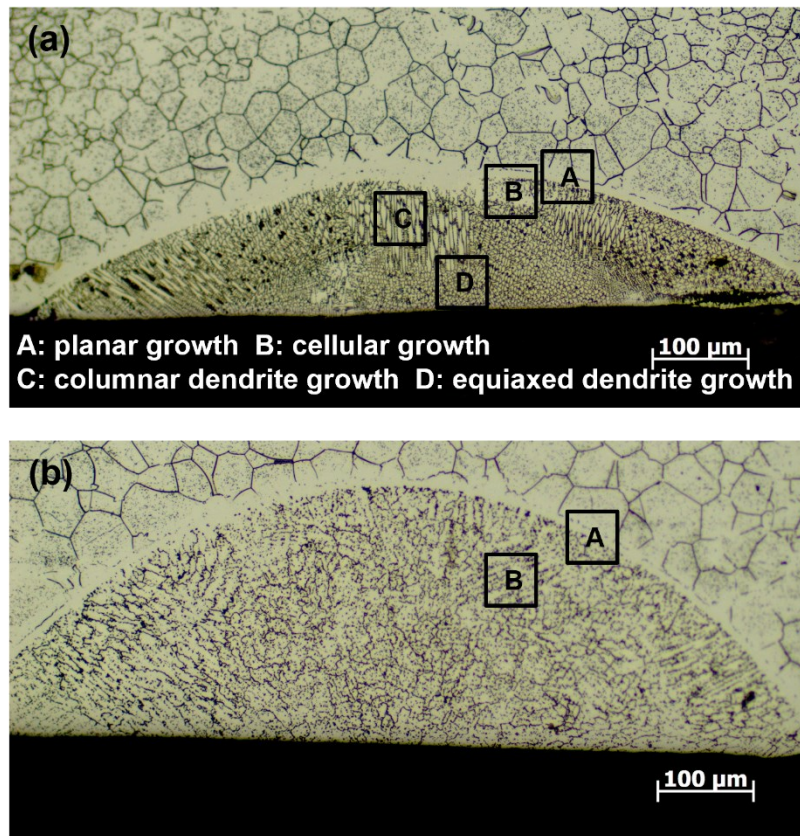


Figure 4-16 Microstructure of carburized area by single laser treatment at (a) 15 kJ/m, (b) 20 kJ/m.

With chosen parameters, both SQ and LC process change visibly the microstructure in FZ and HAZ compared with the as-received material. SQ process yields a continuous FZ and HAZ with ferritic grain coarsening and a small amount of martensite formation by rapid heating and cooling, which is discussed thoroughly in the authors' former work [95]. During LC process, graphite on the surface is introduced into the molten pool and mixed by Marangoni flow [118], and during the cooling cycle, the molten pool forms a carburized area whose morphology depends strongly on LED. LC process generates a clear interface between FZ and HAZ by a planar solidification band at the edge of carburized FZ, where the excess carbon atoms cannot further dissolve into HAZ and accumulate. The HAZ presents similar aspects as the SQ samples, a dramatic grain coarsening and small amount of martensite formation, which is more severe with the increase of LED.

At a lower LED 15 kJ/m, with the distance increasing from this interface, the morphology of the carburized zone follows planar growth (A), cellular growth (B), columnar dendrite growth (C) and equiaxed dendrite growth (D) in Figure 4-13 (a). While at higher LED 20 kJ/m, this transformation stops mainly at cellular growth step ((A) and (B)), only a few dendrites can be found near the surface (Figure 4-13 (b)). This transformation is resulted from the element composition, temperature gradient (G) and solidification rate (R) [114]. For a given material,

the ratio  $G/R$  is the governing parameter for the morphological solidification structure, cellular growth turns into dendrite growth when the ratio  $G/R$  is inferior to a critical value [119,120]. In the molten pool at 15 kJ/m, the latent crystallization heat is released through the liquid phase, the undercooling is more pronounced and the ratio  $G/R$  decreases from the interface liquid/solid to the center, where cellular growth transforms into columnar dendrite growth. An increase in LED leads to a lower cooling rate and a higher  $G/R$  [121], thus the carburized zone at 20 kJ/m present a cell-dominated morphology, only a few dendrites are found near the surface. Also, because the molten pool is deeper and thus poorer in carbon at higher LED, the constitutional undercooling becomes less important upon solidification, which favors the formation of cellular grains.

Austenitic grains are developed in the first place during the cooling cycle and carbon atoms segregate to the grain boundaries. Numerous carbides are formed and inhibit the grain coarsening [90], which is the reason why there is a contrast in grain size between carburized zone and HAZ. While carbides are discretely distributed at grain boundaries and inside cellular grains at higher LED, a large quantity of eutectic structure is formed in interdendritic network at lower LED. BSE and EDS results both show that Cr is richer in interdendritic regions and grain boundaries, it can be assumed that they form chromium-rich carbides like  $M_{23}C_6$ , which is the most common carbide in austenitic structures [122], but the exact type of carbides need to be investigated further. This segregation is observed in other studies where the ferrite promoting element Cr is richer in interdendritic region contrary to the dendritic region [123]. It can also be assumed that the eutectic structure in Figure 4-7 is composed of  $\alpha$ -Fe and carbides from XRD analysis. This interdendritic eutectic solidification is observed in high-alloyed steels and its constitution varies according to initial element composition in the melting pool [123]. In the present study the interdendritic region exhibits a eutectic structure, and ledeburite can be observed in case of more carbon dissolved into the bulk, such as carburizing process of cast iron [66].

Delta ferrite is found to be surrounded by austenite in EBSD images (Figure 4-8 (c) and (g)) at 20 kJ/m with the double laser configuration. Delta ferrite appears widely in stainless steel welds and the content increases with the cooling rate due to the incomplete transformation  $\delta \rightarrow \gamma$  [116]. By using the Schaeffler diagram [124] and taking the carbon content in the FZ approximately as 0.4% in Figure 11, the equivalent of chromium ( $Cr_{eq}$ ) and nickel ( $Ni_{eq}$ ) can be calculated as the Equation 4-1 and 4-2.

$$Cr_{eq} = \%Cr + \%Mo + 1.5*\%Si + 0.5*\%Nb = 19.15\% \quad 4-1$$

$$Ni_{eq} = \%Ni + 30*\%C + 0.5*\%Mn = 12.39\% \quad 4-2$$

The  $Cr_{eq}/Ni_{eq}$  in this zone is around 1.5, which indicates that less than 5%  $\delta$  ferrite will present in the carburized zone. Even though  $\delta$  ferrite can reduce the microcracking and fracture during solidification, it can cause brittleness with long exposure in 300°C – 500°C (the so-called 475°C brittleness) [116]. A structure similar to that of a duplex stainless steel appears in the FZ, which could be controlled more accurately by optimizing the experimental parameters. For other LC

conditions, because the carbon content is even higher, the value of  $Cr_{eq}/Ni_{eq}$  is less than 1.3, thus the FZ is almost entirely austenitic [116].

Laser carburization process has an important hardening effect on chosen ferritic stainless steel according to the Ys and UTS results in Table 4-1. The authors' former result [95] finds that laser process without added graphite increases the microhardness at most by 90%. With graphite coating, the microhardness is improved to 450 Hv in dendritic microstructure and 380 Hv in cellular microstructure, which is 180% and 137% more than the as-received material. The most enhanced  $\sigma_{0.2\%}$  and UTS are found when the bulk is entirely carburized and composed mostly by cellular grains with an increase of 90% and 85% respectively. Both secondary phase strengthening and grain refining contribute to this improvement [90]. More strengthening carbides are formed in dendrite-dominated structure at lower LED and the higher cooling rate leads to more refined grains [119], which explain the difference in enhancement levels. At the same time, the ductility is seriously worsened due to strengthening phases. As the hard surface is advantageous to increase the fatigue life and wear resistance [66], laser carburization can be a potential choice for strengthening the surface of ferritic stainless steel and extending the service life of structural parts.

#### 4.4 Corrugation reinforced materials by localized laser carburization

After microstructural and mechanical property characterization of fully carburized specimens under different laser parameters, double laser treatment at 100 W is chosen to fabricate architected materials. This parameter is adopted because it yields the highest YS and UTS, 667 MPa and 923 MPa respectively, which is 1.90 and 1.85 times of those of untreated material. For a given matrix, a higher YS of reinforcement may have more enhancing effect on necking strain with a corrugated geometry compared to a straight one [6]. It may encourage the unbending of corrugation before stretch. In this part, untreated AISI 430 and laser carburized parts are taken as matrix and reinforcements. Architected materials with geometries in Table 2-6 are fabricated. The period of sinusoidal corrugations is fixed at 15 mm and corrugation height varies from 0 (straight reinforcement) to 1.5 mm. The gauge part width is reduced from 10 mm to 5 mm in this part of study and each reinforcement represents 20% of the volume in the gauge part.

##### 4.4.1 Identification of matrix and reinforcement mechanical properties

Table 4-2 Mechanical properties of matrix and reinforcement in FEM simulation.

	Matrix (untreated)	Reinforcement (treated)
Young's modulus (GPa)		210
Poisson ratio		0.3
Yield strength (MPa)	280	600
Hardening coefficient K (MPa)	711	2551

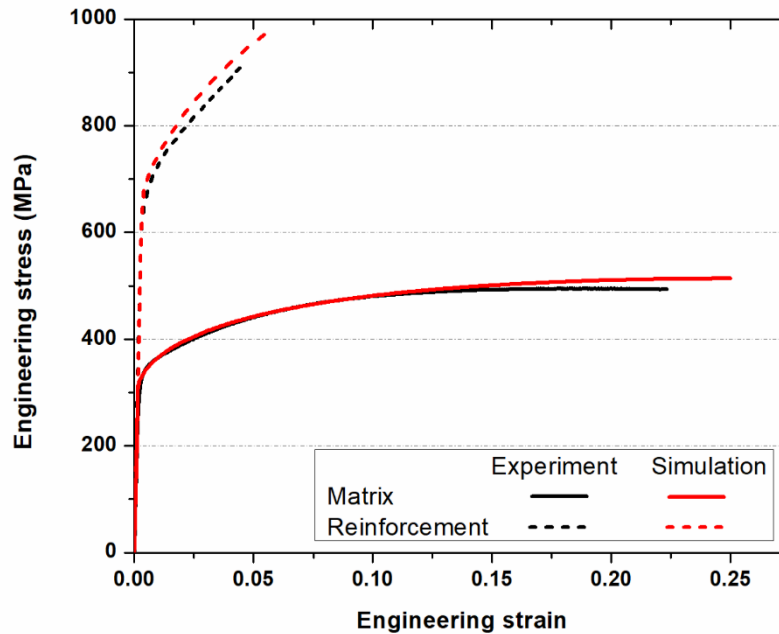


Figure 4-17 Engineering stress-strain behavior of matrix and reinforcement.

Mechanical property parameters of matrix and reinforcement are identified based on the results in Section 4.3.4. Beyond the plasticity onset, Ludwik's strain hardening law is adopted as the same in Section 3.5.1. Parameters in Table 4-2 are adopted for FEM simulation. Matrix parameters are deduced from stress-strain behavior of as-received AISI 430 sheets as in Section 3.5.1, those of reinforcement are decided from fully carburized specimen at 100 W from both sides. Experimental and numerical stress-strain behaviors of matrix and reinforcement are compared in Figure 4-17. Compared to Table 3-2 and Figure 3-16 in Section 3.5.1 which describe mechanical properties of laser hardened AISI 430 as reinforcement, laser carburized reinforcement has higher YS and work hardening rate but lower necking strain. Following FEM simulation results on tensile behaviors of isolated corrugations and architected materials are based on these parameters.

#### 4.4.2 Prediction of isolated straight and corrugated reinforcement

Isolated straight and corrugated reinforcements are hard to be machined due to their small size and fragility. Their stress-strain behavior is predicted by FEM simulation in Figure 4-18 (a) and work hardening evolution in (b) with a period of 15 mm and corrugation heights from 0 (straight reinforcement) to 1.5 mm. Similar to what is explained in Section 3.5.2, for the straight reinforcement, stress increases fast with increasing elastic strain at the beginning and then the increase slows down with the plastic strain. Work hardening rate continues to decrease with increasing strain. For corrugated reinforcements, stress increases slowly with increasing strain due to the unbending process. Once the unbending is completed, stress growth accelerates, which results in a boost in work hardening. With a given period (15 mm in this study), larger corrugation height (H) leads to a higher and more delayed boost in work

hardening, which enhances more the average strain of reinforcement. This part of the study aims to take advantage of this boost to delay the necking strain of architected materials with a corrugated reinforcement compared to a straight one.

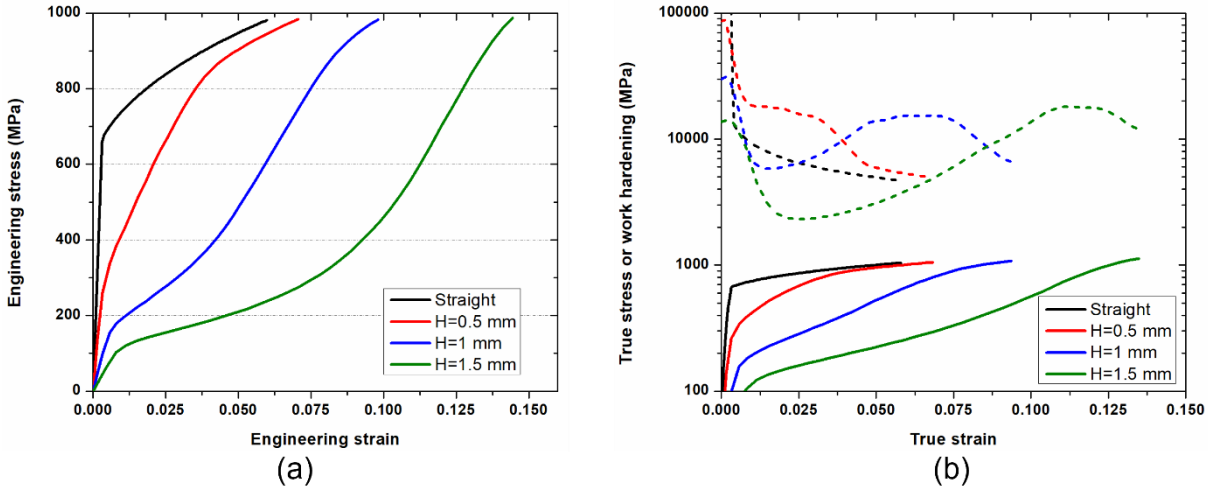


Figure 4-18 (a) Engineering stress-strain behavior of isolated straight and corrugated reinforcement, (b) work hardening rate and true stress-strain of isolated reinforcement.

Figure 4-19 depicts the local stress and strain map development in tensile direction with the evolution of total strain from 0 to 0.1 for a 1-mm-high isolated corrugation. The progression is similar to Figure 3-18, except that the inclination ratio  $H/P$  is much lower, the unbending is completed when the total strain attains around 0.08. the highest strain and stress are found at the inner side of each corrugation peak and trough. In this study, the boosts in work hardening introduced by corrugation unbending are accomplished before a total strain of 0.125 due to the low ratio  $H/P$ . And the configurations contain only one reinforcement in each specimen. This early unbending and single configuration may resolve the problem of early fracture led by too deformed matrix, which leads to an uncompleted unbending and the absence of boosts, in Section 3.5.

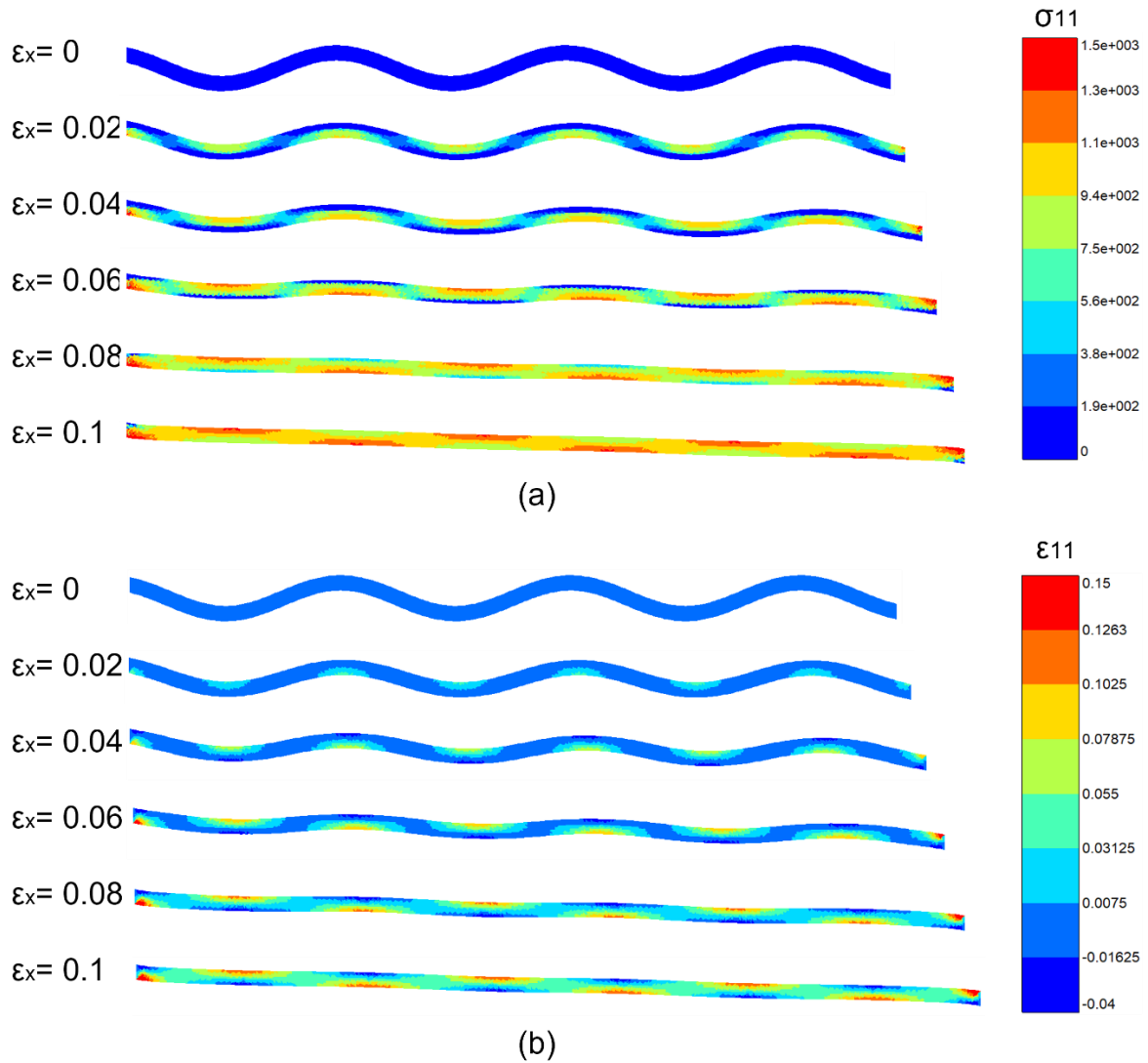


Figure 4-19 (a) Stress and (b) strain map of a 1-mm-high isolated corrugation in the tensile direction at different total strain by FEM simulation.

#### 4.4.3 Tensile test results of architected materials and discussion

Experimental stress-strain behaviors of straight and corrugation reinforcement specimens are shown in Figure 4-20 (a) and work hardening evolutions are shown in (b). UTS of reinforced specimens are improved by about 100 MPa compared to untreated material (around 500 MPa), which implies all geometries are efficient to reinforce the matrix. But the necking strain is reduced to less than 7% due to the brittle carburized reinforcement. Corrugation reinforcement heights seem to have a slight influence on necking strain. The specimen with straight reinforcement has the smallest necking strain and an increasing in corrugation height leads to an improvement in necking strain. Larger corrugation heights can also delay slightly the decrease of work hardening rate due to a higher boost introduced by unbending process as shown in Figure 4-18 (b). But it has to be mentioned that laser carburized reinforcements have

such a poor ductility that the enhancing effect on necking strain is not very convincing and results are not very reproducible.

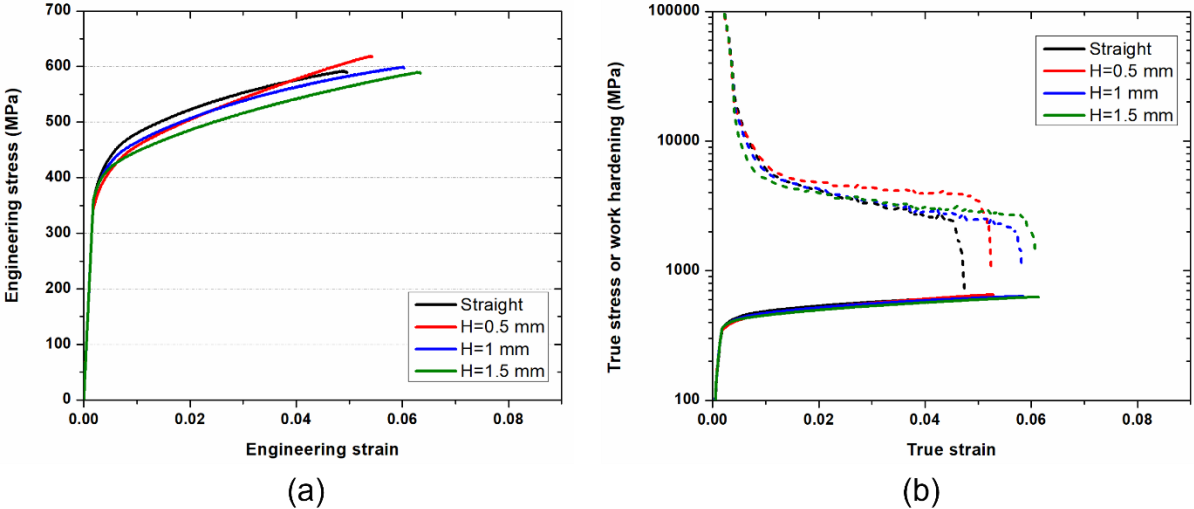


Figure 4-20 Experimental (a) engineering stress-strain behavior and (b) true stress and work hardening rate evolution of straight and corrugation reinforced specimens with different corrugation heights.

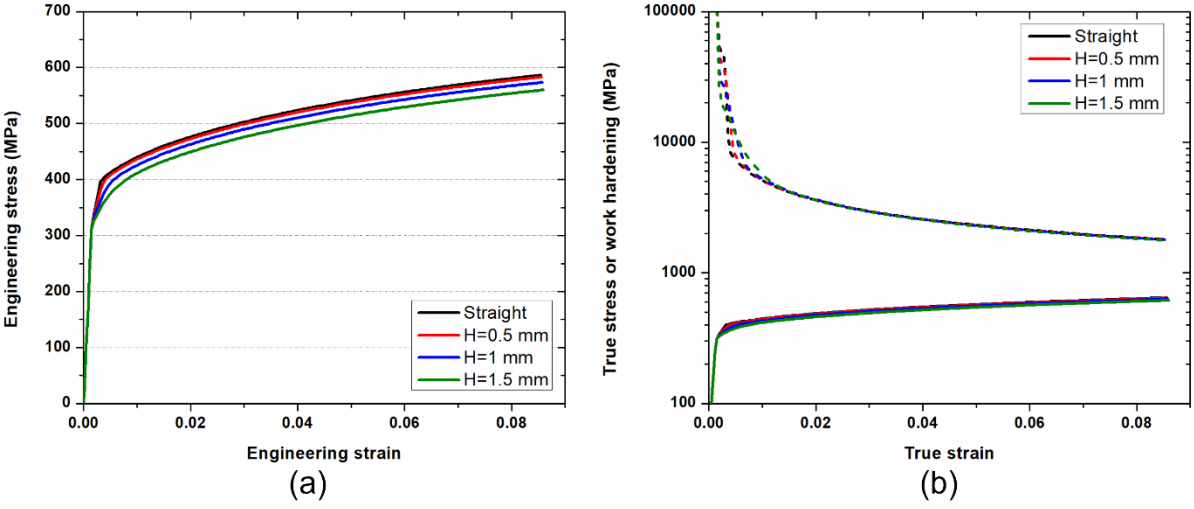


Figure 4-21 FEM simulation (a) engineering stress-strain behavior and (b) true stress and work hardening rate evolution of straight and corrugation reinforced specimens with different corrugation heights.

Figure 4-21 (a) and (b) depict the FEM simulation results of stress-strain behavior and work hardening evolution of the same geometries. It can be observed that a higher corrugation reinforcement height results in a lower YS but has little effect on necking strain. Similarly, the effect of corrugation height on work hardening reducing rate is not visible. The problem of too deformed matrix is resolved in this part by placing only one reinforcement on each specimen. According to Figure 4-18 (b), the corresponding total strains of the work hardening boosts are less than the necking strain of the matrix. Thus, this inefficiency of enhancement effect may be

resulted from the insufficient boosts in work hardening rate of corrugation reinforcements, which is not enough to delay that of the whole specimen. This corresponds also to the YS threshold value to yield an enhancement effect on necking strain proposed by Fraser [6]. More important boosts in work hardening rate during tensile test are needed to compensate the continuous work hardening rate reducing of the matrix.

Even though the macroscopic stress-strain behaviors do not show any enhancing effect of corrugated reinforcements compared to the straight one, it is still interesting to analyze the evolution of local strain map progression at different values of total strain in the tensile direction. Figure 4-22 and 4-23 is the progression of strain maps at different levels of overall tensile strain generated by DIC results and FEM simulation of a specimen with straight reinforcement and another one reinforced by a 1-mm-high corrugation. Experimental results are relatively in accord with numerical ones, which validates the adaptation of hardening model for the matrix and reinforcement.

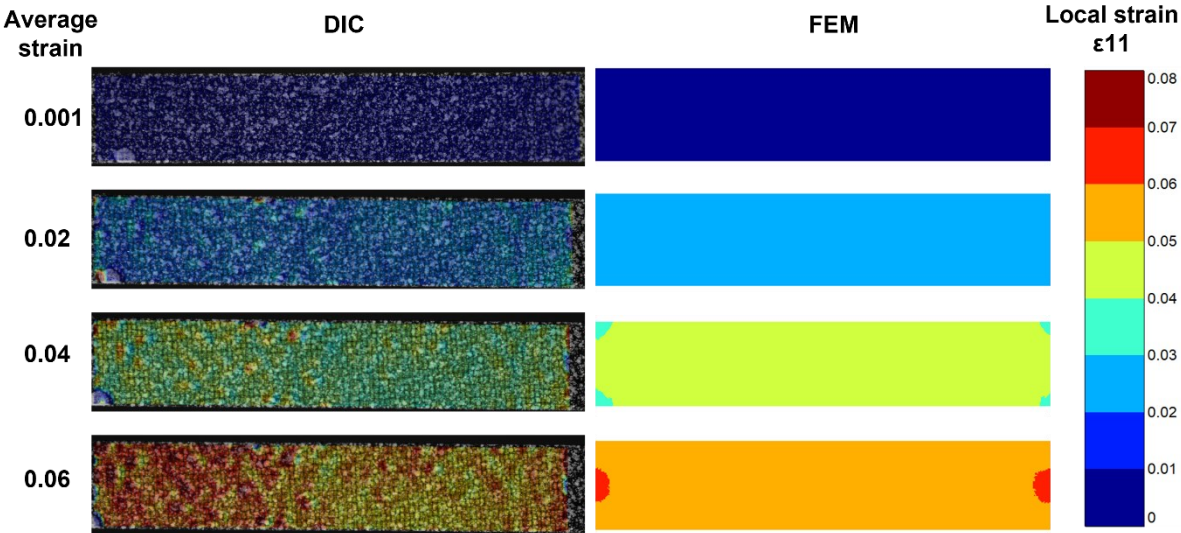


Figure 4-22 DIC results and FEM simulation of local strain evolution during tensile test of specimen with one straight reinforcement.

Below the YS ( $\epsilon_x=0.001$ ), straight and corrugation reinforced specimens both have homogeneous strain maps because the matrix and the reinforcement have the same Young's modulus. Beyond YS, straight reinforced specimen always presents a homogeneous strain map until the necking onset, where the strain concentration happens. But the corrugation reinforced specimen has a heterogeneous strain map after plasticity onset. The matrix is more deformed than the reinforcement and the difference is more pronounced with the increase of total strain in the tensile direction. The most and least deformed parts are found respectively within the matrix underneath and above each corrugation peak by the effect of additional tensile and compressive strain introduced by reinforcement unbending. This additional effect is introduced in Section 3.5.3. For the reinforcement, the inner side of each peak is more deformed than the outer side due to the unbending process and continuity with the matrix. The segments which connect two adjacent peaks present very little strain as they are more turned to change the

direction to align the tensile direction instead of being stretched. The average strain of matrix is at least three times of that of the reinforcement.

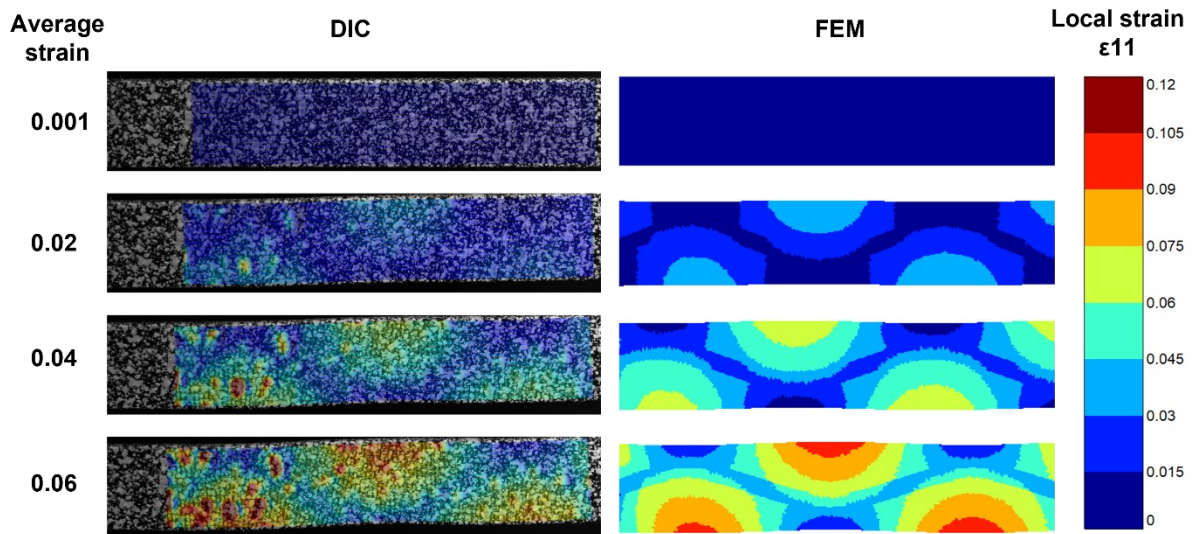


Figure 4-23 DIC results and FEM simulation of local strain evolution during tensile test of specimen with corrugation height of 1 mm.

Figure 4-24 shows the strain maps of straight and corrugation reinforced specimens at different total strain in the tensile direction under the same measuring scale. At the same total strain, the local strain distribution is more heterogeneous when the corrugation height is larger. The increasing corrugation height leads to larger strain in the ductile matrix than the average value, while the brittle reinforcement is less deformed. Smaller corrugation height (straight and  $H=0.5$  mm) results in a more homogeneous strain map, where the strains of matrix and reinforcement are closer to the total strain. As the reinforcement has a very limited ductility (elongation around 3.5%), specimens reinforced by straight line and corrugation of 0.5 mm height have already attained the fracture at a total strain value of 0.06, but the other two specimens can still continue the unbending process of corrugations. The final fracture of all specimens begins by the brittle fracture of reinforcements, so in order to realize the enhancement effect introduced by corrugations, the key point is to reduce the reinforcement strain.

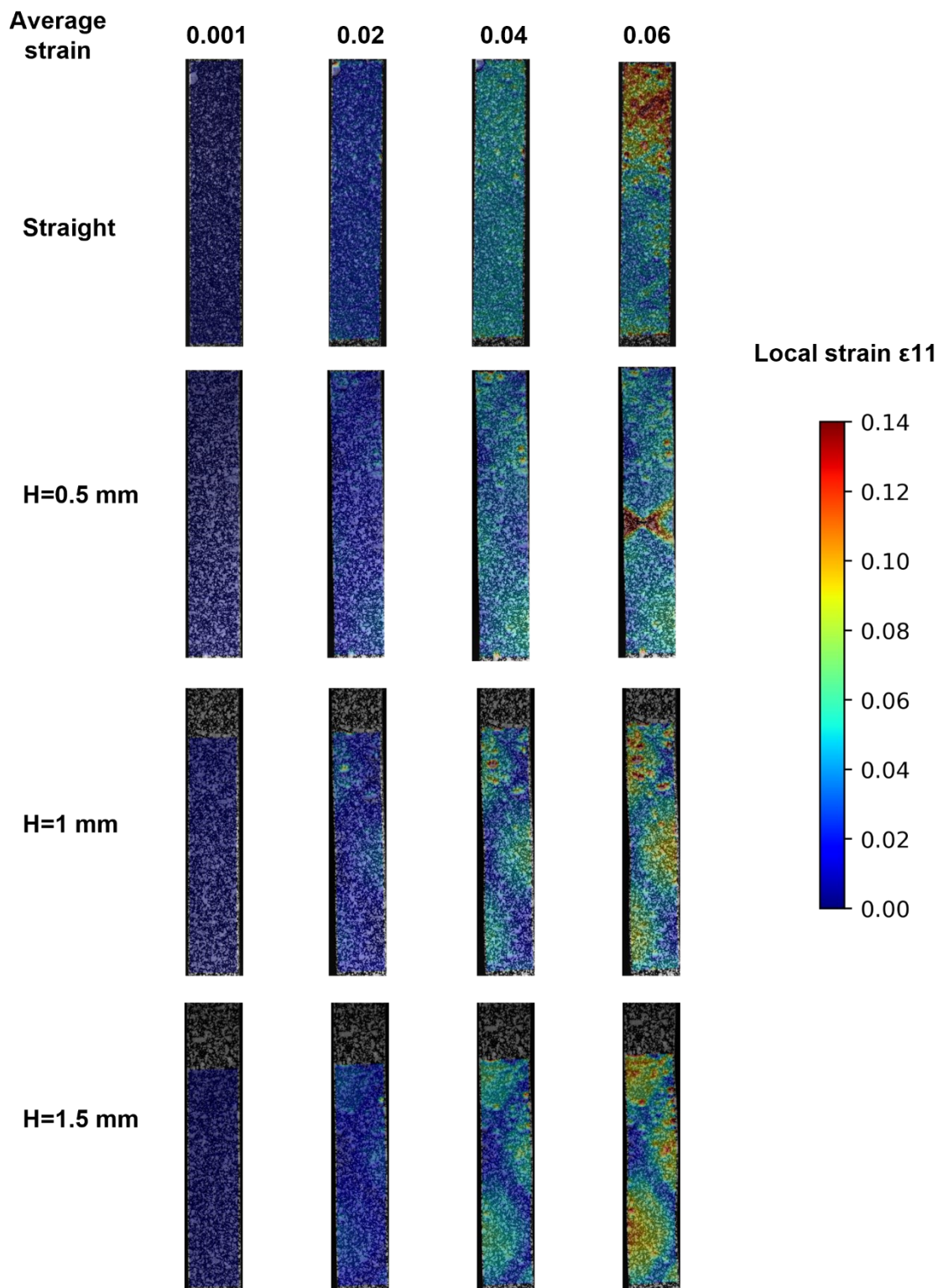


Figure 4-24 Strain maps of specimens with straight and corrugated reinforcements at different values of total strain in tensile direction.

#### 4.4.4 Future improvements

In spite of heterogeneous strain maps and satisfying agreement between DIC results and FEM simulations, the macroscopic stress-strain behavior show little enhancement effect on necking strain induced by corrugation reinforcements. And the expected benefit effect on work hardening induced by geometry is not visible.

One of the possible reasons may be the insufficient boost in work hardening rate evolution of corrugation unbending, which cannot compensate the continuously decreasing work hardening rate of matrix. Reinforcements with a higher YS and UTS and a larger contrast in strength between the matrix and the reinforcement may be a solution for this problem. But the YS of the chosen material, AISI 430 FSS, can hardly be further improved with given experimental condition. Direct laser carburization has achieved a YS and UTS about twofold of those of the untreated material. New combinations of matrix and reinforcement induced by laser treatment should be considered to achieve a larger contrast in strength between them.

Another possibility is to increase slightly the volume percentage of reinforcements to emphasize the boosts in work hardening rate. In this case, laser spot size needs to be enlarged and LED and peak temperature should be adapted.

#### 4.5 Conclusions

In the first part of this chapter, AISI 430 ferritic stainless steel sheets with graphite coating are carburized by direct laser irradiation. Microstructural and mechanical properties are investigated to evaluate the strengthening effect of carburization. Some conclusions emerge as follows.

- (1) Direct laser irradiation on graphite coating is efficient to carburize the substrate ferritic stainless steel within several hundred-micron depth. The least carbon content in the carburized region is around 0.4% compared to 0.026% in the as-received material; the shallower the carburized region, the higher the carbon content.
- (2) The morphology of carburized zone depends on the ratio of temperature gradient and solidification rate caused by different LED. At lower LED, it exhibits mostly austenitic dendrites and eutectic interdendritic structure. At higher LED, cellular austenitic grains are formed with discrete carbides inside and at grain boundaries. Double laser treatment with suitable LED can lead to a uniformly carburized zone through the whole thickness.
- (3) As-received material is remarkably strengthened by laser carburization process. Microhardness is improved to 469 Hv and 380 Hv respectively for dendritic microstructure and cellular microstructure compared to 160 Hv of as-received material. The YS and UTS is increased by 90% and 85% at most. This improvement could be applied to strengthen the ferritic stainless steel parts' surface in order to increase fatigue and wear resistance.
- (4) At higher LED, a small quantity of delta ferrite is found among austenitic grains due to the rapid cooling and suitable  $Cr_{eq}/Ni_{eq}$  value, which creates a duplex region. The formation of  $\delta$

ferrite could be better controlled by adjusting the experimental parameters to achieve a desirable percentage.

In the second part of this chapter, the laser carburization parameter which leads to the highest strength was adopted to fabricate architected materials reinforced by straight line and corrugations of the same volume. Different corrugation heights were tested and the mechanical properties of architected materials are evaluated. Some conclusions are issued from this study.

(1) Straight and corrugated carburized reinforcement can increase YS and UTS of architected specimens by around 100MPa compared to untreated material with a significant loss in ductility.

(2) Unfortunately, very limited enhancement effect on necking strain induced by corrugated geometries is observed compared to the straight one. Specimens of larger corrugation heights (1 mm and 1.5 mm) have a slight advantage in necking strain compared to straight one and 0.5-mm-high corrugation. This is due to insufficient boost in work hardening of corrugations.

(3) Straight reinforced specimens present a homogeneous strain field during uniaxial tensile test, but corrugation reinforced specimens have a heterogeneous strain field. A larger corrugation inclination H/P ratio results in a more heterogeneous strain map. The fracture of all specimens initiates from the brittle fracture of reinforcements.

# **Chapter 5 Corrugation reinforced architected materials by direct laser hardening on annealed carbon steel**

## Résumé

Comme ce qui est introduit dans la revue de la littérature, la ferrite et la martensite sont deux phases qui présentent une grande différence de propriétés mécaniques. La ferrite est douce et ductile, et la martensite est très dure mais fragile. L'acier entièrement ferritique et l'acier entièrement martensitique peuvent présenter une différence en YS de plus de 1000 MPa, ce qui en fait la matrice et le renforcement idéaux. Dans ce chapitre, un acier martensitique (MS1500) a été chauffé au-dessus d'Ac3 à 850 °C pendant une heure pour une entière austénitisation, puis refroidi à température ambiante dans le four éteint afin de former une microstructure de ferrite-perlite. Cet acier recuit est prêt à être la matrice des matériaux architecturés et susceptible de générer un renforcement très dur après un traitement laser. La microstructure et les propriétés mécaniques de l'acier recuit et des éprouvettes trempées au laser sont étudiées. Des matériaux architecturés renforcés par lignes droites et ondulées ont été fabriqués et leur comportement en traction a été prédit par simulation FEM et caractérisé par DIC. L'effet des paramètres géométriques, la hauteur d'ondulation H et la période P, est étudié. L'effet d'amélioration sur la ductilité induit par renforcements ondulés est étudié par FEM sur une large gamme de paramètres géométriques différents, malgré le fait que certains modèles de renfort ne sont pas réalisables dans les conditions expérimentales de cette étude. Les résultats montrent que le traitement laser génère une interface assez forte entre la matrice et le renforcement et que aucune décohésion a été observée durant la traction. Une augmentation du rapport d'inclinaison d'ondulation H/P améliore la ductilité mais réduit YS et UTS. Cet effet bénéfique est dû à l'augmentation du taux de l'érouissage induite par le dépliage des ondulations. L'étude de simulation paramétrique montre que l'UTS et la ductilité dépendent de l'inclinaison de l'ondulation H/P. Les ondulations en tant qu'architecture pour renforcer les matériaux pourraient être un candidat de franchir des zones blanches dans la carte de matériau-propiété, en trouvant un compromis entre la résistance et la ductilité.

## 5.1 Introduction

The two previous chapters present the effect of direct laser hardening and carburization of AISI 430 FSS. Straight and corrugation reinforced architected materials are fabricated with untreated material as matrix and laser strengthened part as reinforcement. Even though DIC and FEM results show that matrix and reinforcement experience heterogeneous strain maps and the heterogeneity level increases with increasing corrugation inclination H/P, little macroscopic enhancing effect is observed on necking strain introduced by corrugation compared to straight reinforcement.

The lack of enhancing effect is due to insufficient boost in work hardening evolution of corrugation unbending during uniaxial tensile loading, which can be improved by increasing the difference in YS between matrix and reinforcement. Nevertheless, it is hard to achieve with the FSS with given experimental condition. New combinations of matrix and reinforcement are expected to bring more obvious architecture effect. The choice criteria for the matrix are that it can be hardened as much as possible by local laser treatment without too much side effect such as sharp interface or brittle intermetallic precipitations.

As what is introduced in the literature review, ferrite and martensite are two common phases of many carbon steels and they present a great difference in mechanical properties. Ferrite is soft and ductile, and martensite is very hard but fragile. Fully ferritic steel and fully martensitic steel may present a difference of more than 1000 MPa in YS, which makes them the ideal matrix and reinforcement. But conventional ferritic steels or other steels containing high percentage ferrite, e.g., DP600, do not have a high enough carbon content which allows a significant hardening effect after laser quenching. A carbon content around 0.2% is needed to achieve a hard martensitic phase. In this context, a martensitic steel (MS1500) is chosen to be fully austenized above  $A_{c3}$  at 850 °C for one hour and then cooled down in furnace to room temperature in order to form a ferrite-pearlite microstructure. This annealed steel is ready to be the matrix for architected materials and is potentially possible to generate a very hard reinforcement after localized laser hardening.

In this chapter, laser hardening on annealed steel is applied and the microstructure and mechanical properties of as-annealed material and laser hardened part are studied. Straight and corrugation reinforced architected materials are fabricated and their tensile behavior is predicted by FEM simulation and characterized by DIC. The effect of chosen geometric parameters, corrugation height H and period P, is investigated. The enhancing effect on necking strain of corrugated reinforcements is systematically studied by FEM simulation for a large range of different geometric parameters, including H, P, and reinforcing volume, in spite of the fact that certain reinforcement patterns are not realizable in the given experimental condition. This parametric study sets the future architecturation aim which is to be explored.

## 5.2 Results

### 5.2.1 Mechanical and microstructural characterization of the matrix and reinforcement

Figure 5-1 (a) is a micrograph of the laser hardened zone section, which consists of a fully martensitic zone, a transition zone and ferritic annealed material. In the fully martensitic zone, a small fusion zone is formed on the upper side due to the high energy density of fiber laser. Microhardness along the section center line (track 1 on Figure 5-1 (a)) is shown in Figure 5-1 (b). The average microhardness in fully martensitic zone is 420 Hv compared to 174 Hv of the annealed material. Between these two zones is the transition region, where decreasing the martensite percentage results in a reduced hardness. Figure 5-1 (c) presents the microhardness along the beam center marked as track 2 on Figure 5-1 (a). Besides the smaller values (380 Hv) near both surfaces due to the decarburization during annealing process in the furnace, the hardness is rather stable through the thickness (440 Hv).

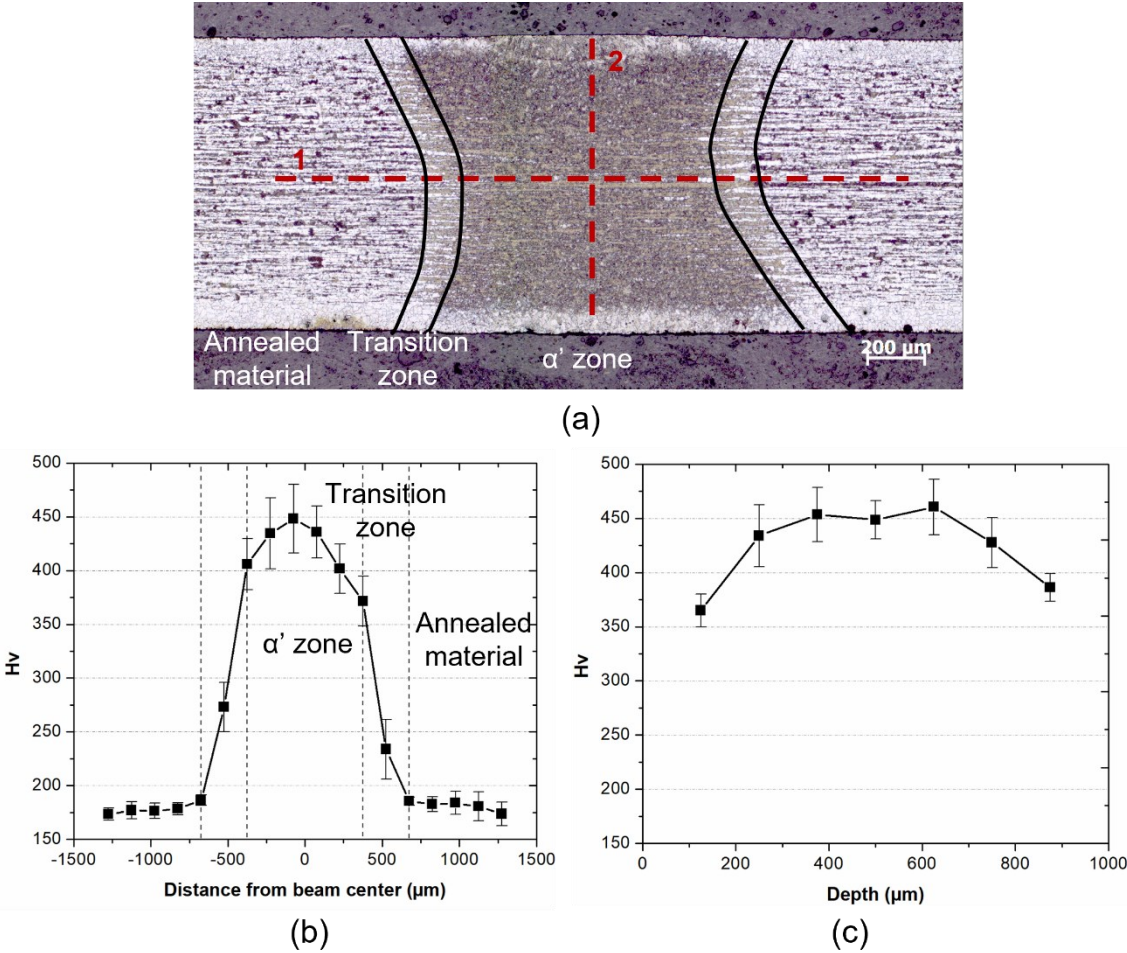


Figure 5-1 (a) Microscopy of the laser hardened zone, (b) microhardness along the center line (track 1), (c) microhardness in the sheet along the beam center (track 2).

Figure 5-2 (a) shows the EBSD image quality (IQ) map of the annealed material, transition region and martensitic zone from top to bottom, with ferrite and pearlite grains being light with high IQ and martensite being dark with low IQ. The annealed material contains mostly ferrite

and embedded pearlite where the excess carbon atoms are rejected during the equilibrium cooling in furnace (cf. Figure 5-2 (b)). In the transition zone, pearlite transforms into austenite when heated above Ac1 and martensite is formed upon cooling, but due to the insufficient temperature and lack of diffusion rate of carbon atom, the austenization is not complete. The transition zone consists of graded martensite, which is formed where pearlite islands were previously embedded, i.e. in ferrite grains (cf. Figure 5-2 (c)). In Figure 5-2 (d), the peak temperature is above Ac3, both ferrite and pearlite transform into austenite so that an almost fully martensitic zone is formed with only a small quantity of ferrite left. This graded microstructure results in the hardness gradient in Figure 5-1 (b) and provides a clear contrast in strength between the matrix and reinforcement for the architected material in this study.

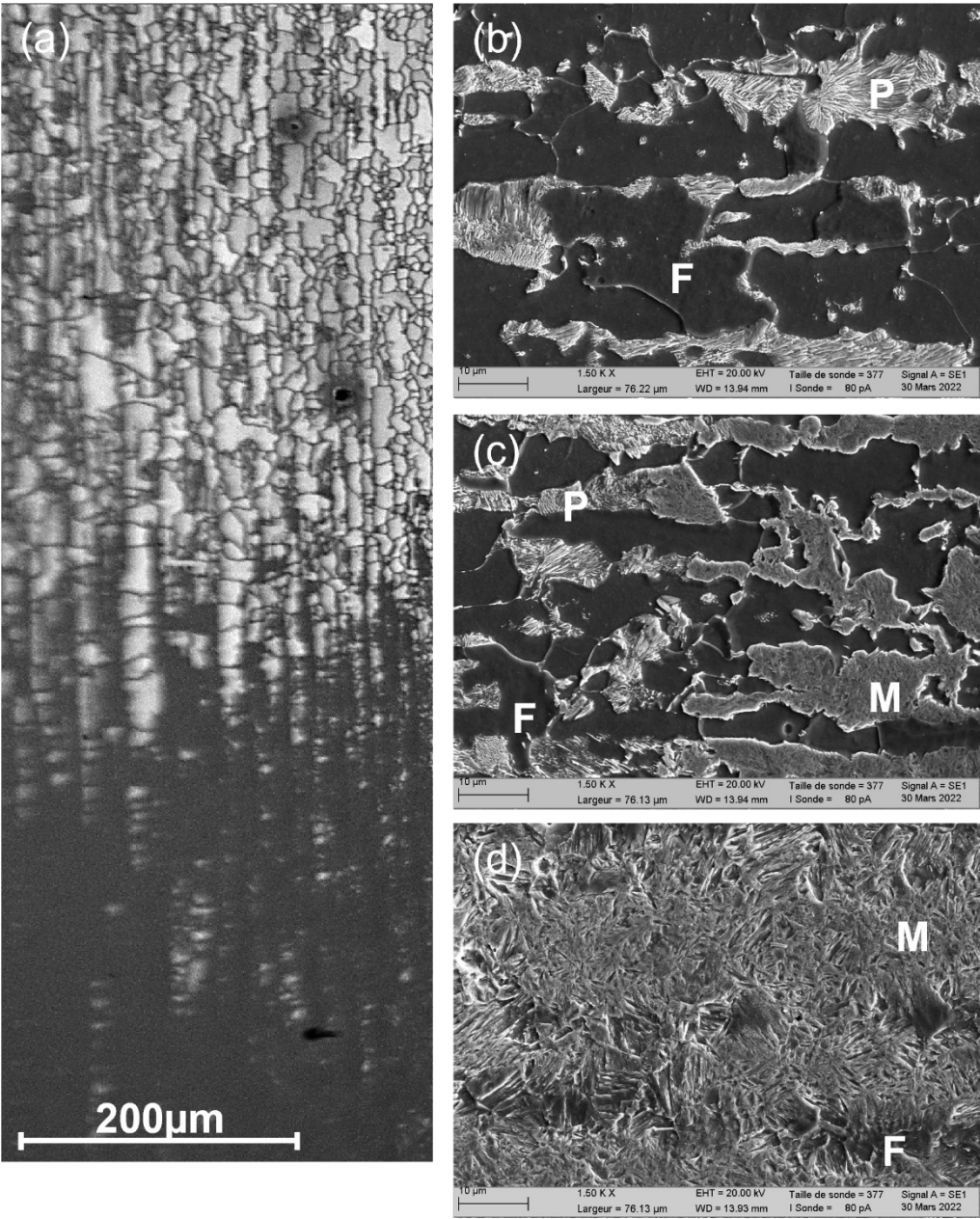


Figure 5-2 (a) Image quality (IQ) of the cross section from annealed material to martensitic zone, microstructure of (b)annealed material, (c) transition zone, (d) martensitic zone.

**5.2.2 Identification of matrix and reinforcement mechanical properties for FEM simulation**

Table 5-1 indicates the material parameters of matrix and reinforcement used in simulations. Beyond the yield strength, plasticity of both matrix and reinforcement is assumed to follow the Hollomon strain hardening model in Equation 5-1, where K and n are respectively the hardening coefficient and strain hardening exponent. Matrix parameters are identified on tensile test of annealed material and those of reinforcement are based on as-received martensitic steel. The behavior of both phases is assumed to be elastically and plastically isotropic.

$$\sigma = K\varepsilon^n \tag{5-1}$$

Table 5-1 Matrix and reinforcement parameters in FEM simulation.

	Matrix (ferritic steel with pearlite)	Reinforcement (martensitic steel)
Young’s modulus (GPa)	210	210
Poisson’s ratio	0.3	0.3
Yield strength (MPa)	280	1300
Hardening exponent, n	0.24	0.06
Hardening coefficient, K (MPa)	986	1966

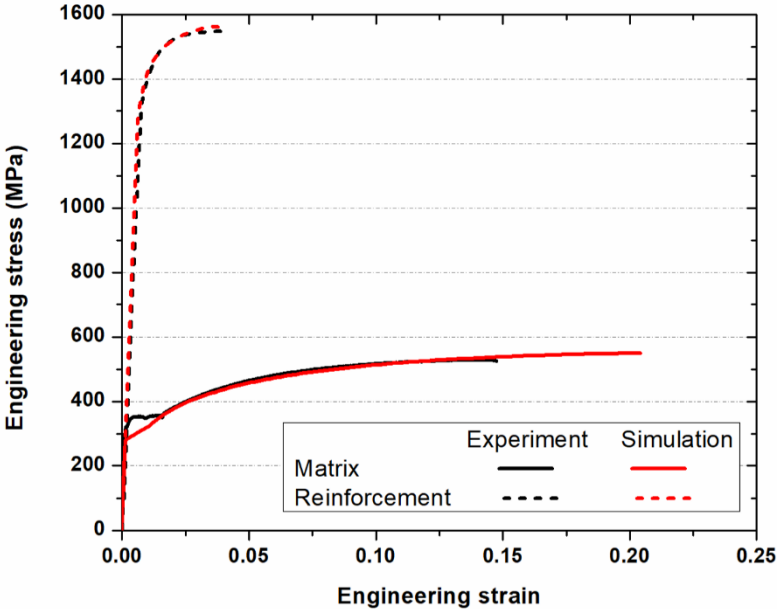


Figure 5-3 Engineering stress-strain behavior of annealed steel matrix and martensitic steel reinforcement.

Figure 5-3 depicts the experimental tensile behavior of matrix and reinforcement and the results obtained by FEM simulation. Except the fact that the YS of matrix is about 40 MPa lower than experimental results because of Piobert-Lüders band appearance at the beginning of

plasticity, FEM simulation corresponds well on stress-strain behavior of both matrix and reinforcement. In the following parts, tensile behavior prediction of architected materials is based on these parameters.

### 5.2.3 Prediction of isolated straight and corrugated reinforcement mechanical properties

Figure 5-4 depicts the tensile behavior of isolated straight and corrugated reinforcements simulated by FEM. (a) and (c) are respectively engineering stress-strain responses of straight and corrugations with fixed period and fixed height, and (b) and (d) are their work hardening evolutions and true stress-strain behaviors. Similar to relative sections in the two precedent chapters, corrugations can increase the total fracture strain compared to straight line due to unbending, but the fracture stress is also reduced.

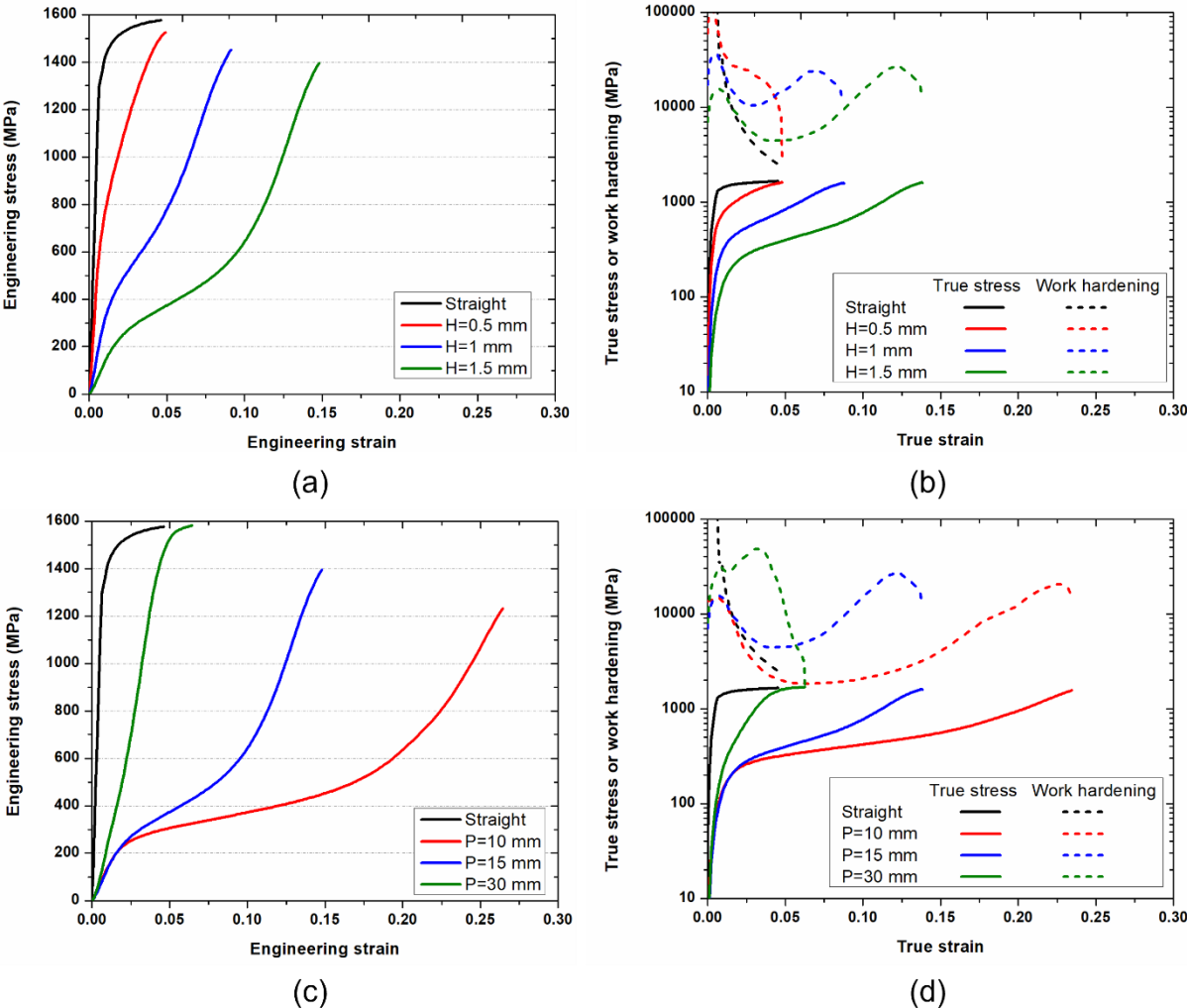


Figure 5-4 FEM simulation results of isolated reinforcements, (a) Engineering stress-strain behavior of straight and corrugations with different H and fixed P = 15 mm, (b) work hardening evolution of (a), (c) Engineering stress-strain behavior of straight and corrugations with different P and fixed H = 1.5 mm, (d) work hardening evolution of (c).

From (a) and (c), it can be inferred that these two geometric circumstances, increasing corrugation height with fixed period and reducing period with fixed corrugation height, have a similar effect. They both lead to a larger corrugation inclination,  $H/P$ , which results in a larger fracture strain and lower fracture stress, and a more delayed boost in work hardening rate. In this case, the mechanical parameters of reinforcement are based on a fully martensitic steel, whose  $Y_S$  is over 1300 MPa, thus the rebounds in work hardening are higher than those with carburized AISI 430 FSS in Chapter 4. This improvement may resolve the precedent problem of insufficient work hardening boost and yield an enhancing effect in necking strain for architected materials. The development of local stress and strain maps during unbending are similar to what are presented in Section 3.5.3 and 4.4.2 and will not be exposed in detail.

### 5.2.4 FEM simulation results of straight and corrugation reinforced specimens

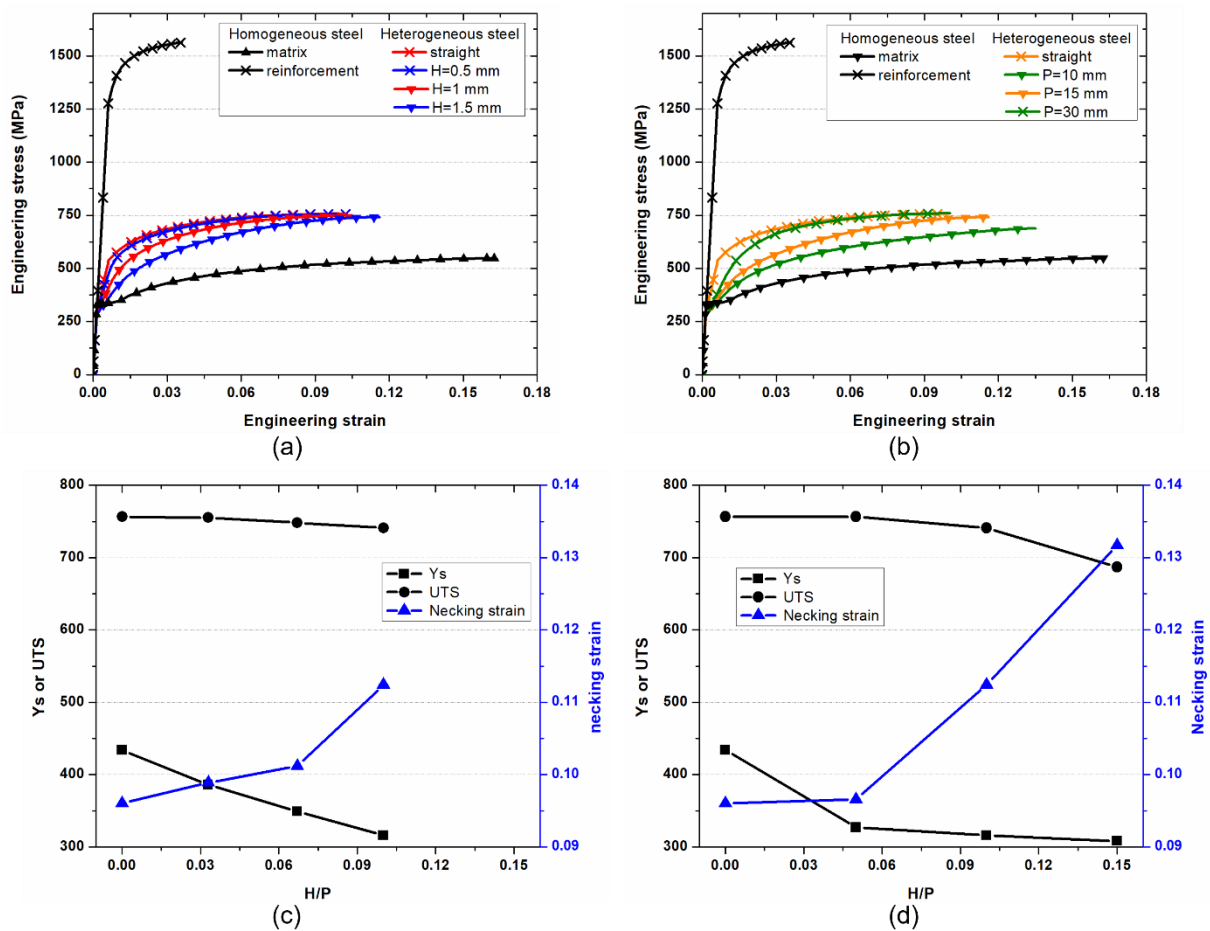


Figure 5-5 (a) Numerical stress-strain curve of matrix, reinforcement, and samples with  $P=15$  mm and different heights, (b) numerical stress-strain curve of matrix, reinforcement, and samples with  $H=1.5$  mm and different periods, (c) (d) variations of  $Y_S$ , UTS and necking strains of all samples in (a) (b).

Figures 5-5 (a) and 5(b) depict the stress-strain curves of architected steel samples with straight and corrugated reinforcements with fixed  $P=15$  mm and fixed  $H=1.5$  mm along with homogeneous matrix and reinforcement. All chosen patterns reinforce the soft matrix,

increasing YS and UTS, and enhancing the necking strain compared to the stronger but brittle martensitic steel. Focusing on heterogeneous reinforced samples, in Figure 5-5(a), the straight reinforced sample has a poorest necking strain and an increase in corrugation height results in a gain in necking strain but a loss in YS and UTS. In Figure 5-5 (b), a smaller period also favors the necking strain and reduce YS and UTS. Figures 5-5 (c) and (d) summarize the mechanical property evolutions according to the H/P ratio for both geometry strategies, i.e., given period or given height. Even though the changes in the two cases do not follow the exact same linear relation, increasing the value of H/P has a similar trend to enhance the necking strain, which accompanies a reduction in YS and UTS. The prediction of FEM simulation is to be verified by experiments in the following paragraphs.

### 5.2.5 Tensile test of architected samples

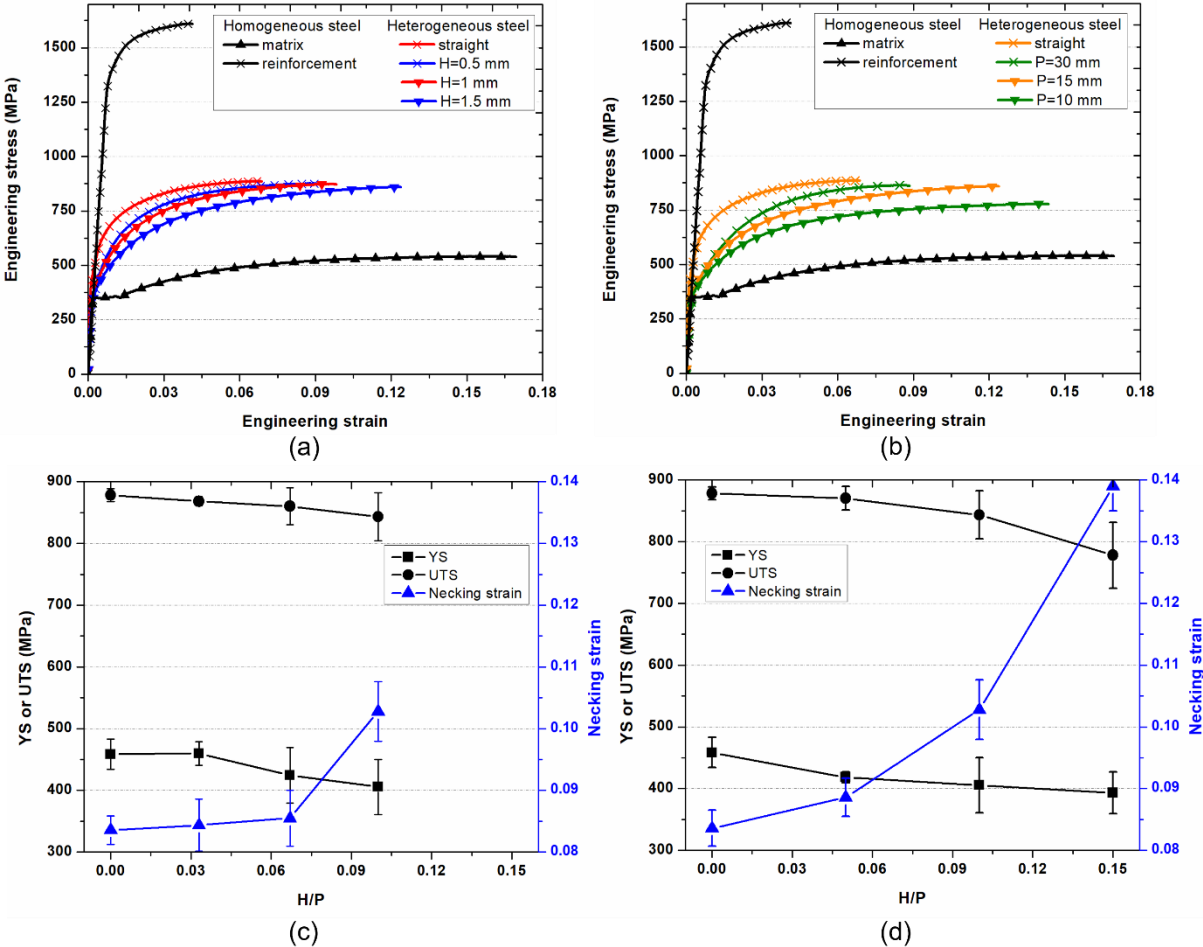


Figure 5-6 Experimental stress-strain curve of ferritic matrix and martensitic reinforcement with (a) architected samples with P=15 mm and different heights, (b) architected samples with h=1.5 mm and different periods, (c) (d) variations of YS, UTS and necking strains of all samples in (a) (b).

Figures 5-6 (a) and (b) show the experimental tensile test results for samples with the reinforcement patterns given in Table 2-7 along with the mechanical response of pure ferritic

matrix and pure martensitic reinforcement. Mechanical properties are summarized in Table 5-2. Homogeneous and heterogeneous samples have the same Young's modulus. All reinforcement geometries have a UTS above 750 MPa compared to 534 MPa of ferrite and a necking strain above 8% compared to 3.6% of martensite, which confirms the reinforcing effect of laser-induced architecture. The brittle reinforcement initiates the first crack with the strain increase and propagates to the matrix, which leads to the ultimate failure for all samples. No decohesion has taken place at the interface between the matrix and the reinforcement during the whole tensile tests, confirming that laser-quenching generated an interface that is strong enough for architecturing steel, contrary to other architected materials in which interfacial strength is commonly identified as a treat to mechanical performance and durability.

For each sample, the experimental YS and UTS are higher than corresponding numerical results. These discrepancies are caused by the hypothesis made in the FEM model of a perfect interface between matrix and reinforcement, without any transition zone. Nevertheless, while being relatively thin, the heat-affected zone between the laser-treated martensitic zone and ferritic matrix is observed experimentally (cf. Figure 5-1 (a)), and this partly reinforced zone leads to a higher strength compared to simulated results.

Despite this systematic gap between experimental and numerical results, similar trends are found while comparing results shown in Figure 5-5 (c-d) with Figure 5-6 (c-d). For a given period P (Samples 2, 3, 4), an increase corrugation height H leads to a gain in necking strain and a loss in YS and UTS. With the given corrugation height H (Samples 4, 5, 6), a reducing P gives the same trend. Comparing Sample 1 (H/P=0) and Sample 6 (H/P=0.15) as an example, the latter has a necking stain of 13.9% while that of the former is only 8.3%, which corresponds to an increase of 67%, but at the same time the loss in YS and UTS are respectively 14% and 11%. Experimental results confirm the prediction of FEM simulation that an appropriate increase in the H/P ratio can enhance the necking strain with a trade-off in YS and UTS.

Table 5-2 Mechanical properties of matrix, reinforcement and architected steels.

	H/P	YS (MPa)	UTS (MPa)	Necking strain
Matrix	- (homogeneous)	300±7	534±12	0.167±0.003
Reinforcement	- (homogeneous)	1388±16	1553±5	0.036±0.001
Sample 1	0 (straight)	458±24	878±10	0.083±0.004
Sample 2	0.033	456±19	868±7	0.085±0.004
Sample 3	0.067	424±45	860±30	0.086±0.005
Sample 4	0.1	405±44	843±39	0.103±0.005
Sample 5	0.05	418±8	870±18	0.089±0.003
Sample 6	0.15	393±33	778±53	0.139±0.004

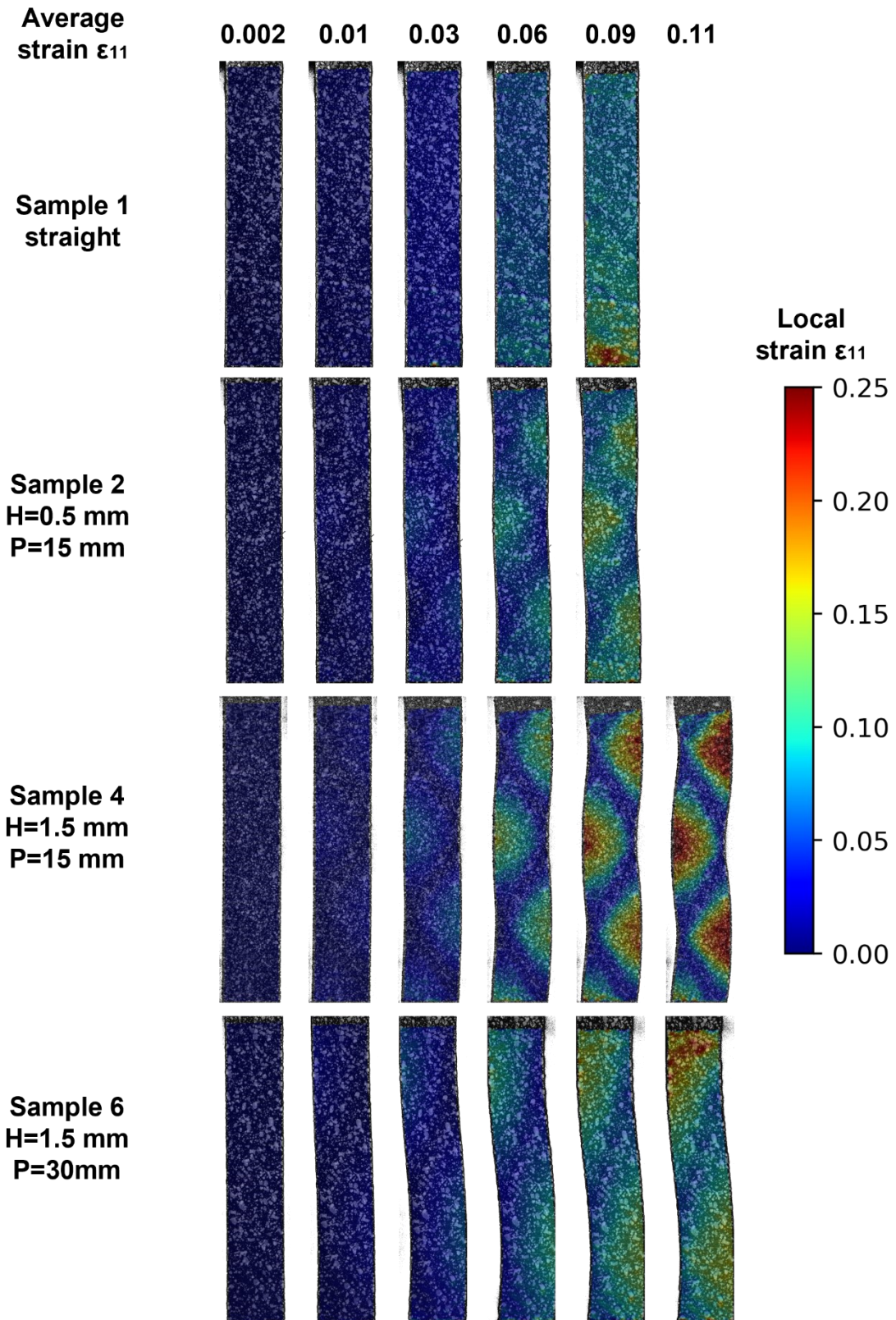


Figure 5-7 Strain field evolution during tensile tests on samples with different geometric patterns.

In order to understand the enhancing effect of corrugated reinforcements on necking strain, strain map evolutions on the gauge length are measured using DIC. Figure 5-7 illustrates the local strain field evolutions, here with the principal strain component  $\epsilon_{11}$  along the loading direction, of samples with different architecture patterns during tensile test. As the matrix and reinforcement have the same Young's modulus, the elastic response is homogeneous for all samples. For Sample 1, with a straight reinforcement, the strain is always homogeneous in both the matrix and reinforcement all over the gauge length, as expected from composite theory, until strain localization gives rise to necking. For corrugation reinforced samples, the strain field becomes heterogeneous as plasticity starts. The local strain level in ferrite is much more important than that of martensite. It is noteworthy that specimens with corrugated reinforcements become wavy during tensile tests because of heterogeneous deformation, the convex side is always opposite to the sinusoidal reinforcement.

Comparing Samples 2 and 4 at the same average total strain, it can be observed that an increase in corrugation height H for a given P results in a smaller strain level for martensite and larger for ferrite. The same influence on local strain can be found while comparing Samples 4 and 6 by reducing P with a given H. Corresponding FEM simulated strain maps for an overall strain of 0.09 are shown in Figure 5-8, which depicts a local strain distribution similar to experimental DIC results. A higher inclination of the reinforced corrugation, i.e., H/P ratio, leads to a localization of deformation in the matrix in place of the reinforcement. The higher the H/P ratio, the more heterogeneous the strain field is. Because of the martensitic reinforcement being very brittle with an elongation of only around 4%, its fracture is always the first step of the specimen final failure. Therefore, a smaller local strain of the reinforcements due to a higher H/P can enhance the necking strain of the whole sample.

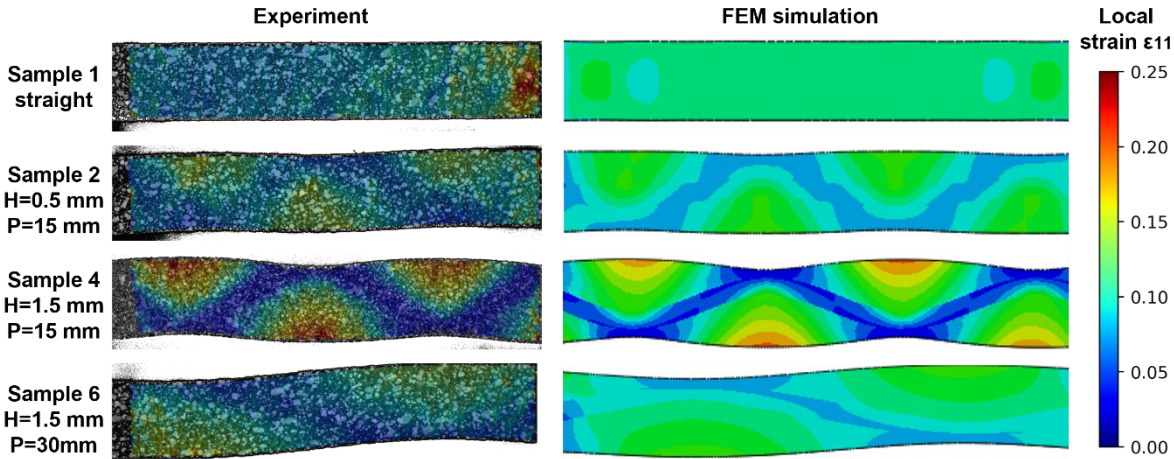


Figure 5-8 Experimental and FEM simulation strain maps of architected samples at a total strain of 0.09.

## 5.2.6 Fractography

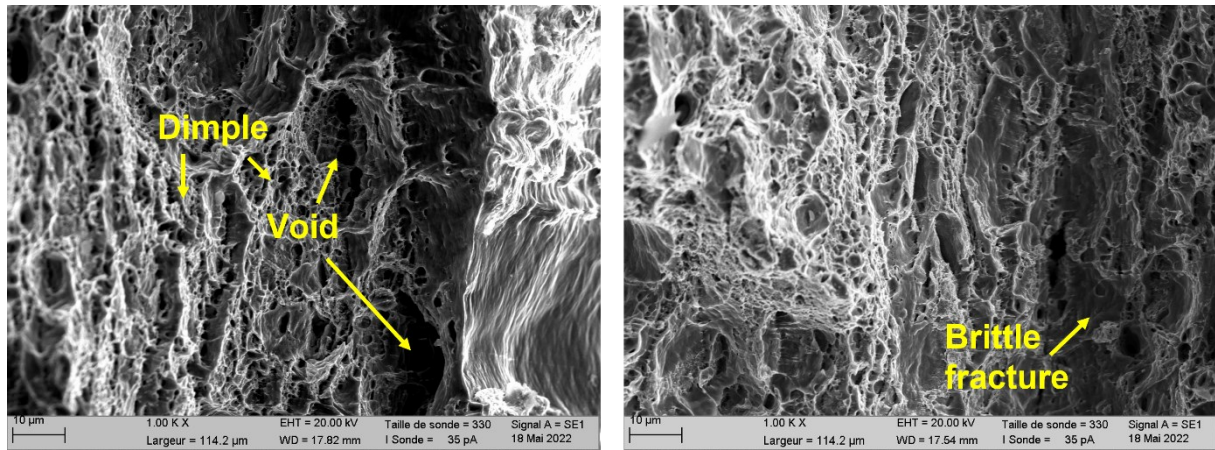


Figure 5-9 SEM micrograph obtained from the fracture surface of annealed steel matrix after tensile test.

Fracture surfaces of architected materials are examined by SEM after uniaxial tensile test. Figure 5-9 shows the fracture surface of the annealed steel matrix. The surface of matrix presents mostly a ductile fracture with numerous dimples and voids due to large percentage of ferrite grains. But some small local brittle fractures can be observed among the general ductile fracture, which is because of the presence of pearlite islands embedded in ferrite as shown in Figure 5-2 (b).

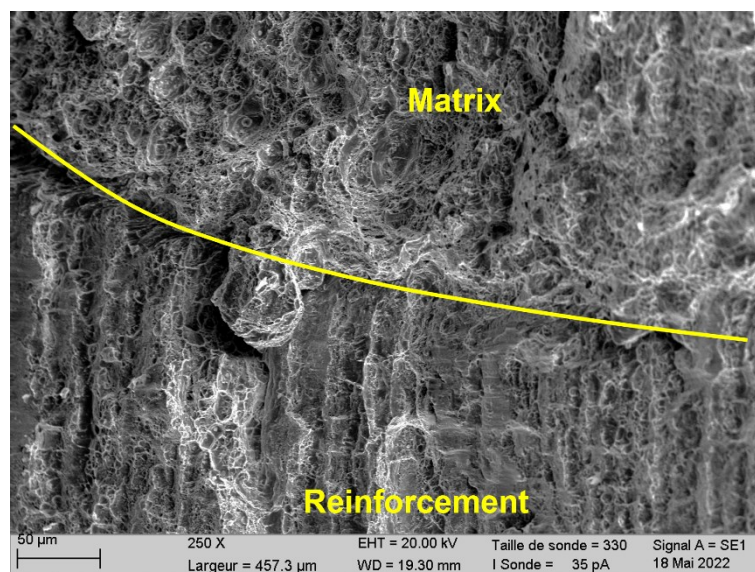


Figure 5-10 SEM micrograph obtained from fracture surface at the interface between matrix and reinforcement after tensile test.

Figure 5-10 shows the fracture at the interface between matrix and reinforcement after tensile test. The fracture of matrix and reinforcement presents quite different characteristics, and the interface is clear between them. The HAZ is not visible on the micrograph. The reinforcement consists of a mixture of brittle and ductile fracture. Figure 5-11 is a zoomed micrograph of the laser hardened reinforcement fracture surface. The brittle fracture is from the martensite phase

generated by quenching after laser treatment and the ductile fracture is from the ferrite phase which is not completely transformed into austenite during laser treatment. This fracture corresponds to the microstructure in Figure 5-2 (d).

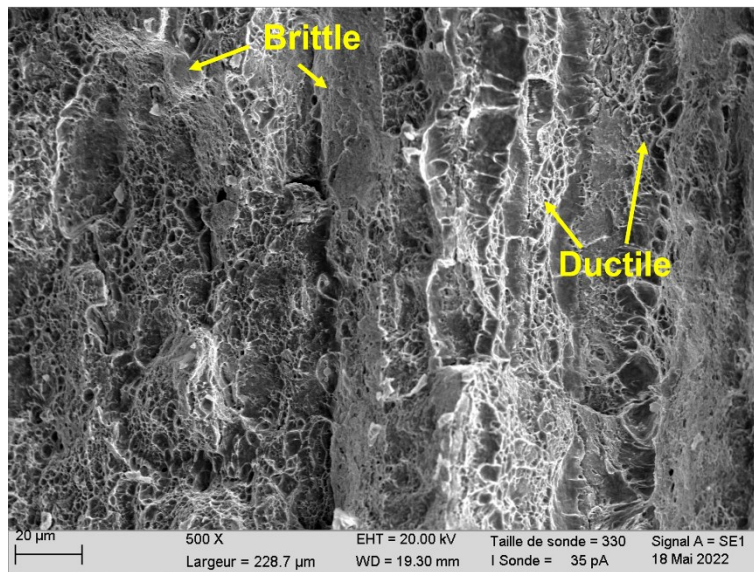


Figure 5-11 SEM micrograph obtained from the fracture surface of laser hardened reinforcement after tensile test.

## 5.3 Discussion

### 5.3.1 Effect of corrugated reinforcement on work hardening

FEM simulation results indicate that corrugated reinforcements in architected steel delay the necking strain compared to straight ones at the cost of a slight loss in YS and UTS. Experimental results shown in Figure 5-6 confirm this trade-off. During tensile test, the work hardening rate of the reinforcement decreases rapidly to intersect the true stress while that of the matrix decrease much more slowly after the onset of plasticity, as shown in Figure 5-12 (a). This intersection corresponds to the necking start point defined by the Considère criterion [91]. Figures 5-12 (b) and (c) show that the intersections of work hardening rates and true stresses for architected materials lie between matrix and reinforcement, and among them the straight reinforced sample has the lowest necking strain. For a given period (cf. Figure 5-12 (b)), a larger height induces a smaller hardening rate, thus yielding a gain in necking strain. For a given height (cf. Figure 5-12 (c)), a smaller period results in a similar effect. For both geometric parameters it can be concluded that a higher H/P ratio delays the intersection point of work hardening and true stress, i.e., the onset of necking.

This benefit on necking strain is due to the unbending process of the corrugation when loaded in tension. The configuration with corrugated reinforcement has a lower strength than straight reinforced configuration because the reinforcement is less aligned to the load direction [5]. During the uniaxial tensile test, the loading on fragments of corrugation can be divided into two perpendicular components. A component parallel to the fragment that accounts for its

stretching, and a perpendicular one responsible for unbending the fragment so that it becomes parallel with the longitudinal loading direction. The unbending process increases the strength of the whole sample with this change in reinforcement direction because the reinforcement is more and more aligned to the load direction. It increases the work hardening rate of the corrugated reinforcement and thus the global work hardening rate drop is delayed. This effect is due to the change in the geometry during tensile test, thus the term called geometrically induced work hardening [125].

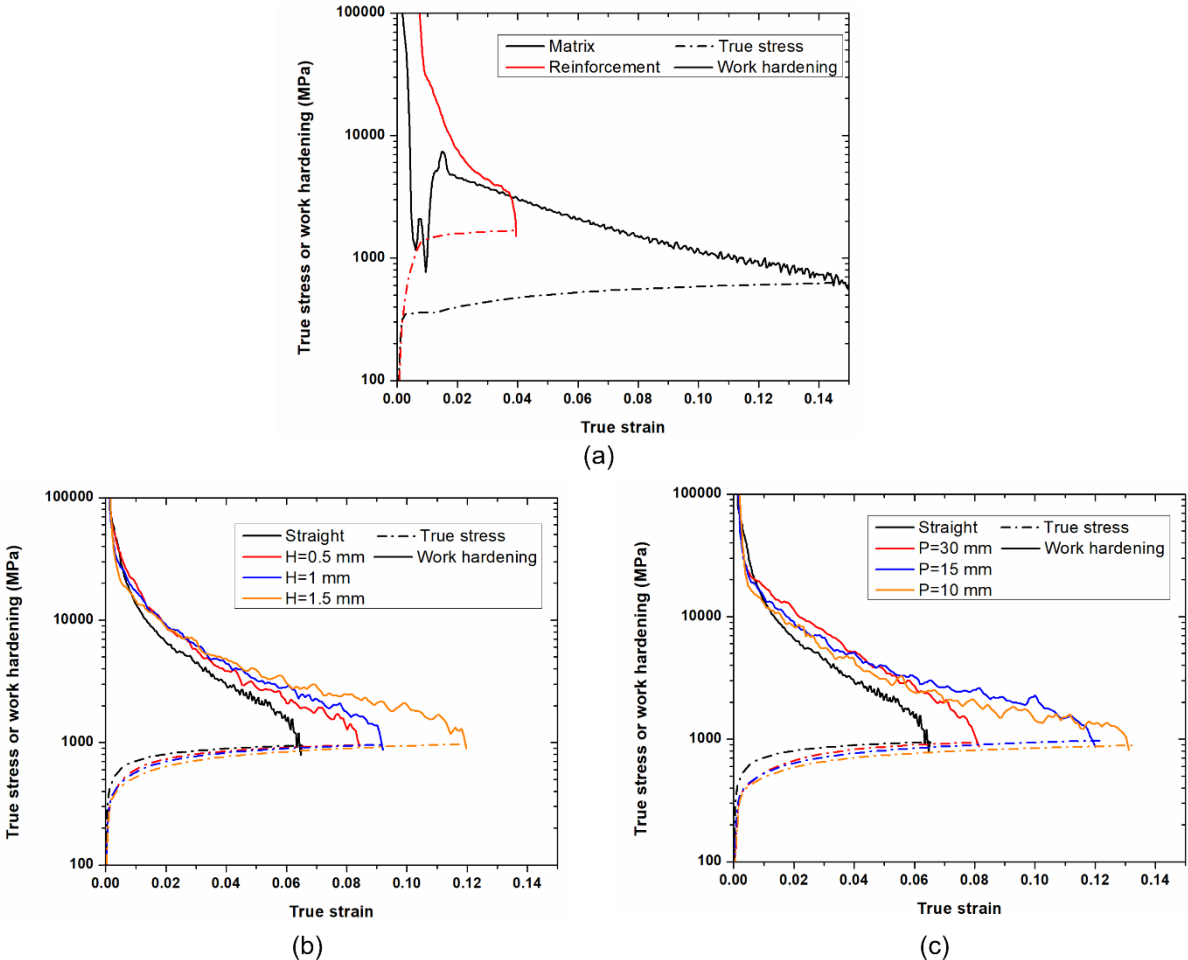


Figure 5-12 True stress and work hardening behavior of (a) matrix and reinforcement, (b) architected steel with straight and corrugated reinforcement of P=15 mm, (c) architected steel with straight and corrugated reinforcement of H=1.5 mm.

With a higher H/P ratio, the initial reinforcement geometry is less aligned, and thus the YS is smaller. During the tensile loading, the increase in strength is more important, thus the geometrically induced work hardening becomes more visible. The work hardening rate drops more slowly and the intersection with true stress, where the necking is supposed to happen, is delayed. The parallel loading component in the reinforcement fragments is smaller and they are less deformed, which is the reason why a higher H/P ratio results in a more heterogeneous strain map at the same average total strain in Figures 5-7 and 5-8.

It is noteworthy that with the present laser hardening method, and the matrix and reinforcement properties, the influence of material architecture on work hardening evolution during tensile tests is limited to slowing down the drop in work hardening rate and delaying the onset of necking. With other combinations of matrix and reinforcement, it is possible to introduce a much more important effect on work hardening evolution thanks to the unbending process. The work of Fraser et al. [5] confirms with FEM simulation that an increase in work hardening rate may happen during tensile test in a system of copper matrix and steel reinforcement. This inspiring result shows that a more obvious difference in strength between matrix and reinforcement may bring more obvious architecture effect, but likely at the cost of interfacial strength.

### 5.3.2 Perspective of the corrugation effect on necking strain

In this study, the chosen experimental geometrical parameters are limited in range for practical reasons, such as laser spot size, robot trajectory and moving velocity approximation, sample cutting precision, etc. But more geometries can be envisaged in order to exploit the corrugated reinforcement architecture effect if experimental conditions allow, for example, adjusting laser spot size or using an oscillation system. Some other parameters are tested by FEM simulation to estimate the corrugated reinforcement effect on mechanical properties, including reinforced volume fraction (from 12% to 48%), corrugation height (from 0.5 to 2 mm) and period (from 5 to 30 mm). Figures 5-13 (a) and (b) summarizes the UTS and necking strain of samples with different geometric and volumetric reinforcement according to the H/P ratio with the chosen matrix-reinforcement material system.

The UTS evolution of samples with various reinforced volume fractions follows a similar trend to previous results, as shown in Figure 5-13 (a). For a given H/P, UTS increases with an increasing reinforced volume fraction, and it decreases with the increasing H/P for a fixed reinforced volume fraction. The higher the reinforced volume fraction, the quicker the UTS drops with the growth of H/P. However, the necking strain evolutions of samples reinforced with different volume fractions do not present the same trend as before in Figure 5-13 (b). With 12% reinforcement, the necking strain decreases at the beginning with H/P below 0.1 and it starts to increase slightly with a H/P between 0.1 and 0.2. With 24% reinforcement, the benefit effect on necking strain is negligible for H/P below 0.067 before increasing. But with 36% and 48% of reinforced volume fraction, the gain in necking strain is visible immediately with an increasing H/P until 0.2. Beyond this value, the gain in necking strain for all samples vanishes, or becomes negative even. Thus, for a certain reinforced volume fraction, a threshold inclination ratio H/P is required in order to achieve an architecture induced benefit on necking strain. This threshold value is lower when the reinforced volume fraction is higher.

Figure 5-13 (c) shows the UTS-necking strain relation of all geometries along with homogeneous matrix and reinforcement. The UTS and necking strain of architected samples are always between those of the matrix and reinforcement. With the change in geometric parameters and reinforcement volume fractions, samples are located in different regions in this property map. The upper right zone is the target to resolve the contradiction between the

ductility and strength of advanced high strength steel, which is hard to access for homogeneous steel by traditional metallurgical method. Corrugated architected steel may provide a potential way to fill gaps in the material-property space. Figure 5-13 (d) summarizes the plastically dissipated energy of all studied geometries with their H/P, which presents a similar trend with the necking strain. With 12% volume reinforced, the absorbed energy decreases with the increasing of H/P. But with more reinforced volume fraction, it increases until H/P is around 0.1 and then decreases due to settled necking strain and reduced UTS. Together with UTS and necking strain, plastically dissipated energy can also be a criterion to evaluate architected material mechanical properties.

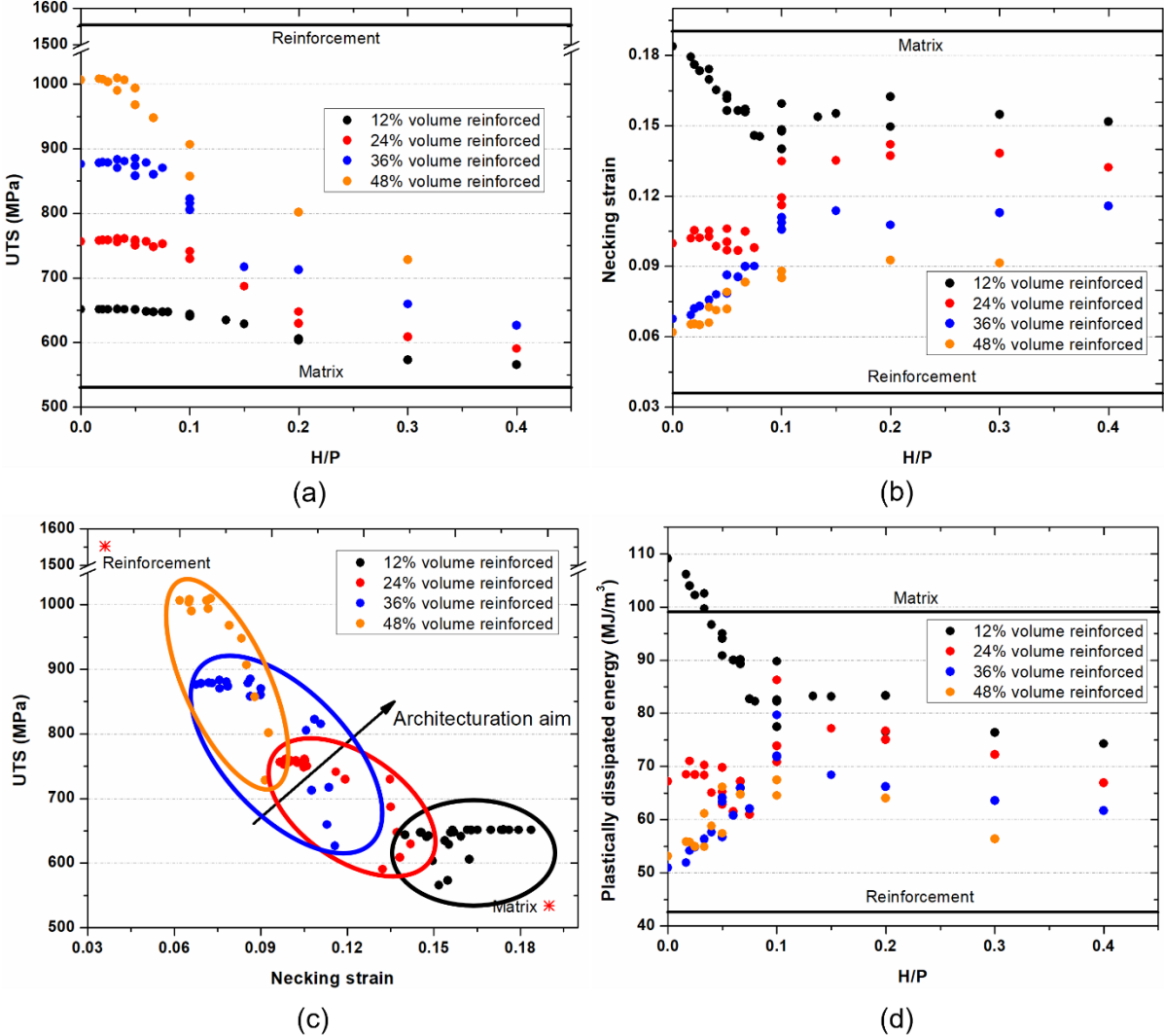


Figure 5-13 FEM simulation results, (a) UTS evolution with H/P, (b) necking strain evolution with H/P, (c) UTS-necking strain relationship, (d) plastically dissipated energy evolution with H/P.

While most of the samples probed using FEM have an intermediate plastically dissipated energy, between those of the pure homogeneous matrix and reinforcement, several architectures generate a higher dissipated energy value than that of the matrix in Figure 5-13 (d). These

configurations correspond to specimens with 12% of reinforced volume and a small corrugation inclination, with H/P below 0.03. Together with the positions of these configurations in Figures 5-13 (a) and (b), this superior dissipated energy comes from a remarkable increase in strength, of about 120 MPa, and relatively low ductility loss, about 2%, compared to ferritic matrix. As shown in Figure 5-14, the black line presents the matrix and the red one presents a specimen with 12% volume reinforced by a corrugation of H=0.5 mm and P=30 mm, and the surface underneath the plastic stress-strain curves is the plastically dissipated energy of tensile specimens. The surface of S2 is larger than S1 and that is the reason why the dissipated energy of the specimen reinforced by laser is higher than that of the matrix. With the increase in H/P, both the strength and necking strain are reduced so the dissipated energy decreases.

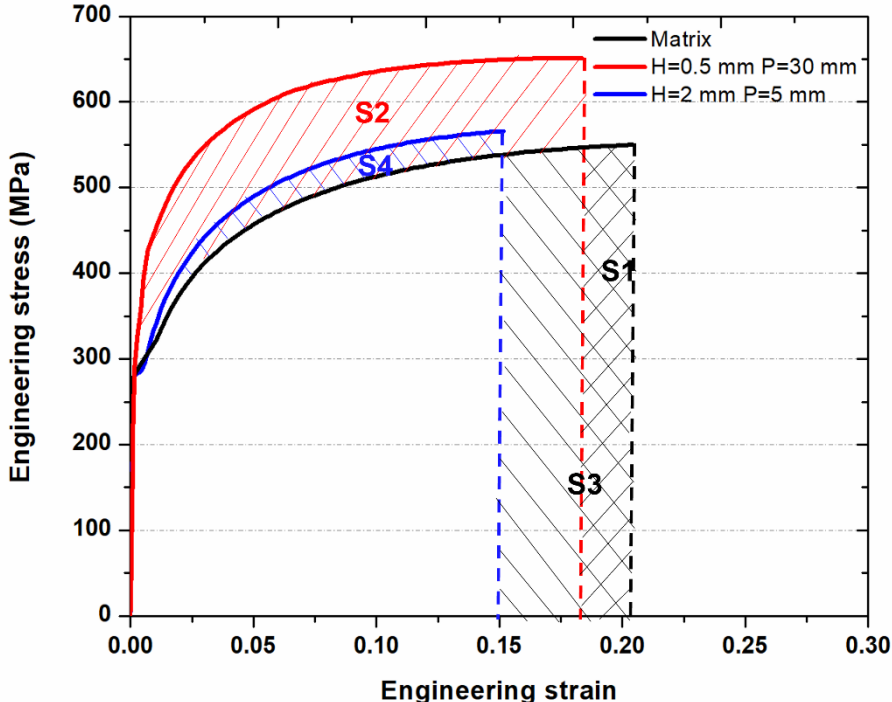


Figure 5-14 Engineering stress-strain response of matrix and 12% volume reinforced specimens by FEM simulation.

Beyond a certain H/P value and reinforced volume fraction, the gain in strength cannot compensate the loss in ductility, thus yielding a lower value for plastically dissipated energy. As shown by the blue line of a corrugation with H=2 mm and P=5 mm in Figure 5-14, the surface of S4 is much smaller than S4, so the dissipated energy is less than that of the matrix. It has to be pointed out that for a reinforced volume of 12%, a straight reinforcement yields the highest dissipated energy. Corrugated reinforcements do not enhance the necking strain compared to a straight line. But straight line and some corrugations with small H/P can increase the dissipated energy during tensile test, which cannot be observed with other reinforced volumes. This threshold H/P value and reinforced volume fraction depend certainly on matrix/reinforcement property combination and these maps are based on the studied system. Therefore, Figure 5-13 gathers several design maps enabling the possibility of choosing the

suitable architecture for specific requirements in terms of mechanical properties, including architectures that outperform their constitutive phases.

Finally, this processing strategy for laser-induced architectures should be applicable to other laser hardenable metallic materials, such as Al and Ti alloys [126,127], but alternative architecture patterns as well as laser treatments, such as laser alloying, laser softening or laser shock peening, could also be considered for future research.

## 5.4 Conclusions

In this study, local laser hardening is performed on ductile ferritic steel to create a strengthened martensitic reinforcement. Microstructure and microhardness are characterized for matrix and reinforcement. Stress-strain behavior is simulated and tested experimentally on samples reinforced by straight line and various corrugation patterns. Simulations are extended on a larger range of geometric parameters to further our understanding of corrugation reinforced architected material. Several conclusions are drawn from this study.

- (1) With suitable parameters, local laser treatment can harden the ferritic matrix efficiently thanks to rapid cooling. The hardness of treated zone is around 430 Hv compared to 174 Hv of the annealed steel and the whole thickness presents a rather stable hardness. This obvious contrast can provide a soft but ductile matrix and a hard but brittle reinforcement.
- (2) Localized laser quenching of ferritic steel generates a strong, diffuse, although limited in thickness, interfacial zone, which mitigates decohesion, therefore avoiding a failure mode commonly observed in architected materials.
- (3) Two geometric corrugation strategies, fixed height with varying periods and fixed period with varying heights, confirm both that an increase in corrugation inclination ratio  $H/P$  improves necking strain but reduces YS and UTS. This beneficial effect on necking strain is due to work hardening boost induced by the unbending process of the corrugated reinforcements.
- (4) Extended simulation prediction on larger parametric range shows that the UTS and necking strain depend on the corrugation inclination  $H/P$ . A threshold for  $H/P$  is needed to improve the necking strain for samples with smaller reinforced volume fraction.
- (5) Computational analysis yielded architectures that outperform both pure ferrite and pure martensite in terms of plastically dissipated energy. Corrugated reinforcement as an architecture material strategy has the potential to fill gaps in the material-property space, by improving the strength-to-ductility trade-off.

## **Conclusions and Perspectives**

## General conclusions

The present research consists of three parts: laser hardening process on AISI 430 FSS, laser carburization process on AISI 430 FSS and laser hardening process on annealed steel. For each laser process, microstructure and mechanical properties evolution of laser treated specimens are studied. Phase transformation during the laser process and phase constitution of treated samples are investigated. Local hardness evolution and global uniaxial tensile behavior are characterized to evaluate the effect of different laser parameters. This is followed by the fabrication of straight and corrugation reinforced architected materials under the condition which leads to the most strengthening effect for each process. The global stress-strain response of architected materials and local strain field are measured to investigate the enhancing effect on necking strain of corrugated reinforcements compared to straight ones. The main conclusions from the results of this study can be summarized as follows.

(1) Laser heat treatment can enhance the mechanical properties of AISI 430 by forming martensite and chromium carbides despite of dramatic grain coarsening. Argon shielding gas can prevent the formation of thick oxides on the specimen surface, which leads to micro cracks and early fracture during tensile test. Laser irradiation from sides of steel sheets at appropriate power can generate a rather homogeneous microstructure though the whole thickness. By adjusting laser parameters and operational environment, hardness can be improved by 90%, YS by 60% and UTS by 45.8% at most.

(2) Straight and corrugated reinforcements induced by localized laser hardening can both increase the YS and UTS of AISI 430 specimens compared to untreated materials and the strengthening effect increases with the reinforced volume. Strain map evolution obtained by FEM simulation and DIC results agree well. Straight reinforced specimens present a homogeneous strain field, but corrugation reinforced specimens present a heterogeneous strain field, where the local strain of matrix is much larger than that of reinforcement. A larger corrugation inclination H/P leads to a more heterogeneous strain map at a given average strain. But corrugation do not yield enhancing effect on necking strain compared to straight lines because of early fracture of matrix caused by excess strain, uncompleted unbending of reinforcements and insufficient contrast in strength between matrix and reinforcement.

(3) Laser irradiation on graphite coating is efficient to carburize substrate AISI 430 steel sheets. The carburized specimens become austenite-dominated due to high carbon content. Different microstructure morphologies can be formed during solidification and they depend on laser parameters. Laser carburization process can increase the strength of the base materials more efficiently than simple laser hardening by forming austenite and numerous carbides. The hardness can be improved by 137%, YS by 90%, UTS by 85% when the specimen is fully carburized, but the loss in ductility is significant. This process can be used to improve the surface wear resistance.

(4) Straight and corrugated reinforcements induced by localized laser carburization can both increase YS and UTS of AISI 430 specimens compared to as-received material. The strain maps

have similar basic features and evolution trends as localized laser-hardened architected materials. Very limited enhancing effect on necking strain are induced by corrugations compared to straight reinforcement due to insufficient boosts in work hardening. A more strengthened reinforcement can possibly bring more enhancing effect on necking strain.

(5) Localized laser quenching on annealed steel with a ferrite-pearlite microstructure under suitable laser parameters can generate an almost fully martensite microstructure, whose YS can attain more than three times that of the untreated material. Martensitic straight and corrugated reinforcements are introduced in ferrite-pearlite matrix by this method. Corrugated reinforcements enhance the necking strain of architected specimens due to the boost in work hardening issued from corrugation unbending. Larger is the corrugation inclination H/P, more important is the benefit on necking strain.

(6) Extended FEM simulation on a large range of reinforcement geometries with martensite reinforcement and ferrite-pearlite matrix shows that the UTS and necking strain depend on the corrugation inclination H/P, a threshold H/P value should be attained to improve necking strain. Some architectural patterns can outperform the pure matrix and reinforcement in terms of plastically dissipated energy. Corrugation reinforced architected materials are potential candidates to improve the strength-ductility trade-off and to fill the blank area in material-property map.

(7) Localized reinforced architected materials obtained by all these processes do not show any decohesion failures between matrix and reinforcement during tensile test. This indicates that laser treatment can generate an interface which is strong enough and solves the interface decohesion problem of post-assembled architected materials.

## **Perspectives**

In this study, the possibility to fabricate steel-based locally reinforced architected materials is studied and the enhancing effect on necking strain by corrugated reinforcements compared to straight ones is investigated. Several complementary studies can be envisaged to expand and enrich this research as follows.

(1) Laser carburization process on AISI 430 can be combined with nitriding to achieve more strengthening effect on mechanical properties by forming nitrides and carbonitrides besides carbides. Nitrogen shielding gas can be used in the place of Argon. Transmission electron microscopy (TEM) studies on laser-alloyed specimens can be carried out to reveal the nature of carbides, nitrides and carbonitrides. More profound research of carburized specimens can be carried out on EBSD and X-ray characterization to reveal the crystallography orientation and dislocation density.

(2) The laser spot size is limited around 1 mm in this study, and it restricts the reinforced volume choice. An oscillation system can be added on the robotic arm of laser treatment platform, which allows a larger reinforced volume. Fabrication of architected materials with a larger thickness may also be possible.

(3) This laser-induced heterogeneous phase repartition can be implanted in other alloying system, whose mechanical properties depend on heat treatments, such as 2XXX-series Aluminum alloys or Titanium alloys. Laser alloying process can also be applied by coating to strengthen laser effect, for example, Aluminum alloys covered by Cu powder.

(4) Other types of mechanical tests besides uniaxial tensile test can be envisaged on straight and corrugation reinforced architected materials, for example, edge crack tensile test equipped with DIC system to investigate the influence of architectural patterns on crack growth path and dissipated energy, crash test can also be implemented and simulated to evaluate effect of architectural patterns.

(5) Besides corrugated patterns, other geometries can be used to architectural metallic sheets, such as honeycomb, auxetic patterns, chiral patterns, Kagome lattice, etc. The introduction of these geometries which present unconventional mechanical responses may bring architectural synergistic effect.

## References

- [1] M. Ashby, Designing architected materials, *Scripta Materialia*. 68 (2013) 4–7. <https://doi.org/10.1016/j.scriptamat.2012.04.033>.
- [2] M.F. Ashby, Y.J.M. Bréchet, Designing hybrid materials, *Acta Materialia*. 51 (2003) 5801–5821. [https://doi.org/10.1016/S1359-6454\(03\)00441-5](https://doi.org/10.1016/S1359-6454(03)00441-5).
- [3] O. Bouaziz, Y. Bréchet, J.D. Embury, Heterogeneous and Architected Materials: A Possible Strategy for Design of Structural Materials, *Adv. Eng. Mater.* 10 (2008) 24–36. <https://doi.org/10.1002/adem.200700289>.
- [4] Y. Zhu, K. Ameyama, P.M. Anderson, I.J. Beyerlein, H. Gao, H.S. Kim, E. Lavernia, S. Mathaudhu, H. Mughrabi, R.O. Ritchie, N. Tsuji, X. Zhang, X. Wu, Heterostructured materials: superior properties from hetero-zone interaction, *Materials Research Letters*. 9 (2021) 1–31. <https://doi.org/10.1080/21663831.2020.1796836>.
- [5] M. Fraser, H.S. Zurob, P. Wu, Corrugation Reinforced Composites: A Method for Filling Holes in Material-Property Space, *Adv. Eng. Mater.* 20 (2018) 1700834. <https://doi.org/10.1002/adem.201700834>.
- [6] M. Fraser, *The Study of Architected Materials with a Corrugated Geometry*, 2017.
- [7] Y. Brechet, J.D. Embury, Architected materials: Expanding materials space, *Scripta Materialia*. 68 (2013) 1–3. <https://doi.org/10.1016/j.scriptamat.2012.07.038>.
- [8] M.F. Ashby, The properties of foams and lattices, *Phil. Trans. R. Soc. A*. 364 (2006) 15–30. <https://doi.org/10.1098/rsta.2005.1678>.
- [9] X. Zhang, Heterostructures: new opportunities for functional materials, *Materials Research Letters*. 8 (2020) 49–59. <https://doi.org/10.1080/21663831.2019.1691668>.
- [10] B. Chéhab, H. Zurob, D. Embury, O. Bouaziz, Y. Brechet, Compositionally Graded Steels: A Strategy for Materials Development, *Adv. Eng. Mater.* 11 (2009) 992–999. <https://doi.org/10.1002/adem.200900180>.
- [11] R. Cioria, B. Chehab, H. Zurob, Diffusion as a method for producing architected materials, *Scripta Materialia*. 68 (2013) 17–21. <https://doi.org/10.1016/j.scriptamat.2012.08.004>.
- [12] H.T. Wang, N.R. Tao, K. Lu, Architected surface layer with a gradient nanotwinned structure in a Fe–Mn austenitic steel, *Scripta Materialia*. 68 (2013) 22–27. <https://doi.org/10.1016/j.scriptamat.2012.05.041>.
- [13] W.A. Chapkin, D.L. Simone, G.J. Frank, J.W. Baur, Mechanical behavior and energy dissipation of infilled, composite Ti-6Al-4V trusses, *Materials & Design*. 203 (2021) 109602. <https://doi.org/10.1016/j.matdes.2021.109602>.
- [14] T. Juarez, A. Schroer, R. Schwaiger, A.M. Hodge, Evaluating sputter deposited metal coatings on 3D printed polymer micro-truss structures, *Materials & Design*. 140 (2018) 442–450. <https://doi.org/10.1016/j.matdes.2017.12.005>.
- [15] M. Assidi, J.-F. Ganghoffer, Composites with auxetic inclusions showing both an auxetic behavior and enhancement of their mechanical properties, *Composite Structures*. 94 (2012) 2373–2382. <https://doi.org/10.1016/j.compstruct.2012.02.026>.

- [16] A. Alderson, K.L. Alderson, D. Attard, K.E. Evans, R. Gatt, J.N. Grima, W. Miller, N. Ravirala, C.W. Smith, K. Zied, Elastic constants of 3-, 4- and 6-connected chiral and anti-chiral honeycombs subject to uniaxial in-plane loading, *Composites Science and Technology*. 70 (2010) 1042–1048. <https://doi.org/10.1016/j.compscitech.2009.07.009>.
- [17] F. Agnese, C. Remillat, F. Scarpa, C. Payne, Composite chiral shear vibration damper, *Composite Structures*. 132 (2015) 215–225. <https://doi.org/10.1016/j.compstruct.2015.05.048>.
- [18] J. Dirrenberger, S. Forest, D. Jeulin, Elastoplasticity of auxetic materials, *Computational Materials Science*. 64 (2012) 57–61. <https://doi.org/10.1016/j.commatsci.2012.03.036>.
- [19] A.V. Dyskin, Y. Estrin, E. Pasternak, H.C. Khor, A.J. Kanel-Belov, Fracture Resistant Structures Based on Topological Interlocking with Non-planar Contacts, *Adv. Eng. Mater.* 5 (2003) 116–119. <https://doi.org/10.1002/adem.200390016>.
- [20] A. Rezaee Javan, H. Seifi, X. Lin, Y.M. Xie, Mechanical behaviour of composite structures made of topologically interlocking concrete bricks with soft interfaces, *Materials & Design*. 186 (2020) 108347. <https://doi.org/10.1016/j.matdes.2019.108347>.
- [21] F. Barthelat, Architected materials in engineering and biology: fabrication, structure, mechanics and performance, *International Materials Reviews*. 60 (2015) 413–430. <https://doi.org/10.1179/1743280415Y.0000000008>.
- [22] B. Yrieix, Architected Materials in Building Energy Efficiency, in: Y. Estrin, Y. Bréchet, J. Dunlop, P. Fratzl (Eds.), *Architected Materials in Nature and Engineering*, Springer International Publishing, Cham, 2019: pp. 393–421. [https://doi.org/10.1007/978-3-030-11942-3\\_13](https://doi.org/10.1007/978-3-030-11942-3_13).
- [23] H. Azizi, H.S. Zurob, D. Embury, X. Wang, K. Wang, B. Bose, Using architected materials to control localized shear fracture, *Acta Materialia*. 143 (2018) 298–305. <https://doi.org/10.1016/j.actamat.2017.10.027>.
- [24] H. Azizi, J. Samei, H.S. Zurob, D.S. Wilkinson, D. Embury, A novel approach to producing architected ultra-high strength dual phase steels, *Materials Science and Engineering: A*. 833 (2022) 142582. <https://doi.org/10.1016/j.msea.2021.142582>.
- [25] H. Azizi, X. Wang, D. Embury, H.S. Zurob, Novel approach for the development of tailored heterogenous structures in steel, *Materialia*. 13 (2020) 100831. <https://doi.org/10.1016/j.mtla.2020.100831>.
- [26] H. Naser, A. Deschamps, M. Mantel, M. Véron, Architected duplex stainless steels micro-composite: Elaboration and microstructure characterization, *Materials & Design*. 145 (2018) 156–167. <https://doi.org/10.1016/j.matdes.2018.02.069>.
- [27] Y.T. Sun, X. Kong, Z.B. Wang, Superior mechanical properties and deformation mechanisms of a 304 stainless steel plate with gradient nanostructure, *International Journal of Plasticity*. 155 (2022) 103336. <https://doi.org/10.1016/j.ijplas.2022.103336>.
- [28] T.-T. Chen, J. Wang, Y. Zhang, P. Jiang, F.-P. Yuan, P.-D. Han, X.-L. Wu, Twin density gradient induces enhanced yield strength-and-ductility synergy in a S31254 super austenitic stainless steel, *Materials Science and Engineering: A*. 837 (2022) 142727. <https://doi.org/10.1016/j.msea.2022.142727>.

- [29] W. Fu, H. Li, Y. Huang, Z. Ning, J. Sun, A new strategy to overcome the strength-ductility trade off of high entropy alloy, *Scripta Materialia*. 214 (2022) 114678. <https://doi.org/10.1016/j.scriptamat.2022.114678>.
- [30] X. Hu, Y.F. Zheng, Y.X. Tong, F. Chen, B. Tian, H.M. Zhou, L. Li, High damping capacity in a wide temperature range of a compositionally graded TiNi alloy prepared by electroplating and diffusion annealing, *Materials Science and Engineering: A*. 623 (2015) 1–3. <https://doi.org/10.1016/j.msea.2014.11.034>.
- [31] X. Li, Z. Wang, F. Zhu, G. Wu, L. Zhao, Response of aluminium corrugated sandwich panels under air blast loadings: Experiment and numerical simulation, *International Journal of Impact Engineering*. 65 (2014) 79–88. <https://doi.org/10.1016/j.ijimpeng.2013.11.002>.
- [32] M. Yazici, J. Wright, D. Bertin, A. Shukla, Experimental and numerical study of foam filled corrugated core steel sandwich structures subjected to blast loading, *Composite Structures*. 110 (2014) 98–109. <https://doi.org/10.1016/j.compstruct.2013.11.016>.
- [33] L. Zhang, R. Hebert, J.T. Wright, A. Shukla, J.-H. Kim, Dynamic response of corrugated sandwich steel plates with graded cores, *International Journal of Impact Engineering*. 65 (2014) 185–194. <https://doi.org/10.1016/j.ijimpeng.2013.11.011>.
- [34] W.Y. Liu, Y. Suzuki, T. Iizuka, T. Shiratori, T. Komatsu, Variation of tensile and bending rigidities of a duplex embossed steel sheet by small uniaxial tensile deformation, *Journal of Materials Processing Technology*. 261 (2018) 123–139. <https://doi.org/10.1016/j.jmatprotec.2018.05.014>.
- [35] O. Bouaziz, Geometrically induced strain hardening, *Scripta Materialia*. 68 (2013) 28–30. <https://doi.org/10.1016/j.scriptamat.2012.08.008>.
- [36] P. Lapouge, J. Dirrenberger, F. Coste, M. Schneider, Laser heat treatment of martensitic steel and dual-phase steel with high martensite content, *Materials Science and Engineering: A*. 752 (2019) 128–135. <https://doi.org/10.1016/j.msea.2019.03.016>.
- [37] S. Zhou, K. Zhang, N. Chen, J. Gu, Y. Rong, Investigation on High Strength Hot-rolled Plates by Quenching-partitioning-tempering Process Suitable for Engineering, *ISIJ Int*. 51 (2011) 1688–1695. <https://doi.org/10.2355/isijinternational.51.1688>.
- [38] J. Speer, D.K. Matlock, B.C. De Cooman, J.G. Schroth, Carbon partitioning into austenite after martensite transformation, *Acta Materialia*. 51 (2003) 2611–2622. [https://doi.org/10.1016/S1359-6454\(03\)00059-4](https://doi.org/10.1016/S1359-6454(03)00059-4).
- [39] H. Ki, S. So, Process map for laser heat treatment of carbon steels, *Optics & Laser Technology*. 44 (2012) 2106–2114. <https://doi.org/10.1016/j.optlastec.2012.03.018>.
- [40] M.F. Ashby, K.E. Easterling, The transformation hardening of steel surfaces by laser beams—I. Hypo-eutectoid steels, *Acta Metallurgica*. 32 (1984) 1935–1948. [https://doi.org/10.1016/0001-6160\(84\)90175-5](https://doi.org/10.1016/0001-6160(84)90175-5).
- [41] A. Jahn, M. Heitmanek, J. Standfuss, B. Brenner, G. Wunderlich, B. Donat, Local Laser Strengthening of Steel Sheets for Load Adapted Component Design in Car Body Structures, *Physics Procedia*. 12 (2011) 431–441. <https://doi.org/10.1016/j.phpro.2011.03.054>.

- [42] K.H. Lo, F.T. Cheng, H.C. Man, Laser transformation hardening of AISI 440C martensitic stainless steel for higher cavitation erosion resistance, *Surface and Coatings Technology*. 173 (2003) 96–104. [https://doi.org/10.1016/S0257-8972\(03\)00347-5](https://doi.org/10.1016/S0257-8972(03)00347-5).
- [43] M.O.H. Amuda, S. Mridha, Grain refinement and hardness distribution in cryogenically cooled ferritic stainless steel welds, *Materials & Design*. 47 (2013) 365–371. <https://doi.org/10.1016/j.matdes.2012.12.008>.
- [44] G.L. Liu, S.W. Yang, W.T. Han, L.J. Zhou, M.Q. Zhang, J.W. Ding, Y. Dong, F.R. Wan, C.J. Shang, R.D.K. Misra, Microstructural evolution of dissimilar welded joints between reduced-activation ferritic-martensitic steel and 316L stainless steel during the post weld heat treatment, *Materials Science and Engineering: A*. 722 (2018) 182–196. <https://doi.org/10.1016/j.msea.2018.03.035>.
- [45] M.M.A. Khan, L. Romoli, G. Dini, Laser beam welding of dissimilar ferritic/martensitic stainless steels in a butt joint configuration, *Optics & Laser Technology*. 49 (2013) 125–136. <https://doi.org/10.1016/j.optlastec.2012.12.025>.
- [46] Y. Zhang, J. Guo, Y. Li, Z. Luo, X. Zhang, A comparative study between the mechanical and microstructural properties of resistance spot welding joints among ferritic AISI 430 and austenitic AISI 304 stainless steel, *Journal of Materials Research and Technology*. 9 (2020) 574–583. <https://doi.org/10.1016/j.jmrt.2019.10.086>.
- [47] E. Taban, E. Deleu, A. Dhooge, E. Kaluc, Laser welding of modified 12% Cr stainless steel: Strength, fatigue, toughness, microstructure and corrosion properties, *Materials & Design*. 30 (2009) 1193–1200. <https://doi.org/10.1016/j.matdes.2008.06.030>.
- [48] Z. Zhang, Z. Wang, W. Wang, Z. Yan, P. Dong, H. Du, M. Ding, Microstructure evolution in heat affected zone of T4003 ferritic stainless steel, *Materials & Design*. 68 (2015) 114–120. <https://doi.org/10.1016/j.matdes.2014.12.018>.
- [49] M.M.A. Khan, L. Romoli, M. Fiaschi, G. Dini, F. Sarri, Laser beam welding of dissimilar stainless steels in a fillet joint configuration, *Journal of Materials Processing Technology*. 212 (2012) 856–867. <https://doi.org/10.1016/j.jmatprotec.2011.11.011>.
- [50] S. Vafaeian, A. Fattah-alhosseini, Y. Mazaheri, M.K. Keshavarz, On the study of tensile and strain hardening behavior of a thermomechanically treated ferritic stainless steel, *Materials Science and Engineering: A*. 669 (2016) 480–489. <https://doi.org/10.1016/j.msea.2016.04.050>.
- [51] B.K. Jha, P. Jha, C.D. Singh, Process Technology for the Continuous Hot Band Annealing of 17%Cr Ferritic Stainless Steel, *Journal of Materials Engineering and Performance*. 11 (2002) 180–186. <https://doi.org/10.1361/105994902770344240>.
- [52] J. Sundqvist, T. Manninen, H.-P. Heikkinen, S. Anttila, A.F.H. Kaplan, Laser surface hardening of 11% Cr ferritic stainless steel and its sensitisation behaviour, *Surface and Coatings Technology*. 344 (2018) 673–679. <https://doi.org/10.1016/j.surfcoat.2018.04.002>.
- [53] B. Mahmoudi, M.J. Torkamany, A.R.S.R. Aghdam, J. Sabbaghzade, Laser surface hardening of AISI 420 stainless steel treated by pulsed Nd:YAG laser, *Materials & Design (1980-2015)*. 31 (2010) 2553–2560. <https://doi.org/10.1016/j.matdes.2009.11.034>.

- [54] H. Pantsar, V. Kujanpää, Diode laser beam absorption in laser transformation hardening of low alloy steel, *Journal of Laser Applications*. 16 (2004) 147–153. <https://doi.org/10.2351/1.1710879>.
- [55] P. Schaaf, M. Kahle, E. Carpena, Reactive laser synthesis of carbides and nitrides, *Applied Surface Science*. 247 (2005) 607–615. <https://doi.org/10.1016/j.apsusc.2005.01.128>.
- [56] M. Izciler, M. Tabur, Abrasive wear behavior of different case depth gas carburized AISI 8620 gear steel, *Wear*. 260 (2006) 90–98. <https://doi.org/10.1016/j.wear.2004.12.034>.
- [57] L.-D. Liu, F.-S. Chen, Super-carburization of low alloy steel in a vacuum furnace, *Surface and Coatings Technology*. 183 (2004) 233–238. <https://doi.org/10.1016/j.surfcoat.2003.08.079>.
- [58] Z. Liu, S. Zhang, S. Wang, Y. Peng, J. Gong, M.A.J. Somers, On the fatigue behavior of low-temperature gaseous carburized 316L austenitic stainless steel: Experimental analysis and predictive approach, *Materials Science and Engineering: A*. 793 (2020) 139651. <https://doi.org/10.1016/j.msea.2020.139651>.
- [59] F. Rotundo, L. Ceschini, C. Martini, R. Montanari, A. Varone, High temperature tribological behavior and microstructural modifications of the low-temperature carburized AISI 316L austenitic stainless steel, *Surface and Coatings Technology*. 258 (2014) 772–781. <https://doi.org/10.1016/j.surfcoat.2014.07.081>.
- [60] G. Michal, F. Ernst, H. Kahn, Y. Cao, F. Oba, N. Agarwal, A. Heuer, Carbon supersaturation due to paraequilibrium carburization: Stainless steels with greatly improved mechanical properties, *Acta Materialia*. 54 (2006) 1597–1606. <https://doi.org/10.1016/j.actamat.2005.11.029>.
- [61] C.J. Scheuer, R.P. Cardoso, R. Pereira, M. Mafra, S.F. Brunatto, Low temperature plasma carburizing of martensitic stainless steel, *Materials Science and Engineering: A*. 539 (2012) 369–372. <https://doi.org/10.1016/j.msea.2012.01.085>.
- [62] A.C. Rovani, R. Breganon, G.S. de Souza, S.F. Brunatto, G. Pintaúde, Scratch resistance of low-temperature plasma nitrided and carburized martensitic stainless steel, *Wear*. 376–377 (2017) 70–76. <https://doi.org/10.1016/j.wear.2017.01.112>.
- [63] T. Hirata, T. Yamaguchi, Y. Yokoyama, H. Hoshino, Surface modification by high-speed laser gas carburization in low-alloy steel, *Materials Letters*. 280 (2020) 128586. <https://doi.org/10.1016/j.matlet.2020.128586>.
- [64] D. Höche, J. Kaspar, P. Schaaf, Laser nitriding and carburization of materials, in: *Laser Surface Engineering*, Elsevier, 2015: pp. 33–58. <https://doi.org/10.1016/B978-1-78242-074-3.00002-7>.
- [65] N. Maharjan, W. Zhou, N. Wu, Direct laser hardening of AISI 1020 steel under controlled gas atmosphere, *Surface and Coatings Technology*. 385 (2020) 125399. <https://doi.org/10.1016/j.surfcoat.2020.125399>.
- [66] Z. Chen, T. Zhou, R. Zhao, H. Zhang, S. Lu, W. Yang, H. Zhou, Improved fatigue wear resistance of gray cast iron by localized laser carburizing, *Materials Science and Engineering: A*. 644 (2015) 1–9. <https://doi.org/10.1016/j.msea.2015.07.046>.

- [67] Q. Sui, H. Zhou, H. Bao, P. Zhang, Y. Yuan, C. Meng, Wear behavior of quenched iron with various shapes and unit processed through two-step laser alloying of C powder, *Optics & Laser Technology*. 104 (2018) 103–111. <https://doi.org/10.1016/j.optlastec.2018.02.015>.
- [68] A.I. Katsamas, G.N. Haidemenopoulos, Laser-beam carburizing of low-alloy steels, *Surface and Coatings Technology*. 139 (2001) 183–191. [https://doi.org/10.1016/S0257-8972\(00\)01061-6](https://doi.org/10.1016/S0257-8972(00)01061-6).
- [69] M. Tayal, K. Mukherjee, Selective area carburizing of low carbon steel using an Nd: YAG laser, *Materials Science and Engineering: A*. 174 (1994) 231–236. [https://doi.org/10.1016/0921-5093\(94\)91093-6](https://doi.org/10.1016/0921-5093(94)91093-6).
- [70] J. Yao, Q. Zhang, M. Gao, W. Zhang, Microstructure and wear property of carbon nanotube carburizing carbon steel by laser surface remelting, *Applied Surface Science*. 254 (2008) 7092–7097. <https://doi.org/10.1016/j.apsusc.2008.05.223>.
- [71] I.A. Bataev, D.O. Mul, A.A. Bataev, O.G. Lenivtseva, M.G. Golkovski, Ya.S. Lizunkova, R.A. Dostovalov, Structure and tribological properties of steel after non-vacuum electron beam cladding of Ti, Mo and graphite powders, *Materials Characterization*. 112 (2016) 60–67. <https://doi.org/10.1016/j.matchar.2015.11.028>.
- [72] D. Dong, Y. Liu, Y. Yang, J. Li, M. Ma, T. Jiang, Microstructure and dynamic tensile behavior of DP600 dual phase steel joint by laser welding, *Materials Science and Engineering: A*. 594 (2014) 17–25. <https://doi.org/10.1016/j.msea.2013.11.047>.
- [73] S. Raghavan, S.N. Melkote, J.-I. Hong, Modeling of Laser-Tempering Process for Hyper-Eutectoid Steels, *Metall and Mat Trans A*. 45 (2014) 2612–2625. <https://doi.org/10.1007/s11661-014-2204-6>.
- [74] G. Krauss, Tempering of Lath Martensite in Low and Medium Carbon Steels: Assessment and Challenges, *Steel Research Int*. 88 (2017) 1700038. <https://doi.org/10.1002/srin.201700038>.
- [75] E. Capello, B. Previtali, Enhancing dual phase steel formability by diode laser heat treatment, *Journal of Laser Applications*. 21 (2009) 1–9. <https://doi.org/10.2351/1.3071316>.
- [76] R. Neugebauer, S. Scheffler, R. Poprawe, A. Weisheit, Local laser heat treatment of ultra high strength steels to improve formability, *Prod. Eng. Res. Devel*. 3 (2009) 347–351. <https://doi.org/10.1007/s11740-009-0186-9>.
- [77] A. Saastamoinen, A. Kaijalainen, J. Heikkala, D. Porter, P. Suikkanen, The effect of tempering temperature on microstructure, mechanical properties and bendability of direct-quenched low-alloy strip steel, *Materials Science and Engineering: A*. 730 (2018) 284–294. <https://doi.org/10.1016/j.msea.2018.06.014>.
- [78] C.-G. Ren, D.-G. Shang, L. Wang, Y.-B. Guo, Effect of single-pulse laser irradiation energy on healing fatigue damage for copper film, *J Mech Sci Technol*. 28 (2014) 1257–1264. <https://doi.org/10.1007/s12206-013-1206-4>.
- [79] V.G. Shmorgun, O.V. Slautin, A.G. Serov, Structure and properties of intermetallic coatings formed by laser alloying of a titanium surface with copper, *Materials Today: Proceedings*. 25 (2020) 493–496. <https://doi.org/10.1016/j.matpr.2019.12.352>.

- [80] Y. Chi, G. Gu, H. Yu, C. Chen, Laser surface alloying on aluminum and its alloys: A review, *Optics and Lasers in Engineering*. 100 (2018) 23–37. <https://doi.org/10.1016/j.optlaseng.2017.07.006>.
- [81] L. Dubourg, H. Pelletier, D. Vaissiere, F. Hlawka, A. Cornet, Mechanical characterisation of laser surface alloyed aluminium–copper systems, *Wear*. 253 (2002) 1077–1085. [https://doi.org/10.1016/S0043-1648\(02\)00218-1](https://doi.org/10.1016/S0043-1648(02)00218-1).
- [82] N. Makuch, M. Kulka, P. Dziarski, D. Przystacki, Laser surface alloying of commercially pure titanium with boron and carbon, *Optics and Lasers in Engineering*. 57 (2014) 64–81. <https://doi.org/10.1016/j.optlaseng.2014.01.019>.
- [83] H. Tada, H. Nakamura, T. Shobu, R. Kitai, K. Kikuta, Y. Kawahito, Effect of laser solution-treatment on a Ti-based shape memory alloy, *Materials Research Bulletin*. 90 (2017) 41–46. <https://doi.org/10.1016/j.materresbull.2017.02.007>.
- [84] B. Panton, A. Michael, Y.N. Zhou, M.I. Khan, Effects of post-processing on the thermomechanical fatigue properties of laser modified NiTi, *International Journal of Fatigue*. 118 (2019) 307–315. <https://doi.org/10.1016/j.ijfatigue.2017.11.012>.
- [85] A.F. Saleh, J.H. Abboud, K.Y. Benyounis, Surface carburizing of Ti–6Al–4V alloy by laser melting, *Optics and Lasers in Engineering*. 48 (2010) 257–267. <https://doi.org/10.1016/j.optlaseng.2009.11.001>.
- [86] D.M. Seo, T.W. Hwang, Y.H. Moon, Carbonitriding of Ti-6Al-4V alloy via laser irradiation of pure graphite powder in nitrogen environment, *Surface and Coatings Technology*. 363 (2019) 244–254. <https://doi.org/10.1016/j.surfcoat.2019.02.038>.
- [87] C. Papaphilippou, M. Jeandin, Spot laser hardening, *J Mater Sci Lett*. 15 (1996) 1064–1066. <https://doi.org/10.1007/BF00274908>.
- [88] K. Somlo, S.S. Chauhan, C.F. Niordson, K. Poullos, Uniaxial tensile behaviour of additively manufactured elastically isotropic truss lattices made of 316L, *International Journal of Solids and Structures*. 246–247 (2022) 111599. <https://doi.org/10.1016/j.ijsolstr.2022.111599>.
- [89] S.G. Jeong, G.M. Karthik, E.S. Kim, A. Zargar, S.Y. Ahn, M.J. Sagong, S.H. Kang, J.-W. Cho, H.S. Kim, Architected heterogeneous alloys with selective laser melting, *Scripta Materialia*. 208 (2022) 114332. <https://doi.org/10.1016/j.scriptamat.2021.114332>.
- [90] P.F. Jiang, C.H. Zhang, S. Zhang, J.B. Zhang, J. Chen, Y. Liu, Microstructure evolution, wear behavior, and corrosion performance of alloy steel gradient material fabricated by direct laser deposition, *Journal of Materials Research and Technology*. 9 (2020) 11702–11716. <https://doi.org/10.1016/j.jmrt.2020.08.074>.
- [91] A. Considère, Mémoire sur l’emploi du fer et de l’acier dans les constructions, *Annales des Ponts et Chaussées* 1 (1885) 574–775, (n.d.). <http://catalogue.bnf.fr/ark:/12148/cb34348188q>.
- [92] R. Payling, D.G. Jones, A. Bengtson, eds., *Glow discharge optical emission spectrometry*, New York : J. Wiley, Chichester, 1997.
- [93] T. Nelis, R. Payling, *Glow discharge optical emission spectroscopy: a practical guide*, Royal Society of Chemistry, Cambridge, UK, 2003.

- [94] M.O.H. Amuda, S. Mridha, Comparative evaluation of grain refinement in AISI 430 FSS welds by elemental metal powder addition and cryogenic cooling, *Materials & Design*. 35 (2012) 609–618. <https://doi.org/10.1016/j.matdes.2011.09.066>.
- [95] Z. Wang, J. Dirrenberger, P. Lapouge, S. Dubent, Laser treatment of 430 ferritic stainless steel for enhanced mechanical properties, *Materials Science and Engineering: A*. 831 (2022) 142205. <https://doi.org/10.1016/j.msea.2021.142205>.
- [96] J.-M. Franssen, P.V. Real, *Fire Design of Steel Structures: Eurocode 1: Actions on structures Part 1-2 - General actions - Actions on structures exposed to fire Eurocode 3: Design of steel structures Part 1-2 -*, Wiley-VCH Verlag GmbH & Co. KGaA, Weinheim, Germany, 2010. <https://doi.org/10.1002/9783433601570>.
- [97] F. Dausinger, J. Shen, Energy Coupling Efficiency in Laser Surface Treatment., *ISIJ International*. 33 (1993) 925–933. <https://doi.org/10.2355/isijinternational.33.925>.
- [98] M. Narazaki, M. Kogawara, Q. MING, Y. Watanabe, Measurement and database construction of heat transfer coefficients of gas quenching, *Strojniški Vestnik*. 55 (2009) 167–173.
- [99] American Welding Society, Alloy Composition and Critical Temperatures in Type 410 Steel Welds, *WJ*. 97 (2018) 286–296. <https://doi.org/10.29391/2018.97.025>.
- [100] C. Capdevila, F.G. Caballero, C.G. de Andrés, Determination of Ms Temperature in Steels: A Bayesian Neural Network Model., *ISIJ International*. 42 (2002) 894–902. <https://doi.org/10.2355/isijinternational.42.894>.
- [101] M. Alizadeh-Sh, S.P.H. Marashi, M. Pouranvari, Resistance spot welding of AISI 430 ferritic stainless steel: Phase transformations and mechanical properties, *Materials & Design (1980-2015)*. 56 (2014) 258–263. <https://doi.org/10.1016/j.matdes.2013.11.022>.
- [102] X. Zhang, Y. Zhang, Y. Wu, S. Ao, Z. Luo, Effects of melting-mixing ratio on the interfacial microstructure and tensile properties of austenitic–ferritic stainless steel joints, *Journal of Materials Research and Technology*. 8 (2019) 2649–2661. <https://doi.org/10.1016/j.jmrt.2018.12.025>.
- [103] Ch.J. Rao, S. Ningshen, J. Philip, Atmospheric air oxidation of 9Cr-1Mo steel: Depth profiling of oxide layers using glow discharge optical emission spectrometry, *Spectrochimica Acta Part B: Atomic Spectroscopy*. 172 (2020) 105973. <https://doi.org/10.1016/j.sab.2020.105973>.
- [104] C.Y. Cui, X.G. Cui, X.D. Ren, M.J. Qi, J.D. Hu, Y.M. Wang, Surface oxidation phenomenon and mechanism of AISI 304 stainless steel induced by Nd:YAG pulsed laser, *Applied Surface Science*. 305 (2014) 817–824. <https://doi.org/10.1016/j.apsusc.2014.04.025>.
- [105] S. Ghorbani, R. Ghasemi, R. Ebrahimi-Kahrizsangi, A. Hojjati-Najafabadi, Effect of post weld heat treatment (PWHT) on the microstructure, mechanical properties, and corrosion resistance of dissimilar stainless steels, *Materials Science and Engineering: A*. 688 (2017) 470–479. <https://doi.org/10.1016/j.msea.2017.02.020>.
- [106] L.R.C. Malheiros, E.A.P. Rodriguez, A. Arlazarov, Mechanical behavior of tempered martensite: Characterization and modeling, *Materials Science and Engineering: A*. 706 (2017) 38–47. <https://doi.org/10.1016/j.msea.2017.08.089>.

- [107] L. Wang, M. Gao, C. Zhang, X. Zeng, Effect of beam oscillating pattern on weld characterization of laser welding of AA6061-T6 aluminum alloy, *Materials & Design*. 108 (2016) 707–717. <https://doi.org/10.1016/j.matdes.2016.07.053>.
- [108] A. Faye, Y. Balcaen, L. Lacroix, J. Alexis, Effects of welding parameters on the microstructure and mechanical properties of the AA6061 aluminium alloy joined by a Yb: YAG laser beam, *Journal of Advanced Joining Processes*. 3 (2021) 100047. <https://doi.org/10.1016/j.jajp.2021.100047>.
- [109] H.M. Espejo, D.F. Bahr, Substrate cracking in Ti-6Al-4V driven by pulsed laser irradiation and oxidation, *Surface and Coatings Technology*. 322 (2017) 46–50. <https://doi.org/10.1016/j.surfcoat.2017.05.001>.
- [110] T. Guo, L. Qiao, X. Pang, A.A. Volinsky, Brittle film-induced cracking of ductile substrates, *Acta Materialia*. 99 (2015) 273–280. <https://doi.org/10.1016/j.actamat.2015.07.059>.
- [111] I.S. Yasnikov, A. Vinogradov, Y. Estrin, Revisiting the Considère criterion from the viewpoint of dislocation theory fundamentals, *Scripta Materialia*. 76 (2014) 37–40. <https://doi.org/10.1016/j.scriptamat.2013.12.009>.
- [112] M. Fraser, H. Zurob, P. Wu, O. Bouaziz, Increasing Necking Strain through Corrugation: Identifying Composite Systems That Can Benefit from Corrugated Geometry, *Materials*. 13 (2020) 5175. <https://doi.org/10.3390/ma13225175>.
- [113] Z. Wang, J. Dirrenberger, P. Lapouge, S. Dubent, H. Jabir, V. Michel, Microstructure Evolution and Mechanical Properties of AISI 430 Ferritic Stainless Steel Strengthened Through Laser Carburization, *Journal of Engineering Materials and Technology*. 144 (2022) 041005. <https://doi.org/10.1115/1.4055025>.
- [114] I.Y. Khalfallah, M.N. Rahoma, J.H. Abboud, K.Y. Benyounis, Microstructure and corrosion behavior of austenitic stainless steel treated with laser, *Optics & Laser Technology*. 43 (2011) 806–813. <https://doi.org/10.1016/j.optlastec.2010.11.006>.
- [115] Y. Hao, J. Li, X. Li, W. Liu, G. Cao, C. Li, Z. Liu, Influences of cooling rates on solidification and segregation characteristics of Fe-Cr-Ni-Mo-N super austenitic stainless steel, *Journal of Materials Processing Technology*. 275 (2020) 116326. <https://doi.org/10.1016/j.jmatprotec.2019.116326>.
- [116] T. Wegrzyn, Delta ferrite in stainless steel weld metals, *Welding International*. 6 (1992) 690–694. <https://doi.org/10.1080/09507119209548267>.
- [117] A. Pineau, A.A. Benzerga, T. Pardoen, Failure of metals I: Brittle and ductile fracture, *Acta Materialia*. 107 (2016) 424–483. <https://doi.org/10.1016/j.actamat.2015.12.034>.
- [118] A.M. Nair, G. Muvvala, A.K. Nath, A study on in-situ synthesis of TiCN metal matrix composite coating on Ti-6Al-4V by laser surface alloying process, *Journal of Alloys and Compounds*. 810 (2019) 151901. <https://doi.org/10.1016/j.jallcom.2019.151901>.
- [119] J.J. Blecher, T.A. Palmer, T. DebRoy, Solidification Map of a Nickel-Base Alloy, *Metall and Mat Trans A*. 45 (2014) 2142–2151. <https://doi.org/10.1007/s11661-013-2149-1>.
- [120] N.A. Berjeza, S.P. Velikevitch, V.I. Mazhukin, I. Smurov, G. Flamant, Influence of temperature gradient to solidification velocity ratio on the structure transformation in

- pulsed- and CW-laser surface treatment, *Applied Surface Science*. 86 (1995) 303–309. [https://doi.org/10.1016/0169-4332\(94\)00446-3](https://doi.org/10.1016/0169-4332(94)00446-3).
- [121] Z. Li, G. Yu, X. He, S. Li, H. Li, Q. Li, Study of thermal behavior and solidification characteristics during laser welding of dissimilar metals, *Results in Physics*. 12 (2019) 1062–1072. <https://doi.org/10.1016/j.rinp.2018.12.017>.
- [122] G.F. Vander Voort, G.M. Lucas, E.P. Manilova, Metallography and Microstructures of Stainless Steels and Maraging Steels, in: G.F. Vander Voort (Ed.), *Metallography and Microstructures*, ASM International, 2004: pp. 670–700. <https://doi.org/10.31399/asm.hb.v09.a0003767>.
- [123] H. Zhang, C.H. Zhang, Q. Wang, C.L. Wu, S. Zhang, J. Chen, A.O. Abdullah, Effect of Ni content on stainless steel fabricated by laser melting deposition, *Optics & Laser Technology*. 101 (2018) 363–371. <https://doi.org/10.1016/j.optlastec.2017.11.032>.
- [124] A.L. Schaeffler, Constitution diagram for stainless steel weld metal, *Metal Progress*. 56 (1949) 680.
- [125] O. Bouaziz, S. Allain, C. Scott, Effect of grain and twin boundaries on the hardening mechanisms of twinning-induced plasticity steels, *Scripta Materialia*. 58 (2008) 484–487. <https://doi.org/10.1016/j.scriptamat.2007.10.050>.
- [126] P. Chandrasekar, V. Balusamy, K.S.R. Chandran, H. Kumar, Laser surface hardening of titanium–titanium boride (Ti–TiB) metal matrix composite, *Scripta Materialia*. 56 (2007) 641–644. <https://doi.org/10.1016/j.scriptamat.2006.11.035>.
- [127] N. Takata, M. Liu, H. Kodaira, A. Suzuki, M. Kobashi, Anomalous strengthening by supersaturated solid solutions of selectively laser melted Al–Si-based alloys, *Additive Manufacturing*. 33 (2020) 101152. <https://doi.org/10.1016/j.addma.2020.101152>.



# Architecturation de tôles métalliques par traitement laser localisé

## Résumé

Les ondulations peuvent introduire une augmentation du taux de l'écrouissage pendant l'essai de traction en raison du dépliage comparées aux lignes droites. Cette augmentation peut retarder la striction des matériaux architecturés renforcés par des ondulations sans trop de perte de résistance, ce qui peut améliorer le compromis résistance-ductilité des matériaux. Le procédé laser est utilisé pour traiter localement les tôles d'acier pour induire des renforts droits et ondulés. A cet effet, un acier inoxydable ferritique AISI 430 a été trempé et carburé, et un acier recuit a été trempé. La microstructure et les propriétés mécaniques des éprouvettes traitées au laser ont été caractérisées. Des matériaux architecturés renforcés par différentes géométries ont été fabriqués et leur comportement mécanique a été mesuré avec un système de corrélation d'images. Les résultats montrent que des géométries et des combinaisons matrice/renforcement appropriées peuvent ralentir la descente du taux d'écrouissage durant la traction, retarder l'apparition de striction et favoriser la ductilité.

**Mots clés :** matériaux architecturés, procédé laser, durcissement, carburation, écrouissage, aciers, propriétés mécaniques, mesures de champs par corrélation d'image

## Résumé en anglais

Corrugations can introduce a geometric work hardening boost during tensile test due to unbending process compared to straight lines. This boost can enhance the necking strain of architected materials reinforced by corrugations without much loss in strength, which can improve the strength-to-ductility trade-off and fill gaps in the material-property space. Laser process is applied as a thermal source to treat locally steel sheets to induce straight and corrugated reinforcements. For this purpose, AISI 430 ferritic stainless steel was hardened and carburized, and an annealed steel was hardened. Microstructure and mechanical properties of laser-treated parts were characterized. Architected specimens reinforced by different geometries were fabricated and their mechanical behavior was measured with a digital image correlation system. Results show that suitable reinforcement geometries and matrix/reinforcement combinations can slow down the work hardening rate decrease when loaded and increase the necking strain.

**Keywords:** architected materials, laser processing, hardening, carburization, work hardening, steels, mechanical properties, Digital Image Correlation (DIC)